DEPARTAMENTO DE FISICA TEORICA Y DEL COSMOS

Universidad de Granada

Galaxies, clusters of galaxies and the magnetic field interchange

Memoria que presenta
Dña. África Castillo Morales
para optar al grado de
Doctora en Ciencias Físicas

UNIVERSIDAD Ð GRANADA
julio de 2004

A mis padres
y a Javi

Agradecimientos

Quisiera expresar mi agradecimiento a las instituciones que han hecho posible la realización de esta tesis: Departamento de Física Teórica y del Cosmos, el instituto de Astrofísica de Liverpool y el instituto de Astrofísica de Innsbruck.

Muchas han sido las personas que han contribuido a que pueda llegar hoy a escribir estas líneas. El comienzo no fue fácil pero he encontrado en el camino buenos amigos que me han ayudado a seguir en él y llegar al final.

Me gustaría en primer lugar dar las gracias a mi directores de tesis y sobre todo amigos Eduardo Battaner y Sabine Schindler. Gracias Eduardo por animarme a emprender esta aventura, por tus consejos siempre sabios, por todo lo que me has ayudado y por estar disponible hasta en los momentos más difíciles. Gracias Sabine por tu amistad y haberme hecho sentir como en casa cuando estaba tan lejos de ella. Os debo a ambos todo lo que he aprendido dentro de este mundo de la Astrofísica, gracias por guiarme, corregirme, enriquecerme y presentarme a las galaxias y a los cúmulos de galaxias.

No puedo olvidarme de mis compañeros de despacho. No sé que hubiera hecho sin la compañía de Betty al comienzo de esta tesis en Liverpool, gracias por compartir tantos buenos momentos conmigo. Gracias Jorge por estar ahí siempre disponible y ayudarme con tantos problemas, por *idllizarme*, por las buenas discusiones, por tu amistad. Gracias Ana por *paralelizarme* de vez en cuando, por contagiarme ese optimismo y alegría en tantas ocasiones, y que sepas que la próxima eres tú. También me gustaría agradecer a Isa, y a la pequeña Sara su compañía, haciendo que las tardes de trabajo sean mucho más agradables escuchando a los lunnis...

A todos mis compañeros: Estrella, Lucas, María Luisa, Almu, Marco, gracias por apoyarme durante todo este tiempo y compartir ratos de charla, además de unas cuantas galletas.

A mis amigos, que siempre han estado conmigo y han valorado mi trabajo, gracias a: Charo, Jose, Ana, JC, Enamo, AnaFru, Almu, Marco, María y Tatín.

Y sobre todo mis gracias a la familia, por confiar en mí, por cuidarme y animarme tanto. Gracias a papá, mamá, Antonio, Fran y a Encarni por estar tan cerca siempre que te he necesitado y a mi abueli que tiene tantas o más ganas que yo de terminar la tesis. A Paco y Genoveva, Mari Ge, Félix, María José, Antonio y a la pequeña María por darme tanto cariño. Y sobre todo a Javi porque sin él no hubiera sido capaz de llegar hasta aquí. Sin su paciencia y su comprensión todo hubiera sido mucho más difícil, él ha dado sentido a tanto esfuerzo.

África
Granada, Julio 2004.

Abstract

We present in this thesis the analysis of gas and dark matter distributions in a sample of ten nearby clusters ($0.03 < z < 0.09$) with temperatures between 4.4 and 9.4 keV. These galaxy clusters have been studied in detail using X-ray data and global physical properties have been determined. Correlations between these quantities have been analysed and compared with the results for distant clusters. We found an interesting dependence between the relative gas extent (expressed as the ratio of gas mass fractions at r_{500} and $0.5 \times r_{500}$) and the total cluster mass. The extent of the gas relative to the extent of the dark matter tends to be larger in less massive clusters. This dependence might give us some hints about non-gravitational processes in clusters.

Furthermore, new X-ray observations for two morphologically different clusters of galaxies CL 0939+4713 and RBS797, are presented in this thesis. The determination of the dynamical state of clusters at different redshifts is very important for cosmology. The X-ray morphology complemented with temperatures maps or galaxy distribution is an indicator of the dynamical state. *XMM-Newton* satellite, with its major capabilities for spectroscopy, allows us to trace better temperature and metallicity maps. We have analyzed the *XMM-Newton* observation of the cluster CL 0939+4713 (z=0.41). The X-ray image shows pronounced substructure, with two main subclusters which have even some internal structure, confirming this system is a dynamically young cluster. This conclusion is supported by the temperature distribution: a hot region is found between the two main subclusters indicating that they are at the beginning of a major merger, and that they will probably collide in a few hundreds of Myr. The intra-cluster gas of CL 0939+4713 shows inhomogeneities in the metal distribution, with the optically richer subcluster having a higher metallicity.

Interaction between the intra-cluster gas and radio sources in the centre of galaxy clusters has been found in several nearby clusters with an anticorrelation of X-ray emission and radio emission. Such an interaction of two different components is particularly interesting because one can infer physical conditions and processes in the cluster centre, e.g. heating and cooling effects, magnetic fields or energies of relativistic particles, from the pressure balance. We show the presence of depressions in the X-ray emission of the distant galaxy cluster RBS797 in a *Chandra* observation. They reveal clear X-ray minima in the cluster centre. We hypothesise that these minima are caused by interaction between the radio source embedded in the central cluster galaxy and the intra-cluster medium. RBS797 would be the first *distant* cluster in which evidence for such interaction has been found.

Radio observations of clusters of galaxies show the presence of other interesting components in these objects: relativistic particles and magnetic fields. They are dynamically important in both, galaxies and intra-cluster medium. However the interaction of the intra- and extra- galactic

magnetic fields has hardly been considered so far although the interconnection may be of high interest. In order to determine how much magnetic field is ejected from the galactic nucleus or from the innermost disk of spiral galaxies we can study the detailed dynamics of stars and gas in the central regions (≤ 1 kpc) of spiral galaxies with intermediate inclination, with some type of nuclear activity. The fiber system INTEGRAL in combination with the fiber spectrograph WYFFOS at the William Herschel Telescope is used for this task in this thesis. We use 2-D spectroscopy to study the circumnuclear region of two galaxies NGC 5033 and NGC 4321. We identify their structure of ionization from different emission lines maps and study the kinematics of the ionized emitters from the comparison between the kinematics of stars and gas.

In the case of NGC 5033, the intensity map of the Hβ emission line represents a spiral or ring like pattern of HII regions. On the contrary, the [OIII] intensity map morphology is markedly anisotropic. The strong morphological differences imply that the [OIII] emitters represent highly ionized gas illuminated by the central source. The [OIII] map morphology is compatible with a biconical structure of ionization induced by strong extinction in the galaxy disc that also obscures half of the spheroidal stellar bulge. The Seyfert 1 nucleus (identified from the Hβ broad emission lines) is located at the apex of the biconical structure and could be offcentered with respect to the stellar rotation center. This result has been also found in other Seyfert galaxies and interpreted in terms of a past merger. The offcentering could indicate the presence of nonsymmetric departures in the gravitational potential which could be fueling the active nucleus. The kinematics of the [OIII] emitters presents important deviations at kpc scale with respect to the stellar velocity field and shows features related to the biconical geometry.

In the case of NGC 4321, the Hα intensity map shows the emission distributed in a ring ovally shaped where several HII regions can be distinguished. The intensity maps computed from [N II] and [S II] emission lines are quite similar between them and the Hα intensity map. They show a centrally peaked emission in addition to the emission connecting two bright Hα regions in th NE and SW directions. The Hα velocity field in the inner region ($r < 1.2$kpc) of this galaxy shows the basic spider pattern which indicates circular motions in a rotating disk. But at the same time the velocity field shows the effect of the non-circular motions. We can see a curved kinematical minor axis indicating probably the presence of another kinematic system. Furthermore the isovelocity contours are deformed following the structure of the spiral arms. The optical nucleus appears located asymmetrically at the higher resolution continuum maps and seems to be not coincident with the kinematical centres defined. We have derived the Hα rotation curve out to $15''$using the three available INTEGRAL angular resolutions. This curve shows a steep rise, reaching ~ 130 kms^{-1} in $3''$ (249 pc), indicating a high concentration of mass at the galactic centre. Furthermore residual velocity maps have been derived to study the presence of non-circular motions showing higher absolute values at the positions ot the inner incoming spiral arms. The stellar velocity field derived from the Na absorption line is quite complicated and not easy to interpret. The lower resolution stellar velocity map shows clearly two maxima not present in the ionized gas velocity field. The higher resolutions velocity maps shows a dramatic difference between the stellar and ionized gas velocity field, with the stellar veloticity map extremely distorted in its inner region. However, there are similitudes between both velocity fields (ionized gas and stellar) related with the distorsions produced in the velocity field by the spiral structure in this galaxy.

Contents

1

General Introduction

Clusters of galaxies are fascinating objects because their observations allow us to constrain the parameters of the standard cosmological model. In particular, they are widely used as indicators of the mean matter density of the Universe. Galaxy clusters have been shown to harbour very large quantities of dark matter since the pioneering work of Zwicky (1933), but its exact amount, its spatial distribution and above all its very nature are still awaiting answers. They offer a laboratory for studying such diverse astrophysical problems as the form of the initial fluctuation spectrum, the evolution and formation of galaxies, environmental effects on galaxies, and the nature and amount of dark matter in the Universe, as well as providing tracers of the large-scale structure.

The major part of the matter in the Universe is and cannot be visible and is therefore called dark matter. The determination of the mass of galaxy clusters, large and massive bound structures, gives therefore information on the distribution and amount of this dark matter – an important criterion for cosmological models. The total mass of a cluster can be determined by various independent ways: strong and weak lensing, X-ray observations and galaxy velocities The ratio of visible to total mass is a measure of the baryon fraction Ω_{baryon} – a much discussed quantity since current measurements of 10-30% are in contradiction with primordial nucleosynthesis for $\Omega_m = 1$, a famous discrepancy termed "baryon catastrophe", (White et al., 1993), which is therefore one of the important hints for a low Ω Universe. The relative distribution of gas and dark matter within a cluster also gives useful information on physical processes going on in clusters.

Furthermore, the distribution of the different cluster components can be studied when mass profiles are available. From X-ray observations the gas density and the gas temperature can be determined, which yield not only the gas mass profile, but under the assumptions of hydrostatic equilibrium and spherical symmetry also the total mass profile of the cluster. Numerical simulations showed that these masses are quite reliable for virialised clusters (Dolag & Schindler, 2000; Evrard et al., 1996; Schindler, 1996b). A comparison of both radial profiles (gas and total mass) gives information on the relative distribution of dark and gaseous matter. This can be used to learn about the cluster formation process: whether all the energy comes from the gravitational collapse, or whether there are additional physical heating processes involved.

In this thesis we analyze ten nearby clusters of galaxies using the best X-ray observations from ROSAT and ASCA satellites. We determine various cluster properties for massive systems and compare the distribution of the different components within these clusters. Moreover, we use the determined masses to derive relations between the masses and other cluster quantities, which give more information about cluster formation and evolution.

The formation and evolution of clusters sensitively depends on cosmological parameters like the mean matter density in the Universe Ω_m and the dark energy. Therefore it is important to determine the dynamical state of clusters at different redshifts, i.e. at different evolutionary states. The X-ray morphology alone is not the best indicator of the dynamical state, but it should be complemented with all other information available, e.g. the temperature map or the galaxy distribution. The combination of all data gives a detailed picture of the state of a cluster. *XMM-Newton* satellite, with its major capabilities for spectroscopy, allows us to trace better temperature and metallicity maps. We present in this thesis the analysis of an *XMM-Newton* observation of the cluster CL 0939+4713 (z=0.41), where we confirm this system is a dynamically young cluster.

Radio observations of clusters of galaxies show the presence of other interesting components in these objects: relativistic particles and magnetic fields. They are dynamically important in both, galaxies and intra-cluster medium. Magnetic fields in clusters are observed through the diffuse cluster-wide synchrotron radiation (radio halos and relics) and the Faraday rotation of polarized sources within or behind the cluster. Magnetic fields are important in the evolution and dynamics of clusters (Lesch & Chiba, 1997). Also the determination of the cluster mass with X-ray observations may be seriously affected in merging clusters if magnetic fields are ignored (Dolag & Schindler, 2000). First analysis have shown that cluster magnetic fields are not constant but decrease with radius (Dolag et al., 2001). Magnetic fields in galaxies are responsible of many morphological features and are a non-negligible factor in galactic dynamics (Florido & Battaner, 1997). However the interaction of the intra- and extra- galactic magnetic fields has hardly been considered so far although the interconnection may be of high interest for a series of reasons.

Observations reveal a clear matter interaction characterized by ejections, infall, convective motions in the galactic corona. This interaction produces a very large β (i.e. the coefficient of turbulent magnetic diffusion). It can be estimated that β may be as large as 6 kpc^{2}Gyr^{-1}. Mainly the vertical component of the galactic field strength should maintain an equilibrium between the magnetic fields in the galaxies and the intracluster medium (ICM) (Battaner & Florido, 2000). In this way, the evolution of magnetic fields in the different structures and their interaction can be traced. Galaxies also eject magnetic fields as shown by radio halos at large distance from the disks. An especially well studied galaxy with a radio halo ejected from the disk, is M82 (Golla et al., 1996; Reuter et al., 1992). It has been even proposed that the intra-cluster field could be fed by field ejections from M82-like galaxies (Kronberg et al., 1999). On the other hand, the reverse field flux is well possible: the pregalactic cluster could have been already magnetized, and pregalactic magnetic fields could provide the seed for the present galactic ones (Battaner & Lesch, 2000)

Interaction between the intra-cluster gas and radio sources in the centre of galaxy clusters has been found in several nearby clusters with an anticorrelation of X-ray emission and radio emission, e.g. in the Perseus cluster Fabian et al. (2000), in Hydra-A McNamara et al. (2000), and in Abell clusters A4059 Huang & Sarazin (1998), A2597 McNamara (2001), A2052 Sarazin (2001), A2199 Fabian (2001), and A2634 Schindler (1996a) and others. Such an interaction of two different components is particularly interesting because one can infer physical conditions and processes in the cluster centre, e.g. heating and cooling effects, magnetic fields or energies of relativistic particles, from the pressure balance. We present in this thesis the discovery of depressions in the X-ray emission of the distant galaxy cluster RBS797 in a *Chandra* observation.

In order to determine how much magnetic field is ejected from the galactic nucleus or from the innermost disk of spiral galaxies we can study the detailed dynamics of stars and gas in the central regions (≤ 1 kpc) of spiral galaxies with intermediate inclination, with some type of nuclear activity. The fiber system INTEGRAL (Arribas et al., 1998) in combination with the fiber spectrograph WYFFOS at the William Herschel Telescope is used for this task in this thesis. We use 2-D spectroscopy to study the circumnuclear region of two galaxies NGC 5033 and NGC 4321 which forms part of the Virgo cluster. We identify their structure of ionization from different emission lines maps and we study the kinematics of the ionized emitters from the comparison between the kinematics of stars and gas. The dynamics of gas and stars are completely decoupled. The inward flux required to feed the central black hole has been detected, but much more observational effort is required. Ejections from this central part are particularly intense and are considered to fuel synchrotron galactic halos.

The title of this thesis encloses the study of various different aspects of galaxies and clusters of galaxies. On one hand we study clusters of galaxies deriving the gas distribution and properties from their X-ray observations. On the other hand we present results about galaxies, obtaining the kinematics of their most inner regions. Magnetic fields and mass interchange are a link between both, galaxies and clusters of galaxies. Different processes allow the exchange and the interaction of magnetic fields between these two structures. This topic has not been developed completely since it is very ambitious and exceeds the scope of a single thesis, but this work intends to be the beginning in a more extensive investigation.

The contents in this thesis are organized as follows:

In chapter 2 we present a review about the presence of magnetic fields in galaxies, clusters of galaxies and the different mechanicisms that contribute to the interchange of magnetic fields between galaxies and clusters of galaxies.

Chapters 3, 4, 5 and 6 are dedicated to the X-ray observations of clusters of galaxies. In chapter 3 we introduce some generalities of clusters of galaxies, how they are observed in the X-ray band, their main components and the mass determination. In Chapter 4 we present the analysis of a sample of nearby clusters where we have applied the X-ray method to calculate masses. This work has been published by Castillo-Morales & Schindler (2003). In chapters 5 and 6 are presented the morphological and spectral analysis of the X-ray observations of two different clusters CL 0939+4713 observed with *XMM-Newton* and RBS797 observed with *Chandra*. These results have been published by De Filippis, Schindler, & Castillo-Morales (2003) and Schindler, Castillo-Morales, De Filippis, Schwope, & Wambsganss (2001), respectively.

Chapters 7, 8 and 9 are dedicated to the analysis of the central part of galaxies. In Chapter 7 we introduce the instrument *INTEGRAL* at WHT, the observations and the data reduction process. In Chapter 8 and 9 we present the analysis and results for the case of NGC 5033 and NGC 4321 respectively. The main results for the galaxy NGC 5033 have been submitted to A&A and for NGC 4321 the main results will be included in a paper that is currently in preparation.

2

Magnetic fields in galaxies and clusters of galaxies and their origin

The aim of this chapter is to describe how we obtain information about the presence of magnetic fields in galaxies and in clusters of galaxies, how magnetic fields are distributed and how they originate and evolve. Magnetic fields in galaxies are responsible of many morphological features and are a non-negligible factor in galactic dynamics (e.g. Battaner & Florido, 2000; Beck, 2004; Florido & Battaner, 1997). Moreover, magnetic fields are important in the evolution and dynamics of clusters (e.g. Lesch & Chiba, 1997). However the interaction of the intra- and extra-galactic magnetic fields has hardly been considered so far although the interconnection may be of high interest for questions related to the origin and evolution of magnetic fields.

2.1 Introduction

Magnetic fields are ubiquitous in the Universe. They play an important role in various branches of astrophysics. Magnetic fields are an important dynamical constituent of cosmic plasma acting on charged particles by the Lorentz force. They are able to induce highly anisotropic transport processes like heat conduction, ambipolar diffusion, and propagation of cosmic rays. They are essential for the acceleration of cosmic rays. Magnetic fields are particularly important for angular momentum transport, producing a magnetic brake, without which the Sun and similar stars would not spin as slowly as they do today or even they would not exist. They play a crucial role in driving turbulence in accretion disks providing perhaps the crucial viscosity needed for accretion. Large scale fields in these disks are also thought to be important in driving jets. In the outermost parts of galaxies the magnetic field energy density may even reach the level of global rotational energy density. If so, the rotation curves at large radii could be affected by magnetic fields, as discussed by Battaner & Florido (2000).

Magnetic fields with micro-gauss strengths and coherence scales of order several kiloparsecs are also observed in nearby galaxies and perhaps in galaxies which have just formed. The magnetic field strength in galactic spiral arms can be up to 30 microgauss (e.g. in M51). Fields of order several micro-gauss and larger, with even larger scales are observed in clusters of galaxies. Strengths of ordered magnetic fields in the intracluster medium of cooling flow clusters exceed those which are typical of the ionized interstellar medium of the Milky Way. These observations suggest that galaxy formation, and even cluster dynamics are, at least in some circumstances influenced by magnetic forces, which also could possibly affect the global dynamics in areas of some galaxies, especially dwarf galaxies, which are rich in interstellar gas and cosmic rays. The understanding of the origin of galactic and extragalactic magnetic fields is one of the most fascinating problems in modern astrophysics.

2.2 Observations of cosmic magnetic fields

Magnetic fields observed in the Universe have a homogeneous (or uniform) component and a non-uniform component that we can write in this way: $\mathbf{B}_{\rm tot} = \mathbf{B} + \delta\mathbf{B}$, where $\mathbf{B}$ is the uniform component and δB is the non-uniform component. Different experimental techniques can probe different components of large-scale magnetic fields. Another important distinction is between $B_\perp$ and $B_{||}$: there are measurements (like the synchrotron emission) which are sensitive to $B_\perp$ i.e. the transverse component of the magnetic field; there are other measurements (like the Faraday rotation or the Zeeman splitting of spectral lines) which are sensitive to $B_{||}$ i.e. the magnetic field along the line of sight.

The galactic and extragalactic magnetic fields observations can be summarized in this way:

Magnetic fields with strength $\sim 10\mu$G are found in spiral galaxies. These fields include a large-scale component whose coherence length is comparable to the size of the visible disk. There are also small-scale tangled fields with energy densities approximately equal to that of the coherent component. The magnetic field in spiral galaxies often exhibits patterns or symmetries with respect to both the galaxy's spin and the equatorial plane. Magnetic fields are ubiquitous in elliptical galaxies, though in contrast with the fields found in spirals they appear to be random with a coherence length much smaller than the galactic scale. Magnetic fields have also been observed in irregular galaxies.

Microgauss magnetic fields have been observed in the intracluster medium of a number of rich clusters. The coherence length of these fields is comparable to the scale of the cluster galaxies. There is a compelling evidence for galactic-scale magnetic fields in a redshift up to $z \approx 0.4$. Moreover, microgauss fields have been detected in radio galaxies at $z > 2$. Magnetic fields may also exist in damped Lyman alpha (Ly α) systems at cosmological redshifts. There are no detections of purely cosmological fields (i.e., fields not associated with gravitationally bound or collapsing systems). Constraints on cosmological magnetic fields have been derived by considering their effect on big-bang nucleosynthesis, the cosmic microwave background, and polarized radiation from extragalactic sources.

2.2.1 Observational methods

The basic information about the presence and structure of magnetic fields in galaxies is obtained from optical and radio observations. Measurements of magnetic fields are *indirect* in the sense that what we are detecting is only the signature of magnetic fields recorded in electromagnetic wave radiations. We describe the four most common methods used to study astrophysical magnetic fields.

Synchrotron emission

Polarized radio emission originates in the synchrotron process. Synchrotron emission, the radiation produced by relativistic electrons spiraling along magnetic fields lines, is used to study magnetic fields in astrophysical sources ranging from pulsar to superclusters. The energy emitted from a unit volume, per unit time, per unit frequency interval and per unit solid angle for the synchrotron emission is a function of $B_\perp$ and of the relativistic electron density: $W(B_\perp, \nu) = W_0 n_0 B_{tot,\perp}^{(1+\gamma)/2} \nu^{(1-\gamma)/2}$, where ν is the frequency, W_0 is a proportionality constant depending only upon the spectral index γ which also determines the relativistic electron number density distribution for electrons with energies in the range dE: $n_e dE = n_0 E^{-\gamma} dE$

A useful estimate for the maximal emission from electrons of energy E is given by Ruzmaikin et al. (1988): $\left(\frac{\nu}{MHz}\right) \simeq 15 \left(\frac{B_{tot,\perp}}{\mu G}\right) \left(\frac{E}{\mathrm{GeV}}\right)^2$. With the typical values for galactic magnetic fields, synchrotron radiation is observed in the radio range, i.e. at m, cm and mm wavelengths. One can proceed in the following way for the magnetic field measurement: we can measure the emission intensity; from this estimate, defining as L the typical size of the source, we can deduced the quantity $B_{tot,\perp}^{(\gamma+1)/2}\mathrm{W_0 L}$ and finally the magnetic field can be obtained by specifying the electron density distribution of the source. While the second step is rather well defined (γ can indeed be determined from the observed emission spectrum), we need to assume a model for the third step. One generally assumes that the energy densities of the field and particles are in equipartition. Sometimes, equipartition means equal amounts of turbulent and magnetic energy densities. We call here "equipartition" the assumption of equal amounts of cosmic ray and magnetic energy densities. The unknown contribution of protons to cosmic ray energy densities introduce difficulties in the interpretation of the synchrotron continuum. In our Galaxy we have independent measurements of the local cosmic-ray electron energy density from direct measurements and about the cosmic-ray proton distribution from γ-ray data.

Synchrotron emission is intrinsically highly linearly polarized, 70-75% in a completely regular magnetic field, which can give the orientation of the magnetic field. The strength of synchrotron polarization is proportional to $(B_\perp/B_{tot,\perp})^2$, i.e. the ratio between the magnetic energy densities of the uniform and total magnetic field. Thus, the synchrotron polarization is sensitive to the random component of the large-scale magnetic field.

The linearly polarized intensity reveals the strength and the structure of the resolved regular field in the plane of the sky. The orientation of the linear polarization shows the direction of the magnetic field and the degree of polarization is an important indicator of the field's uniformity and structure.

Faraday rotation

However, the observed polarization vectors suffer Faraday rotation and depolarization (i.e. a decrease of the degree of linear polarization when compared to the intrinsic one) on the way from the radiation's origin to us. Such situations occur in nature in cases where a polarized radio galaxy is located behind the magnetized medium of a galaxy, or behind or embedded in a galaxy cluster. Electromagnetic waves, propagating through a region of both magnetic field and free thermal electrons, experience Faraday rotation wherein left- and right-circular polarization states travel with different phase velocities. For linearly polarized radiation, this results in a rotation with time, or equivalent path length, of the electric-field vector by an angle: $\phi = \frac{e^3\lambda^2}{2\pi m_e^2 c^4} \int_0^{l_s} n_e(l) B_{\|}(l) dl + \phi_0$, where m_e is the electron mass, λ is the wavelength of the radiation, ϕ_0 is the initial polarization angle, and $B_{||}$ is the line-of-sight component of the magnetic field. Here $n_e(l)$ is the density of thermal electrons along the line of sight from the source ($l = l_s$) to the observer ($l = 0$). The angle ϕ is usually written in terms of the rotation measure, RM: $\phi = (RM)\lambda^2 + \phi_0$, where $RM = \frac{e^3}{2\pi m_e^2 c^4} \int_0^{l_s} n_e(l) B_{||}(l) dl \simeq 810 \frac{\text{rad}}{\text{m}^2} \int_0^{l_s} \left(\frac{n_e}{\text{cm}^{-3}}\right) \left(\frac{B_{||}}{\mu G}\right) \left(\frac{dl}{\text{kpc}}\right)$.

In general, the polarization angle must be measured at three or more wavelengths in order to determine RM accurately and remove the degeneracy in the angle: $\phi = \phi \pm n\pi$. The rotation measure RM depends not only on the magnetic field ($B_{||}$) but also on the column density of electrons. From radio observations, different techniques can be used to determine n_e. One possibility is to use the regular pulses of electromagnetic radiation emitted by pulsars which periods are ranging from few milliseconds to few seconds. By comparing the arrival times of different radio pulses at different radio wavelengths, it is found that signals are slightly delayed as waves travel faster in the vacuum than in an ionized medium. Hence, from pulsars the column density of electrons can be obtained in the form of the dispersion measure, i.e. $DM \propto \int n_e dl$. If we divide the RM by DM, an estimate of the magnetic field can be obtained. Due to their abundance, pulsars lead to the best determination of the magnetic field in the galactic disk (Han & Qiao, 1994), but of course they cannot be used for extragalactic sources.

When clusters of galaxies are involved in Faraday rotation studies, X-ray observations are used to determine the electron density of electrons.

The rotation measure itself is a measure of the magnetic field strength parallel to the line of sight, whereas its sign gives the direction of this magnetic field component. By convention, RM is positive for a magnetic field directed toward the observer and negative for a field directed away. The Faraday rotation includes contributions from all magnetized regions along the line of sight to the source. Following Kronberg & Perry (1982), we can decompose RM intro three basic components: $RM = RM_g + RM_s + RM_{ig}$, where RM_g, RM_s and RM_{ig} are the contributions to the rotation measure due to the Galaxy, the source itself and the intergalactic medium respectively. The field strength of both components, parallel and perpendicular to the line of sight, together with the information of the intrinsic polarization vectors enables us in principle to perform a "tomography" of the magnetic field.

Zeeman splitting

We can make use of the Zeeman splitting effect to determine the large-scale magnetic field in our Galaxy. The energy levels of an hydrogen atom in the background of a magnetic field are not degenerate. The presence of a magnetic field produces a well known splitting of the spectral lines: $\frac{\Delta\nu_z}{\nu} = 1.4g \left(\frac{B_{||}}{\mu G}\right) \left(\frac{\text{Hz}}{\nu}\right)$, where $B_{||}$ is the uniform component of the magnetic field along the line of sight and g is the Landé factor which relates the angular momentum of an atom to is magnetic moment. From the estimate of this splitting, the magnetic field intensity can be deduced. This technique is the one commonly employed to measure the magnetic field of the Sun. But the Zeeman effect is extremely difficult to observe in other galaxies. For the two most common spectral lines in Zeeman effect observations - the 21-cm line for neutral hydrogen and the 18-cm OH line for molecular clouds- $\Delta\nu/\nu \simeq 10^{-9} g(B_{||}/\mu G)$. A shift of this amplitude is to be compared with Doppler broadening, $\Delta\nu/\nu \simeq \text{v}_{\text{th}}/\text{c} \simeq 6 \times 10^{-7}(\text{T}/100\text{K})^{1/2}$, where v_{th} and T are the mean thermal velocity and temperature of the atoms, respectively. Therefore Zeeman splitting is more aptly described as abnormal broadening, i.e., a change in shape of a thermally broadened line.

Positive detections have been restricted to regions of low temperature and high magnetic fields. Within the Galaxy, Zeeman effect measurements have provided information on the magnetic fields in star forming regions and near the Galactic center. Unfortunately, Zeeman splitting has not been observed in external galaxies, much less in intergalactic space, because of Doppler smearing of the radio lines due to dynamical effects, combined with the weak field strengths.

Polarization of optical starlight

Polarized light form stars can reveal the presence of large-scale magnetic fields in our Galaxy and those nearby. The first observations of polarized starlight were made by Hall (1949) and Hiltner (1949). It was found that while the polarization degree for individual stars did not show the expected time variability, polarization levels appeared to correlate with position in the sky. This observation led to think that a new property of the interstellar medium had been discovered. At that time Alfven (1949) and Fermi (1949) were proposing the existence of a galactic magnetic field as a means of confining cosmic rays. A connection between polarized starlight and a galactic magnetic field was made by Davis & Greenstein (1951) who suggested that elongated dust grains would have a preferred orientation in a magnetic field: for prolate grains, one of the short axes would coincide with the direction of the magnetic field. The grains, in turn, preferentially absorb light polarized along the long axis of the grain, i.e., perpendicular to the field. The net result is that the transmitted radiation has a polarization direction parallel to the magnetic field. Polarized starlight does provide information that is complementary to what can be obtained from radio observations.

2.2.2 Galactic magnetic fields

Spiral galaxies are a favorite laboratory for the study of cosmic magnetic fields. There exist estimates of the magnetic field strength over more than 100 spirals and detailed studies of their magnetic structure and morphology have been made over many of them.

The magnetic field of the Galaxy has been studied through the synchrotron emission, Faraday rotation, optical polarization and Zeeman splitting. The latter provides the direct determination of the magnetic field at specific sites in the Galaxy. Measurements of the 21-cm Zeeman effect in galactic HI regions reveal regular magnetic fields with $B \approx 2 - 10\mu G$, with higher values found in dark clouds and HI shells (Heiles, 1990). Faraday rotation studies with surveys of galactic and extragalactic sources have obtained similar values for the galactic field. The first estimates of magnetic field strength from synchrotron data were derived from Phillipps et al. (1981). Their analysis was based on a model for galactic synchrotron emission in which the magnetic field in the Galaxy is decomposed into regular and tangled components. It was obtained an excellent fit to the data when each component was assumed to have a value of $3\mu G$. In more recent estimates (Beck, 2002), a regular field strength of $4\mu G$ and a total local field strength of $6\mu G$ has been obtained.

The study of magnetic fields in other galaxies have been developed mainly through synchrotron and Faraday rotation observations. M31 is an interesting case. Polarized radio emission in this galaxy is confined to a prominent ring of about 10 kpc from the galaxy's center. The equipartition field strength in the ring is found to be $\approx 4\mu G$ for both the regular and random components. The study of a sample of 146 late-type galaxies (Fitt & Alexander, 1993) provided a relatively narrow distribution of the field strength with an average value of $< B_{eq} >\sim 11 \pm 4\mu G$. The magnetic field strength does not appear to depend strongly on galaxy type, although early-type galaxies have a slightly higher mean. Extremal values found in normal galaxies can be up to $20\mu G$ in spiral arms, as in NGC 6946 (Beck, 1991) and NGC 1566 (Ehle et al., 1996). Strongly interacting galaxies or galaxies with a strong radio emission tend to have generally stronger total magnetic fields. The strengths of the regular fields are typically $1-5\mu G$ in the interarm regions in nearby spirals but can reach locally $13\mu G$ in NGC 6946 (Beck & Hoernes, 1996). There are few cases of galaxies with very strong magnetic fields, being M82 an example. The field strength derived in this galaxy from radio continuum observations is $\sim 50\mu G$ (Klein et al., 1988). This galaxy is characterized by a very high star formation rate.

The global structure of the regular magnetic field and the total field (regular + random) is also of interest. The random field is almost always strongest within the spiral arms and thus follows the distribution of cool gas and dust. The regular field is generally weak within spiral arms, except for rare cases like M51 with strong density waves. Therefore the total field is also strongest within the spiral arms where the random field dominates. In the case of M51, the strongest total and regular field are located at the positions of the prominent dust lanes on the inner edges of the optical arms (Neininger, 1992), as expected if it were due to compression by density waves. But in this case the regular field also extend far into the interarm regions. In M31, the regular magnetic field is nearly aligned with the spiral arms forming the bright 'ring' of emission seen in this galaxy (Berkhuijsen et al., 2003).

The large-scale magnetic field in spiral galaxies can be classified according to the parity of the toroidal field (defined as the vector sum of the radial and azimuthal components) under reflections of the azimuthal angle (Ruzmaikin et al., 1988; Vallee, 1997). For some authors, this distinction plays an important role in order to asses the primordial (or non-primordial) nature of the observed field Beck et al. (1996); Zweibel & Heiles (1997). We can plot the toroidal component of the measured magnetic field as a function of the azimuthal angle θ. This is equivalent to plot the $RM(\theta)$ for instance near the symmetry plane of the galaxy. We can have two qualitatively different situations. In the first case $RM(\theta)$ upon rotation of π around the galactic center is even and this corresponds to axis-symmetric spiral galaxies (ASS). In the second case $RM(\theta)$ upon rotation of π around the galactic center is odd and this corresponds to bi-symmetric spiral galaxies (BSS). Since few years ago, there has been a long discussion about the primordial nature of the galactic magnetic field in nearby galaxies. Theorists believing the primordial nature of the galactic magnetic field supported the BSS model, while dynamo theorists supported the conclusion that most of the nearby galaxies are ASS. Summarizing recent results, we can say that there are galaxies where BSS structure dominates (like M81, M51) and at the same time in some galaxies the ASS dominates. In most galaxies the data cannot be described by only a single mode, but require a superposition of several modes which still cannot be resolved by the existing observations.

Radio observations of magnetic fields in edge-on spiral galaxies suggest that in most cases the dominant component of the magnetic field is parallel to the disk plane (Dumke et al., 1995). However in a few cases like M82 (Reuter et al., 1994), NGC 4631 (Golla & Hummel, 1994), NGC 4666 (Dahlem et al., 1997) and NGC 5775 (Tüllmann et al., 2000), magnetic fields are found to extend well away from the disk plane and have strong vertical components. The presence of huge radio halo or radially directed field lines, may be related to the vigorous star-formation activity triggered by galaxy interaction. This hypothesis is implied from the radio data of NGC 4631: radio spurs appear, whose footpoints are connected with star-forming regions in the disk, probably due to newly produced cosmic rays bay supernova explosions. It is not clear whether halo fields are the result of dynamo action in the halo or, fields produced in the disk and carried into the halo by galactic winds or magnetic buoyancy.

Magnetic fields are ubiquitous in elliptical galaxies although they are difficult to observe because of the paucity of relativistic electrons. Nevertheless the presence of magnetic fields is inferred from synchrotron observations. Moreover, Faraday rotation has been observed in the polarized radio emission of background objects in a few cases. While the evidence for microgauss fields in ellipticals is strong, there are no positive detections of polarized synchrotron emission or any other manifestation of a regular magnetic field (Moss & Shukurov, 1996). Therefore, while the inferred field strengths are comparable to those found in spiral galaxies, the coherence scale for these fields is much smaller than the scale of the galaxy itself.

Ordered magnetic fields with strengths similar to those in grand design spirals have also been detected in flocculent galaxies like M33 (Buczilowski & Beck, 1991), NGC 4414 (Soida et al., 2002), NGC 3521 and NGC 5055 (Knapik et al., 2000). These are galaxies with a flocculent spiral structure without signs of the action of density waves. The mean degree of polarization is similar between flocculent and grand-design galaxies.

There are observations of galactic magnetic fields at intermediate redshifts coming from RM studies of radio galaxies and quasars. The evidence of this presence has a serious challenge to the galactic dynamo theory because it would imply that there is a limited time available for field amplification. Athreya et al. (1998) studied 15 high-redshift ($z > 2$) radio galaxies at multiple frequencies in polarized radio emission and found significant RM's in almost all of them, with several of the objects in the sample having $RM > 1000$ radm^{-2}.

2.2.3 Magnetic fields in clusters of galaxies

Clusters of galaxies are large gravitationally bound structures which consist in various components (see Section 3.2). X-ray observations reveal the presence of the hot intracluster gas (10^7 to 10^8 K) which extend to Mpc radii and which dominate the baryonic mass of these systems (10^{13} to 10^{14} $M_\odot$). Nowadays it is well established that clusters of galaxies contain two relevant dynamical components that induce non-thermal processes: magnetic fields and relativistic particles. Their presence in the intracluster medium has been inferred from radio observations. Magnetic fields in clusters are playing an important role in determining the energy balance in cluster gas through their effect on heat conduction, and in some cases perhaps even becoming important dynamically.

Magnetic fields in galaxy clusters have been measured using a variety of techniques: studies of synchrotron relic and halo radio sources within clusters, studies of inverse Compton X-ray emission from clusters, surveys of Faraday rotation measures of polarized radio sources both within and behind clusters.

Radio halos and relics

Giovannini & Feretti (2000) and Giovannini et al. (1999) have performed moderately deep VLA observations, which have doubled the number of known radio halo sources. Several new radio halos have also been identified from the Westerbork Northen Sky Survey (Kempner & Sarazin, 2001). These radio halos have typically sizes of 1 Mpc, steep spectral indices ($S_\nu \propto \nu^\alpha, \alpha < -1$), low fractional polarizations ($< 5\%$), low surface brightnesses ($\sim 10^{-6}$ Jy arcsec^{-2} at 1.4 GHz), and centroids that are close to the cluster center defined by the X-ray emission.

The presence of diffuse radio emission is not common in clusters of galaxies. There is a steep correlation between the cluster X-ray and radio halo luminosity, and also between radio and X-ray surface brightnesses in clusters (Feretti et al., 2001; Govoni et al., 2001a; Liang et al., 2000).

We can derive magnetic fields in cluster radio halo minimizing the total non-thermal pressure, i.e. the sum of the relativistic particles and magnetic fields pressures. Because this analysis leads to comparable field and particle energies, it is called "equipartition". With this assumption the magnetic field strengths in cluster radio halos range from 0.1 to 1 μG (Feretti, 1999).

In the outskirts of some clusters there is the presence of other radio sources may be related to radio halos known as radio relics. These sources are very extended as the radio halos and are not associated with individual galaxies. Unlike radio halos, radio relics are often elongated, located at the cluster periphery and are strongly polarized. An explanation for these radio sources could be that the relics are the result of first order Fermi acceleration of relativistic particles in shocks produced during cluster mergers (Ensslin et al., 1998), or are fossil radio sources revived by compression associated with cluster mergers (Enßlin & Gopal-Krishna, 2001).

The difficulty to explain the radio halos and relics is related to their large size and the short synchrotron lifetime of relativistic electrons. These particles need to be reaccelerated by some mechanism acting with an efficiency comparable to the energy loss processes. There seems to be convincing evidence that diffuse sources are preferentially associated with high X-ray luminosity clusters with recent mergers events. Mergers generate shocks, bulk flows, turbulence in the intracluster medium and these processes would provide the energy to reaccelerate the radiating particles all around the cluster. All the clusters where radio halos or relics have been found, show the presence of a merger. But not all merging clusters host diffuse radio emission.

The relativistic particles could be injected in the cluster volume from AGN activity (quasars, radio galaxies, etc.), or from star formation in normal galaxies (supernovae, galactic winds, etc.). Most of the particle production has occurred in the past and is therefore connected to the dynamical history of the clusters. This population of primary electrons needs to be reaccelerated (Petrosian, 2001) to compensate the radiative losses. The shock acceleration has been recently questioned (Gabici & Blasi, 2003). Instead, stochastic acceleration by a turbulent intracluster medium seems to be an efficient process (Fujita et al., 2003). Another mechanism proposed for in situ relativistic particle injection is secondary electron production via the decay of π-mesons generated in collisions between cosmic ray ions (mostly protons) and the thermal intracluster medium (Enßlin & Gopal-Krishna, 2001).

Different models have been suggested for the origin of the relativistic electrons radiating in the radio relics. There is an increasing evidence that the relics are tracers of shock waves in merger events.

Mini-halos are diffuse radio sources of moderate size ($\sim$ 500kpc) surrounding a dominant powerful radio galaxy at the center of cooling flow clusters, as detected in Perseus and Virgo clusters. Gitti et al. (2002) argued that a connection between the central radio galaxy and the mini-halo in terms of particle diffusion or buoyancy is not possible in the Perseus mini-halo and suggested that the relativistic electrons are reaccelerated by turbulence in the cooling flow region of the intracluster medium. We need deeper studies of a large sample of mini-halos to clarify the connection between the central radio galaxy and the formation of mini-halos.

Faraday rotation

Indirect evidence of the existence of cluster magnetic fields derives from the studies of Faraday rotation measure (see Section 2.2.1) of radio galaxies embedded within the intracluster medium or located behind them. The Faraday rotation measure is proportional to the integral along the line-of-sight over the parallel component of the magnetic field, times the thermal electron density. This integral is affected by the poorly known topology of the magnetic field. Field reversals along the line of sight will greatly reduced the rotation measure. Radio observations are combined with X-ray measurements of the electron density to estimate the clusters magnetic field along the line of sight, the results depend on the assumed magnetic field topology.

This kind of studies has been performed on several individual clusters, with or without cooling flows, and on statistical samples (see the review by Carilli & Taylor (2002)). Minimum cluster magnetic field estimates can be obtained by assuming a constant magnetic field along the line-of-sight through the cluster. In general, the data suggest that magnetic fields values of 1-5 μG are common in clusters, regardless of the presence of not of diffuse radio emission (Clarke et al., 2001; Feretti et al., 1999; Govoni et al., 2001b; Taylor et al., 2001). This would imply that the fields are still significantly subthermal; the ratio of magnetic to gas pressures is only $(P_B/P_{gas}) \sim 0.05$. Magnetic field strengths can be larger by about a factor of 2 at the center of cooling flow clusters, which suggest that the magnetic fields in these regions may approach equipartition with the gas pressure. The rotation measure distributions tend to be patchy indicating magnetic field coherence scales of about 5 - 10 kpc. Beyond measuring a mean line-of-sight field, the next level of RM modeling entails "cells" of constant size and magnetic field strength, but random magnetic field direction, uniformly filling the cluster. The RM produced with this field configuration will give an average value of 0 radm^{-2}, but a dispersion in the RM that is proportional to the square root of the number of cells along the line-of-sight through the cluster. Although the simplest model is an uniform field throughout the cluster, possible filaments and flux ropes may be present (Eilek, 1999). Moreover, the magnetic field intensity is likely to decrease with the distance from the cluster center, as is found in A119 (Dolag et al., 2001).

Inverse Compton emission

The relativistic electrons present in the intracluster medium produce inverse Compton (IC) radiation because of the scattering with the low energy cosmic background photons. Depending on the electron Lorentz factor γ, the radiation is detected as hard X-ray emission ($\gamma \sim 10^4$) or extreme ultraviolet emission ($\gamma \sim 310^2$).

The detection of the hard X-ray emission (20 -100 keV) provide additional information that, when combined with results of radio measurements from the same population of relativistic electrons (i.e. the ratio of hard X-ray IC emission to radio synchrotron emission), enables the determination of the electron density and mean magnetic field directly, without the need to assume equipartition. However, one needs to assume that the particles and magnetic field have the same distribution and that both are reasonable uniform, which may not be true. Non-thermal hard X-ray emission at energies $\geq$ 20 keV has been detected in the Coma cluster (Fusco-Femiano et al., 1999; Rephaeli et al., 1999) and in A2256 (Fusco-Femiano et al., 2000). These observations have lead to a magnetic field of 0.16 μG in the case of the Coma cluster and a value of $\sim 0.05\mu$G for the northern region of A2256 where a radio relic is detected, while a higher field value of $\sim 0.5\mu$G could be present at the cluster center in the region of the radio halo.

The Extrem Ultraviolet Explorer have revealed EUV (0.1 to 0.4 keV) emission in excess of the expected thermal emission in Virgo (Berghöfer et al., 2000) and Coma (Lieu et al., 1996). The EUV detections in other clusters (Abell 1795, Abell 2199, Abel 4038, Abell 4059 and Fornax) remain quite controversial. The EUV emission has luminosities of $\sim 10^{44}$ergs^{-1} and has spectra which decline rapidly going from the EUV to the X-ray band. The non-thermal interpretation of this emission requires an electron population with energies of $\sim$ 150MeV. These electrons have too low energy to produce detectable radio emission. Sarazin (1999) pointed out that these electrons have lifetimes comparable with the Hubble time and should be present in essentially all clusters.

The IC estimations of the cluster magnetic fields are typically 0.2 to 1 μG, being consistent with the values obtained from equipartition arguments in radio halos. Instead, the fields derive using RM observations are an order of magnitude higher. About this discrepancy Goldshmidt & Rephaeli (1993) suggested that the IC estimate is expected to be lower that the Faraday rotation one, because of the expected spatial profiles of the magnetic fields and gas density. Petrosian (2001) showed that IC models which include the effects of more realistic electron spectra in combination with the expected radial profile of the magnetic field and anisotropies in the pitch angle distribution of the electrons, provide higher values of the intracluster medium magnetic field in better agreement with the Faraday rotation measurements.

2.3 Magnetic field origin

After establishing with observations the existence of μG-level fields in clusters of galaxies it follows the question about its origin, how are these fields generated and maintained?, are they of primordial origin?.

We can think that the simplest origin of the cluster magnetic field is compression of an intergalactic field. Clusters have present day overdensities of $\delta \sim 10^3$. To obtain intracluster magnetic fields of $B_{ICM} > 10^{-7}$G by adiabatic compression ($B \propto \delta^{2/3}$) then requires intergalactic fields $B_{IGM} > 10^{-9}$G. Faraday rotation measurements of high z radio loud QSOs have set an upper limit to IGM fields of 10^{-9}G, assuming a cell size of 1 Mpc (Kronberg, 1996). Considering the effects of magnetic fields on the CMB allows for upper limit to IGM magnetic fields at the time of recombination. Studies by Barrow et al. (1997) showed that the comoving IGM fields must be less than a few$\times 10^{-9}$G. The magnetism affects the evolution and cluster formation if comoving IGM magnetic fields are $B_0 \gtrsim 10^{-8}$G (Florido & Battaner, 1997).

There are other different possible mechanisms for generating cluster magnetic fields, ranging from injection of fields into the IGM (or early ICM) by active star forming galaxies and/or radio jets at high redshift, to field amplification by cluster mergers. It is possible that a combination of these mechanisms give rise to the μG fields observed in clusters of galaxies. We need observations of (proto-) clusters atmospheres at high redshifts and a better understanding of the general IGM field to test these mechanisms.

Many authors have considered the problem of the IGM origin. There are models which involve the large scale magnetic field generation prior to the recombination era. Since these first models many others have appeared. There is a problem with them related to the survivability of the fields on relevant scales during the radiation era. Battaner & Lesch (2000) argued that magnetic diffusion produced by Thomson scattering finite resistivity will destroy fields on comoving scales of few Mpc during the radiation epoch. Therefore either a) the generation of fields in a post-recombination Universe is required by normal plasma processes during proto-galactic evolution, or b) superhorizon coherence scales were generated at inflation.

There are a number of sources of seed magnetic fields in clusters of galaxies. The metallicity in the intracluster medium is about 30% solar. This implies that metals originate in stars in galaxies must have been ejected into the galactic interstellar medium and then into the ICM by some mechanisms. The ISM is magnetized with fields of the order of μG which would lead to a seed field in the ICM. But the exact way in which the ICM is polluted with metals from the ISM is not completly known: possibly tidal and ram pressure stripping of the galactic gas are involved together with galactic outflows (Brandenburg, 2000). We can obtain a rough estimate of the seed field resulting from stripping the galactic gas using flux conservation; that is $B_{\rm seed} \sim (\rho_{ICM}/\rho_{ISM})^{2/3} B_{\rm gal}$. For typical values of galactic magnetic fields of 3μG and $\rho_{ICM}/\rho_{ISM} \sim 10^{-2} - 10^{-3}$, one gets $B_{seed} \sim 0.1 - 0.03\mu$G. Larger seed fields ($B_{\rm seed} \sim 0.3\mu$G) can be obtained if clusters of galaxies have substantial magnetized outflows (Brandenburg, 2000). Kronberg et al. (1999) show that a substantial fraction of the intergalactic medium can be permeated with magnetic fields by dwarf galaxy outflow winds in the 'volcanic early Universe' ($z > 6$), but that at lower redshifts the intergalactic volume is too large for galaxy outflows to affect a significant fraction of the volume.

Other source of seed fields could be also the outflows from earlier generation of active galaxies (radio galaxies and quasars) (Colgate et al., 2001; Furlanetto & Loeb, 2001; Rees, 1994). These outflows may leave behind magnetized bubbles of plasma in some fraction of the intergalactic medium (typically 10%), which when incorporated into the ICM would seed the general cluster gas with magnetic fields that can be as large as $0.1 - 1\mu$G. Although AGNs and galaxies provide a strong seed magnetic field, propably there would be a need for a posterior amplification and maintenance against turbulent decay.

In galaxies, the way of amplifying the field is probably accomplished by the conversion of turbulent kinetic energy into magnetic energy, a process generally referred to as a dynamo; see Kronberg (1994); Widrow (2002) for excellent reviews about dynamo theory and comparisons with observations of astrophysical magnetic fields. It was generally assumed that the large scale magnetic fields observed in disk galaxies were amplified and maintained by an $\alpha\omega$ dynamo wherein new field was regenerated continuously by the combined action of differential rotation (ω) and helical turbulence (α).

On the other hand, the dynamo can be considered incomplete since it does not explain the origin of the initial fields that act as seeds for subsequent dynamo action. Moreover, the time scale for field amplification in the standard $\alpha\omega$ dynamo may be too long to explain the fields observed in very young galaxies. Furthermore, it is recognized a serious problem with this dynamo mechanism is the presence of intense small-scale magnetic fields (Kulsrud, 1999). The dynamo theory has its own difficulties. The linear version which is valid when the magnetic field is too weak to significantly affect the velocity field, is relatively well developed but does not favorably agree with observations wherever such a comparison is meaningful. The nonlinear saturation of the dynamo is not well understood and the conventional ideas have been strongly criticized. In recent years our understanding of nonlinear properties of dynamos has advanced rapidly. This is partly due to the new high resolution numerical simulations which have also triggered further developments in analytic approaches (see Brandenburg & Kandaswamy (2004) for a review).

By contrast, the magnetic fields in non rotating or slowly rotating systems such as elliptical galaxies and clusters of galaxies appear to have a characteristic coherence scale much smaller than the size of the system itself. These fields may be generated by a local, small scale turbulent dynamo action where, in the absence of rapid rotation, the field does not organize on large scales (Ruzmaikin et al., 1989). The turbulence was thought to be generated by wakes of galaxies which move through the intracluster medium. But probably galaxy wakes are inefficient, being required another source of cluster turbulence.

A source for turbulence in clusters can be merges between clusters (Ricker & Sarazin, 2001a). In the hierarchical structure formation theories, clusters of galaxies are thought to be formed relatively recently. They form at the intersection of filaments in the large scale structures, involving major mergers between clusters with comparable mass and the accretion of smaller mass clumps. Clusters simulations shown that the intracluster medium becomes 'turbulent' during cluster formation, with the turbulence persisting after about 5 Gyr after the last major merger. Simulations of clusters of galaxies help us to understand how magnetic fields formed and evolved. They have showed (Roettiger et al., 1999) two different stages of evolution of the field. In the first stage, the field becomes quite filamentary as a consequence of stretching and compression caused by shocks and bulk flows during infall. Later on, as the bulk flows are replaced by more turbulent motions, the magnetic energy increases by an average factor around 3 to localized enhancements of ~ 20. Smooth particle hydrodynamics simulations of cluster collapse (Dolag et al., 1999, 2002) has found that compression and shear in random flows during cluster formation can increase the magnetic field strengths by factors of order 10^3.

It is possible that cluster magnetism is the result of compression, random shear and turbulent amplification of seed fields from galaxies and AGNs, but we still need to do much work to understand the details and efficiency of these processes.

We have seen that there are different mechanisms that connect and allow the magnetic field interchange between the intergalactic and intracluster medium. Observations reveal a clear matter interaction between IGM and ICM characterized by ejections, infall, convective motions in the galactic corona. This interaction produces a very large β (i.e. the coefficient of turbulent magnetic diffusion). This means there exist large turbulent motions connecting the disc and the corona and the intergalactic medium. Fountain models (Breitschwerdt et al., 1991; Kahn, 1994) provide a very active convection. Ohter effects such as Parker instabilities also contribute (Hanasz & Lesch, 1993).

3

Clusters of galaxies in X-rays

In this chapter we describe the observations of clusters of galaxies in the X-ray wavelength. We explain the basis of the observations with X-ray telescopes and study in more detail one of the cluster components observable in this X-ray wavelength: the intracluster gas. The study of these objects in X-rays allow us to derive the X-ray luminous gas and the total cluster mass.

3.1 Observing in X-rays

Absorption by the Earth's atmosphere restricts ground-based observations to radio, near infrared, and visible wavelengths. X-rays are absorbed in the upper Earth's atmosphere through photoionization processes. Even though the atoms in the atmosphere are widely spaced, the total thickness of the atmosphere is large and the total number of atoms is enormous. Because the Earth's upper atmosphere absorbs X-rays, X-ray observatories must be placed high above the Earth's surface. This means that the ultra-precise mirrors and detectors, together with the sophisticated electronics that conveys the information back to Earth must be able to withstand the rigors of a rocket launch, and operate in the hostile environment of space.

X-ray telescopes in orbit above the Earth's atmosphere can collect X-rays from energetic sources. These cosmic X-rays are focused by barrel-shaped mirrors onto an instrument especially designed to measure properties such as the incoming direction and energy of the X-ray photon. A gaseous or solid material in the instrument absorbs the X-rays by the photo-electric effect.

Focusing X-ray is not an easy task. X-rays do not reflect off mirrors in the same way that visible light does. Because of their high-energy, X-ray photons that strike a mirror directly will penetrate into it. These properties mean that X-ray telescopes must be very different from optical telescopes. Grazing incidence is needed to achieve total reflection for X-rays, the maximum angle between the incoming flux and the surface being of a few degrees for a photon of ~ 1 keV. The efficiency of the reflection depends on the incident angle and the properties of the reflecting surface. Reflection becomes more difficult at higher photon energies, as the angle for total reflection becomes smaller and the mirrors need to be placed almost parallel to the optical axis. The mirrors look more like barrels than the familiar dish shape of optical telescopes (Fig. 3.1 right). Two reflections are used to focus the X-rays to a point. The area of an X-ray telescope can be increased by nesting the mirrors inside one another. The mirrors focus X-ray photons onto the detectors which record

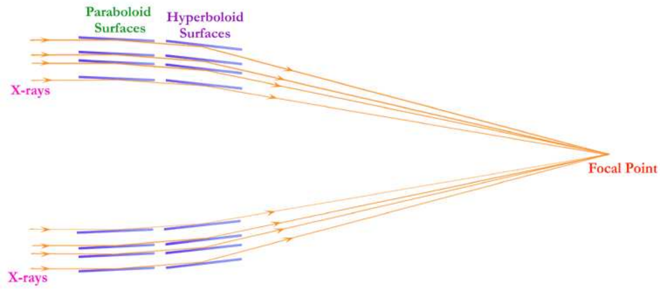

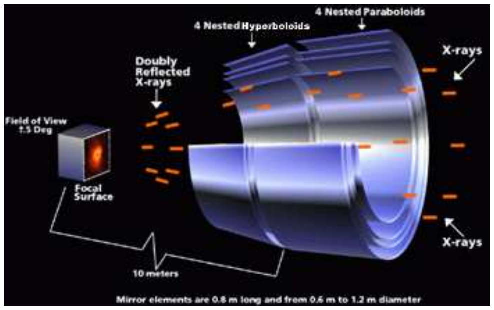

Figure 3.1— Left: Schematic of grazing incidence, X-Ray mirror. Right: Four 'mirror' shells are nested inside one another to increase the total reflecting area of the telescope. The inner, reflecting surfaces of the mirrors have to be precisely shaped, and aligned nearly parallel to the incoming X-rays. Pictures taken from *www.chandra.harvard.edu*.

position, and in some cases the energy, of the photons. These X-ray data are then analyzed and reconstructed into images of the celestial objects that produce the emissions. In Fig. 3.1 left, we see how light in a conventional X-ray telescope is collected and focused at a single point. Photons of visible light from a celestial object (shown in red) enter the telescope at the left, reflect off the parabolic and hyperboloid mirror surfaces and are collected at the focus. The greater the area of reflecting surface, the greater is the brightness of the image at the focus. In fact, it is this capability (light gathering power) that is the primary reason that telescopes are used, as opposed to the ability to "magnify" any given object. It is also the reason why astronomers are continuously seeking to build larger telescopes; in that way, more light can be collected from faint and distant objects.

The first imaging X-ray telescope was made by a team of scientists under the direction of Riccardo Giacconi at American Science and Engineering in Cambridge, MA. It was flown on a small sounding rocket in 1965 and made crude images of hot spots in the upper atmosphere of the Sun.

3.1.1 X-ray telescope configurations

The critical angle for total external reflection of X-rays from materials composed of heavy elements is approximately: $\alpha_c = 69.4(\sqrt{\rho})/E$, where α_c is in arcminutes, ρ is the mass density of the reflecting material in gcm^{-3} and E is the X-ray energy in keV (Aschenbach, 1985). This gives a critical angle of around 1° for X-rays of a few keV. For incidence angles greater than this, the X-rays will be absorbed by the mirrors.

The requirement for grazing incidence reflections leads to telescope designs that are far from those used at longer wavelengths. Aberrations observed with grazing incidence optics are different to those produced at more normal incidence and need to be dealt with in different ways. Further to this, the grazing incidence condition demands extremely low levels of surface roughness. The practicality of polishing the mirrors to the necessary standard must also be considered when choosing a design.

Kirkpatrick-Baez telescope

The first grazing incidence system to form a real image was proposed by Kirkpatrick and Baez in 1948. This consisted of a set of two orthogonal parabolas of translation as shown in Fig. 3.2a.

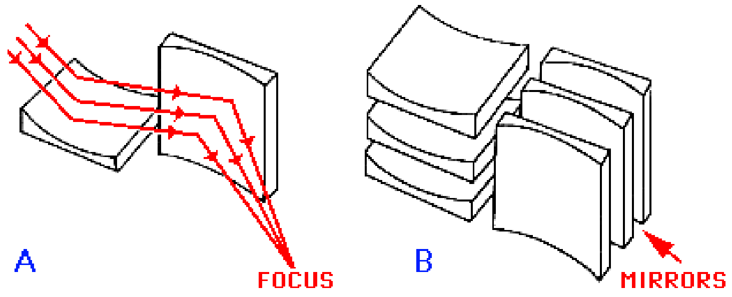

Figure 3.2— Kirkpatrick-Baez telescope configuration (from *www.imagine.gsfc.nasa.gov*).

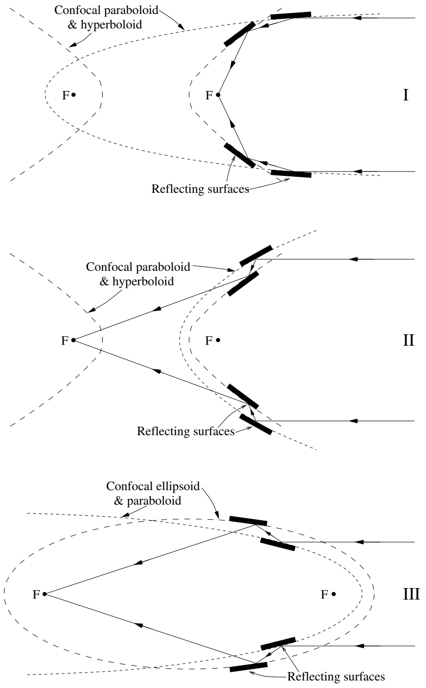

Figure 3.3— Wolter grazing incidence imaging systems, types I - III (from imagine.gsfc.nasa.gov)

The first reflection focused to a line, which the second reflection then focused to a point. This was necessary to avoid the extreme astigmatism suffered by a single mirror but was by no means free from geometric aberrations. The system was attractive for the ease of constructing the reflecting surfaces. These could be polished to a high level of accuracy as flat plates and then mechanically bent to the required curvature. In order to increase the aperture a number of mirrors could be nested together (Fig. 3.2b), although this introduces further aberrations.

Wolter telescopes

In 1952, Wolter set out to design an aplanatic system of grazing incidence mirrors that would be free of both spherical aberration and coma. This required that the 'Abbe sine condition' be fulfilled. For on-axis rays this occurs when the forward projection of the incident rays meet the backward projection of the focused rays on the surface of a sphere centred on the image focus. Wolter showed such a system could be produced using a combination of a paraboloid with either a hyperboloid or ellipsoid secondary. The three simplest designs are outlined in Fig. 3.3 and are known as Wolter types I, II and III.

In each of the three types of Wolter telescope, the mirrors are arranged in a coaxial configuration and share a common focus. For the type I system, reflections are off the internal surface of a paraboloid and hyperboloid in a simple configuration that lends itself to nesting several mirrors inside one another. For this reason, Wolter type I systems are the most widely used in astronomical telescopes.

The type II system involves a secondary reflection off the external surface of a hyperboloid leading to a longer focal length and therefore higher magnification than the type I system. Though almost free from spherical aberration and coma, these systems still suffer from astigmatism and field curvature. For the type II system off-axis blurring is much more pronounced than for type I. Wolter type II systems are therefore usually employed as narrow field imagers.

In comparison to the total system length, the Wolter type III configuration has the shortest focal length of all. Its relative complexity compared to the type I system is the primary reason why no telescopes have been built using this system.

By whichever method X-rays are focused or collimated their properties must be measured on arrival at the X-ray detector. The quality of the X-ray data will depend on the performance of the detector in a number of areas, namely: spatial resolution and extent, temporal resolution and 'dead-time', energy resolution and bandwidth, quantum efficiency, spurious background rate and the overall stability of these characteristics with time. A number of different types of X-ray detector exist, optimised for best performance in one or more of these areas.

3.2 Components of clusters of galaxies

Clusters of galaxies are formed by different observable components: hundreds of galaxies, hot gas between the galaxies and sometimes relativistic particles. These components are emitting in different wavelengths from radio to X-rays. With the combination of all these observations at different frequencies and also with theoretical models we can derive a good understanding of these massive objects.

Clusters were first discovered as associations of hundreds to thousands of galaxies. These galaxies move around with velocities of the order of 1000 km/s. The galactic mix of morphological types of galaxies in clusters differs from the mix in the field (Dressler, 1980): in clusters an excess of elliptical galaxies is visible, which is an indication of interaction. This interaction can be between galaxies or between galaxies and another component: the intra-cluster gas which is emitting X-rays. X-ray astronomy allowed the observation of clusters in this wavelength and gave a new step in the understanding of cluster structure.

X-rays clusters of galaxies were found to be spatially extended sources. The fact that the clusters' sizes were comparable with the size of the galaxy distribution in the cluster was an indicator that there was a emission coming from hot gas filling the whole potential well of the cluster. Although different emission mechanisms were proposed, the X-ray spectra of clusters were most consistent with thermal bremsstrahlung from this hot gas. In that way it is easier to detect clusters in X-rays than in the optical because the X-ray emission is proportional to the square of the gas density while in optical we see only the galaxy density (see Fig. 3.4). Furthermore, the morphology

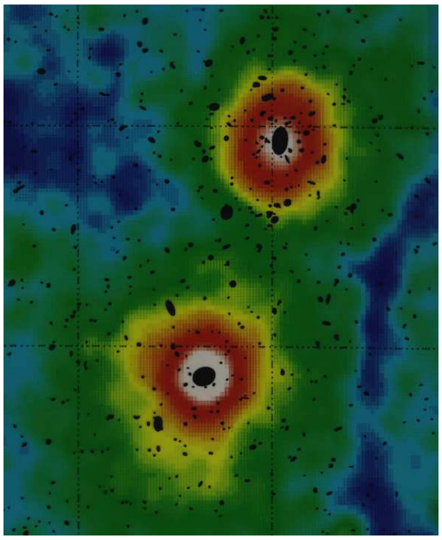

Figure 3.4— ROSAT/PSPC image of A3528 (Schindler, 1996a). The superposed galaxy distribution shows all galaxies observed in direction of the cluster (not only cluster galaxies). While in the optical one sees only an enhancement of the galaxy density, the X-ray image shows clearly the shape of the cluster potential - in this case a bimodal structure.

of a cluster can be seen much better in X-rays, even for distant clusters. X-ray observations have revealed that clusters have very different morphologies: some have substructure while others show spherically symmetric X-ray emission. These are indicators for different dynamical states: in the former case merging processes are taking place while the latter clusters are already in virial equilibrium. These morphological studies are important for cosmology. In a low Ω universe the merging processes should stop earlier so that more clusters with virialized X-ray emission are expected. Therefore the fraction of virialized clusters at a certain redshift can be used to constrain the mean density of the universe Ω (Richstone et al., 1992).

We can learn interesting properties studying clusters of galaxies in X-rays. The X-ray surface brightness distribution reflects the plasma density distribution in the cluster. X-ray spectroscopy provides the means to determine the temperature for the hot intracluster plasma. Assuming that the plasma is approximately in hydrostatic equilibrium in the cluster one can use the density and temperature profile in connection with the hydrostatic equation to derive the mass of the X-ray luminous gas and the total cluster mass.

The current generation of X-ray observatories (*Chandra, XMM-Newton*) with large effective area, excellent angular resolution and better energy resolution over a wide energy range are improving the accuracy of the spatially resolved spectroscopy. *Chandra* is mostly an imaging observatory, while *XMM-Newton* has its major capabilities for spectroscopy. That means that with new missions the temperature gradient in the intracluster medium can be constrain in a better way.

But not only X-ray emission was detected in clusters, among others frequencies e.g. non thermal, hard X-ray emission; in many clusters radio emission was found. This radio emission from clusters (as well as most other extragalactic objects) is synchrotron emission due to the interaction of a non-thermal population of relativistic electrons (with an assumed power-law energy distribution) with magnetic fields.

From all the studies of galaxy clusters in different wavelengths, a rough general picture of the mass, composition and the structure of these objects has emerged. The major results are

Size: Mpc
Gravitational mass: $10^{14} - 10^{15} M_\odot$
Galaxies: $\sim 2 - 7\%$ of the total mass
Intra-cluster medium (ICM): $\sim 10 - 30\%$ of the total mass
X-ray luminosity: $\sim 10^{44} - 10^{45} \mathrm{erg \cdot s^{-1}}$
energy content:$\sim 10^{62} - 10^{63}$erg
Radio halo: luminosity $\sim 10^{41} - 10^{42} \mathrm{erg \cdot s^{-1}}$
energy density in relativistic particles:$\sim 10^{-12} - 10^{-11} \mathrm{erg \cdot cm^{-3}}$
energy density in magnetic fields:$\sim 10^{-12} \mathrm{erg \cdot cm^{-3}}$
energy content of the relativistic plasma: $\sim 10^{59} - 10^{60}$erg
necessary energy input to power the radio halo: $\sim 10^{42} \mathrm{erg \cdot s^{-1}}$

Table 3.1— Components of massive clusters of galaxies

summarized in Table 3.1. These results imply that the gas mass is larger than the mass in galaxies and that most of the gravitationally inferred matter is "dark".

3.3 The hot intra-cluster medium and X-ray emission

In this section we describe in more detail the major baryon component in the cluster, the hot intracluster medium. Clusters of galaxies are filled with this diffuse, hot plasma, with typical temperatures of $T \sim 10^7 - 10^8$K, optically thin and with low density $n_p \sim 10^{-4} - 10^{-2} \mathrm{cm^{-3}}$, containing heavy elements.

It is generally assumed that the ICM is in approximate hydrostatic equilibrium unless recent major merger processes have taken place. The gas density decreases with radius and extends out to distances of $r \geq 3.5$Mpc from the cluster center with a total mass of $M_{gas} \sim 10^{14} M_\odot$.

At temperatures of $10^7 - 10^8$K and densities of $n_p \sim 10^{-4} - 10^{-2} \mathrm{cm^{-3}}$, the dominant radiation mechanism of a plasma is thermal bremsstrahlung. As a result, clusters of galaxies are generally very luminous X-ray emitters, with luminosities of $L_X \sim 10^{43} - 10^{45} \mathrm{erg \cdot s^{-1}}$.

In a typical X-ray spectrum of a cluster (Fig. 3.5) one can distinguish the continuum, due primary to **thermal bremsstrahlung** (free-free emission), and line emission.

The emissivity at a frequency ν of ions of charge Z_i in a plasma with an electron temperature T_{gas} is given by:

$$\epsilon_\nu^{ff} = \frac{2^5 \pi e^6}{3 m_e c^3} (\frac{2\pi}{3 m_e k})^{1/2} n_e T_{gas}^{-1/2} exp(-h\nu/kT_{gas}) \sum_i Z_i^2 n_i g_{ff}(Z_i, T_{gas}, \nu) \quad (3.1)$$

This X-ray emissivity is proportional to the square of the gas density. And it is defined as the emitted energy per unit time, frequency and volume. The sum is over the various ions in the plasma, dominated by hydrogen and helium. The Gaunt factor $g_{ff}(Z_i, T_{gas}, \nu)$ corrects for quantum mechanical effects and for the effect of distant collisions, and is a slowly varying function of frequency and temperature. As a result, the dominant dependence of the free-free emissivity on frequency is the Boltzmann exponential factor, and the main dependences on temperature are this

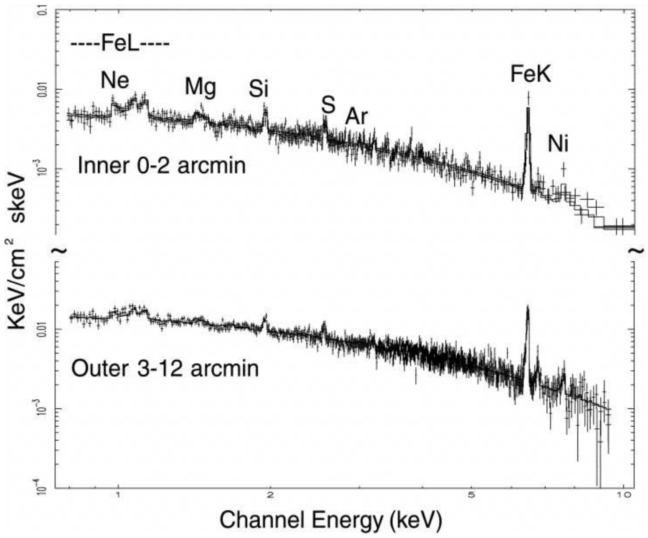

Figure 3.5— GIS2 and 3 unfolded spectra for inner (top) and outer (bottom) regions in cluster A496 from (Dupke & White, 2000b); solid lines represent the best-fitting isothermal model; individual lines and line complexes are identified.

factor and the square-root factor $T_{gas}^{-1/2}$. Thermal bremsstrahlung produces a roughly exponential continuum component in the X-ray spectrum. This mechanism is relatively insensitive to the heavy element abundances. For a typical set of abundances, the emissivity (Eq. 3.1) can be rewritten as:

$$\epsilon(r)_\nu = \Lambda_\nu(T_{gas}) n_p^2 \quad \mathrm{erg} \cdot \mathrm{s}^{-1} \cdot \mathrm{cm}^{-3} \tag{3.2}$$

where $n_p = \rho_{gas}/(2.3\mu m_p)$ is the proton density, m_p is the proton mass and $\Lambda_\nu(T_{gas})$ is the cooling function.

As not all the ions are completely ionised at that temperature line emission can be observed. In most of the clusters Fe lines are visible, but sometimes also Si and other elements are detectable (see Fig. 3.5). The metallicities (calculated from the Fe lines) are typically in the range between 0.2 and 0.5 in solar units (Fukazawa et al., 1998; Mushotzky & Loewenstein, 1997; Tsuru et al., 1997), with possible gradients across the cluster, but remarkable homogeneity across the cluster population. Therefore in addition to the continuum there is the iron K **line emission** about 7 keV coming from Fe XXV. It was the satellite *OSO-8* which first detected Fe XXV in clusters of galaxies. This result confirmed the thermal emission from a hot gas is an intrinsic property of clusters of galaxies. The origin of this gas is uncertain. Being metal-enriched, it cannot be all primordial. Some of the gas must have been processed through an early population of stars before being released back into intracluster space.

There have been suggested some processes to transport the gas from galaxies to the ICM: supernova driven galactic winds (De Young, 1978a), *ram-pressure stripping* (Gunn & Gott, 1972), interaction between individual galaxies and jets from active galaxies. Several *Chandra* observations show the interaction between the radio source embedded in the central cluster galaxy and the intracluster medium. Examples of this type of interaction are the clusters, Perseus: Fabian et al. (2000), Hydra-A: McNamara et al. (2000), RBS797: Schindler et al. (2001). The other two processes *ram-pressure stripping* and the galaxy-galaxy interaction are influenced by the environment, e.g. clusters merging. The process of *ram-pressure stripping* occurs when a galaxy is moving through the ICM to the cluster center. At certain point, the ICM pressure is so large that the galactic gravitational potential is not strong enough to retain the gas in the galaxy. The gas is pulled out from the external parts of the galaxy to the intracluster medium. The galaxies NGC 4501 and NGC 4548 (Cayatte et al., 1990) in Virgo cluster are an spectacular example where we can observed this process of *stripping*.

Prior to *XMM-Newton* and *Chandra*, most information on abundances referred only to iron, but now information from other elements (e.g. C, N,O) is available. *ASCA* data revealed clear evidence of central excess of Fe in clusters with cooling flows (see Section 3.6) and in clusters not involved in recent major mergers (Dupke & White, 2000a,b; Ezawa et al., 1997; Ikebe et al., 1997, 1999; Kikuchi et al., 1999; Matsumoto et al., 1996; Xu et al., 1997), which are consistent with generally flat metallicity profiles down to the central $\sim 2'$ (Irwin et al., 1999; Tamura et al., 1996; White, 2000). This abundance gradient could be the result of the spatial distribution of gas-losing galaxies within the cluster being more centrally condensed than the primordial hot gas. The new instruments allow us to trace more accurately the gradients in abundances and abundances ratios. Therefore metal abundances provide basic information on the origin and evolution of the intracluster gas, and on the history of star formation and the chemical evolution of clusters of galaxies. At present, results from *XMM-Newton* confirm an intracluster medium metallicity of $Z \sim (0.3 \pm 0.1) Z_{\odot}$ and with no evolution out to a redshift of 0.5. New results demonstrate that the central Fe excess is concentrated to within 100 kpc of the cluster centre (Iwasawa et al., 2001; Kaastra et al., 2001; Lewis et al., 2002; Smith et al., 2002), that there may be a central metallicity inversion (Blanton et al., 2003; Dupke & White, 2003; Johnstone et al., 2002; Sanders & Fabian, 2002; Schmidt et al., 2002), and that abundance profiles are generally very flat from ~ 100 kpc out to a significant fraction of the virial radius (Schmidt et al., 2001; Tamura et al., 2001).

3.4 Distribution of the intracluster gas: The β - model.

The intracluster gas can be considered in hydrostatic equilibrium unless the cluster gravitational potential varies on a shorter time scale (during cluster mergers) or the gas is heated or cooled in a temporal scale much shorter than the cluster age ($\sim 10^{10}$ years). But the cooling time by thermal bremsstrahlung is in general longer than the cluster age and therefore we can write the equation of hydrostatic equilibrium as:

$$\nabla P_{gas} = -\rho_{gas} \nabla \phi(r). \tag{3.3}$$

P_{gas} and ρ_{gas} are the gas pressure and density and $\phi(r)$ is the gravitational potential well of the spherical cluster. The gas pressure P_{gas} is given by:

$$P_{gas} = \rho_{gas} k T_{gas} / \mu m_p. \tag{3.4}$$

Here μ is the mean molecular weight of the gas and k is Boltzmann's constant. If we assume that the cluster is spherically symmetric, Eq. 3.3 becomes:

$$\frac{1}{\rho_{gas}} \frac{dP_{gas}}{dr} = -\frac{d\phi}{dr} \tag{3.5}$$

where r is the radius from the cluster center.

The galaxies in the cluster move in the same gravitational field as the gas and assuming that they move in isotropic orbits, they also satisfy an hydrostatic equation:

$$\frac{1}{n_{gal}}\frac{d(n_{gal}\sigma^2)}{dr} = -\frac{d\phi}{dr} \tag{3.6}$$

in this case n_{gal} is the number density of galaxies and σ is the one-dimensional velocity dispersion.

Relating both gas and galaxies distributions, Eq.s 3.5 and 3.6, we can write:

$$\frac{1}{\rho_{gas}}\frac{dP_{gas}}{dr} = \frac{1}{n_{gal}}\frac{d(n_{gal}\sigma^2)}{dr}. \tag{3.7}$$

Now we can adopt a very simple model where the gas and galaxies are assumed to be isothermal, that means T_{gas} = constant and σ = constant and Eq. 3.7 becomes:

$$\frac{kT}{\mu m_p}\frac{d\ln\rho_{gas}}{dr} = \sigma^2\frac{d\ln n_{gal}}{dr}. \tag{3.8}$$

A parameter β can be defined as,

$$\beta \equiv \frac{\mu m_p \sigma^2}{kT_{gas}} \tag{3.9}$$

representing the ratio of energy per unit mass in galaxies to the energy per unit mass in gas. If the value of β is bigger than unity that means the galaxies are "hotter" than the gas, they move faster and vice versa if $\beta < 1$. Therefore Eq. 3.8 can be written as follows:

$$\beta\frac{d\ln\rho_{gas}}{dr} = \frac{dn_{gal}}{dr}. \tag{3.10}$$

Being very easily integrated when assuming a constant value for β:

$$\beta\ln\rho_{gas} = \ln n_{gal} + C \rightarrow \rho_{gas}^{\frac{1}{\beta}} \propto n_{gal}$$

$$\rho_{gas} \propto n_{gal}^{\beta}. \tag{3.11}$$

Very often the galaxy distribution in clusters is fitted to the analytic King model (King, 1962) where the number density of galaxies can be expressed as:

$$n_{gal} = n_{gal}^0\left[1+\frac{r^2}{r_c^2}\right]^{-3/2} \tag{3.12}$$

being n_{gal}^0 the central value and r_c the core radius of the distribution. With this approximation, the gas density in Eq. 3.11 can be written as:

$$\rho_{gas} = \rho_0\left[1+\frac{r^2}{r_c^2}\right]^{-3\beta/2}. \tag{3.13}$$

This Eq. 3.13 represents the widely known β-model (Cavaliere & Fusco-Femiano, 1976) which assumes that both the gas and galaxy distributions are static and isothermal. Although these assumptions are not strictly justified and the gas probably is not isothermal, this model has the advantage that the gas distribution is analytic and basically all the integrals needed when the model and the observations of clusters are compared, are also analytic. For example the surface brightness profile observed at the projected radius b, S(b) has an analytic solution:

$$S(b) = n_0^2 r_c \Lambda(T_{gas}) B(3\beta - 0.5, 0.5)\left[1+\frac{b^2}{r_c^2}\right]^{0.5-3\beta} = S_0\left[1+\frac{b^2}{r_c^2}\right]^{0.5-3\beta} \tag{3.14}$$

where n_0 is the central proton density and B(a,b) is the beta function.

3.5 Mass determination in galaxy clusters

Several methods have been used for measuring total cluster masses, with generally consistent results. This suggests that the total cluster masses can be measured with reasonable accuracy although systematic variations between the different methods do exist.

The oldest method uses optical spectroscopic observations and determines the mass from the velocity distribution of cluster galaxies with the assumption of virial equilibrium (Girardi et al., 1998).

A second method is based on the gravitational lensing effect: light from galaxies behind clusters is deflected by the large mass of the cluster, so that we see distorted images of these galaxies. The giant arcs (strong lensing) as well as the statistical distortion of all background objects (weak lensing) can be used for the mass determination (Mellier, 1999; Molikawa et al., 1999; Wambsganss, 1998).

A third method based in the X-ray emission is described in the next section.

The methods above mentioned have been applied to many clusters. In some cases there is an agreement between the results obtained with the different methods. But in other cases there are discrepancies that typically follow the relation:

$$M_{\mathrm{X}} \approx M_{\mathrm{visible}} \lesssim M_{\mathrm{weak\ lensing}} \lesssim M_{\mathrm{strong\ lensing}},$$

with differences between the X-ray and strong lensing estimations that in some cases become a factor 2-3. Between the possible explications that have been suggested to understand these discrepancies are: non-equilibrium configurations, projection effects, multiphase medium.

3.5.1 X-ray mass estimator

The X-ray emitting gas can be used as a tracer of the cluster potential. Assuming that the intracluster gas is spherically symmetric and in hydrostatic equilibrium supported solely by thermal pressure, Eq. 3.3 can be written as:

$$\frac{dP_{gas}}{dr} = \rho_{gas}\frac{GM(<r)}{r^2} \tag{3.15}$$

where M(< r) is the total cluster mass within a radius r from the cluster center. If the gas pressure given by Eq. 3.4 is substituted in 3.15, we can easily derive the total cluster mass within a radius r:

$$M(<r) = -\frac{kr}{\mu m_p G}T(r)\left(\frac{d\ln\rho_{gas}(r)}{d\ln r} + \frac{d\ln T(r)}{d\ln r}\right) \tag{3.16}$$

Hence, the mass depends on both the gas density and temperature radial profiles. The gas density profile can be accurately determined from X-ray images. Measurements of the temperatures profiles, however require detailed spatially resolved spectroscopy. Crude temperature maps can be obtained using the spatially resolved *ASCA* spectra, after applying corrections for the point spread function (PSF) of the *ASCA* mirrors. Studies with *ASCA* data using different PSF-correction techniques provide conflicting results; Markevitch et al. (1998) have observed declining temperature profiles whereas in the analysis of 106 cluster of galaxies by White (2000) it is found that 90 percent of the temperature profiles are consistent with isothermality at the 3-sigma confidence level. *XMM-Newton* observations show that, except for the core (with a few $\times$ 100 kpc), cluster gas is isothermal (or perhaps with a slowly decaying temperature) out to the distances where X-ray emission can be detected (less than the virial radius). In addition, azimuthal variations in the gas temperatures have been observed in a number of clusters that are indicative of recent merger activity. In such clusters, the assumption of hydrostatic equilibrium can break down, and the applicability of X-ray mass estimates can be questioned.

3.6 Cooling flow clusters

In the central regions of many clusters of galaxies the cooling time of the intracluster medium is significantly smaller than the age of the Universe, and therefore that gas will cool if no other phenomena prevent it (Fabian, 1994). Maintaining hydrostatic equilibrium with the hotter outer gas implies that gas should be steadily flowing inwards, increasing the density towards the cluster center. Mass deposition rates are of the order of $\sim$100-1000 $M_\odot yr^{-1}$, which integrated over a Hubble time result in a substantial contribution to the mass of a large galaxy.

Cooling flows manifest themselves as a peaked surface emissivity at the center of the cluster, where the X-ray spectrum shows cooler gas. They occur almost invariably in cD clusters (i.e., those dominated by a large central-dominant early type galaxy), but very rarely happen in more non-relaxed structures, possibly due to the disruption of cooling flows by mergers. The most intriguing question is where does all this gas go. cD galaxies present at the centre of cooling flow clusters are red and, although they do form some stars, they certainly do not form $\sim$100-1000 $M_\odot$ *normal* stars every year. A high pressure ambient as that present in cooling flows could favour the formation of low-mass stars.

A major *XMM-Newton* result has been to show that the gas in cooling flow clusters does not cool below a temperature which is 1/2 to 1/3 of the outer intracluster medium temperature (Kaastra et al., 2001; Peterson et al., 2001, 2003; Sakelliou et al., 2002; Tamura et al., 2001). Cluster gas at temperatures $\sim$1 keV should cool mostly through Fe L lines, which should be very strong. Instead they are almost absent for the *XMM-Newton* RGS spectra. The amount of gas that cools is probably 1/10 of the gas expected from simple cooling flow models (Fabian & Allen, 2003), suggesting a much modest role of cooling flows in galaxy formation (Molendi & Pizzolato, 2001). This result was present in previous *ASCA* and *ROSAT* studies but the lack of emission had been attributed to intrinsic absorption. Although some absorption has not been completely ruled out, the improved new spectra show that it is not dominant.

The reasons for that lack of emission are still unclear. It is most likely that some heating is taking place with the potential to inject enough energy into the keV gas to balance radiative losses. Candidate heating mechanisms include energy injection from a central active galactic nucleus (AGN) (Brüggen & Kaiser, 2002; Churazov et al., 2002; Ciotti & Ostriker, 2001; Kaiser & Binney, 2003), and diffusive transport of heat from the outer regions of the cluster to the center via conduction (Bregman & David, 1988; Narayan & Medvedev, 2001; Tucker & Rosner, 1983; Voigt et al., 2002) or turbulent mixing (Cho et al., 2003; Kim & Narayan, 2003; Voigt & Fabian, 2004). Conduction should probably be decreased by the presence of magnetic fields, as a temperature gradient is indeed seen. Heating by the central source, is also non-trivial, as it should deposit heat uniformly over a large volume, but on the contrary *Chandra* images show lots of structure in cluster cores.

3.7 Cluster formation

A further cosmologically interesting result from cluster studies with X-rays is that of scaling. The hierarchical clustering model for the formation of structure in the Universe predicts that dark matter halos should be scaled versions of each other (Navarro et al., 1995). While some energy transfer between dark matter and gas is possible through gravitational interaction and shock heating, simulations suggest that the gas and dark matter halos will be almost self-similar in the absence of additional heating or cooling processes (Eke et al., 1998). Comparison of the structure of real galaxy systems with this predicted self-similarity provides an excellent probe of extra physical processes that may be taking place in galaxy clusters and groups. Therefore many of the properties of clusters are well characterized by self-similar scaling relations, like the mass-ICM temperature relation which is predicted to have a logarithmic slope of 1.5 which is approximately observed for massive clusters. A closer comparison of groups and clusters shows, however, that the predicted scaling relations are not always very well observed - the temperature- X-ray luminosity (bolometric luminosity) relation is a good example where the observed slope is steeper that predicted.

Non-gravitational heating, such as extra energy inputs by galactic winds, is thought to play an important role in the ICM physics. In "pre-heating" scenarios, early winds add roughly a constant entropy to the system and thus affect cooler clusters more strongly, hence breaking the similarity law. The main expected effect of these winds is to inflate the gas distribution. Preheating scenarios can thus explain the observed steepening of the $L_X - T$ and size-temperature relations relative to the similarity scaling (Arnaud & Evrard, 1999; Cavaliere et al., 1999; Mohr & Evrard, 1997). Further support to this scenario was given by Ponman et al. (1999) who showed that the entropy of cool systems is indeed higher than can be achieved through gravity alone. They consistently found evidence for similarity breaking in the surface brightness profiles of clusters: cooler clusters have systematically shallower profiles than hotter systems.

4

Distribution of gas and dark matter in clusters of galaxies†

In this chapter we present the analysis of gas and dark matter distribution in a sample of ten nearby clusters of galaxies ($0.03 < z < 0.09$) with temperatures between 4.7 and 9.4 keV. These galaxy clusters are studied in detail using X-ray data and global physical properties are determined. Correlations between these quantities are analysed and compared with the results for distant clusters. We use a sample of nearby clusters with the best ROSAT and ASCA data. This sample is complemented with four new observations of distant clusters performed by CHANDRA and XMM-Newton. We find an interesting correlation between the extent of the intra-cluster gas relative to the dark matter distribution. The extent of the gas relative to the extent of the dark matter tends to be larger in less massive clusters. This correlation might give us some hints on non-gravitational processes in clusters. We do not see evolution in the gas mass fraction out to a redshift of unity. Within r_{500}, the mean gas mass fraction obtained is $(0.16 \pm 0.04)h_{50}^{-3/2}$.

Throughout this chapter we use $H_0 = 50$ km/s/Mpc and $q_0 = 0.5$ for a direct comparison of the results with other authors.

4.1 The sample

Since the aim of this work is the analysis of the total and gas mass distribution in nearby galaxy clusters we selected clusters in which an accurate total mass determination is possible, i.e with relaxed and symmetric morphologies, good temperature measurements and well determined surface brightness profiles. Therefore we obtain a high quality sample that consists of ten best clusters in the redshift range $0.03 < z < 0.09$ observed with the ROSAT PSPC. Cluster temperatures measured by the ASCA satellite are taken from Markevitch et al. (1998, 1999); Sarazin et al. (1998), and Bauer & Sarazin (2000) resulting in a temperature range of 4.7-9.4 keV. In Table 4.1 the different properties for each cluster are listed.

Of all the new observations only the best data are selected in order to obtain the most reliable X-ray mass estimate. In Table 4.2 the published data we use to derive masses are listed.

†This Chapter is based on an article written together with Sabine Schindler. It is published in Astronomy & Astrophysics, vol. 403, p.433-442, 2003.

Table 4.1— In Cols. 1 and 2 the clusters and their redshift are shown. In Col. 3 the hydrogen column density from (Dickey & Lockman, 1990) is listed. The temperatures in Col. 4 are ASCA emission-weighted temperatures excluding cooling flows and other contaminating components. Col. 5 lists the ratio of the bolometric flux to the ROSAT PSPC countrate in the energy range 0.5-2.0 keV using the program PIMMS (http://www.heasarc.gsfc.nasa.gov/Tools/w3pimms.html). ASCA temperatures are taken from references: 1—Markevitch et al. (1998); 2—Markevitch et al. (1999); 3—Sarazin et al. (1998); 4—Bauer & Sarazin (2000).

Cluster	z	N_H (10^{20}cm^{-2})	kT_{gas} (keV)	F_{Xbol}/countrate (10^{-11}erg/counts/cm^2)	Ref.
A496	0.033	4.58	4.7 ± 0.2	4.3	2
A2199	0.030	0.863	4.8 ± 0.2	3.9	2
A3112	0.075	2.61	$5.3^{+0.7}_{-1.0}$	4.4	1
A1651	0.085	1.81	6.1 ± 0.4	4.5	1
A3571	0.040	3.71	6.9 ± 0.2	4.9	1
A1795	0.062	1.19	7.8 ± 1.0	4.9	1
A401	0.075	10.5	8.0 ± 0.4	6.0	1
A478	0.088	15.1	$8.4^{+0.8}_{-1.4}$	6.8	1
A644	0.070	6.82	$8.6^{+0.7}_{-0.6}$	5.8	4
A2029	0.077	3.04	$9.4^{+0.6}_{-0.5}$	5.6	3

4.2 Mass determination

Once we de-project the surface brightness to three-dimensional density with the β model, together with the assumptions of hydrostatic equilibrium and spherical symmetry the integrated mass within radius r can be determined as

$$M(r) = \frac{-kr}{\mu m_p G} T_{gas}(r) \left(\frac{d \ln \rho(r)}{d \ln r} + \frac{d \ln T_{gas}(r)}{d \ln r} \right), \tag{4.1}$$

with ρ and T_{gas} being the density and the temperature of the intra-cluster gas, respectively. k, μ, m_p, and G are the Boltzmann constant, the molecular weight, the proton mass, and the gravitational constant.

The determination of the cluster mass with X-ray observations may be seriously affected in merging clusters if magnetic fields are ignored (Dolag & Schindler, 2000). But in our sample, we are analyzing clusters that for their X-ray morphology seem to be relaxed. Dolag & Schindler (2000) have shown that magnetic fields in relaxed clusters do not generally lead to any under- or overestimate of masses and they cannot be the dominant reason for the mass discrepancy between X-ray mass and lensing mass found in the central region of some clusters. The maximum difference of averaged mass profiles between models with high magnetic field and no magnetic field is 15% (at radius $\sim$ 50 kpc), while observational discrepancies between different methods of a factor of 2-3 are found. At radii larger than 200 kpc there is no difference at all between the profiles of models with different magnetic fields. For this reason we have not taken into account the magnetic pressure in the hydrostatic equilibrium equation above.

Table 4.2— Published data from XMM-Newton and CHANDRA observations used to derived the total and gas mass. In Cols. 1 and 2 the clusters and their redshift are listed. The gas temperature is shown in Col. 3. The published fit parameters of the β model are listed in Cols. 4, 5 and 6: the slope β, the core radius r_c and the central electron density n_{e0}. The quoted errors are 90% confidence level for all quantities except for the parameters in cluster RX-J0849+4452 and the value of the temperature in A1835 which are 68% confidence level. References: (1) Stanford et al. (2001); (2) Schindler et al. (2001); (3) Arnaud et al. (2002); (4) Majerowicz et al. (2002).

Cluster	z	kT_{gas} (keV)	β	r_c (kpc)	n_{e0} (10^{-2}cm^{-3})	Ref.
RX-J0849+4452	1.26	$5.8^{+2.8}_{-1.7}$	0.61 ± 0.12	100.2 ± 30.7	1.42	Chandra (1)
RBS797	0.354	$7.7^{+1.2}_{-1.0}$	0.63 ± 0.01	49 ± 4	8.86	Chandra (2)
RX-J1120.1+4318	0.6	5.3 ± 0.5	$0.78^{+0.06}_{-0.04}$	201^{+27}_{-18}	0.81	XMM-Newton (3)
A1835	0.25	7.6 ± 0.4	0.704 ± 0.005	202.3 ± 7.1	1.47	XMM-Newton (4)

Table 4.3— X-ray quantities as measured from ROSAT/PSPC and ASCA observations. The clusters are listed in Col. 1. Col. 2 shows the emission-weighted gas temperature. In Cols. 3, 4, 5, 6 and 7 the fit parameters of the β model are shown: the slope β, the core radius r_c, the central surface brightness S_0, the central electron density n_{e0} and the background B in the energy band 0.5 - 2.0 keV. S_0 is in units of 10^{-2} ROSAT/PSPC counts/s/arcmin^2. B is in units of 10^{-4} ROSAT/PSPC counts/s/arcmin^2. In Col. 8 r_f denotes the radius range fitted.

Cluster	kT_{gas} (keV)	β	r_c (kpc)	S_0	n_{e0} (10^{-2}cm^{-3})	B	r_f (Mpc)
A496	4.7±0.2	0.64 ± 0.02	185 ± 16	4.0	0.434	4.4	0.14 - 2.9
A2199	4.8±0.2	0.64 ± 0.01	132 ± 7	9.4	0.751	2.4	0.15 - 2.8
A3112	$5.3^{+0.7}_{-1.0}$	0.65 ± 0.03	181 ± 46	6.6	0.609	2.9	0.27 - 5.8
A1651	6.1±0.4	0.68 ± 0.03	224 ± 24	7.3	0.591	3.5	0.13 - 6.4
A3571	6.9±0.2	0.66 ± 0.02	235 ± 20	7.1	0.530	4.4	0.14 - 2.8
A1795	7.8±1.0	0.68 ± 0.01	197 ± 16	11.3	0.744	2.8	0.19 - 2.8
A401	8.0±0.4	0.67 ± 0.02	284 ± 21	5.4	0.485	2.5	0.11 - 5.7
A478	$8.4^{+0.8}_{-1.4}$	0.69 ± 0.02	201 ± 20	11.7	0.911	1.5	0.22 - 6.1
A644	$8.6^{+0.7}_{-0.6}$	0.72 ± 0.02	239 ± 17	6.9	0.591	2.3	0.20 - 5.4
A2029	$9.4^{+0.6}_{-0.5}$	0.68 ± 0.02	244 ± 24	9.7	0.650	5.1	0.29 - 5.9

Table 4.4— Results of the isothermal analysis: total mass, gas mass and gas mass fraction for the cluster sample. The first column gives the cluster name. Col. 2 denotes the radius r_{500} which comprises an overdensity of 500 over the critical density. Cols. 3, 4 and 5 list the total mass, the gas mass and the gas mass fraction within r_{500}, respectively. In Cols. 6, 7 and 8 the same quantities are listed for a radius $0.5 \times r_{500}$. For all the quantities the reported errors are 90% confidence level.

Cluster	r_{500} (Mpc)	$M_{tot}(r_{500})$ ($10^{14} M_\odot$)	$M_{gas}(r_{500})$ ($10^{14} M_\odot$)	$f_{gas}(r_{500})$	$M_{tot}(\frac{r_{500}}{2})$ ($10^{14} M_\odot$)	$M_{gas}(\frac{r_{500}}{2})$ ($10^{14} M_\odot$)	$f_{gas}(\frac{r_{500}}{2})$
A496	1.42 ± 0.03	$4.6^{+0.3}_{-0.7}$	0.69	$0.15^{+0.03}_{-0.02}$	$2.2^{+0.2}_{-0.1}$	0.27	0.12 ± 0.02
A2199	1.45 ± 0.03	$4.8^{+0.3}_{-0.7}$	0.68	0.14 ± 0.02	$2.4^{+0.2}_{-0.1}$	0.28	0.12 ± 0.01
A3112	$1.44^{+0.09}_{-0.14}$	$5.3^{+0.7}_{-1.7}$	0.94	$0.18^{+0.06}_{-0.03}$	$2.5^{+0.3}_{-0.5}$	0.37	0.15 ± 0.03
A1651	1.55 ± 0.05	$6.9^{+0.6}_{-1.9}$	1.24	$0.18^{+0.05}_{-0.02}$	$3.2^{+0.3}_{-0.5}$	0.50	$0.16^{+0.03}_{-0.02}$
A3571	$1.73^{+0.03}_{-0.02}$	$8.5^{+0.5}_{-1.0}$	1.50	$0.18^{+0.03}_{-0.02}$	$4.0^{+0.3}_{-0.2}$	0.60	0.15 ± 0.02
A1795	$1.82^{+0.12}_{-0.13}$	$10.4^{+1.4}_{-2.5}$	1.49	$0.14^{+0.04}_{-0.02}$	5.0 ± 0.7	0.64	0.13 ± 0.02
A401	$1.78^{+0.04}_{-0.05}$	$10.2^{+0.7}_{-2.1}$	1.93	$0.19^{+0.04}_{-0.02}$	$4.7^{+0.4}_{-0.3}$	0.75	0.16 ± 0.02
A478	$1.83^{+0.09}_{-0.16}$	$11.5^{+1.2}_{-3.6}$	1.83	$0.16^{+0.05}_{-0.02}$	$5.5^{+0.6}_{-1.0}$	0.80	$0.14^{+0.03}_{-0.02}$
A644	1.94 ± 0.07	$13.0^{+1.2}_{-5.8}$	1.52	$0.12^{+0.05}_{-0.02}$	$6.2^{+0.6}_{-1.6}$	0.68	$0.11^{+0.03}_{-0.01}$
A2029	$1.95^{+0.06}_{-0.05}$	$13.4^{+1.1}_{-3.5}$	2.16	$0.16^{+0.04}_{-0.02}$	$6.4^{+0.5}_{-1.0}$	0.90	$0.14^{+0.03}_{-0.02}$

4.3 Data analysis

We use X-ray imaging data retrieved from the ROSAT archive[1] to determine the surface brightness profiles of the clusters. For each cluster a ROSAT PSPC (the Position Sensitive Proportional Counter) image was reduced using the standard analysis with the EXSAS software. In order to maximize the signal-to-noise ratio, we choose the hard energy band (0.5-2.0 keV) corresponding to channel numbers 52-201.

In each PSPC image various detector/telescope effects are apparent. Three of the most noticeable are:

a) Vignetting. The ROSAT mirror assembly has more effective area on-axis than off-axis, i.e., the mirrors are more efficient at collecting photons from on-axis sources than from off-axis sources. This effect is known as vignetting. Vignetting causes the effective exposure time to decrease with increasing off-axis angle.

b) Point-spread function variations. The ROSAT point spread function is also dependent on the off-axis position. The width of the point spread function is smallest for sources observed on-axis and increases rapidly with off-axis angle. Thus point sources observed at large off-axis angles look much larger than they would if observed on-axis.

c) The shadow of the supporting structure of the PSPC. The spacecraft is "wobbled" in order to minimize the shadow. The direction of the spacecraft wobble is usually parallel to one of the PSPC support ribs. Any X-ray source under this rib will be occulted by the rib for the entire observation. Thus the area of the sky along this rib receives almost no exposure and appears dark in PSPC images. Other sources in the field not under this rib will in general be occulted by some part of the PSPC window support structure for only part of the observation.

The images were corrected for exposure variations and telescope vignetting using exposure maps generated with MIDAS/EXSAS software. The different PSPC cluster images can be seen in appendix A. The cluster cores are somewhat blurred in PSPC images by the point spread function (PSF) ($\approx 20-30$ arcsec FWHM for ROSAT/PSPC). This effect is more important for compact clusters. For example for the compact cluster A780 (r_c=62±2 kpc), Neumann & Arnaud (1999) estimated the core radius to be overestimated by about 10%. For the other clusters in our sample, which have a larger core radius, we estimate that the effects of the PSF are much smaller than the statistical errors. Therefore no correction for the PSF is necessary.

We generate radial surface brightness profiles in concentric annuli (centred on the emission maximum of the cluster) excluding manually obvious point sources in the field of view and cluster substructure if they show up as a local maximum. The observed profiles are fitted with a β-model, (Cavaliere & Fusco-Femiano, 1976) plus background. In appendix A the surface brightness profiles and the best fits for all the clusters in the nearby sample are shown.

$$S(b) = S_0 \left[1 + \frac{b^2}{r_c^2}\right]^{-3\beta+\frac{1}{2}} + B. \tag{4.2}$$

The parameters r_c (core radius), β, S_0 (central surface brightness) and the background B are obtained from a least-squares fit to the X-ray profile. The β-model parameters are found to range between 0.6 and 0.8 for the slope β and between 130 and 290 kpc for the core radius r_c, respectively.

[1]http://www.xray.mpe.mpg.de/rosat/archive

However, the overall β-model fit is a poor description of the central region of some clusters where excess emission is observed. Indeed we find in most of the cases very large χ^2 values when fitting the entire cluster emission. We reduce the χ^2 values ($\chi^2_{red} < 1.4$) by excluding the central bins from the fit. The best fit β -model was determined excluding the data within the cooling radius taken from Allen & Fabian (1997); Peres et al. (1998); White et al. (1997). For the clusters in our sample with excess central emission, the exclusion of the central part of the profile yields larger β values and core radii values compared to the overall β-model fit.

In Table 4.3 the resulting parameters are shown. The reported errors are 90% confidence level.

4.3.1 Isothermal analysis

As well as the density profiles we need temperature profiles to determine the total cluster mass. We follow two different approaches for the temperature profile. In our first study we assume isothermality. In § 4.3.2 we include the temperature gradients derived from Markevitch's ASCA analysis to see how the total cluster mass is affected. In the isothermal approach we neglect the term associated with the temperature gradient in Eq. (4.1). In this case the total mass profile is:

$$M(< r) = \frac{3kT_{\rm gas} r^3 \beta}{G\mu m_{\rm p}} \left(\frac{1}{r^2 + r_{\rm c}^2} \right), \tag{4.3}$$

where the mean atomic weight μ is assumed to be 0.61.

The total mass thus depends linearly on both β and $T_{\rm gas}$. In the case of clusters with central X-ray excess and with references 1 and 2 in Table 4.1, we use emission-weighted gas temperature obtained by excluding the cooling flow component. For clusters with central X-ray excess and references 3 and 4 in Table 4.1 we use the temperature obtained when a simple spectral model for ambient gas plus a cooling flow model is applied. In appendix A the different mass profiles obtained for the cluster sample are shown and as an example, typical mass profiles are shown in Fig. 4.1 for the cluster Abell 2199.

After having determined the gravitational mass profiles for the clusters, it is important to fix the radius within which the cluster masses can be calculated. As the mass of a cluster increases with radius, masses can only be compared when derived within equivalent volumes. Simulations by Evrard et al. (1996) showed that the assumption of hydrostatic equilibrium is generally valid within at least radius r_{500}, where the mean gravitational mass density is equal to 500 times the critical density $\rho_{\rm c}(z) = 3H_0^2(1+z)^3/8\pi G$. The resulting cluster masses and gas masses within r_{500} and $0.5 \times r_{500}$ for all the clusters are listed in Table 4.4.

The errors on the total mass can be estimated as follows. The total cluster mass is affected by the errors in the parameters of the β-model. If we consider the upper (lower) values of β and $\rm r_c$, the total cluster mass at radius $\rm r_{500}$ increases (decreases) but not more than 5% for all the clusters in the sample.

The uncertainties in the total mass estimate are much larger due to the uncertainty in temperature estimates and possible temperature gradients. We calculate the difference in the total cluster mass caused by the existence of a temperature gradient for two different radii, $\rm r_{500}$ and $\rm r_{500}/2$. The total isothermal cluster mass at $\rm r_{500}$ is overestimated compared with the mass obtained considering a temperature gradient. This difference ranges between 10% (Abell 3571) and 27% (Abell 1651) with an specially high difference (44%) for the cluster Abell 644. At radius $\rm r_{500}/2$ this difference is smaller compared with the values at r_{500}. In this case the isothermal total cluster mass is overestimated in some clusters and subestimated in others, with differences ranging between 2% (Abell 2199) and 14% (Abell 2029) having the cluster Abell 644 the highest difference (24%).

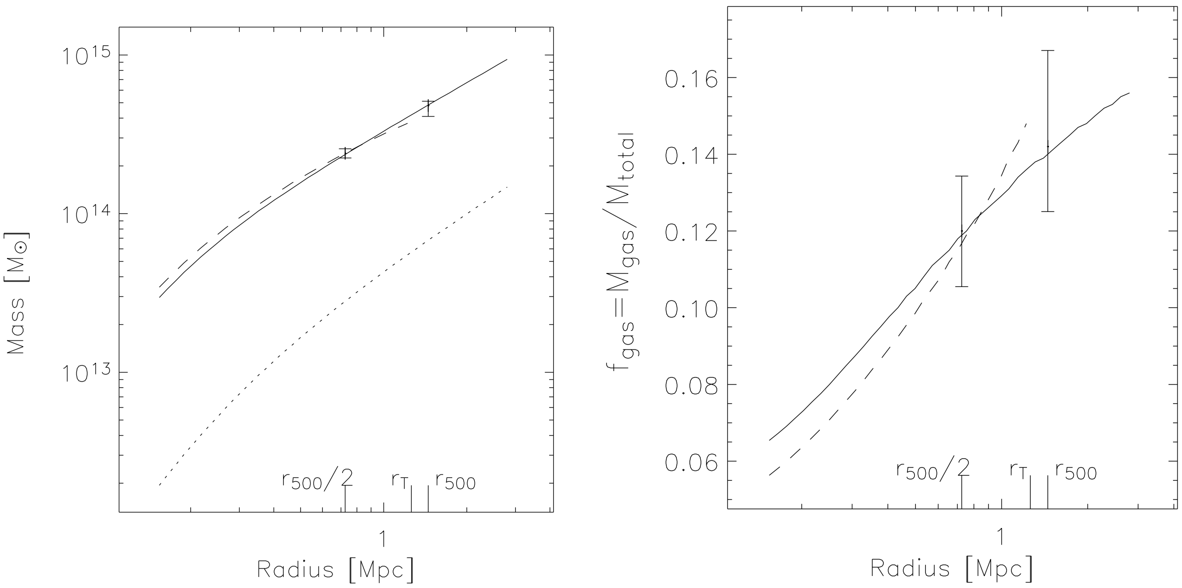

Figure 4.1— Left: Total mass profile assuming isothermality (solid line) and gas mass profile (dotted line) for the cluster A2199. The dashed line represents the total mass profile derived with a temperature gradient. r_{500} is the radius which comprises an overdensity of 500 over the critical density. r_T represents the maximum radius out to which the temperature profile is known. A typical error bar for the isothermal total cluster mass is shown at radii r_{500} and $r_{500}/2$. Right: Gas mass fraction assuming isothermality (solid line) for cluster A2199. Dashed line represents the gas mass fraction derived with a gradient of temperature. A typical error bar for the isothermal gas mass fraction is shown at radii r_{500} and $r_{500}/2$.

There are also additional uncertainties coming from deviations from spherical symmetry (Piffaretti et al., 2003), deviations from hydrostatic equilibrium and projection effects that are together about 15% – 30%, (Evrard et al., 1996; Schindler, 1996b), but these are hard to quantify for each cluster individually. As only well relaxed clusters where chosen, these errors should be relatively small in the clusters of this sample and therefore they are not taken into account.

We compute the error in the total cluster mass as the convolution of the error coming from the uncertainty in the fit parameters, the error in the temperature and the error coming from the assumption of non isothermality. However we keep in mind that the true uncertainty of the total mass is probably greater than this value.

In the energy range considered, the gas mass estimate is almost independent on the temperature measurement. The gas mass estimate can be affected by the uncertainty in the central surface brightness S_0, the error in the flux/countrate estimation and the uncertainties in the β-model parameters, β and r_c. Although the uncertainties in the above mentioned quantities are small ($\sim 5\%$), we calculate the error in the gas mass to be about 10% due to the convolution of the error coming from the uncertainty in these factors.

4.3.2 Temperature gradients

The isothermal assumption may give poor estimates of the total mass if strong temperature gradients are present. Studies with ASCA data using different PSF-correction techniques provide conflicting results; Markevitch et al. (1998) have observed declining temperature profiles whereas in the analysis of 106 cluster of galaxies by White (2000) it is found that 90 percent of the temperature profiles are consistent with isothermality at the 3-sigma confidence level.

To estimate the effect of the temperature gradients on cluster masses, we have calculated $M_{\rm tot}$ using the temperature profiles derived by Markevitch et al. (1998, 1999); Sarazin et al. (1998) and Bauer & Sarazin (2000). In some clusters, the temperature outside the cooling core can be well approximated by a polytropic function

$$T_{\rm gas} \propto \rho_{\rm gas}^{\gamma-1} \tag{4.4}$$

where γ is the polytropic index (values between 0.9 and 1.5). In this case the total mass enclosed in a sphere of radius r (Eq. (4.1)) is:

$$M(<r) = \frac{3\beta\gamma r^3}{G m_{\rm p}\mu}\frac{kT_{\rm gas}(r)}{(r^2+r_{\rm c}^2)}. \tag{4.5}$$

Here $T_{\rm gas}$ is the true temperature, rather than a projection on to the plane of the sky[2].

Markevitch et al. (1999) showed that as long as the temperature is proportional to a power of the density, and the density follows a β-model, the true temperature differs from the projected temperature only by a constant factor, given by:

$$\frac{T_{\rm proj}}{T_{\rm true}} = \frac{\Gamma\left[\frac{3}{2}\beta(1+\gamma)-\frac{1}{2}\right]\Gamma(3\beta)}{\Gamma\left[\frac{3}{2}\beta(1+\gamma)\right]\Gamma(3\beta-\frac{1}{2})}, \tag{4.6}$$

where $\Gamma(x)$ is the Gamma function.

In our analysis, the projected temperature profiles are parametrized using a linear function of the form

$$T_{\rm gas}(r) = T(0) - \alpha r. \tag{4.7}$$

The parameters T(0) and α are determined by fitting a straight line to the projected temperature profiles mentioned before, excluding the central cluster region in the case of clusters with central X-ray excess. It is not useful to fit a more complex function because the temperatures for consecutive annuli are determined with low accuracy.

We do not de-projected the temperatures for the mass analysis with temperature gradient. Although this introduces some additional uncertainty in the total mass we show below that the results using true temperatures or projected temperatures are very similar.

For the cluster A2199 we compare the total mass derived using the linear gradient Eq. (4.7) (see temperature gradients and linear fit in Appendix B for all the clusters in the sample) and the mass calculated with the polytrope Eq. (4.4) by Markevitch et al. (1999). The estimated values for the total cluster mass agree within the errors. There is a difference $\leq$ 10% at large radii ($r >$ 1Mpc) and $\leq$ 15% at the small radius ($r =$ 0.2Mpc). For example Markevitch et al. (1999)

[2]One can calculate a temperature profile that is emission-weighted distanced (by ρ^2) along the line of sight l, as a function of the projected distance from the center x (such that $r^2 = x^2 + l^2$), as $T_{proj}(x) = \frac{\int_0^\infty T(r)\rho^2 dl}{\int_0^\infty \rho^2(r) dl}$

using a polytrope equation with $\gamma = 1.17$ find a total cluster mass of $(0.65 \pm 0.11) \times 10^{14}\mathrm{M}_\odot$, $(2.9 \pm 0.3) \times 10^{14}\mathrm{M}_\odot$ and $(3.6 \pm 0.5) \times 10^{14} M_\odot$ at a radius of 0.2 Mpc, 1 Mpc and $r_{500} = 1.3$ Mpc respectively, for cluster A2199. We derive the total cluster mass for this cluster using the linear gradient $T(r) = -2.1r + 5.6$ where r is units of Mpc and temperature is in keV. The masses obtained in this case are quite similar, $(0.56 \pm 0.14) \times 10^{14}\mathrm{M}_\odot$, $(3.1 \pm 0.8) \times 10^{14}\mathrm{M}_\odot$ and $(3.9 \pm 1.0) \times 10^{14}\mathrm{M}_\odot$ at a radius of 0.2 Mpc, 1 Mpc and 1.3 Mpc, respectively. Therefore we conclude that for our purpose of comparison, it is sufficient to use a linear gradient of projected temperatures.

In the following we will apply only a linear temperature gradient. In this case we estimate the errors in the total cluster mass and gas mass as follows. Due to the errors in the temperature, the errors in the linear fit are large. We estimate the errors in the total cluster mass using the different possible temperature gradients given by the lower and upper values of T(0) and α (see Eq. (4.7)). When the different possible temperature gradients are used, the radii r_{500} and $r_{500}/2$ change significantly and hence the total and gas mass enclosed by them.

In Appendix A and as an example in Fig. 4.1 (left) for the cluster Abell 2199, the different mass profiles calculated using the isothermal model and a linear gradient of temperature can be seen. With the assumption of constant temperature (solid line) the total mass is overestimated (between 10% and 44%) at large radii (r_{500}) and underestimated or subestimated depending on the cluster, at small radii (between 2% and 24% at $r_{500}/2$), compared to the temperature gradient analysis (dashed line). The overestimation of the total cluster mass is increasing with radius. For some clusters in the sample (Abell 2199, 496, 1795 644 and 2029) the radius out to which the temperature was measured r_T is smaller than r_{500} estimate. In that cases an extrapolation to the area not covered by the temperature profile was necessary to give an estimation of the total mass using the temperature gradient analysis.

Figure 4.1 (left) also shows the gas mass profile (dotted line) in the radius range that has been used to fit the data with the β-model.

Figure 4.1 (right) shows the gas mass fraction, defined as the ratio between the gas mass M_gas and the total mass M_tot. The difference in the gas mass fraction between the isothermal and non-isothermal cluster studies is shown as well (solid and dashed lines, respectively). At small radii ($r_{500}/2$) the differences are not large (between 2% and 17%, with the exteme case of Abell 644 with 32%). At larger radii the temperature profile analysis yields steeper profiles and higher values (between 11% and 40%, with the extreme case of Abell 644 with 78%) compared to the isothermal one. The gas mass fraction derived using a gradient of temperature is not reliable beyond the radius r_T where the gradient is determined and thus it is not plotted.

In Appendix B the temperature profiles and the isothermal temperatures used in the analysis of the nearby sample are shown. The overall cluster temperature we use to determine isothermal masses (dashed line) seems to be overestimated in clusters Abell 644 and 2029. In both cases, the isothermal temperature lies above the fit we find for the temperature gradient at all radii. It is for this reason the isothermal analysis of these clusters provide total cluster masses larger at all radii compared with the temperature gradient analysis and therefore the gas mass fraction values are subestimated.

The masses calculated with both analyses (isothermal and temperature profile) are compared in Fig. 4.2 for each cluster in the sample at radius r_{500}. The symbols correspond to the cluster name listed in Fig. 4.4 right. The smaller symbols represent the values for the temperature profile analysis. Although the gas mass profile is not influenced by the change in the cluster temperature, the gas mass at radius r_{500} is different in the two analyses due to the difference in the value r_{500}

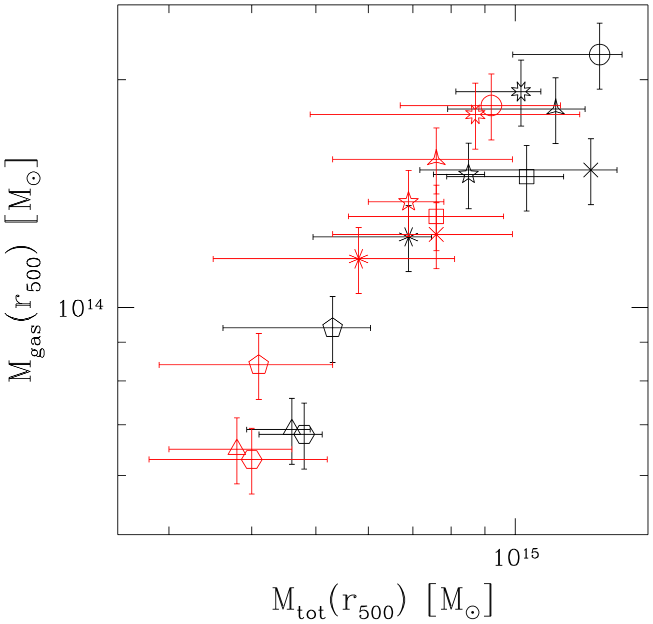

Figure 4.2— Comparison of masses obtained with the isothermal and temperature profile analysis at radius r_{500}. The red symbols represent the temperature profile analysis.

which depends on the temperature.

The current generation of X-ray observatories (CHANDRA, XMM-Newton) with large effective area, excellent angular resolution (0.5″ for CHANDRA) and better energy resolution over a wide energy range (0.1-15 keV for XMM-Newton) are improving the accuracy of the spatially resolved spectroscopy. That means that with the new missions the temperature gradient in the intracluster medium can be constrained in a better way. XMM-Newton observations show that, except for the core (with a few $\times$ 100 kpc), cluster gas is isothermal (or perhaps with a slowly decaying temperature) out to the distances where X-ray emission can be detected (less than the virial radius).

4.4 Results and discussion

Clusters of galaxies are very important structures in the Universe and the understanding of the different physical processes taking place during cluster formation is a very attractive task. Studying the possible correlations between different properties as the temperature, total mass, gas mass or relative gas extent, we can draw conclusions about their formation processes, thermal history and hence about cosmological parameters. Many authors have analyzed samples of clusters looking for these fundamental relations (Arnaud & Evrard, 1999; Ettori & Fabian, 1999; Horner et al., 1999; Jones & Forman, 1999; Mohr et al., 1999; Neumann & Arnaud, 1999; Nevalainen et al., 2000; Schindler, 1999) In this section we present the analysis of several correlations between some quantities mentioned above. In the following all the results presented and discussed are refered to the analysis of the cluster sample assuming isothermality.

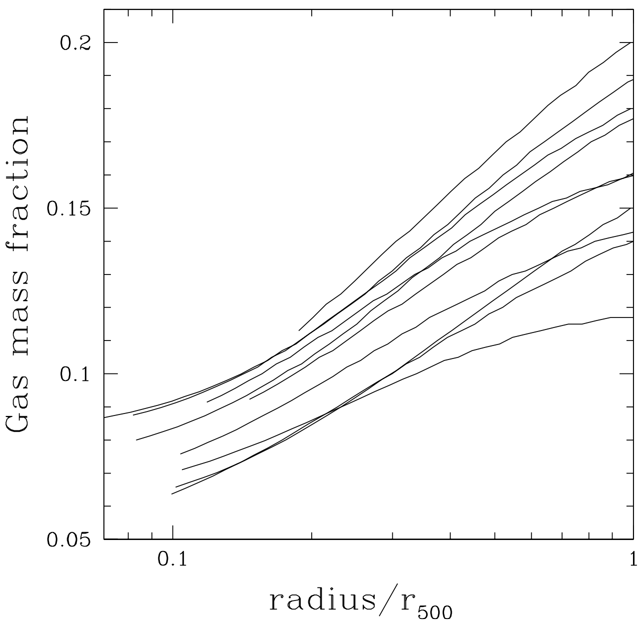

Figure 4.3— Gas mass fraction profiles derived for the nearby cluster sample. Profiles are plotted from the minimum radius fitted in the β model.

4.4.1 Gas mass fraction

The gas mass fraction defined as $f_{\rm gas} = M_{\rm gas}/M_{\rm tot}$ is calculated for each cluster in the sample. The errors associated with the gas mass fractions are calculated by the convolution of errors in the total cluster mass and the gas mass. We find that inside each cluster the gas mass fraction increases with radius (see Fig. 4.3 and Appendix A) implying that the gas distribution is more extended than dark matter.

A low Ω_{Matter} is required to reconcile the high gas mass fraction of $< f_{\rm gas} >_{r_{500}} = 0.16 \pm 0.04$ (in this work), with the baryon fraction predicted by primordial nucleosynthesis. The gas mass fraction provides a lower limit for the baryon fraction in the Universe,

$$< f_{\rm gas} >_{r_{500}} = \frac{\rho_{\rm gas}/\rho_{\rm crítica}}{\rho_{\rm cúmulo}/\rho_{\rm crítica}} \lesssim \frac{\Omega_{\rm Barions}}{\Omega_{\rm Matter}}. \tag{4.8}$$

On the other hand, studies about primordial nucleoshyntesis (Burles & Tytler, 1998a,b) and the new results obtained with WMAP from the analysis of the cosmic microwave background (Spergel et al., 2003), predict a baryonic density of $\Omega_{\rm B} \sim 0.08 h_{50}^{-2}$. In this way, a low Ω_M is required, $\Omega_{\rm M} < \Omega_{\rm B}/f_{\rm gas} \approx 0.4$ (for $H_0 = 70$ km/s/Mpc), to be able to explain the high gas mass fraction found in our sample of nearby clusters with $< f_{\rm gas} >= (0.16 \pm\ 0.04) h_{50}^{-3/2}$. In this analysis only the mass from the major baryonic component in clusters, the intracluster gas, has been included while the barions from galaxies are ignored.

To test whether there is any evolution of the gas mass fraction we plot this quantity versus redshift (Fig. 4.4) including the analysis from Schindler (1999) for distant clusters (0.3<z<1.0). In this figure, as well as in all other following figures, each cluster is plotted with a different symbol (see

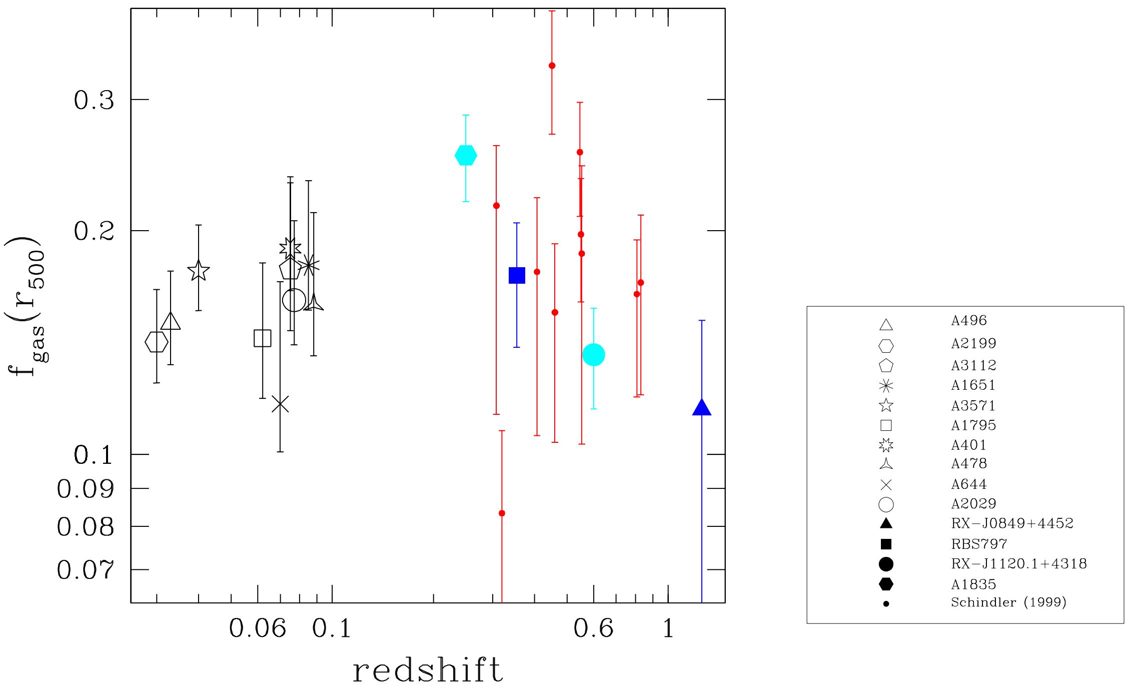

Figure 4.4— Left: Gas mass fraction versus redshift. No clear evolution of the gas mass fraction can be seen out to a redshift of unity. Right: Symbols used for the various clusters in the figures

Fig. 4.4 right). We include in the comparison another distant clusters: RX−J0849+4452 (z=1.26), RBS797 (z=0.354), A1835 (z=0.25) and RX−J1120.1+4318 (z=0.6) where we calculate the total and gas mass using the published parameters from the CHANDRA and XMM-Newton data analysis (see Table 4.2).

In the gas mass fraction we see no clear trend with redshift. The mean value in our sample is $< f_{\rm gas} >= 0.16 \pm 0.04$ (with $\sigma = 0.02$), where the associated error is calculated as the mean value of the errors in the gas mass fractions. Our mean gas mass fraction is in agreement with other nearby samples, Mohr et al. (1999): $f_{\rm gas}$=0.21, Ettori & Fabian (1999): $f_{\rm gas}$=0.17 and also in agreement with the value for distant sample by Schindler (1999), $f_{\rm gas}$=0.18. Therefore we conclude that we do not see evolution in the gas mass fraction out to a redshift of unity. In contrast to this result Ettori & Fabian (1999) found indications for a decrease of $f_{\rm gas}$ with increasing redshift in a nearby sample. Matsumoto et al. (2000) found no clear evidence of evolution of $f_{\rm gas}$ for the clusters at z < 1.0.

In Fig. 4.5 left we compare the gas mass with the total cluster mass. A trend of an increasing gas mass with total mass is visible in our sample. This trend was also found for distant clusters by Schindler (1999) (dotted line in Fig. 4.5). A linear fit regression yields

$$M_{\rm gas}(r_{500}) = 0.12 M_{\rm tot}(r_{500})^{(1.1\pm0.2)}. \tag{4.9}$$

$M_{\rm gas}(r_{500})$ and $M_{\rm tot}(r_{500})$ are in units of $10^{14} M_{\odot}$. This trend is in agreement with the analysis by Arnaud & Evrard (1999).

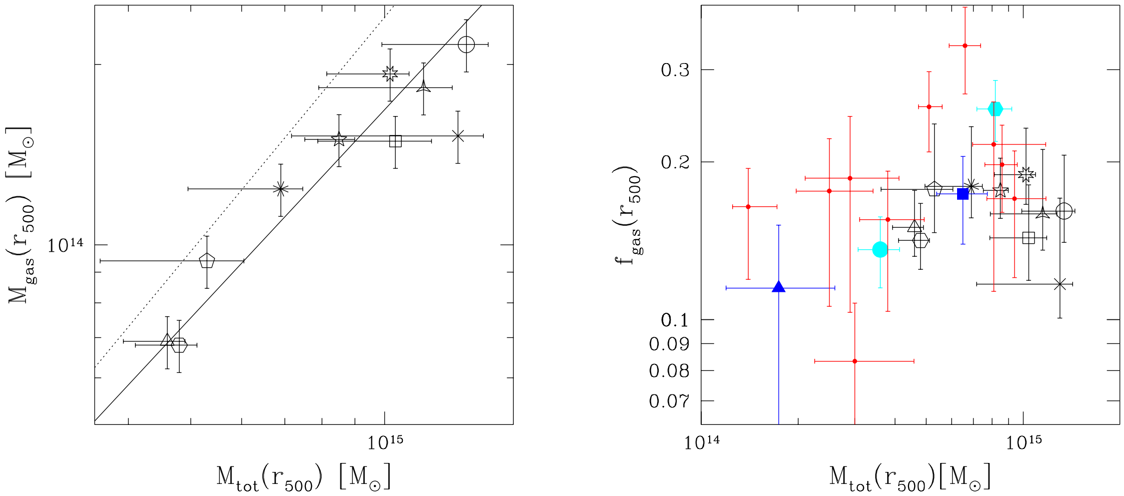

Figure 4.5— Left: Gas mass versus total mass. In solid line is shown the best fit for the nearby sample. For comparison, in dotted line is plotted the best fit obtained for the distant sample by Schindler (1999). Right: Gas mass fraction versus total cluster mass for the nearby and distant sample. The gas mass fraction shows no clear dependence on the total mass.

Because the exponent in Eq. (4.9) is close to unity, we find no clear dependence of the gas mass fraction on the total mass in our sample (see Fig. 4.5 right, where the nearby and distant sample are shown).

Several authors have also related measured values of $f_{\rm gas}$ and $M_{\rm tot}$ or $T_{\rm gas}$. Up to now the results are discordant concerning the form of this relation. For example, David et al. (1995) found indications for an increase of $f_{\rm gas}$ with increasing $T_{\rm gas}$. Allen & Fabian (1997) found in a sample of X-ray luminous clusters indications for a decrease of $f_{\rm gas}$ with increasing $T_{\rm gas}$. Ettori & Fabian (1999) found no dependence of $f_{\rm gas}$ on $M_{\rm tot}$ for high luminosity clusters.

As mentioned before the gas mass fraction is not constant with radius. In order to plot this increase against other cluster properties, we compare the gas mass fraction at radius r_{500} with the gas mass fraction at $0.5 \times r_{500}$ in each cluster. The mean gas mass fraction at $0.5 \times r_{500}$ is 0.14 ± 0.02, i.e. smaller than the mean of 0.16 ± 0.04 at r_{500}. The ratio of these fractions is a measure for the extent of the gas distribution relative to the dark matter extent: $E = \frac{f_{\rm gas}(r_{500})}{f_{\rm gas}(r_{500}/2)}$.

The error in the relative gas extent E is not easy to determine. We estimate its uncertainty by testing how much this value changes when:

- we consider the uncertainty in the gas temperature
- the fit parameters change

Since the relative gas extent is calculated as the ratio of gas mass fractions at different radii, the errors coming from the uncertainty in the temperature are cancelled out. The relative gas extent E changes significantly when the fit parameters (β and r_c) are varied. This error coming from the uncertainties in the fit parameters is included in the following graphs.

For all the clusters in our sample the relative gas extent E is larger than 1 (see Fig. 4.6 left). This means that in general the gas distribution is more extended than the dark matter, which is in agreement with other results for nearby cluster samples by David et al. (1995); Ettori & Fabian

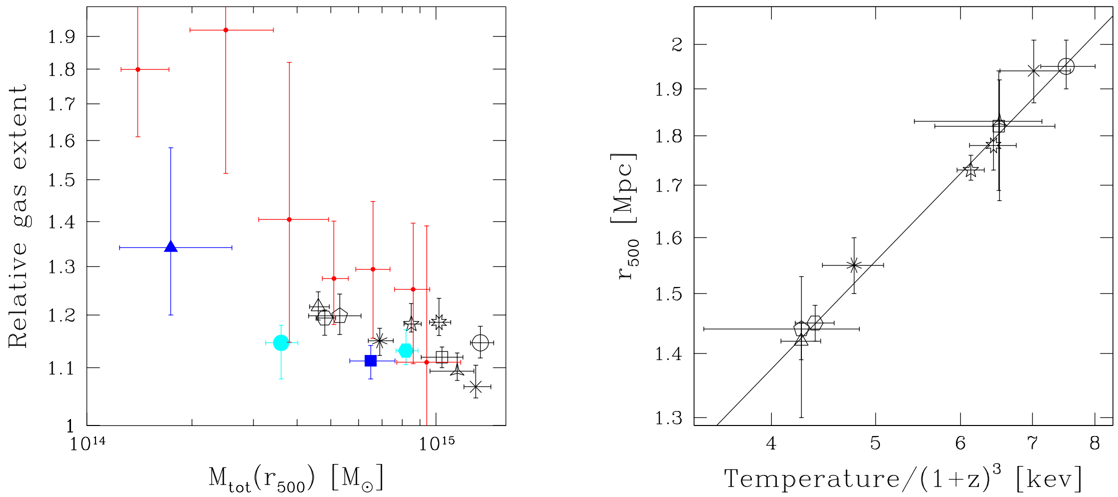

Figure 4.6— Left: Ratio of gas mass fraction at r_{500} and $r_{500}/2$ as a measure for the relative extent of the gas distribution versus total cluster mass at r_{500}. For clarity, clusters with the largest error bars from Schindler (1999) are not shown. Right: Radius r_{500} versus gas temperature. The solid line shows the best linear fit obtained.

(1999); Jones & Forman (1999) and for distant samples by Schindler (1999) and Tsuru et al. (1997). The distant sample by Schindler (1999) and the other CHANDRA and XMM-Newton observations are also shown in Fig. 4.6 left for comparison.

In the nearby sample ($4.7 < T < 9.4$ keV) this relative gas extent E shows a mild dependence on the total cluster mass (see Fig. 4.6 left) similar to the result by Schindler (1999). Clusters with larger masses tend to have smaller relative gas extents (similar dependence confirmed by Reiprich & Böhringer (1999) although they used different radii).

The differences in the gas and dark matter distribution cannot be explained by purely gravitational energy coming from the collapse of the cluster. Additional energy input is necessary to explain it, e.g. from supernova-driven galactic winds. It might be that this additional energy affects low mass clusters more than massive clusters, so that a massive cluster can maintain a ratio $E \approx 1$, while in the smaller clusters the gas is more extended.

Entropy studies by Ponman et al. (1999) of cool clusters ($T <$ 4keV) observed with ROSAT and GINGA suggested that for these systems, (pre-)heating processes play an important role in cluster formation.

Equation (4.1) shows that for a given radius $M_{\rm tot} \propto T \times \beta$. If there is a temperature rise due to preheating processes, a cluster with a certain $M_{\rm tot}$ should have shallower gas density profile or more extended gas distribution (β value smaller). Then if that heating is more effective in cooler cluster, i.e. less massive clusters, one should expect an anticorrelation between total mass and gas extent and lower values of β in cooler systems. This seems to be consistent with observations (e.g. Mohr & Evrard (1997); Nevalainen et al. (2000); Ponman et al. (1999); Vikhlinin et al. (1999)). Our sample also exhibits this behavior, see Fig. 4.8 in § 4.5.

4.4.2 Mass-Temperature relation

Accurate measurements of the cluster total mass are possible only for a limited number of clusters. For this reason there are currently not enough data available for a direct derivation of the mass function, which is crucial for the determinations of the cosmological parameters using the cluster abundances at different redshifts. A more practical way of determining the mass function is to observe the distribution of readily available average cluster gas temperatures and to convert these to masses, taking advantage of the tight correlation between mass and temperature predicted by hydrodynamic cluster formation simulations (Evrard et al., 1996). Therefore, a well-established $M_{\rm tot} - T$ relation can be used as a powerful cluster mass estimator. Furthermore the $M_{\rm tot} - T$ relation is also interesting in itself, because deviations from the predicted self-similar scaling of $M \propto T^{3/2}$ would indicate that more physical processes are at play than gravity alone.

Assuming self-similarity and a velocity dispersion proportional to the X-ray temperature, the virial theorem provides a relation between total mass, radius and X-ray temperature: $M_{\rm tot}(r_{500})/r_{500} \propto T$. Equivalently, r_{500} can be expressed by the definition of the overdensity $r_{500} \propto M_{\rm tot}(r_{500})^{1/3}/(1+z)$ yielding the relation $M_{\rm tot}(r_{500}) \propto (T/(1+z))^{3/2}$. We see this correlation in our data (see Fig. 4.7a). A fit taking into account the errors in the temperature and the error in the mass yields the following relation $M_{\rm tot}(r_{500}) = 0.37(\frac{T}{1+z})^{(1.7\pm0.3)}$ shown in Fig. 4.7a as solid line. $M_{\rm tot}(r_{500})$ is in units of $10^{14} M_\odot$ and T in units of keV. The slope is greater than the virial value of 3/2 but consistent within the errors. If we do the same fit using the masses calculated with the temperature profiles the slope found is 1.4 ± 0.3.

We can see the same relation if we relate the radius to the temperature: $r_{500} \propto T^{1/2}/(1+z)^{3/2}$. In Fig. 4.6 right this correlation between the radius and temperature is shown. The fit gives a slightly greater slope than the expected 0.5 value, $r_{500} = 0.63 \left(\frac{T}{(1+z)^3}\right)^{0.56\pm0.06}$ with r_{500} in Mpc and T in keV. This correlation is telling us the cooler clusters are more compact systems.

Other observational analyses, with only high-temperature ($kT > 4 - 5$keV) clusters, have achieved results consistent with the theoretical prediction (Hjorth et al., 1998; Neumann & Arnaud, 1999).

However many studies (e.g. Finoguenov et al. (2001); Horner et al. (1999); Nevalainen et al. (2000); Ponman et al. (1999)) have shown that the influence of energy feed-back into ICM in low-temperature clusters/groups can become more significant than that in high-temperature systems. Consequently, the self-similarity may break at the low-temperature end. If supernovae release a similar amount of energy per unit gas mass in hot and cool clusters, the coolest clusters would be affected more significantly and exhibit a stronger shift to higher temperatures in the M-T diagram than the hotter clusters. This will steepen the M-T relation.

Furthermore, we test the relation between the gas mass and gas mass fraction and the temperature. As expected from the gas mass−total mass relation, there is also a relation between gas mass and temperature (see Fig. 4.7b). A linear regression fit yields $M_{\rm gas}(r_{500}) = 0.05 T^{(1.72\pm0.19)}$ with $M_{\rm gas}(r_{500})$ in units of $10^{14} M_\odot$ and T in keV. This correlation is in agreement with other results in nearby clusters (Jones & Forman, 1999; Reiprich & Böhringer, 1999). For comparison, Reiprich & Böhringer (1999) find an exponent of 2.08 and Schindler (1999) a larger exponent 4.1 ± 1.5 for distant clusters.

As expected from the non-correlation of the gas mass fraction with the total mass, we find also no correlation between the gas mass fraction and the temperature (see Fig. 4.7c). This result is in good agreement with Mohr et al. (1999). They find a mild dependence comparing low temperature clusters ($T < 5$keV) with high temperature clusters ($T > 5$keV). For the high temperature clusters alone, in which category all our clusters fall, they find no dependence.

We find an interesting correlation between the relative gas extent and the temperature (see Fig. 4.7d), which is of course related to the dependence of the relative gas extent on the total mass, shown above. The relative gas extent tends to be slightly larger in lower temperature clusters.

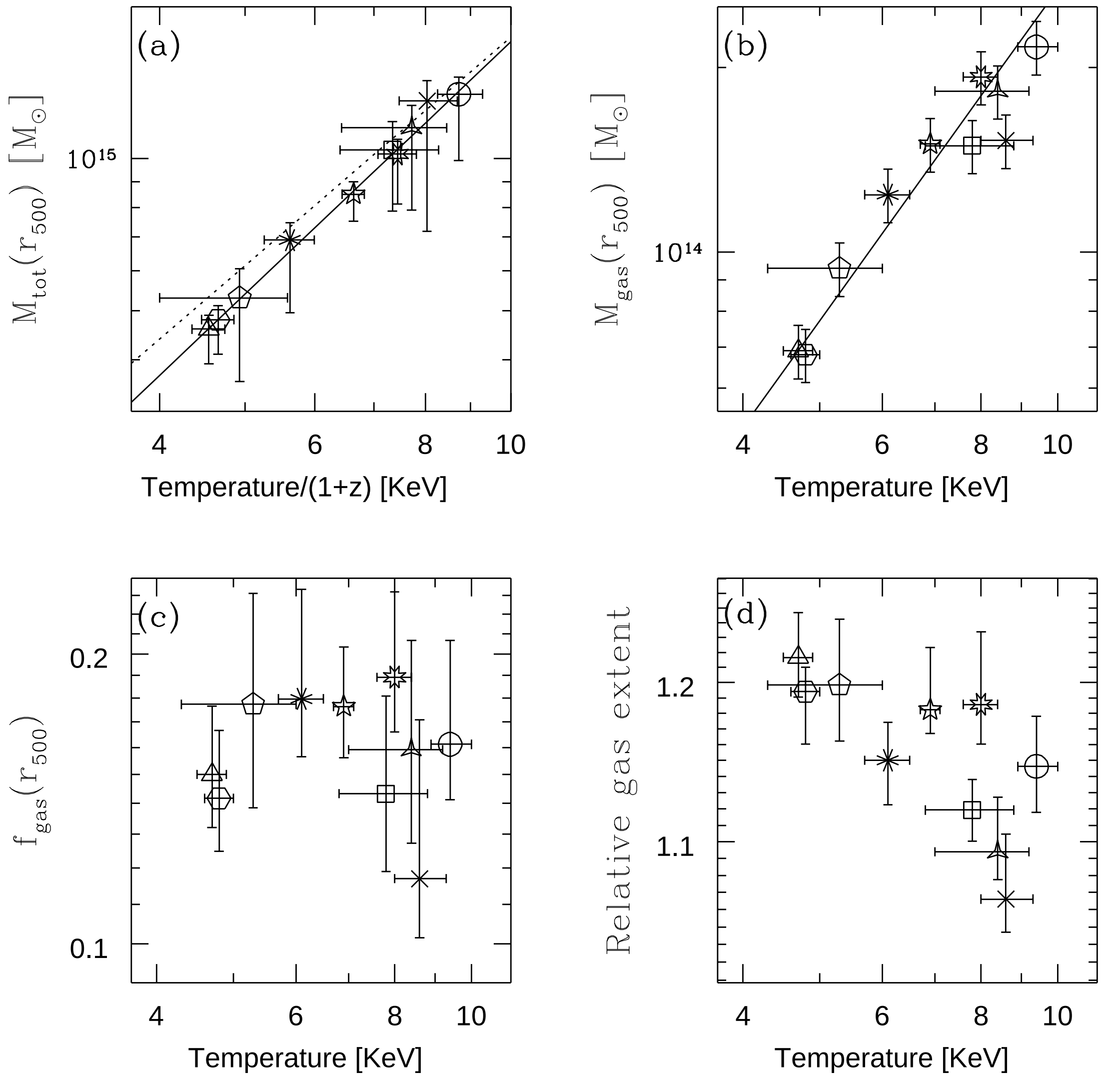

Figure 4.7— Various quantities versus temperature. (a) Total mass. (b) Gas mass. Solid lines show the best fit for our sample. The dashed line is not a fit but the curve expected from virial considerations with an arbitrary normalisation. (c) Gas mass fraction. (d) Ratio of gas mass fractions at r_{500} and $r_{500}/2$.

4.5 β-model parameters

The slope β and the core radius r_c seem to be not independent parameters, with β increasing when r_c increases. In Fig. 4.8 left the correlation between this two parameters is shown. Neumann & Arnaud (1999) found a correlation between the fit parameters of the β-model for a nearby sample of clusters when normalising the core radius. They normalised their core radii to r_{200}. In our case we normalised the core radii to r_{500}. A fit with a power law taking into account the errors in both parameters yields: $\beta = 0.4(rc/r_{500})^{(0.12\pm0.06)}$

In Fig. 4.8 right we show the dependence of β on the temperature. There is a trend to find larger β values for larger temperatures as was also found for more nearby clusters (Mohr & Evrard, 1997; Nevalainen et al., 2000; Ponman et al., 1999; Vikhlinin et al., 1999) and for distant clusters Schindler (1999). We find $\beta = 0.5T^{0.13\pm0.03}$, with T in keV.

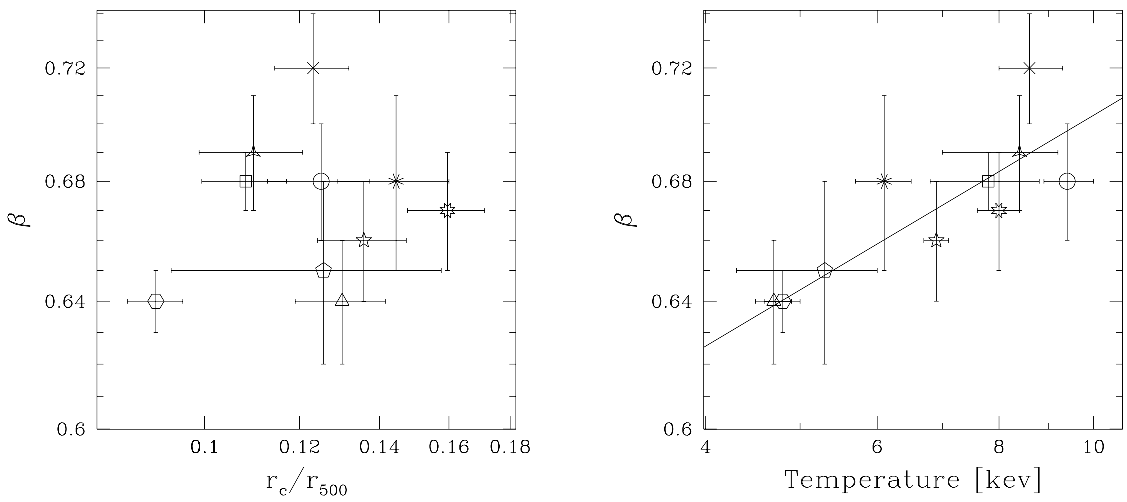

Figure 4.8— β-temperature and β-r_c relation. β is the parameter obtained when fitting with a $\beta-$model the X-ray surface brightness profile. There is a trend to find larger β values for larger temperatures.

4.6 Summary

We have analysed a sample of ten nearby clusters of galaxies using the X-ray data provided by the ROSAT and ASCA satellites. For this sample physical quantities like gas mass, total mass, gas mass fraction and relative gas extent have been derived. Correlations between the above quantities have been studied and our findings are

- The gas mass fraction increases with radius for all our clusters implying that gas is more extended than dark matter, confirming previous results (David et al., 1995; Ettori & Fabian, 1999; Jones & Forman, 1999). This behaviour is more pronounced when temperature profiles are taking into account in the mass analysis.

- Within r_{500}, the mean gas mass fraction obtained is $(0.16 \pm 0.04)h_{50}^{-3/2}$.

  We see no trend in the gas mass fraction with redshift.

- The gas extent relative to the dark matter distribution shows a mild dependence on the total mass and gas temperature. Clusters with larger masses have smaller relative gas extents, as we would expect if non-gravitational processes are important in cluster formation. Hints for this kind of behaviour have been found previously in distant clusters. These new results confirm this trend.

- Studying the mass-temperature relation we find a slope slightly steeper compared with the theoretical value of 3/2 although consistent within the errors. The self-similar slope 3/2 is found when using temperature gradient analysis. Other observational analyses, with only high-temperature clusters, have achieved results consistent with the theoretical prediction (Hjorth et al., 1998; Neumann & Arnaud, 1999; Nevalainen et al., 2000).

5

XMM-Newton observation of the dynamically young galaxy cluster CL 0939+4713†

The formation and evolution of clusters sensitively depends on cosmological parameters like the mean matter density in the Universe Ω_m (Beisbart et al., 2001; Jenkins et al., 1998; Thomas et al., 1998). Therefore it is important to determine the dynamical state of clusters at different redshifts, i.e. at different evolutionary states. The X-ray morphology alone is not the best indicator of the dynamical state, but it should be complemented with all other information available, e.g. the temperature map or the galaxy distribution. The combination of all data gives a detailed picture of the state of a cluster. We do this analysis here for the moderately distant cluster CL 0939+4713, which can be used as a basis for comparisons at lower and higher redshifts. XMM-Newton satellite, with its major capabilities for spectroscopy, allows us to trace better temperature and metallicity maps. We present an XMM observation of the distant galaxy cluster CL 0939+4713 where the X-ray image shows pronounced substructure, with two main subclusters which have even some internal structure. This is an indication that the cluster is a dynamically young system. This conclusion is supported by the temperature distribution: a hot region is found between the two main subclusters indicating that they are at the beginning of a major merger, and that they will probably collide in a few hundreds of Myr. The intra-cluster gas of CL 0939+4713 shows inhomogeneities in the metal distribution, with the optically richer subcluster having a higher metallicity.

5.1 Introduction

The galaxy cluster CL 0939+4713 (Abell 851) at a redshift $z = 0.41$ is an exceptionally rich cluster. It was extensively observed in morphological and spectroscopic studies of the galaxy population. These studies are based on ground-based optical and near-infrared (Belloni et al., 1995; Belloni & Röser, 1996; Dressler & Gunn, 1992; Dressler et al., 1999; Fukugita et al., 1995; Iye et al., 2000; Martin et al., 2000; Poggianti et al., 1999; Stanford et al., 1995) and HST observations (Dressler et al., 1994, 1993; Ferreras & Silk, 2000; Smail et al., 1999; Ziegler et al., 1999) as well as observations in UV (Buson et al., 2000) and sub-millimeter (Cowie et al., 2002) wavelengths. A high number of star-burst and post-starburst galaxies was found in this distant cluster.

†This Chapter is an article written together with Elisabbeta De Filippis and Sabine Schindler. It is published in Astronomy & Astrophysics, vol. 404, p.63-74, 2003.

To study the evolution of galaxies, this number was compared with the corresponding number in nearby clusters. In the surroundings of the cluster a network of galaxy filaments and subclumps was found (Kodama et al., 2001).
The cluster was also the target of several gravitational lensing analyses (Geiger & Schneider, 1999; Iye et al., 2000; Seitz et al., 1996) aiming at the determination of the cluster mass distribution. The comparison between the masses determined by the weak lensing analysis by Seitz et al. (1996) and the X-ray analysis by Schindler et al. (1998) showed a discrepancy of a factor of 2-3.
Previous X-ray observations by ROSAT and ASCA showed that the cluster has a very irregular structure indicating that the cluster is not relaxed but dynamically young (Schindler et al., 1998; Schindler & Wambsganss, 1996): this result is in good agreement with the conclusion from larger scales by Kodama et al. (2001).

The capability of XMM-Newton to perform spatially resolved spectroscopy can be used also to determine the distribution of the metal abundances. Not only the overall value of metallicity but also its spatial distribution gives important indications on the metal enrichment processes and the cluster formation process. Early enrichment would point preferentially towards galactic winds driven by supernovae (De Young, 1978b). For this process one would expect a priori no metallicity variations, because there was enough time to distribute the metals uniformly throughout the cluster. However, numerical simulations of this mechanism gave very discordant results. Aguirre et al. (2001) and Metzler & Evrard (1994, 1997) concluded that winds are very efficient in enriching the ICM, but the latter authors found a very steep radial metallicity gradient, which is not observed in any cluster. Murakami & Babul (1999) and Gnedin (1998) on the other hand found that galactic winds play only a minor role.
At a later stage ram pressure stripping (Gunn & Gott, 1972) is expected to become increasingly important. If considerable amounts of metals are stripped recently, a spatial variation – not necessarily radial gradients – should be observable. To test these effects it is particularly important to analyse clusters at different redshifts to see how the efficiency of the different enrichment mechanisms changes with time.

Throughout this chapter we use $H_0 = 50$ km s^{-1}Mpc^{-1} and $q_0 = 0.5$; all errors are 90% confidence levels.

5.2 Observation and data analysis

In the following sections we detail the observation and the main steps in the data reduction process.

5.2.1 Observation and data processing

The XMM-Newton observation of the galaxy cluster CL 0939+4713 (ID 0106460101) was performed with the European Photon Imaging Camera (EPIC) on November 6th, 2000 during the satellite's 167$^{\text{th}}$ revolution. It consists of one pointing obtained operating the EPIC cameras in the standard Full Frame Mode. For all the three EPIC cameras (MOS1, MOS2, and pn) the thin filter was used for a total exposure time of 51 ks.
We used the SASv5.0.1 processing tasks *emchain* and *epchain* to generate calibrated event files from raw data.
The XMM-Newton observations are strongly affected by high internal and external background

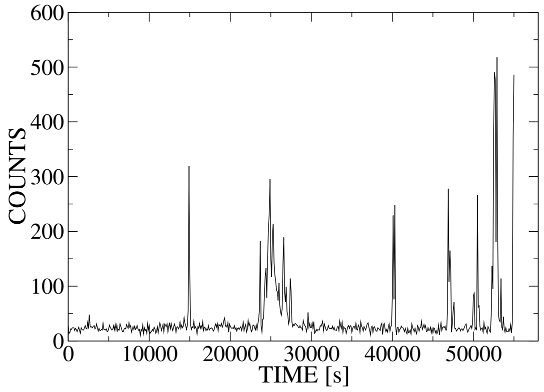

Figure 5.1— MOS1 light curve in the energy range 10 − 12 keV.

levels. Efficient ways of subtracting these background components were extensively discussed by Pratt et al. (2002) and Lumb et al. (2002).

5.2.2 Flare rejection

Low energy (< 1 MeV) protons from solar flares are stopped in the first microns of silicon of the EPIC CCDs. They give a signal identical to X-rays, which makes it impossible to recognize them via a pattern selection. We obtained a cleaner set of data by visually inspecting the light curves and applying an intensity filter. In the energy range 10 − 12 keV for MOS1 & MOS2 cameras (12 − 14 keV for pn) we excluded all the intervals of exposure time having a count rate higher than a certain threshold value.

The three light curves, one for each instrument, were analyzed separately in order to find the best threshold values (see Fig. 5.1). Different threshold values lead to different cuts in the exposure time (see Fig. 5.2); the selected values were therefore a compromise between maximizing the exposure time and minimizing the presence of events caused by flares.
The chosen threshold values are 15 counts $\cdot 100\ s^{-1}$ for MOS1 and MOS2 and 25 counts $\cdot 100\ s^{-1}$ for pn; the threshold for the pn camera is higher because of the larger effective area of the instrument compared to MOS. The resulting effective exposure times for the three cameras are

MOS1: 45800 s
MOS2: 46300 s
pn: 41800 s

5.2.3 Vignetting correction

The vignetting is the reduction in the effective area of the telescope at a given energy and it is dependent on the detected position of the photon in the field of view. This effect must be taken into account in any analysis and specially so in the case of extended sources such as clusters of galaxies.

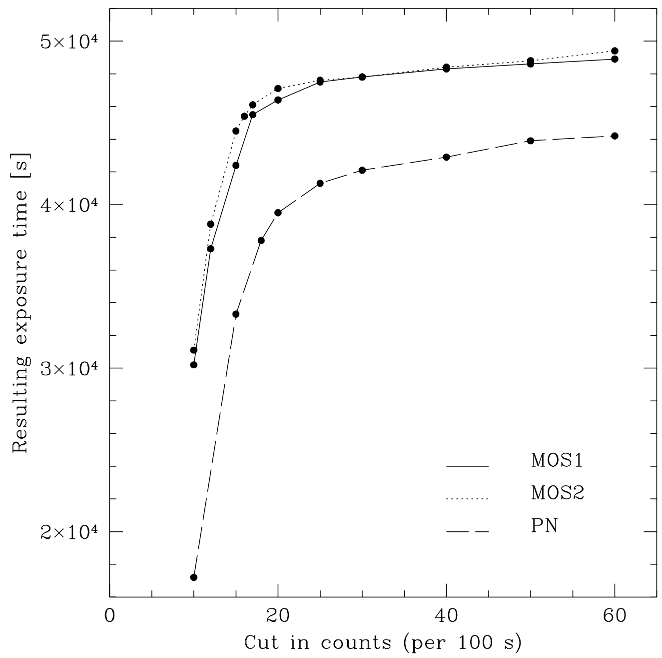

Figure 5.2— Effective exposure time versus the threshold in the count rate in the energy band $10 - 12$ keV and $12 - 14$ keV for MOS1 & MOS2 and for pn, respectively.

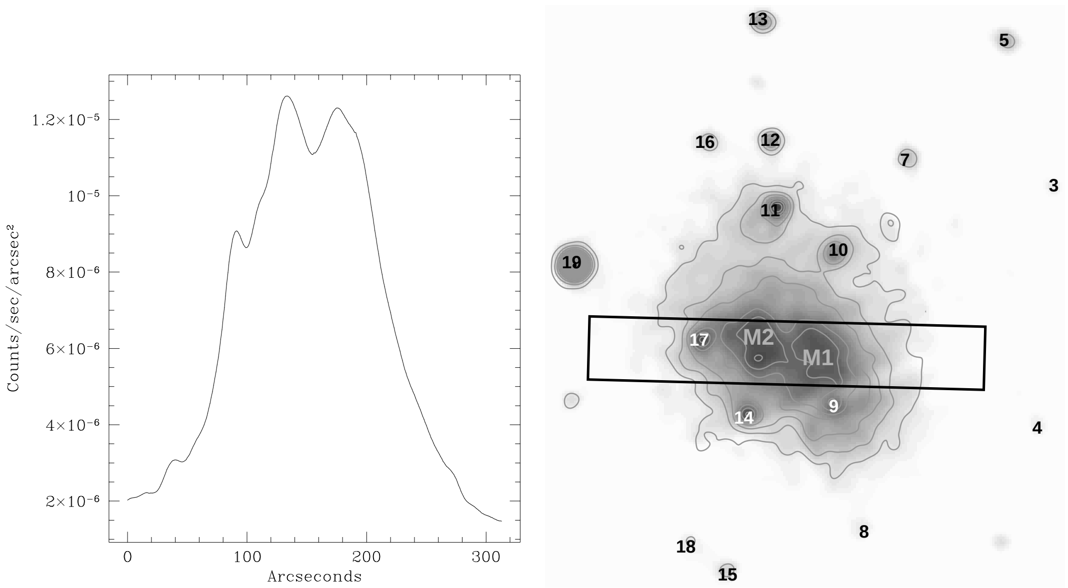

Figure 5.3— **Left**: Projection of the cluster surface brightness extracted from the rectangular region shown in the right panel. **Right**: X-ray image of the cluster. Superposed are the linearly spaced X-ray contours, the identification numbers of the point sources detected in the field (see § 5.3.4) and the location of the two subclusters forming the cluster core: M1 and M2, correspondent to the two maxima in the X-ray emission.

To correct for vignetting the method described in detail by Arnaud et al. (2001a) has been used. A weighting, given by the ratio of the effective area at the centre of the detector -$A_{0,0}(E_i)$- to the effective area at the event position -$A_{x_j,y_j}(E_i)$-, is assigned to each photon extracted in each spectrum. The vignetting corrected photon counts -$C(E_i)$- in each energy channel E_j ($E_i - \Delta E_i/2 < E_j < E_i + \Delta E_i/2$) are

$$C(E_i) = \sum_j w_j(x_j, y_j)$$

with the weights w_j being, as described above:

$$w_j = \frac{A_{0,0}(E_i)}{A_{x_j,y_j}(E_i)}$$

which therefore all have values greater than unity.
The errors in the spectra are recomputed taking into account the vignetting correction; the variances in each energy channel are therefore given by

$$\sigma^2(C(E_i)) = \sum_j w_j^2.$$

The above method is easily generalized for imaging, as described by Majerowicz et al. (2002).

5.2.4 Background subtraction

In order to subtract both the cosmic and the non cosmic X-ray background (Arnaud et al., 2002), the blank field observations, collected by D. Lumb were used. * These are homogeneous collections of high Galactic latitude observations where no bright source is present, for a total exposure time of about 400 ksec. These observations were all taken in a period of very low flare occurrence and almost exclusively with the use of a thin filter; bad pixels and sources were also removed.
We applied to the background event files the same intensity filter applied to our observations; this yields final exposure times for the blank fields of MOS1: 373425 s, MOS2: 358904 s, and pn: 332646 s. Since the cosmic ray induced background might slightly change with time, the count rate in the 10.0 − 12.0 keV (12.0 − 14.0 keV) energy band for MOS1 & MOS2 (pn) cameras in the blank field was compared with the count rate in our observation (after flare rejection). The obtained normalization factors (0.995, 0.992 and 1.038 for MOS1, MOS2 and pn, respectively) are then used to renormalize the blank field data.
We then looked for a possible residual soft background due to the soft component (E < 1.5 keV) of the cosmic X-ray diffuse emission, which varies with the position in the sky. At the position in the sky of CL 0939+4713, no excess of soft cosmic background was observed in previous observations (Snowden et al., 1997).
Nevertheless, we performed a further check. We chose a region in our pointing where no emission from the cluster, or from other point sources, was observed. For all the three detectors, spectra were extracted from this region, together with background spectra from the blank fields by D. Lumb. No evident excess of flux, associated with the soft X-ray background, is observed in any of the three detectors. We then subtracted the blank field spectra from the ones extracted in our

*Event files can be downloaded via anonymous ftp at *xmm.vilspa.esa.es* in the directory /pub/ccf/constituents/extras/background.

observation; the resulting spectra yield no significant signal and are dominated by noise only. No additional correction for excess of soft background is therefore needed for CL 0939+4713.

5.3 Morphological analysis

Figure 5.4 shows an image of CL 0939+4713 in the 0.3 – 2.0 keV band. The image is an adaptively smoothed and exposure corrected mosaic of photon events from the three detectors (MOS1, MOS2 and pn).
The cluster emission has an elliptical shape, centred at RA= $9^h\ 43^m\ 01.00^s$, DEC= $+46^\circ\ 59'\ 37.50''$ (J2000). The axis ratio of major to minor axis is 1.3. The position angle of the ellipse is P.A.$\approx 63^\circ$ (N over E).

5.3.1 Substructure

Figure 5.4 clearly indicates that the core of CL 0939+4713 does not consist of a single spherically symmetric structure, but is composed of two subclusters: M1 and M2.
In Fig. 5.3 (left panel) a surface brightness projection of the cluster is shown, which is extracted from the region shown in the right panel. The two extended substructures forming the core are of similar size and of similar brightness, the subcluster in the East –M2– being slightly brighter than the subcluster in the West –M1–). They both have an irregular shape, showing signs of further internal substructure. Their shapes are roughly elliptical with minor axis of $\approx$ 120 kpc ($19''$) and major axis of $\approx$ 180 kpc ($28''$).[†] Their peaks are $\approx$ 280 kpc apart and their coordinates (J2000) are:

$$P_{M1}\text{: RA}= 9^h\ 42^m\ 58.9^s,\ \text{DEC}= +46^\circ\ 59'\ 36.0''$$
$$P_{M2}\text{: RA}= 9^h\ 43^m\ 03.3^s,\ \text{DEC}= +46^\circ\ 59'\ 26.5''$$

They are slightly offsetted ($P_{M1} \approx 44''$ north and $P_{M2} \approx 21''$ south) compared to the position observed by Schindler et al. (1998), and reach a maximum surface brightness of 5.0×10^{-2} counts s^{-1} arcmin^{-2} and 5.8×10^{-2} counts s^{-1} arcmin^{-2}, respectively.
The smaller peak in Fig. 5.3 (left panel), located on the left of the projection at a distance of about $90''$ from the left border of the region, is caused by the presence of a QSO (Dressler et al., 1993) (see § 5.3.4).

5.3.2 Surface brightness profile

Although the cluster morphology is not spherically symmetric we perform a standard surface brightness analysis to obtain approximate values, which give a quantitative indication of the size of the cluster and also for comparison with other clusters. We generate an azimuthally averaged surface brightness profile for the cluster in the 0.3 – 2.0 keV energy band for each camera. This energy band was selected to optimize the signal–to–noise (S/N) ratio. Point sources were removed manually and the photons were binned into concentric annuli with a width of $3.3''$ (3 pixels of the MOS camera). The vignetting correction and the background subtraction was done as described

[†] $1' = 389$ kpc at the cluster distance of $z = 0.406$.

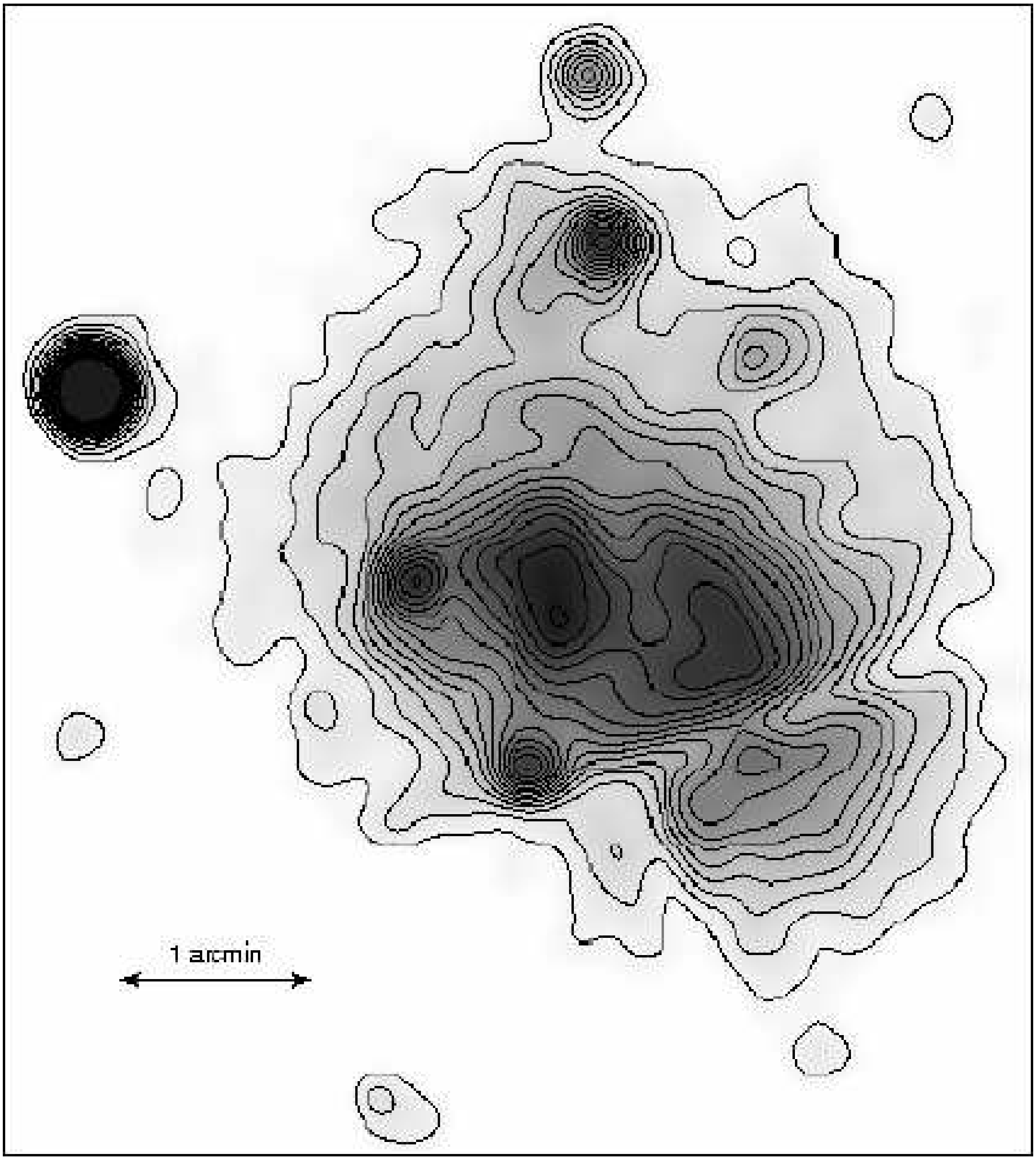

Figure 5.4— X-ray image of the galaxy cluster CL 0939+4713 in the energy range 0.3-2.0 keV. The image is a mosaic of the three MOS1, MOS2 & pn cameras. The core of CL 0939+4713 does not show a simple single central structure, but is composed of two subclusters. The two subclusters in turn show internal structure. Several other point sources are visible. The X-ray image is adaptively smoothed with a Gaussian with $\sigma_{\rm max} = 6$ arcsec to keep an uniform signal-to-noise ratio of 3 σ. The contours are linearly spaced with a spacing of 0.006 counts s^{-1} arcmin^{-2}. The highest contour line corresponding to 0.10 counts s^{-1} arcmin^{-2}.

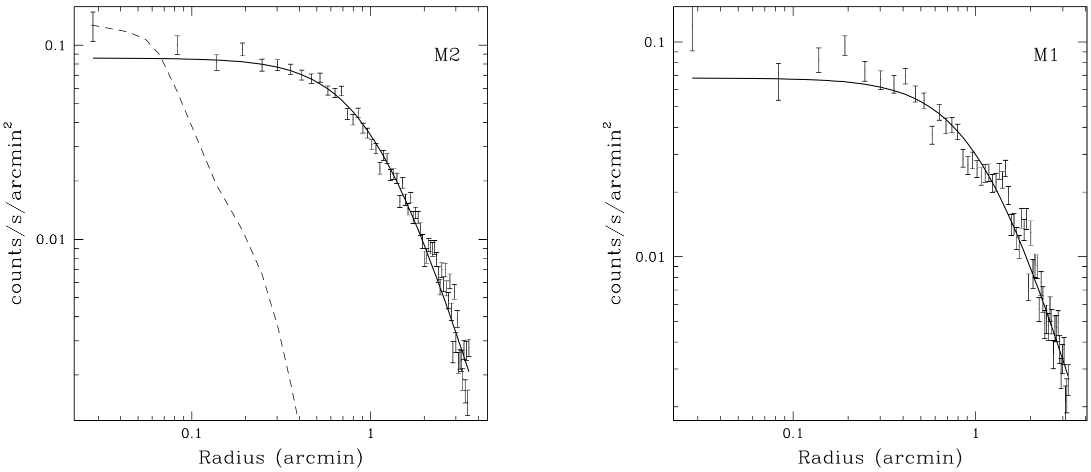

Figure 5.5— Combined MOS1, MOS2 and pn surface brightness profile around the maxima M2 (left) and M1 (right) with spherically symmetric β-model fits (solid line). The fit parameters are given in Table 5.1. The dashed line shows the on-axis PSF, normalized to the central intensity.

in § 5.2.3 and § 5.2.4. The three profiles were then added.
As the cluster is clearly not spherically symmetric the profiles were centred on the positions of the two peaks (P_{M1} and P_{M2}) of both subclusters. The profile centred on P_{M2} is obtained excluding a sector of 120° in the direction of the other subcluster. In the case of the profile centred on P_{M1} a wider sector was excluded (240°) in order to avoid the emission coming from the region located at the southern-west part of M1. The resulting surface brightness profiles $S(r)$ are shown in Fig. 5.5 where the overall XMM point spread function (PSF) binned as the observed profiles is plotted as a dashed line. The overall PSF is obtained by adding the PSF of each camera, estimated at an energy of 1 keV and weighted by the respective cluster count rate in the $0.3 - 2.0$ keV energy band. The comparison of the surface brightness profile data with the PSF shows that the effect of the PSF on the profile is negligible.

After the subtraction of the corresponding blank field profile we find no residual CXB background left (as already mentioned in § 5.2.4). We therefore fit the surface brightness with a β-model without the need of an additional background component:

$$S(r) = S_0 \left[1 + \left(\frac{r}{r_c}\right)^2\right]^{-3\beta+1/2} .$$

where S_0 is the central surface brightness, r_c is the core radius, β is the slope parameter. The profiles for the two subclusters M1 and M2 are fit out to radii of $3.5'$ and $3.2'$ respectively, at which the $S/N > 3\sigma$. Results of the different fits are given in Table 5.1. We obtain similar fit parameters for the two subclusters; however the central region of the profile centred on P_{M1} is not well fitted probably because of internal structure of the subcluster that flattens the central part. The derived beta and core radii parameters for both subclusters are larger compared with the ones obtained by Schindler et al. (1998). These discrepancies could be due to the low S/N ratio of the HRI

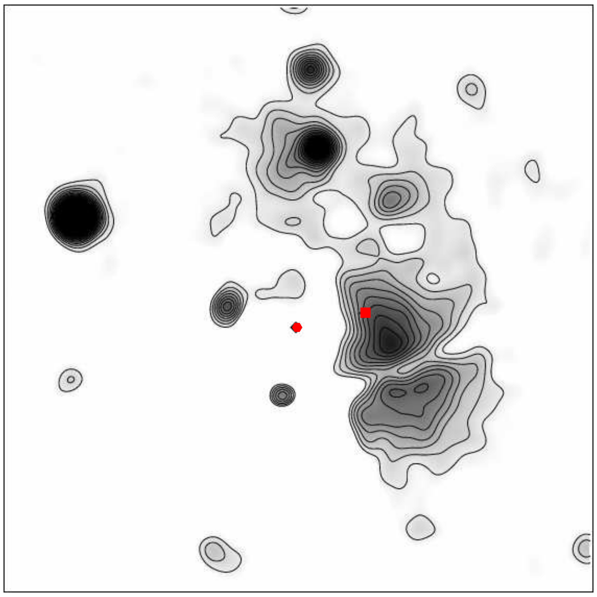

Figure 5.6— Residual image in the energy band 0.3-2.0 keV after subtracting the spherical β model centred on subcluster M2 from the original image. The positions of M1 (red square) and M2 (red circle) are indicated. After the subtraction there is extended and structured emission around the centre M1. The emission from the quasar and the point sources that appear in Fig. 5.4 is visible. The contours are linearly spaced with a spacing of 0.005 counts s^{-1} arcmin^{-2}. The highest contour line corresponding to 0.10 counts s^{-1} arcmin^{-2}.

observation that provides artificially low values for the beta-parameters. The HRI profiles decrease rapidly to background level (see Fig. 2 in Schindler et al. (1998)), therefore a beta model fit is actually probing only the central part of the profile. In order to test this possibility decreasing cut off radii were applied to the XMM profiles. Smaller values of the core radius and beta were indeed derived: for a cut off radius of $2'$, $r_c = 0.5'$ and $\beta = 0.41$ were obtained for the profile centred on P_{M1} and $r_c = 0.8'$ and $\beta = 0.57$ for the profile centred on P_{M2}.

For a more detailed analysis of the substructure, we subtract the emission coming from the subcluster M2 from the original image by using the β-model with the fit parameters in Table 5.1. The residual image is shown in Fig. 5.6. In this residual image the emission from the quasar and from the point sources that appear in Fig. 5.4 is still visible. There is clearly extended emission left from the subcluster M1, but its peak has shifted to the south-west of about 25 arcsec. North of M1 there is also residual emission surrounding some point sources, which is clearly extended and structured. South-west of M1, separated by an artifact minimum caused by the gap in the detector chips is a last piece of residual extended emission.

Table 5.1— Fit parameters for a β model centred on M1 and M2: S_0 is the central surface brightness, r_c is the core radius, and β is the slope parameter.

region	S_0 in counts s^{-1} arcmin^{-2}	r_c in arcmin	β
M2	$8.6\pm0.4\times10^{-2}$	1.11 ± 0.07	0.68 ± 0.03
M1	$6.8\pm0.5\times10^{-2}$	$1.16^{+0.18}_{-0.15}$	$0.66^{+0.07}_{-0.05}$

Table 5.2— List of point sources detected in the field covered by MOS CCD#1. Columns 1-3 give the source identification number, and its coordinates (J2000). In Cols. 4 and 5 the source count rate (in counts per second) and the radius (in arcseconds) out to which the source can be detected, respectively, are listed.

ID	RA	DEC	count rate	radius [″]
1	$9^h\,42^m\,29.23^s$	$+46°\,56'\,25.27''$	0.0025	30
2	$9^h\,42^m\,34.90^s$	$+46°\,55'\,58.35''$	0.0024	30
3	$9^h\,42^m\,40.53^s$	$+47°\,01'\,40.41''$	0.0006	22
4	$9^h\,42^m\,41.72^s$	$+46°\,58'\,32.43''$	0.0004	20
5	$9^h\,42^m\,44.04^s$	$+47°\,03'\,36.45''$	0.0016	25
6	$9^h\,42^m\,51.09^s$	$+47°\,05'\,14.49''$	0.0028	35
7	$9^h\,42^m\,51.88^s$	$+47°\,02'\,04.49''$	0.0023	25
8	$9^h\,42^m\,55.21^s$	$+46°\,57'\,10.50''$	0.0011	17
9	$9^h\,42^m\,57.36^s$	$+46°\,58'\,46.50''$	0.0048	15
10	$9^h\,42^m\,57.39^s$	$+47°\,00'\,50.12''$	0.0054	22
11	$9^h\,43^m\,01.85^s$	$+47°\,01'\,24.50''$	0.0078	30
12	$9^h\,43^m\,02.25^s$	$+47°\,02'\,16.50''$	0.0025	22
13	$9^h\,43^m\,03.03^s$	$+47°\,03'\,52.50''$	0.0026	25
14	$9^h\,43^m\,04.20^s$	$+46°\,58'\,40.49''$	0.0036	15
15	$9^h\,43^m\,05.36^s$	$+46°\,56'\,36.49''$	0.0019	18
16	$9^h\,43^m\,07.14^s$	$+47°\,02'\,16.48''$	0.0025	25
17	$9^h\,43^m\,07.72^s$	$+46°\,59'\,40.48''$	0.0036	15
18	$9^h\,43^m\,08.88^s$	$+46°\,57'\,00.45''$	0.0021	27
19	$9^h\,43^m\,17.69^s$	$+47°\,00'\,38.40''$	0.0089	30

5.3.3 Count rate

The X-ray emission of the cluster can be traced out to 3.5 arcminutes (1.4 Mpc). The MOS and pn count rates within the $R \leq 3.5'$ region and in the considered energy band (0.3-2.0 keV) are 0.125 ± 0.013 counts s^{-1} and 0.31 ± 0.03 counts s^{-1} respectively.

5.3.4 Other sources in the pointing

In the pointing many other sources are found around the cluster. 19 point sources, located in the area covered by MOS CCD#1, were detected by both the pipeline detection and a peak density finding algorithm. Their coordinates, extension and count rates (after background subtraction) are listed in Table 5.2. Most of these sources are shown in Fig. 5.3 (right panel) together with their identification number.

For the sources corresponding to member galaxies, or located within 4.3 arcmin from the cluster centre, a more detailed analysis has been performed.

ID #3 For this source no optical counterpart was found. The low statistics of the data do not allow us to constrain the photon index, even using a simple power law model. Assuming a power law spectrum with photon index $\Gamma = 1.7$ we obtain an unabsorbed flux of $f_X(0.3 - 10.0) = 5.7 \times 10^{-15}$ erg s^{-1}cm^{-2}.

ID #4 No optical counterpart. Assuming a power law spectrum with photon index $\Gamma = 1.7$: $f_X(0.3 - 10.0) = 3.5 \times 10^{-15}$ erg s^{-1}cm^{-2}.

ID #7 No optical counterpart. Assuming a power law spectrum with photon index $\Gamma = 1.7$: $f_X(0.3 - 10.0) = 2.2 \times 10^{-14}$ erg s^{-1}cm^{-2}.

ID #8 Probable member galaxy Abell 0851:[DG92] 124. Assuming a power law spectrum with photon index $\Gamma = 1.7$: $f_X(0.3{-}10.0) = 1.0 \times 10^{-14}$ erg s^{-1}cm^{-2}, and a bolometric luminosity of $L_X(\mathrm{bol}) = 1.6 \times 10^{43}$ erg s^{-1}.

ID #9 Member galaxy Abell 0851:[DG92] 311 at a redshift of $z = 0.4007$. It is also a radio source known as [CDS90] R082. Its spectrum was fitted with a power law giving a photon index $\Gamma = 1.6 \pm 0.2$; the unabsorbed flux is $f_X(0.3 - 10.0) = 4.7 \times 10^{-14}$ erg s^{-1}cm^{-2}, and the bolometric luminosity $L_X(\mathrm{bol}) = 7.5 \times 10^{43}$ erg s^{-1}.

ID #10 Probable member galaxy Abell 0851:[SED95] 074. The spectral fit yields $\Gamma = 1.3 \pm 0.1$; $f_X(0.3 - 10.0) = 6.5 \times 10^{-14}$ erg s^{-1}cm^{-2}; $L_X(\mathrm{bol}) = 1.1 \times 10^{44}$ erg s^{-1}.

ID #11 This source was already detected during a ROSAT PSPC observation as RXJ0943.0+4701 by Schindler & Wambsganss (1996) and had a measured flux in the ROSAT (0.1 – 2.4 keV) band of $f_{\mathrm{ROSAT,PSPC}} = 4 \times 10^{-14}$ erg s^{-1}cm^{-2}. During a second ROSAT observation of the cluster done by Schindler et al. (1998) using the HRI, the source was hardly visible with a resulting flux in the (0.1 – 2.4 keV) band of $f_{\mathrm{ROSAT,HRI}} = 5 \times 10^{-15}$ erg s^{-1} cm^{-2}, indicating that this source has a very strong variability. The source coordinates observed by PSPC are slightly offset ($\approx 38''$ south) with respect to the coordinates observed with XMM.
We find the galaxy Abell 0851:[SED95] 066 as a possible optical counterpart, which is a probable member galaxy. The spectral fit yields $\Gamma = 1.8 \pm 0.1$; $f_X(0.3 - 10.0) = 6.8 \times 10^{-14}$ erg s^{-1}cm^{-2}; $L_X(\mathrm{bol}) = 1.2 \times 10^{44}$ erg s^{-1}. We compute a flux in the (0.1 – 2.4 keV) band of $f_{\mathrm{XMM}} = 4.7 \times 10^{-14}$ erg s^{-1}cm^{-2}, which is only slightly higher than the values computed by Schindler & Wambsganss (1996) in their first X-ray observation of the cluster. Considering the changing values of the luminosity and the results of the spectral analysis, the conclusion drawn by Schindler et al. (1998), of source #11 being a strong X-ray variable AGN, is, up to now, the most reliable one.

ID #12 No optical counterpart was found for this source. The spectral fit yields $\Gamma = 1.95 \pm 0.2$; $f_X(0.3 - 10.0) = 2.0 \times 10^{-14}$ erg s^{-1}cm^{-2}.

ID #13 No optical counterpart. The spectral fit yields $\Gamma = 1.7^{+0.2}_{-0.3}$; $f_X(0.3 - 10.0) = 2.5 \times 10^{-14}$ erg s^{-1}cm^{-2}.

ID #14 Probable member galaxy Abell 0851:[DG92] 292. The spectral fit yields $\Gamma = 1.6 \pm 0.1$; $f_X(0.3 - 10.0) = 3.3 \times 10^{-14}$ erg s^{-1}cm^{-2}; $L_X(\mathrm{bol}) = 5.4 \times 10^{43}$ erg s^{-1}.

ID #15 Probable member galaxy Abell 0851:[DG92] 064. Assuming a power law spectrum with photon index $\Gamma = 1.7$ we obtain an unabsorbed flux of $f_X(0.3{-}10.0) = 1.8 \times 10^{-14}$ erg s^{-1}cm^{-2}, and a bolometric luminosity of $L_X(\mathrm{bol}) = 2.9 \times 10^{43}$ erg s^{-1}.

ID #16 No optical counterpart was found. Assuming a power law spectrum with photon index $\Gamma = 1.7$: $f_X(0.3 - 10.0) = 3.7 \times 10^{-14}$ erg s^{-1}cm^{-2}.

ID #17 This source is a QSO (known as Abell 0851:[DG92] 440) lying in the field of view of the cluster and at a redshift of $z = 2.055$ (Dressler et al., 1993). The spectral fit yields $\Gamma = 1.72 \pm 0.05$; $f_X(0.3-10.0) = 3.1 \times 10^{-14}$ erg s^{-1}cm^{-2}; $L_X(\mathrm{bol}) = 2.3 \times 10^{45}$ erg s^{-1}. In the ROSAT energy band the QSO has a luminosity of $L_{\mathrm{XMM}}\,(0.1 - 2.4) = 8.6 \times 10^{44}$ erg s^{-1}, which is slightly lower than was measured by Schindler et al. (1998) ($L_{\mathrm{ROSAT}}\,(0.1 - 2.4) = 1.4 \times 10^{45}$ erg s^{-1}). Due to the low number of counts Schindler et al. (1998) could not fit any spectral model to the data and, to compute the luminosity, they fixed the photon index at $\Gamma = 2.3$. Using the same value for the photon index the two luminosities, computed by ROSAT and XMM, are perfectly consistent.

ID #18 Probable member galaxy Abell 0851:[DG92] 105. Assuming a power law spectrum with photon index $\Gamma = 1.7$ we obtain an unabsorbed flux of $f_X(0.3-10.0) = 1.9 \times 10^{-14}$ erg s^{-1}cm^{-2}, and a bolometric luminosity of $L_X(\mathrm{bol}) = 3.1 \times 10^{43}$ erg s^{-1}.

ID #19 J0943.2+4700; has no optical counterpart. The spectral fit yields $\Gamma = 1.8 \pm 0.1$; $f_X(0.3-10.0) = 7.8 \times 10^{-14}$ erg s^{-1}cm^{-2}.

5.3.5 Comparison with the optical waveband

In Fig. 5.7 an HST image of the central area of the cluster is shown. On it, superposed, are the X-ray contours.
An extensive redshift survey of the galaxies in the field of view of CL 0939+4713 was performed by Dressler et al. (1999) and at least 60 galaxies were spectroscopically proven to belong to the cluster. Among these galaxies, those falling within the field of view of HST, can be seen in Fig. 5.7 surrounded by rectangles.
Some of these galaxies (e.g. #9) are very luminous also in X-rays but, nevertheless, the X-ray luminosity of the central region of the cluster is strongly dominated by extended hot emission from the intra-cluster gas, peaked in the two subclusters.
Both the galaxy number density distribution and the X-ray emission show two main peaks. The peaks of these two distributions are in similar regions. It is also interesting that the mass distribution (as computed by Seitz et al. (1996) using a weak lensing analysis) has a similar bimodal structure.
The subcluster M1 coincides with the strongest maxima in both the galaxy number density and the mass distribution. The peaks of the galaxy density and of the mass distributions are ≈ 26 arcsec West and ≈ 15 arcsec South of the X-ray peak M1.
The other subcluster, M2, is located near the second maxima in the galaxy number density and in the mass distribution (their peaks are, respectively, ≈ 16 arcsec west and ≈ 20 arcsec south-east of the X-ray one).

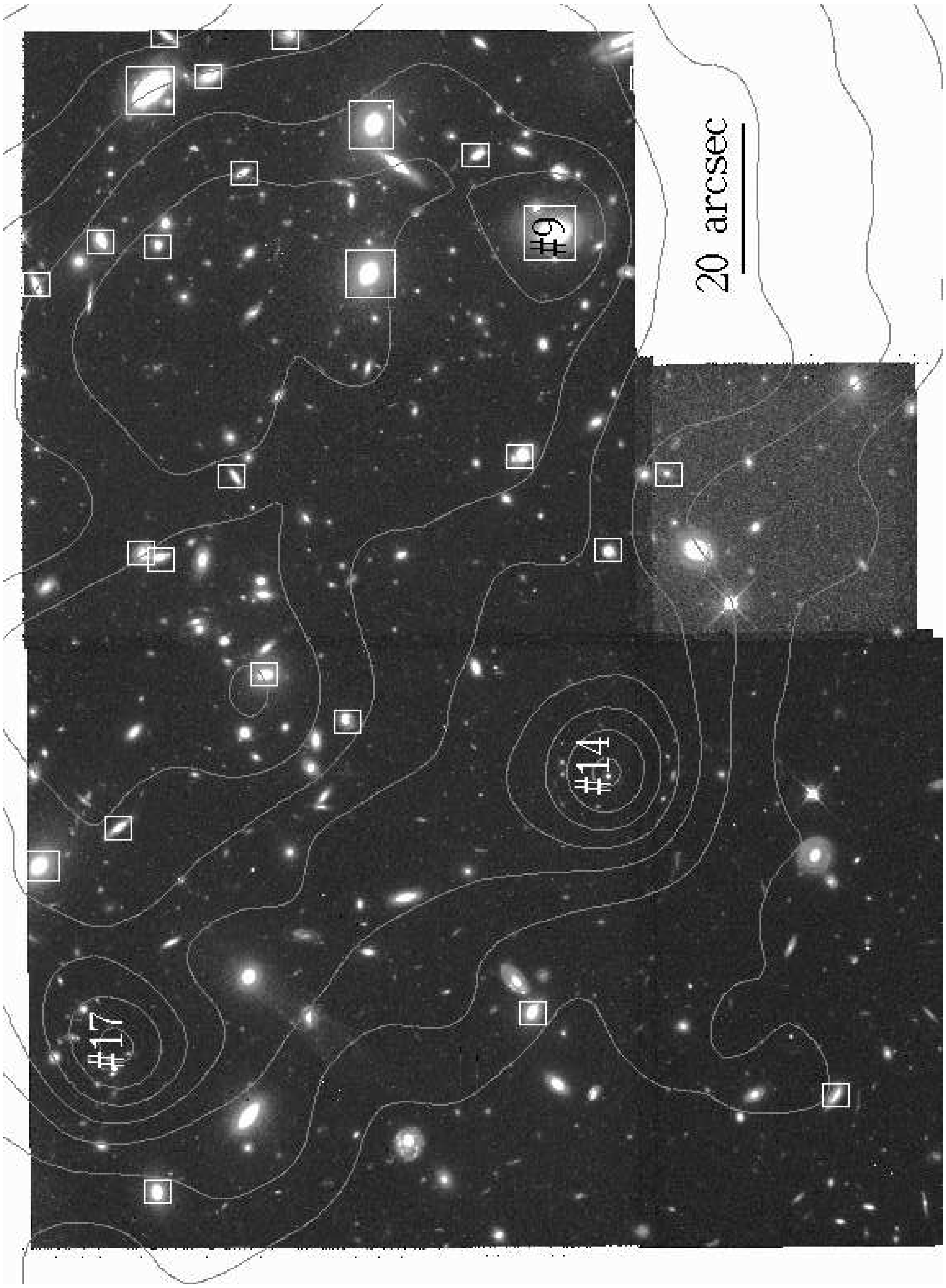

Figure 5.7— HST image of the central region of CL 0939+4713 (Buson et al., 2000). Superposed are the (0.3 – 10.0 keV) XMM X-ray contours linearly spaced from 0.24 to 0.98 of the maximum. White rectangles surround galaxies known to be cluster members.

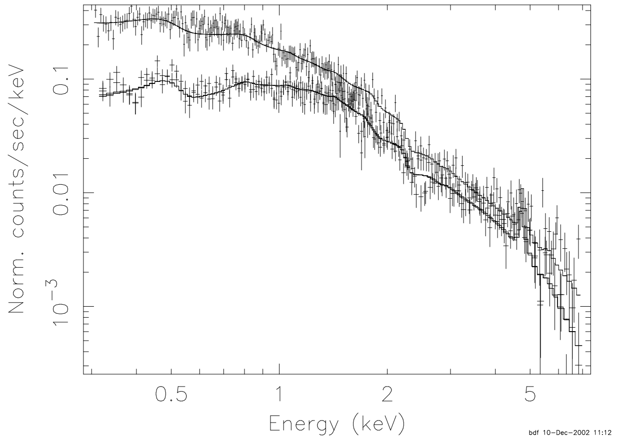

Figure 5.8— MOS1, MOS2 & pn spectra with MeKaL model superimposed (plotted in different shades of gray).

5.4 Spectral analysis

For the whole spectral analysis, the ready-made on-axis response files (m1_r5_all_15.rsp for MOS1, m2_r5_all_15.rsp for MOS2 [1] and epn_ff20_sY9.rmf for pn [2]) were used. [3]
Source and background spectra were accumulated separately for each detector. Spectra were rebinned in order to obtain $S/N > 5\ \sigma$ in each bin after background subtraction.
As the spectra are already corrected for vignetting, spectra of the same physical region, observed with the three different detectors, can simply be fitted simultaneously in order to maximize the signal to noise ratio.
All the spectral analysis was performed in the $0.3 - 10.0$ keV band. Data below 0.3 keV have been excluded to avoid residual calibration problems in the MOS & pn response matrices below these energies.

5.4.1 Results

The spectra for the cluster analysis were extracted from a circular region centered at RA = $09^{\rm h}\ 43^{\rm m}\ 01.0^{\rm s}$, DEC = $+46^\circ\ 59'\ 37.5''$ (J2000) and of radius r=3.0$'$. The emission coming from all the point sources inside the region was excluded.
X-ray temperatures, metal abundances, fluxes and luminosities, were computed with XSPEC fitting the data to an absorbed isothermal plasma emission code of Kaastra & Mewe (1993) including the FeL calculations of Liedahl et al. (1995) [4], folded through the appropriate response matrices. In Table 5.3 is a detailed description of the results obtained fitting the theoretical model to data from the three detectors at the same time, and for each detector independently.
Temperatures obtained using MOS and pn detectors independently are largely consistent. The fit results for the redshift are consistent with its spectroscopic value computed by Dressler et al.

[1] Both MOS files are for patterns from 0 to 12.
[2] pn response file is for single-pixel events only.
[3] All response files can be downloaded via anonymous ftp at *xmm.vilspa.esa.es* in the directory /pub/ccf/constituents/extras/responses.
[4] MeKaL code from now on.

Table 5.3— Results of the spectral fits for the whole cluster. Column 1: line number. Column 2: detectors in use. In Cols. 3-6 the fit parameters (temperature in keV, metallicity in solar units, redshift and HI column density in 10^{20} cm^{-2}) are listed. In Col. 7 is the fit reduced χ^2.

	Detector	Temperature kT in keV	Metallicity in solar units	Redshift	HI column density $[10^{20}\ \mathrm{cm}^{-2}]$	χ^2/d.o.f.
1	MOS1,MOS2 & pn	4.5 ± 0.2	0.20 ± 0.06	0.406 (fixed)	1.24 (fixed)	1.09
2	MOS1,MOS2 & pn	4.6 ± 0.2	0.22 ± 0.06	$0.418^{+0.006}_{-0.010}$	1.24 (fixed)	1.10
3	MOS1,MOS2 & pn	$4.6^{+0.4}_{-0.2}$	$0.24^{+0.06}_{-0.07}$	$0.41^{+0.01}_{-0.01}$	$0.3^{+0.9}_{-0.3}$	1.10
4	MOS1,MOS2	4.6 ± 0.3	0.23 ± 0.08	0.406 (fixed)	1.24 (fixed)	1.11
5	MOS1,MOS2	4.6 ± 0.3	0.24 ± 0.08	0.41 ± 0.01	1.24 (fixed)	1.11
6	pn	4.4 ± 0.4	$0.16^{+0.09}_{-0.08}$	0.406 (fixed)	1.24 (fixed)	1.09
7	pn	4.5 ± 0.4	0.19 ± 0.1	0.43 ± 0.02	1.24 (fixed)	1.10
8	pn	$5.1^{+0.5}_{-0.3}$	0.21 ± 0.1	0.43 ± 0.02	$0.2^{+1.0}_{-0.2}$	1.10

(1999) ($z = 0.406$); good agreement is also observed between the fit value of the hydrogen column density and its Galactic value of $n_{\mathrm{H}} = 1.24 \times 10^{20}$ cm^{-2} (Dickey & Lockman, 1990). When fixing these two parameters the best fit temperature and metal abundance of the cluster based on a simultaneous fit of all (MOS+pn) the spectra (using independent normalizations for the MOS and the pn cameras) are $kT = 4.5 \pm 0.2$ keV and $Z = 0.20 \pm 0.06\ Z_{\odot}$, respectively (the corresponding MOS1, MOS2 & pn spectra with the fitted MeKaL model superimposed are plotted in Fig. 5.8). Using the best fit model parameters we derived, out to a radius of 210″, an unabsorbed flux of $f_{\mathrm{X}}(0.3 - 10.0) = 1.3 \pm 0.1 \times 10^{-12}$ erg s^{-1}cm^{-2}, corresponding to a luminosity, in the cluster rest frame, of $L_{\mathrm{X}}(0.3 - 10.0) = 1.1 \pm 0.1 \times 10^{45}$ erg s^{-1} and a bolometric luminosity of $L_{\mathrm{X}}(\mathrm{bol}) = 1.3 \pm 0.1 \times 10^{45}$ erg s^{-1}.

5.4.2 Temperature map

Since the cluster has been observed to have an irregular morphology, a deeper analysis of its internal structure and dynamical state is required in order to gain a better understanding of it.
The cluster was subdivided into 18 regions; their sizes have been chosen such that each region (after background subtraction) has similar number of photon counts. We fixed the HI column density and the redshift to the average values for the whole cluster and then fitted the spectrum for each region to obtain the values of the temperature.

The resulting temperature map is shown in Fig. 5.9, where different shades of gray reflect the different temperatures of the various regions. Superposed are linearly spaced X-ray contours.
A clear trend of higher temperatures is observed in the region situated in the centre between the two clumps forming the core. The region of higher temperature also extends in the NW and SE directions.
Average temperatures were also computed from spectra extracted from the central hotter region and from the two regions surrounding it. All three regions have elliptical shapes and the

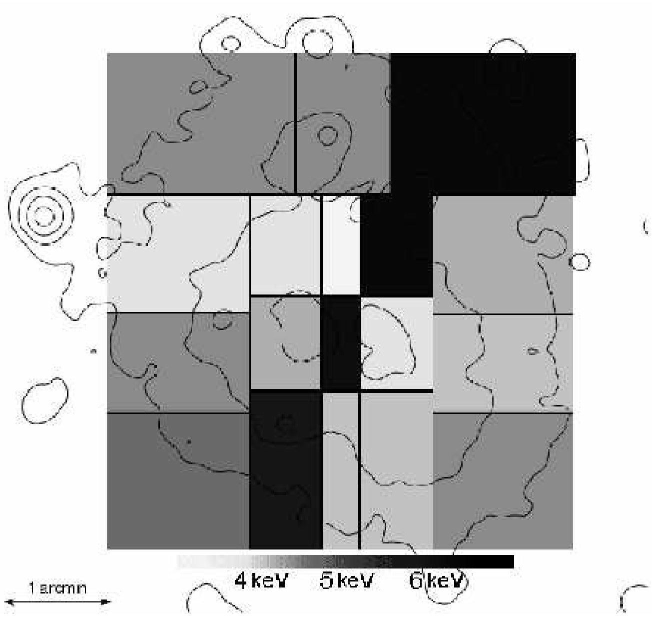

Figure 5.9— Cluster temperature map; superposed are linearly spaced X-ray contours. Darker shades of gray indicate higher temperature. A trend of higher temperatures is observed in the central region, located between the two peaks (P_{M1} and P_{M2}) in the X-ray emission. The high temperature region also extends in the NW and SE directions.

coordinates of their centres, and the major and minor axes are: M2. RA= 9^h 43^m 08.11^s, DEC= $+47^\circ$ $00'$ $03.48''$ (J2000), $a = 1.5'$, $b = 1.2'$, P.A.= 140°; Central. RA= 9^h 43^m 01.58^s, DEC= $+46^\circ$ $59'$ $18.02''$ (J2000), $a = 2.1'$, $b = 0.4'$, P.A.= 159°; M1. RA= 9^h 42^m 55.50^s, DEC= $+46^\circ$ $58'$ $35.50''$ (J2000), $a = 1.4'$, $b = 1.0'$, P.A.= 179°. A MeKaL model was used; HI column density and the redshift are fixed to the average values for the whole cluster. The resulting temperatures, which clearly confirm the trend observed in the temperature map, are $kT = 4.8^{+0.5}_{-0.4}$ keV, $kT = 6.0^{+0.7}_{-0.6}$ keV and $kT = 4.7^{+0.4}_{-0.3}$ keV (for M2, central and M1 regions, respectively). Detailed results of the fits are presented in Table 5.4.

The temperature map in Fig. 5.9 is similar to the predictions of simulations of cluster merging, for an almost head-on encounter of two subclusters of similar mass, shortly before the merging process (Ricker & Sarazin, 2001b; Ritchie & Thomas, 2002; Takizawa, 1999). Similar temperature structure has also been observed in clusters such as A399 and A401 (Markevitch et al., 1998) and A3528, A1750, and A3395 (Donnelly et al., 2001).
The central hotter region therefore delineates an area where the two subclusters are compressing and heating intra-cluster gas, while moving one towards the other in the beginning of a merging process. Simulations by Schindler & Müller (1993) show that this hotter region between the two merging structures begins to appear $\approx 0.5 - 1.0$ Gyr before the merging. Comparing this result with simulations performed by Takizawa (1999, 2000) allows a determination of the dynamical state: the two subclusters in CL 0939+4713 will collide in a few hundreds of Myr.

Table 5.4— Results of the spectral fits for the three subregions using a MeKaL model. HI column density and redshift are fixed to the average values for the whole cluster. Column (1): region analyzed. In Cols. (2) and (3) the fit parameters (temperature in keV and metal abundance, respectively) are listed. In Col. (4) is the reduced χ^2 of the fit.

Region	Temperature kT in keV	Metallicity in solar units	χ^2/d.o.f.
M2	$4.8^{+0.5}_{-0.4}$	0.15 ± 0.11	0.96
Central	$6.0^{+0.7}_{-0.6}$	$0.11^{+0.18}_{-0.11}$	1.03
M1	$4.7^{+0.4}_{-0.3}$	$0.33^{+0.14}_{-0.12}$	1.07

5.4.3 Metallicity variation

A higher metal abundance is observed in region M1 compared to the abundance in M2 and to the abundance in the central region (see Table 5.4). While in M1 a metallicity of $0.33^{+0.14}_{-0.12}$ is found, the metallicity in M2 amounts only to 0.15 ± 0.11 in solar units. The errors are relatively large because only photons from small areas were used. The 90% errors overlap slightly. But there is a clear trend that the metallicity is not constant. The high-metallicity region M1 coincides with a strong peak in the galaxy number density distribution. It seems that the galaxies present in this region have enriched the intra-cluster gas with heavy elements. It is interesting that the high metal content is still localised within this region despite the active dynamical state of the cluster. In order to maintain such a high metallicity during the merger process, the subcluster M1, on its way towards the subcluster M2, did obviously, not accumulate a lot of gas from the front and did not leave large quantities of its gas behind, always retaining the same gas. An additional explanation could be that the gas in this region has been metal enriched only recently, so that the motion of the gas has not had time yet to distribute the metals.

5.5 Mass analysis

The major difficulty to estimate the total mass in this cluster is its active dynamical estate. CL 0939+4713 is undergoing a major merger and the hypothesis of hydrostatic equilibrium and spherical symmetry are in principle not valid. We therefore instead assume a bimodal model where each subcluster follows an isothermal beta-model. To estimate the gas and total mass of the cluster we analyse each subcluster separately assuming for each of them hydrostatic equilibrium and spherical symmetry.
The integrated mass contained within a radius r for each subcluster can be calculated from the equation (see § 3.5.1)

$$M(< r) = -\frac{kr}{\mu m_{\rm p} G} T_{\rm gas} \left(\frac{d \ln \rho_{\rm gas}(r)}{d \ln r} + \frac{d \ln T_{\rm gas}(r)}{d \ln r} \right) \tag{5.1}$$

where $\rho_{\rm gas}$ and $T_{\rm gas}$ are the density and the temperature of the intracluster gas, and $r,k,\mu,m_{\rm p}$, and G are the radius, the Boltzmann constant, the molecular weight, the proton mass, and the

gravitational constant, respectively.
To estimate the gas and total mass for each subcluster, the β parameters obtained in the fits of the profiles centred on the peaks P_{M1} and P_{M2} are used (see Table 5.1). We assume a constant temperature of 4.7 and 4.8 keV for the subclusters M1 and M2, respectively. The two subclusters are very close each other: the outer radius of $\approx 22''$ (140 kpc) corresponds to half the distance between the subclusters. Therefore we can compute the gas mass and total cluster mass out to this radius adding the masses corresponding to each subcluster. Figure 5.10 shows the integrated gas and total masses out to 140 kpc for the two subclusters independently and the numerical values are given in Table 5.5.
For an estimation of the total cluster mass out to a larger radius we use the fit centred on the subcluster M2, where the X-ray emission is higher. In Table 5.6 the gas and total masses found at two different radii are listed. At radius $r_{500} = 0.85$ Mpc the total cluster mass and gas mass are: $M_{tot}(r_{500}) = 2.3 \times 10^{14} M_{\odot}$ and $M_{gas}(r_{500}) = 0.49 \times 10^{14} M_{\odot}$. The gas mass fraction tends to increase slightly outwards ($\approx$17% at 0.5 Mpc and $\approx$22% at 1 Mpc).
The tabulated errors on the total mass come from the uncertainty in the temperature and the errors in the β parameters. The emissivity of the gas in the XMM energy band $0.3 - 2.0$ keV is almost constant inside the uncertainties for the estimate temperature. Therefore we can derive the gas density distribution without the uncertainty of the temperature estimate.
The mass distribution of part of CL 0939+4713 has been reconstructed with a weak lensing analysis by Seitz et al. (1996) and a comparison with our cluster mass estimation would be interesting. Unfortunately the restricted region within which the total mass has been calculated with the gravitational lensing analyses makes a proper comparison impossible.

Table 5.5— Numerical values for the mass determination in the two subclusters M1 and M2.

	gas mass ($10^{12} M_{\odot}$) within 140 kpc	total mass $M(r)$ ($10^{12} M_{\odot}$) within 140 kpc
M1	0.56	$4.2^{+0.8}_{-0.7}$
M2	0.65	$4.8^{+0.6}_{-0.5}$

Table 5.6— Numerical values for the mass determination in cluster CL 0939+4713 for two specific radii; the masses are computed using the fit parameters for the profile centred on subcluster M2.

	mass within 0.5 Mpc	mass within 1.0 Mpc
gas mass ($10^{14} M_{\odot}$)	0.18	0.67
total mass $M(r)$ ($10^{14} M_{\odot}$)	1.01 ± 0.3	2.98 ± 0.7

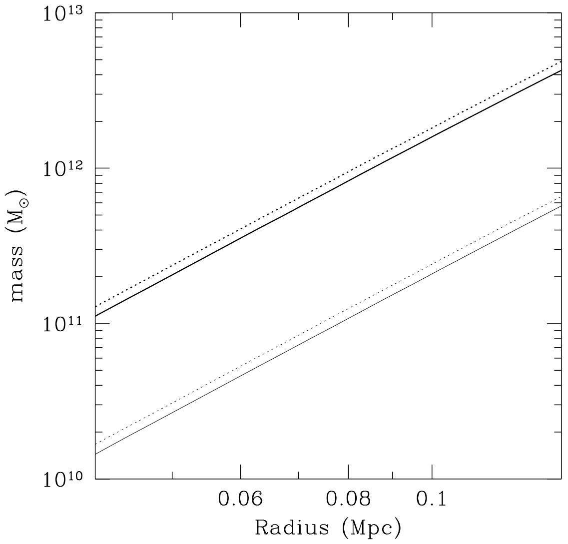

Figure 5.10— Integrated total mass (thick lines, top) and gas mass (thin lines, bottom) profiles for the subclusters M1 (solid lines) and M2 (dotted lines).

5.6 Discussion of the merger hypothesis

Several observed characteristics of CL 0939+4713, either in the X-rays and in the optical, point to a scenario in which the two subclusters M1 and M2, forming the cluster core, with masses of $4.2\times10^{12}M_\odot$ and $4.8\times10^{12}M_\odot$ respectively, are in the course of a merging process, moving one towards the other along a direction coincident with the cluster major axis. The cores of the subclusters will pass through each other in a few Myr.

1) The spectral analysis of CL 0939+4713 has revealed an elongated region of heated gas located between the two X-ray peaks, and almost perpendicular to the cluster major axis. Hydrodynamic simulations (Ricker & Sarazin, 2001b; Ritchie & Thomas, 2002; Schindler & Müller, 1993; Takizawa, 1999) show that the gas located between two subclusters is compressed and heated during the approach of the subclusters. This hotter gas tends to expand in the direction perpendicular to the collision axis, therefore it shows an elongated shape perpendicular to the collision axis. The gas temperature and the elongation of the central region increase as the two subclusters get closer, while the bulk of the X-ray emission still comes from the cores of the two subclusters until the two cores collide.

2) CL 0939+4713 shows an elongated X-ray morphology. Also this feature is consistent with simulations of merging clusters (Schindler, 2002), which show that before the merger the intracluster gas is elongated along the collision axis.

3) The X-ray maxima of the two subclusters are displaced with respect to the peaks in the galaxy density distribution. In M1 the X-ray peak seems to be ahead of the galaxy concentration.

Obviously, the galaxies do not trace the dark matter distribution well in this region. This is not surprising as during a merger the distributions of the different components can be quite different.

4) CL 0939+4713 has a high velocity dispersion, $\sigma \approx 1300$ km s^{-1} (Dressler & Gunn, 1992; Dressler et al., 1999), indicating a relative motion of two or more components along the line of sight. The velocity dispersions of the two subclusters, computed independently, are instead slightly lower: $\sigma \approx 1000$ km s^{-1} and $\sigma \approx 750$ km s^{-1} for regions M2 and M1, respectively.

5) Dressler et al. (1999) observed a very high fraction of post-starburst galaxies, in CL 0939+4713, compared to other rich clusters and to field galaxies. Fujita et al. (1999) have investigated the effect of ram pressure in merging clusters. They find (in contrast to what was predicted previously by Evrard (1991)) that the increase in the star-formation rate caused by compression is less important than the ram-pressure stripping, which dramatically increases before a merging process. The stripping of the interstellar medium causes a decrease of the star formation rate, with a subsequent increase of the post starburst galaxy fraction.

6) Andreon et al. (1997) found that early-type galaxies in CL 0939+4713 do not show a radial symmetry, but are distributed along a privileged direction. This direction roughly coincides with the X-ray major axis and therefore with the possible collision axis.

5.7 Summary and Conclusions

We confirm earlier results that CL 0939+4713 is a dynamically young system (Schindler et al., 1998; Schindler & Wambsganss, 1996). The X-ray morphology has pronounced substructure. New findings of a hot region between the two main clumps are particularly indicative of a merger process, in which the two major subclusters will collide in a few hundreds of Myr.

Particularly interesting are the metallicity variations found in this cluster. Metallicity variations were found before as radial gradients in clusters with cD galaxies (De Grandi & Molendi, 2001; Gastaldello & Molendi, 2002; Kaastra et al., 2001; Lewis et al., 2002; Molendi & Gastaldello, 2001). Clusters without cD galaxies were found to show no radial gradients (Arnaud et al., 2001b; De Grandi & Molendi, 2001). The problem when binning the cluster into radial bins is, that one averages over metallicity values coming from very different regions of the clusters. Therefore it is not surprising that the profiles are usually flat for non-cD clusters. We took a different approach here and found a hint that the metal abundances vary over the cluster. Of course it is quite difficult to do this in a relatively distant cluster. We therefore suggest to use this method in nearby clusters, instead of determining radial metallicity profiles.

6

Discovery of depressions in the X-ray emission of the distant galaxy cluster RBS797 in a CHANDRA observation †

Interaction of the different components in clusters of galaxies yields important information on physical quantities like e.g. the pressure, the energy or the strength of the magnetic field. The knowledge about these quantities enables us to understand cluster formation as well as physical processes in clusters, being both important steps to use clusters as diagnostic tools for cosmology. The unprecedented spatial resolution ($\sim 0.5''$) now available with the new generation of X-ray satellite CHANDRA allow us to study in more detail this interaction. We present CHANDRA observations of the X-ray luminous, distant galaxy cluster RBS797 at $z = 0.35$. In the central region the X-ray emission shows two pronounced X-ray minima, which are located opposite to each other with respect to the cluster centre. These depressions suggest an interaction between the central radio galaxy and the intra-cluster medium, which would be the first detection in such a distant cluster. The minima are symmetric relative to the cluster centre and very deep compared to similar features found in a few other nearby clusters. A spectral and morphological analysis of the overall cluster emission shows that RBS797 is a hot cluster ($T = 7.7^{+1.2}_{-1.0}$keV) with a total mass of $M_{\rm tot}(r_{500}) = 6.5^{+1.6}_{-1.2} \times 10^{14} M_\odot$.

6.1 Introduction

Interaction between the intra-cluster gas and radio sources in the centre of galaxy clusters has been found in several nearby clusters with an anticorrelation of X-ray emission and radio emission, e.g. in the Perseus cluster (Fabian et al., 2000), in Hydra-A (McNamara et al., 2000), and in Abell clusters A4059 (Huang & Sarazin, 1998), A2597 (McNamara, 2001), A2052 (Sarazin, 2001), A2199 (Fabian, 2001), and A2634 (Schindler, 1996a). Such an interaction of two different components is particularly interesting because one can infer physical conditions and processes in the cluster centre, e.g. heating and cooling effects, magnetic fields or energies of relativistic particles, from the pressure balance. The observations suggest that the cavities in the X-ray gas rise outwards

†This Chapter is an article written together with Sabine Schindler, Elisabbeta De Filippis, Axel Schwope and Joachim Wambsganss. It is published in Astronomy & Astrophysics, vol. 376, p.L27-L30, 2001.

by buoyancy (Churazov et al., 2001; McNamara et al., 2000) while a model by Heinz et al. (1998) predicts shocked gas around the cavities which is not observed. Models by Reynolds et al. (2001) and David et al. (2001) suggest a weak shock regime with radio lobes moving at the local sound speed.

We present here recent CHANDRA observations of the galaxy cluster RBS797. They reveal clear X-ray minima in the cluster centre. We hypothesize that these minima are caused by interaction between the radio source embedded in the central cluster galaxy and the intra-cluster medium. RBS797 would be the first *distant* cluster in which evidence for such interaction has been found. Only the high spatial resolution of CHANDRA makes it possible to observe such details in distant clusters. This X-ray observation is part of a broader programme to search for strong gravitational lensing in X-ray selected, X-ray luminous clusters. The goal is to take both deep optical images of these clusters and high resolution X-ray exposures. In this way we can use the clusters for arc statistics as well as for the determination and comparison of cluster masses estimated by X-ray observations and by gravitational lensing. Throughout this paper we use $H_0 = 50$ km/s/Mpc and $q_0 = 0.5$.

6.2 Cluster identification

The X-ray source RXS J094713.2+762317 (or RBS797), found in the ROSAT All-Sky Survey (RASS), was observed optically in the course of the ROSAT Bright Survey (RBS), aiming at optical identification of all bright (count rate $> 0.2\,\mathrm{cts\,s^{-1}}$), high-galactic latitude ($|b| > 30°$) X-ray sources detected in the RASS (Fischer et al., 1998; Schwope et al., 2000). A spectrum of the central cluster galaxy at RA(2000) = 09 47 12.5, DEC(2000) = +76 23 14, taken with the SAO 6m telescope shows a strong O[II]λ3727 emission line, and weak, narrow Hβ and O[III]$\lambda\lambda$4959/5007 emission lines at a redshift of $z = 0.354$. The emission lines can be due to a cooling flow or due to nuclear activity of the central cluster galaxy.

6.3 X-ray observation of RBS797 with CHANDRA

RBS797 was observed on October 20^{th}, 2000 with the CHANDRA Advanced CCD Imaging Spectrometer (ACIS) I detector for a total exposure time of 13.3 ksec. No time was lost due to flares. For the data analysis we used the standard set of event grades and applied no a priori filtering. The energy range used for the images is 0.5-7 keV, for the spectra it is given in Table 1. The response matrices from the CHANDRA Calibration Database package (CALDB) version 2.0 are used.

Figure 6.1 shows the X-ray image of the cluster RBS797 on a scale of 4.7 arcmin ($\equiv$ 1.7 Mpc). The cluster emission is elliptical with axis ratios of major to minor axis varying slightly from 1.3 at a radius of 0.26 arcmin to 1.4 at a radius of 1.7 arcmin. The centre and the position angle ($\approx -70°$, N over E) of the ellipses are almost the same over the entire radius range.

The innermost (32 arcsec)^2 region of the galaxy cluster RBS797 is shown in Fig. 6.2. Two emission minima are obvious in ENE and WSW direction at distances of about 3-5 arcseconds from the cluster centre. The minima are opposite to each other with respect to the cluster centre. In perpendicular directions excess X-ray emission is visible. At radii of 4 arcsec there is a factor of 3-4 between the X-ray emissions from the different regions (see Fig. 6.3). The sizes of the

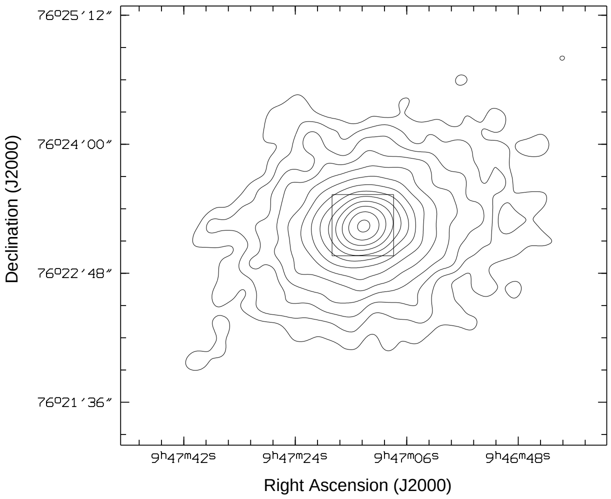

Figure 6.1— CHANDRA image of the cluster RBS797. The cluster is relatively regular with an ellipticity of 1.3-1.4 in E-W direction. The contours are logarithmically spaced with 5 contours per decade and the highest corresponding to 3.9 cts/s/arcmin^2. The image is smoothed with a Gaussian of $\sigma = 5$ arcsec. The size of the image is 4.7 arcmin on the side. The central square marks the region shown with higher resolution in Fig. 6.2.

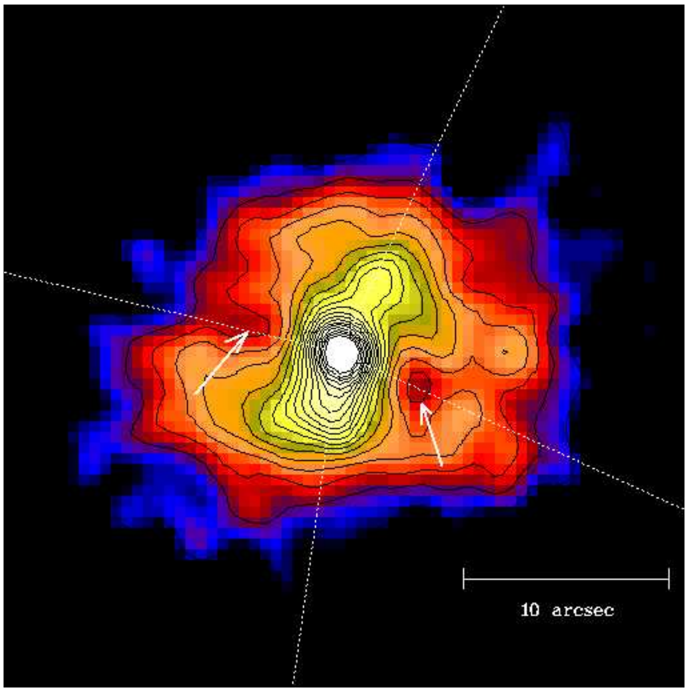

Figure 6.2— X-ray image of the central (32 arcsec)^2 of the cluster RBS797. There are clear minima in the X-ray emission in ENE and WSW direction at about 5 arcseconds from the cluster centre (see arrows). An excess of emission is found in perpendicular directions. The dotted lines mark the traces shown in Fig. 6.3. The contours have a linear spacing of 0.7 cts/s/arcmin^2 with the highest being 14 cts/s/arcmin^2. The image is smoothed with a Gaussian of $\sigma = 0.75$ arcsec.

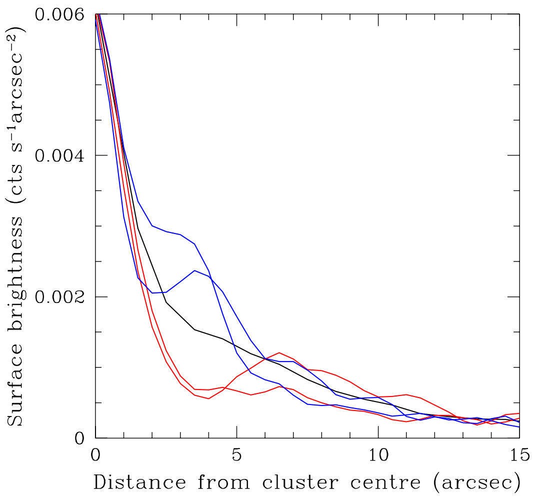

Figure 6.3— Dependence of the surface brightness on direction: the X-ray emission from the centre in direction of the minima (solid red lines, position angles 77° and 243°, N over E) and in direction of the maxima (solid blue lines, position angles 171° and 337°). There is an X-ray deficit of a factor of 3 - 4 in the "holes" compared to the perpendicular directions. The solid black line shows an average profile integrated over all angles. A surface brightness of 0.001 cts/s/arcsec^2 corresponds to 3 counts per ACIS pixel (0.5 arcsec on the side).

X-ray depressions are about 20 - 30 kpc. It is likely – but largely a hypothesis up to now – that the gas has been pushed from the low X-ray emission regions to the high X-ray emission regions by the pressure of relativistic particles in radio lobes, as has been observed in a number of nearby clusters. Although a good hardness ratio map cannot be derived from the data due to the limited number of photons, we find that the hardness ratio in the depressions is not harder than the overall cluster emission, which excludes absorption or hot gas bubbles as explanations for the minima. The depressions are very significant and deep, and also very symmetric compared to other clusters. Therefore this cluster appears to be an ideal object to investigate the interaction of jets and the intra-cluster medium. We will study the interaction in detail with radio follow-up observations.

6.4 Spectral analysis, luminosity and mass determination

The CHANDRA data can be used to derive the temperature, metallicity, luminosity and mass of RBS797. For the spectral fits the energy range is restricted to $0.5 - 10$ keV and $2 - 10$ keV, respectively, because the calibration of the low energy channels is still uncertain. We treat the central point-like source (radius $\lesssim 2$ arcseconds) separately, because this source is probably an AGN, which would distort the thermal spectrum of the intra-cluster gas.

Table 6.1— Results of the spectral fits to the X-ray emission of the galaxy cluster RBS797. Column 1 shows the radii in arcsec of the region, from which the photons have been extracted. Column 2 lists the model used for the fit: MeKaL = Kaastra & Mewe (1993), Liedahl et al. (1995), PL = power law. Column 3 lists the energy range. In columns 4-7 the fit parameters are given: hydrogen column density in 10^{20} cm^{-2}, temperature in keV (for power law fits it is the power law index), metallicity in solar units, redshift. The errors are 90% confidence levels. Columns 8 and 9 are the degrees of freedom of the fit and the reduced χ^2.

1	2	3	4	5	6	7	8	9
radius in arcsec	model	energy range in keV	n_H in 10^{20} cm^{-2}	temp. kT in keV	metallicity Z in solar units	redshift z	d.o.f.	χ^2/d.o.f.
$2-80$	MeKaL	$0.5-10$	2.22(fixed)	$7.7^{+1.2}_{-1.0}$	0.26 ± 0.10	0.39 ± 0.02	272	1.2
$2-80$	MeKaL	$0.5-10$	$6.1^{+1.5}_{-1.4}$	6.3 ± 0.6	0.26 ± 0.09	0.38 ± 0.02	271	1.1
$2-80$	MeKaL	$2-10$	2.22(fixed)	$8.1^{+1.6}_{-1.5}$	0.25 ± 0.12	0.39 ± 0.02	109	0.9
$2-80$	MeKaL	$2-10$	2.22(fixed)	$7.4^{+1.7}_{-1.1}$	0.17 ± 0.11	0.354(fixed)	91	1.0
$2-10$	MeKaL	$0.5-10$	2.22(fixed)	$5.7^{+0.7}_{-0.5}$	$0.38^{+0.17}_{-0.16}$	0.39(fixed)	117	1.6
$10-30$	MeKaL	$0.5-10$	2.22(fixed)	$8.4^{+1.2}_{-1.0}$	0.25 ± 0.18	0.39(fixed)	139	1.0
$30-80$	MeKaL	$0.5-10$	2.22(fixed)	$11.7^{+4.3}_{-2.5}$	$0.20^{+0.35}_{-0.20}$	0.39(fixed)	95	1.2
arms	MeKaL	$0.5-10$	2.22(fixed)	$4.4^{+0.7}_{-0.6}$	0.26(fixed)	0.39(fixed)	52	1.2
$0-2$	PL	$0.5-10$	2.22(fixed)	1.2 ± 0.2	-	0.39(fixed)	20	0.9
$0-2$	0.59×MeKal + 0.41×PL	$0.5-10$	2.22(fixed)	7.7(fixed) 1.1 ± 0.2	0.26(fixed)	0.39(fixed)	19	0.9

The results of the spectral analysis are summarised in Table 6.1. The overall emission is well fit by a thermal bremsstrahlung model with a temperature of 7.7 keV and a metallicity around 0.26 in solar units when the hydrogen column density is fixed to the Galactic value (Dickey & Lockman, 1990). We find somewhat higher temperatures for fits in the 0.5-10 keV band, compared to the results of the 2-10 keV band, probably indicating problems with the calibration of the low energy channels. Attempting to see radial variations in the fit parameters, we extract photons from three different annuli. There is a trend of increasing temperature and decreasing metallicity with radius, which, however, is not statistically significant due to the limited number of photons in this pointing.

The best-fit value for the redshift ($z = 0.39 \pm 0.02$) is slightly higher than the optically determined redshift ($z_{\rm opt} = 0.354$), but they still agree with each other within 2σ. If we fix the redshift to the optical value, the resulting metallicity is lower because the location of the Fe lines does not correspond well with the bump in the observed X-ray spectrum.

Although the "arms" – the regions of higher emission surrounding the minima – contain only 1387 source counts, we attempt a spectral fit, because the temperature measurement is important for distinguishing different models. We find a slightly lower temperature (4.4 keV, see Table 6.1) than for the rest of the cluster, suggesting that the "arms" are probably not shocked regions. This would rule out the model by Heinz et al. (1998). Similar results have been found in other clusters (Fabian et al., 2000; McNamara et al., 2000).

In the centre of the cluster there is a point-like source, which has a source count rate of about 0.026 cts/s and a flux $F_{\rm centre}$(2-10keV)$= 2.2 \times 10^{-13}$ erg/s/cm^2. The spectrum of this source is very flat and cannot be fitted with a thermal spectrum of reasonable temperature. A power law spectrum, which is an indication for an AGN, (and also a sum of a power law and a thermal spectrum) yields a good fit with a very low index of 1.2 ± 0.2.

The NRAO VLA Sky Survey (NVSS) lists a radio source at the central cluster position with a peak flux of 0.02 Jy/beam (Condon et al., 1998) which is another indication for an active galaxy in the centre of the cluster. A complementary explanation for the central X-ray peak would be a cooling flow as the central cooling time is $\approx 10^9$ yr.

The X-ray emission of the cluster can be traced out to a radius of 4.1 arcmin ($\equiv$ 1.5 Mpc). Within this radius there are 11000 source counts. For the above mentioned parameters, this corresponds to a flux of f_X(0.5-7.0 keV)$= 7.1 \times 10^{-12}$erg/s/cm^2 and $f_X({\rm bol}) = 1.1 \times 10^{-11}$erg/s/cm^2 and for a redshift of $z = 0.354$ to a luminosity of L_X(0.5-7.0 keV)$= 4.0 \times 10^{45}$erg/s and $L_X({\rm bol}) = 6.7 \times 10^{45}$erg/s. Only 3% of the total emission comes from the central source.

The X-ray surface brightness profile of RBS797 (centred on the central galaxy) can be fitted well by a β model (Cavaliere & Fusco-Femiano, 1976) when ignoring the central region. A fit excluding the central 6 arcsec radius yields a slope $\beta = 0.63 \pm 0.01$, a core radius $r_c = 8.1(\pm 0.6)$ arcsec [or 49($\pm$4) kpc] and a central surface brightness $S_0 = 6.6$ cts/s/arcmin^2. With the assumption of spherical symmetry this corresponds to a gas mass of $M_{\rm gas}$(1Mpc)$= 0.90(\pm 0.07) \times 10^{14} M_\odot$ and $M_{\rm gas}(r_{500}) = 1.13(\pm 0.09) \times 10^{14} M_\odot$ with $r_{500} = 1.22(\pm 0.08)$ Mpc. Assuming hydrostatic equilibrium, the total mass of the cluster can be estimated. For an isothermal cluster of $T =$ 7.7 keV the total mass is $M_{\rm tot}$(1Mpc)$= 5.3^{+0.8}_{-0.7} \times 10^{14} M_\odot$ and $M_{\rm tot}(r_{500}) = 6.5^{+1.6}_{-1.2} \times 10^{14} M_\odot$ (see Fig. 6.4). This corresponds to a gas mass fraction $f_{\rm gas}(r_{500}) = 0.17^{+0.06}_{-0.05}$ which is in good agreement with the gas mass fractions found in samples of nearby and distant clusters (Castillo-Morales & Schindler, 2003; Ettori & Fabian, 1999; Mohr et al., 1999; Schindler, 1999). Taking into account the temperature gradient changes the results slightly (see Fig. 6.4).

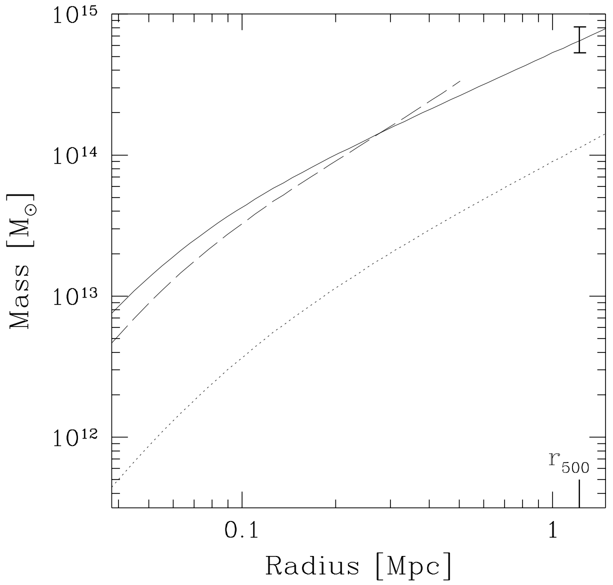

Figure 6.4— Integrated mass versus radius: total gravitational mass (solid line) and gas mass (dotted line). A typical error bar is shown at r_{500}. The total mass profile taking into account a temperature gradient (dashed line) is shown up to the radius to which the temperature gradient can be determined.

6.5 Summary

The X-ray luminous cluster RBS797 reveals remarkable depressions in the X-ray emission of the central region. The depressions are roughly circular and arranged symmetrically with respect to the cluster centre. They have diameters of 20 - 30 kpc and are very deep: a factor of 3-4 less emission than in the other directions. The discovery of these minima shows the ability of CHANDRA to investigate physical effects even in clusters as distant as RBS797 (z=0.35).

The spectral and morphological analysis of RBS797 shows that the cluster has a high temperature of $T = 7.7$ keV, a metallicity $Z = 0.2 - 0.3$, and a high luminosity $L_X(\mathrm{bol}) = 6.7 \times 10^{45}$erg/s. The total mass within r_{500} is $M_{\mathrm{tot}}(r_{500}) = 6.5 \times 10^{14} M_\odot$ with a gas mass fraction $f_{\mathrm{gas}}(r_{500}) = 0.17$. In follow-up radio observations the interaction between the radio lobes and the intra-cluster gas will be studied in detail.

7

INTEGRAL Observations and Data Reduction

In this chapter we describe the integral field spectrograph, INTEGRAL, used to observe the selected galaxies (NGC 5033 and NGC 4321). We also detail the different steps followed in the data reduction process.

7.1 Description of INTEGRAL

INTEGRAL (Arribas et al., 1998) is an optical fibre unit for performing 2D spectroscopy of extended objects at the 4.2 m. William Herschel Telescope (WHT), located at the Observatorio del Roque de Los Muchachos (ORM), La Palma, Spain. It is mounted at one of the Nasmyth focus together with the acquisition, guiding, and calibration units. It makes use of the specially designed fibre spectrograph WYFFOS (Bingham et al., 1994).

In the next sections we will describe the main characteristics of INTEGRAL. A complete technical description can be found in the INTEGRAL's web page [1].

7.1.1 Overview

INTEGRAL consists in a 2D array of fibres located in the focal plane, the Acquisition, Guiding and Calibration (AG&C) box and the WYFFOS spectrograph.

The Swing Plate (SP) is a rotating plate located in the telescope focal plane, to which the acquisition and scientific fibre bundles are attached. The SP can rotate, allowing the location of the desired bundle at the center of the focal plane.

Up to six scientific bundles can be simultaneously mounted in the SP, although in the standard configuration only three are used. They are called SB1, SB2, and SB3, which are formed by optical fibres with a core diameter of 100 μm, 200 μm and 600 μm, respectively. The bundles are simultaneously connected at the entrance (pseudo-slit) of the WYFFOS spectrograph. They can

[1] http://www.ing.iac.es/ bgarcia/integral/html/integral_home.html

Table 7.1— Characteristics of the standard INTEGRAL bundles

Characteristic	SB1	SB2	SB3
Fibre core diameter ($\mu m/arcsec$)	100/0.45	200/0.90	600/2.70
Fibre image size on the CCD[1] (pixel)	0.7	1.4	4.0
Total number of fibres[2]	205 (175+30)	219 (189+30)	135 (115+20)
Field of view[3](arcsec× arcsec)	7.80×6.40	16.0×12.3	33.6×29.4
Distance between adjacent apertures (pixels)	4.0-8.5	4.6	7.4
Diameter of the sky fibre ring (arcsec)	90	90	90

[1]without convolving with the PSF
[2]rectangle + sky fibre ring
[3]central rectangle

be interchanged very easily, with an overhead of a few seconds. Hence, depending on the prevailing seeing conditions the instrument can be easily optimized for the scientific program.

For acquisition a coherent fibre bundle transmits the light from the focal plane (via the SP) to a standard TV camera. This camera has a field of view of $22.5'' \times 30.2''$ in the telescope focal plane.

Calibration may be accomplished with the aid of calibration lamps which can be reached by the different scientific bundles by moving the SP. The acquisition bundle transmits the light from two arc lamps (copper-argon and copper-neon) and a white lamp (quartz-halogen tungsten) to the focal plane.

7.1.2 The Standard Bundles

At the focal plane the fibres of each standard bundle are arranged in two groups: one forming a rectangle to observe the object, and the other one forming a ring which is intended for collecting background light (for small-sized objects). Table 7.1 and Fig. 7.1 show the main characteristics of each bundle. Each fibre it is defined by a number that corresponds to its position along the spectrograph entrance.

7.1.3 Spectral resolution

Given a particular grating, the spectral resolution depends on the fibre bundle as a consequence of the different fibre image size on the detector. In Table 7.2 the mean spectral resolution, spectral coverage and linear dispersion at a central wavelength of 6000 Å are listed for the different gratings and bundles.

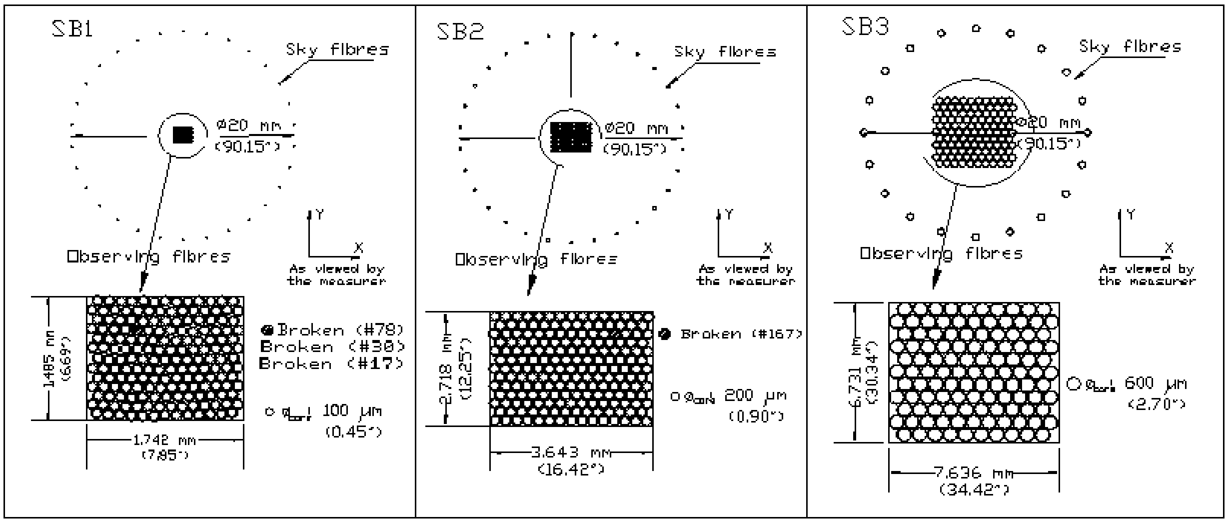

Figure 7.1— Configuration of the fibres in SB1, SB2 and SB3 bundles (del Burgo, 2000). In the SB2 fibre bundle there is one broken fibre (# 167) while in the SB1 fibre bundle there are three broken fibres (# 17, # 30 and # 78).

Table 7.2— Spectral parameters at 6000Å

Parameters	grating (grooves mm^{-1})			
	1200	600	316	300
Spectral coverage(Å)	1445	3140	5837	6144
Linear dispersion (Åpixel^{-1})	1.4	3.0	5.9	6.0
Spectral resolution (for SB1) (Å)	2.8	6.0	11.8	12.0
Spectral resolution (for SB2) (Å)	2.8	6.0	11.8	12.0
Spectral resolution (for SB3) (Å)	4.8	9.8	19.4	19.6

7.2 Observations

We observe with the two-dimensional spectrograph INTEGRAL the central region of the galaxies presented in this thesis: NGC 5033 and NGC 4321. In Table 7.3 the dates, objects, exposure times, mean seeing values and the configurations used for these galaxies are summarized. Dome-flats (tungsten lamp), twilight and arc images (CuAr, CuNe lamps) were also obtained to perform the spectra extraction, throughput correction and wavelength calibration.

A typical INTEGRAL SB3 (SB2, SB1) exposure consists of 135 (219,205) individual spectra displayed on the CCD (see Fig. 7.2).

7.3 Data Reduction

The procedure required for INTEGRAL data reduction is very similar to the long-slit spectra reduction process, but there are some differences. We summarize in Table 7.4 the different steps

Table 7.3— Galaxies observed with INTEGRAL

Object	Dates	Seeing	Bundle	λ_c^1	Grating[2]	Exp.T.[3]
NGC 5033	2001/04/10		SB3	5003	1200	3×1800+4×600
NGC 4321	2002/03/16	1″.3	SB3	6247	R1200R	3×1200
			SB2	6247	R1200R	3×1200
			SB1	6247	R1200R	3×1200

[1] λ_c: central wavelength
[2] Grating: dispersion of the spectrum (6 Åpixel^{-1} for R300B)
[3] Exp. T.: exposure time in seconds

Table 7.4— Scheme of the reduction procedure

Step	Goal	Package	Task
1	Bias subtraction	imutil	imstat, imarith
2	Trim	imutil	imcopy
3	Cosmic ray rejection	imred	imcombine
4	Aperture definition and trace	integral	int_apall
5	Extraction of spectra	integral	int_apall
6	Arc line identification	onedspec	identify, reidentify
7	Dispersion correction	onedspec	dispcor
8	Throughput correction	specred	msresp1d
9	Image reconstruction	starlink	inter2r
			home made IDL program

followed in the reduction process.

The steps detailed in this section are made using the INTEGRAL data reduction package running in IRAF environment. This package together with other own IDL programs allow us: (i) to produce a wavelength-calibrated data from a set of raw CCD exposures and (ii) to extract the physical quantities (e.g. line-intensity maps, continuum maps, etc.). More details about the reduction procedure can be found in Arribas et al. (1991).

7.3.1 CCD Preprocessing and Cosmic ray rejection

The CCD preprocessing includes, bias subtraction and image trimming. This bias level is introduced onto the CCD to ensure that it is working in a linear regime. We localized the position of the bias region in the image. We subtract the bias level in the combined exposition taking into account the mean value in the bias region. Furthermore during the observations we took a set of bias exposures and no structure in the bias images was detected. The images were trimmed manually after bias correction. In this step an special care must be taken when trimming the images in the x axis (spatial coordinate) because a tight cut may cause the partial loss of the fibres.

After the CCD preprocessing, the different expositions we have for the same object were com-

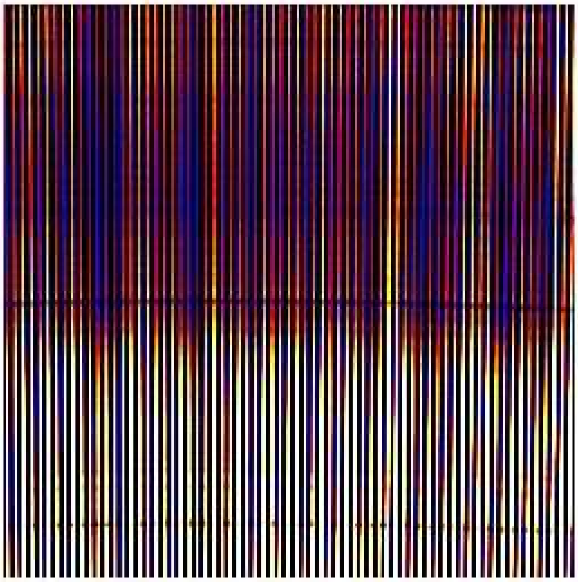

Figure 7.2— Sky-flat exposure raw image. The dispersion axis goes along columns and the spatial axis along rows.

bined (see Fig. 7.3) to increase the S/N ratio. We eliminate cosmic rays with the task `imcombine`, setting the rejection parameter to `crreject` and modifying interactively the `hsigma` parameter until most of the cosmic rays are removed. We are sure that only cosmic rays are being rejected comparing the frame that results in the subtraction of the combined image with `reject=crreject` from the combined image with `reject`=none.

7.3.2 Aperture Definition and Trace

We have the positions on the CCD of each spectrum $(x_i, y_i, \lambda(x_i, y_i))$ corresponding to the fibre *i*. The total flux that corresponds to each fibre can be calculated. This is a critical point because an error will affect the spectrophotometric accuracy of the extracted spectrum. To extract the spectra we need first to define the aperture and trace it for each fibre. The optic distorsions of the system make the apertures to be not along the dispersion axis, i.e each fibre follows a curved locus. Therefore the different loci must be fitted by a polynomial. We use the task `int_apall` in the package `integral` to define and trace the peak profile fo the fibres in a well exposed flat lamp. INTEGRAL/WYFFOS is a very stable system and hence we can use the same extraction parameters determined on the flat lamp to define, trace and extract the spectra in all the images obtained during the same night.

The aperture definition consists on selecting the centers and widths of the apertures along the spatial axis at a fixed row (dispersion axis). In Fig. 7.4 we show the aperture definition of SB3 bundle. When we execute the task `int_apall` the profiles of the apertures along the middle line in the dispersion axis are displayed. The apertures will appear identified and ordered. We need to revise all the apertures are identified and ordered in the riht way. Special care must be taken with the bundles with broken fibres. In this case we need to mark the broken fibres if the task has not detected them and reorder the rest of them.

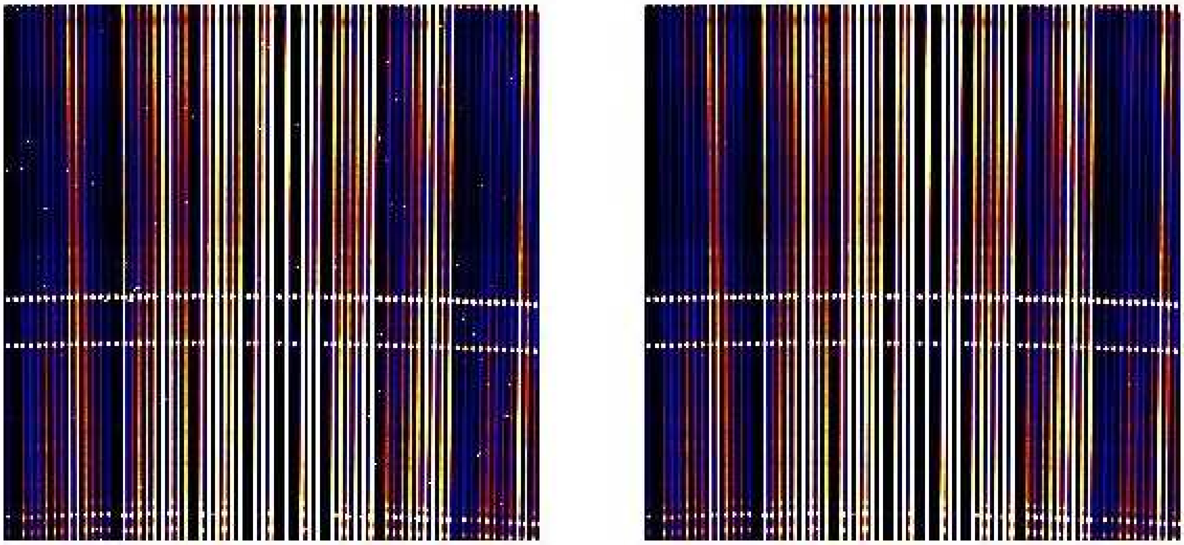

Figure 7.3— Combined frame of NGC 4321 for SB3 bundle with `reject=none` (left) and `reject=crreject`, `hsigma=7.5` (right).

Once we define the apertures we have to trace them. The tracing is carried out by fitting a polynomial to each signal peak along the dispersion axis. This step is done interactively for each fibre to check them. The order of the fitting polynomial can be changed interactively, we typically use a seventh degree Legendre polynomial.

7.3.3 Extraction of Spectra

To extract each aperture we need to sum up the pixels along the spatial axis into a final one-dimensional spectrum. We extract the apertures with the standard widths using the previously determined trace polynomial and using the task `intapall`.

A two-dimensional image of N×M pixels results after the aperture extraction. In this new image N is the number of pixels along the dispersion axis and M is the number of apertures/spectra. The flat lamp after aperture definition and extraction is shown in Fig. 7.5.

7.3.4 Wavelength Calibration

For the wavelength calibration we use a CuNe (for SB3 fibre bundle) and CuNe+CuAr (for SB2 and SB1 fibre bundels) lamp reference exposure with the same wavelength range ($\sim$ 1500 Å). There was no need to use filters for this wavelength range.

The wavelength calibration consists in the emission line identification and the dispersion correction. For the line identification the task `identify` in the package INTEGRAL was runned to identify the known arc lines (20) in the central fibre where the S/N ratio is higher. This individual spectrum is calibrated interactively. Although it is difficult to estimate the uncertainties in the wavelength calibration we use the standard deviation (RMS) of the polynomial fit as an error indicator. In the NGC 4321 observations the RMS was not larger than 0.08Å, fitting a fourth degree

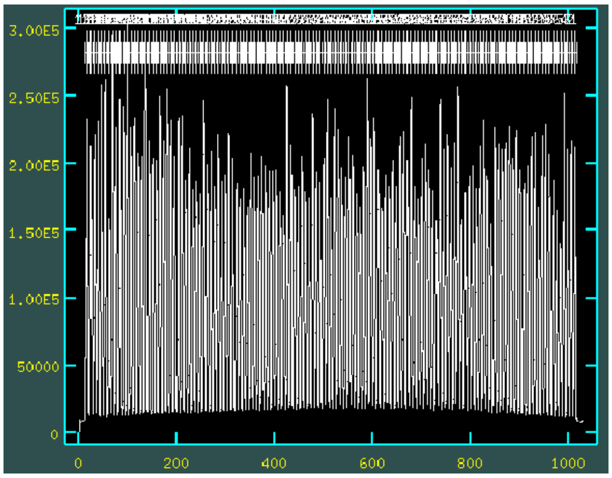

Figure 7.4— Aperture definition for spectra extraction. The x-axis represents the position in pixels and the y-axis is the flux counts.

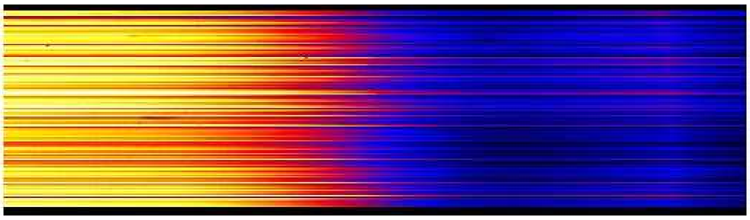

Figure 7.5— Flat lamp exposure after aperture extraction. The x-axis represents the wavelength dispersion and the y-axis the spatial coordinates (apertures).

polynomial.

After obtaining the polynomial degree and selecting the most suitable lines for this individual spectrum, the wavelength calibration for the other fibres is done automatically by cross-correlation with the central fibre, each one having its corresponding polynomial fit. For this purpose we use the IRAF task `reidentify`. The mean RMS of the fitting for all the fibres is not larger than 0.16Å.

We use the polynomials obtained with this procedure to calibrate the other images. The arc spectrum is assigned as a reference for each objet image. Finally we run the task `dispcor` to apply the wavelength calibration to all the images.

7.3.5 Throughput Correction

We use the sky-flat exposure to correct for the differences in pixel sensitiviy on the CCD. The sky flat is a function of the coordinates (x, y) and the wavelength λ. When observing with optical fibres, the focal plane is uniformly illuminated to obtained the so-called *flat spectrum*. Therefore for each wavelength the flat spectrum represents the different response of each fibre.

The white lamp exposure provides a featureless spectra and could be use to eliminate the wavelength signature of the sky-flat. But the white lamp does no emit in the whole wavelength range we are using (see Fig. 7.5) and therefore it is not the best way to correct for the spatial variation of the flat spectra. Instead we use the twilight exposures

The wavelength-calibrated spectra obtained from the sky-flat were used to correct for the relative fibre transmission. This throughput correction was perfomed with the IRAF task `msresp1d`. The result is a two dimensional frame with a spectrum per aperture whose profile is proprotional to the relative transmission of the corresponding fibre. In the next step all the frames were divided by the throughtput correction (see Fig. 7.6).

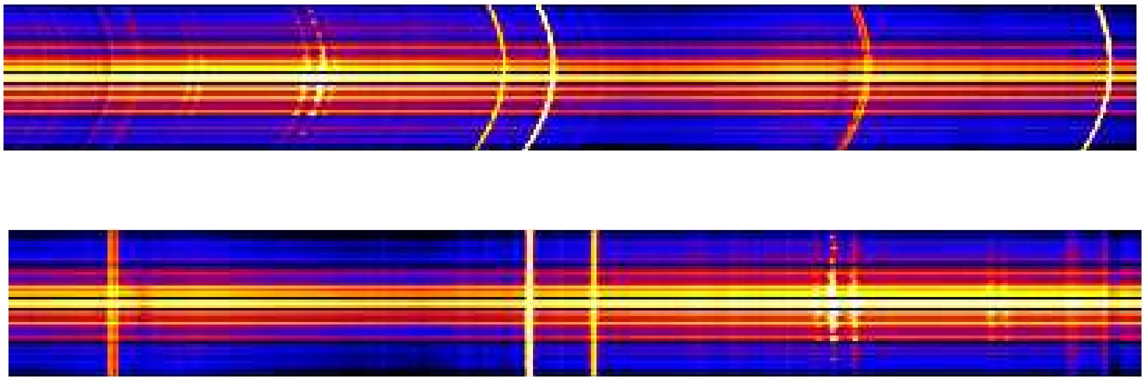

Figure 7.6— Top: NGC 4321 image after combination, bias, trim, cosmic ray rejection and aperture extraction. Bottom: the same image after wavelength calibration and throughput correction.

7.3.6 Image Reconstruction

If we want to do a further analysis we need to measure some parameters from each final spectrum. For each fibre which has a spatial location in the bundle, several numbers e.g. flux, lines ratio, velocity, can be associated. We can then build two-dimensional images of these quantities, giving e.g. continuum, velocity or emission maps, using interpolation techniques.

We create files with the X and Y positions of the fibres in the telescope focal plane and the physical parameter we want to represent. The two-dimensional maps presented in this thesis in Chapter 8 are obtained using the routine `inter2r` which runs in `starlink.figaro` environment, and the maps presented in Chapter 9 are home made using IDL programs. We have developed an easy-handle program in IDL to manage with the reconstruction of INTEGRAL two-dimensional maps. This program results in a very helpful tool which can be used to derive the different velocity, intensity and continuum INTEGRAL maps, to compare the morphology of several maps, to visualize the spectrum associated with each fibre and to obtain the final postcript file.

8

Biconical Structure of Ionization and Kinematics in the Seyfert Galaxy NGC 5033

The 2D spectroscopy with optical fibre allow us to obtain simultaneously spatial and spectral information for extended objects. This technique can be applied to many research fields in astrophysics as for example the study of nuclear and circumnuclear regions in galaxies. We present 2D spectroscopy of NGC 5033, a low luminosity Seyfert galaxy. The observations were made with INTEGRAL, a fibre based system operating at the WHT. The intensity map of the Hβ emission line represents a spiral or ring like pattern of HII regions. On the contrary, the [OIII] intensity map morphology is markedly anisotropic. The strong morphological differences imply that the [OIII] emitters represent highly ionized gas illuminated by the central source. The [OIII] map morphology is compatible with a biconical structure of ionization induced by strong extinction in the galaxy disc that also obscures half of the spheroidal stellar bulge. The Seyfert 1 nucleus (identified from the Hβ broad emission lines) is located at the apex of the biconical structure. In spite of the anisotropic morphology of the high ionization region, the wide aperture of the cones, their alignment perpendicular to the galaxy major axis, and the good agreement with the morphology of the stellar bulge (partly extincted by the disc), make not necessary the existence of an inner torus or disc of blocking material collimating the radiation coming from the active nucleus. Instead, the alignment of the ionizing flux seem to be related to the large scale bipolar CO structure (likely a CO ring) present in the galaxy disc. The Seyfert 1 nucleus could be offcentered with respect to the stellar rotation center. This result has been also found in other Seyfert galaxies and interpreted in terms of a past merger. The offcentering could indicate the presence of nonsymmetric departures in the gravitational potential which could be fueling the active nucleus. The kinematics of the [OIII] emitters presents important deviations at kpc scale with respect to the stellar velocity field and shows features related to the biconical geometry.

8.1 Introduction

According to observations, the narrow emission line regions in Seyferts and other active galaxies extend anisotropically over a significant fraction of the host galaxy. These Extended Narrow Line Regions (ENLR) trace the illumination of the gas by the ionizing continuum coming from the active nucleus that, in the framework of the unified models, should be collimated in two opposite cones along the axis of symmetry of a central obscuring torus. Sometimes, this biconical structure of

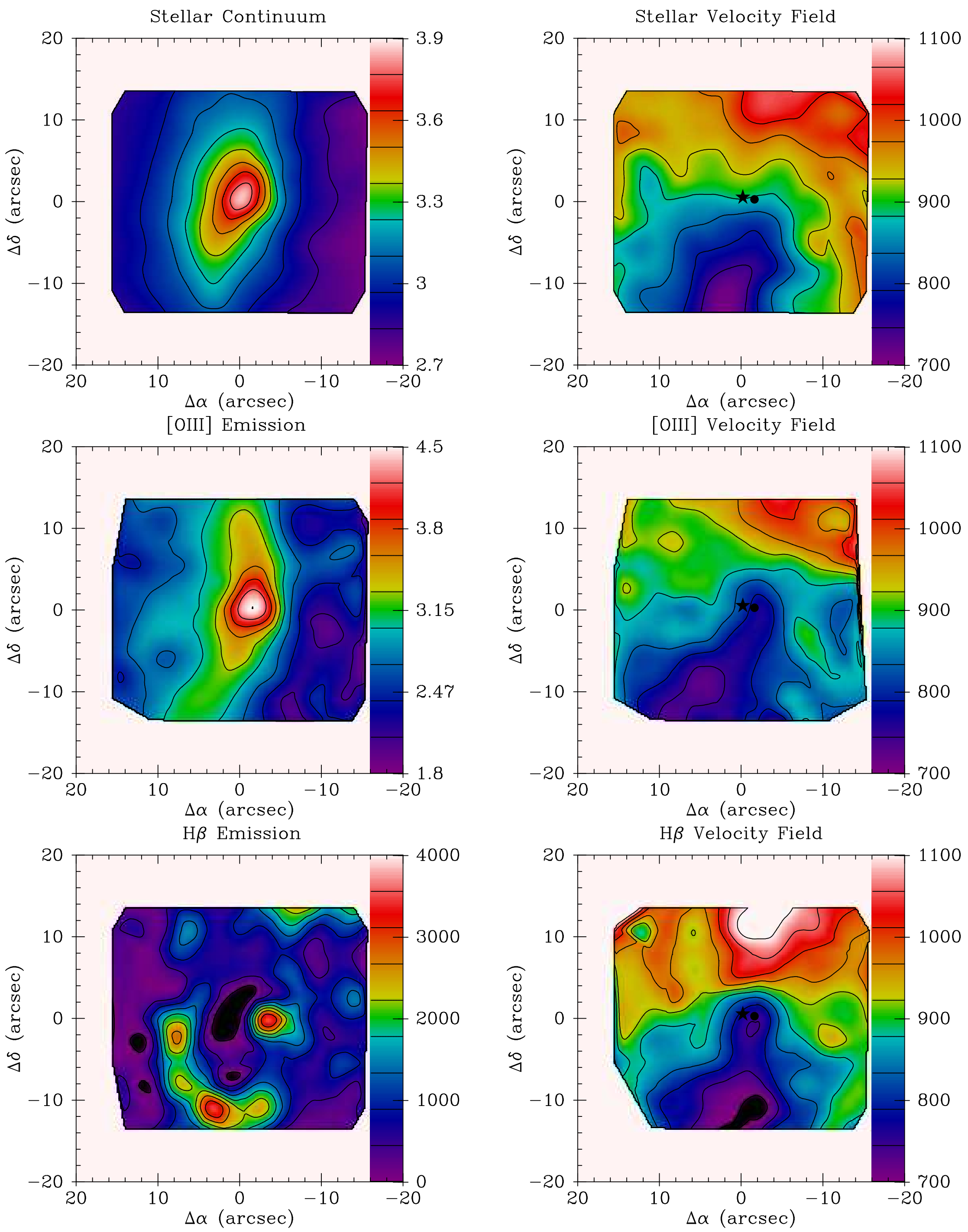

Figure 8.1— Intensity (arbitrary units) and velocity (kms^{-1}) maps for NGC 5033 (see text). The intensity maps correspond to the stellar continuum, the [OIII] λ5007 and Hβ emission. The star and the circle in the velocity maps represent, respectively, the location of the intensity peak in the stellar continuum and [OIII] intensity maps.

ionization can be directly seen (e.g. NGC 5728, Arribas & Mediavilla (1993); Wilson et al. (1993)), but in most cases the scenery is complex and the shape of the ionization structure appears not clearly defined. The shape and size of the ENLR depend not only on the relative inclination and widening of the radiation cones but also on the spatial distribution of the gas in the galaxy. Thus, the final appearance of the ENLR can be very amorphous if, as it seems to be the rule for high luminosity Seyfert nuclei, several gaseous systems of different spatial location and kinematics are ionized. In this case a kinematic analysis (as in NGC 1068, Arribas et al. (1996)) is needed to reveal the bipolar structure of ionization. The study of the ENLR in the circumnuclear region of typical high luminosity Seyfert galaxies is also compromised since most of them are very distant.

Nearby galaxies that host Low Luminosity Active Galactic Nuclei (LLAGNs) are potentially very interesting sceneries to study the ionization structure and, in general, to probe the unified scheme for AGNs. However the detection and mapping of the line emission in the circumnuclear region of LLAGNs is difficult. In these objects the emission lines are weak with respect to the continuum and filter imaging can give very doubtful results. A better observational option to study the ENLR is to obtain 2D spectroscopy from the circumnuclear region to measure directly the narrow line emission after properly fitting the continuum (see, for instance, the case of the LINER galaxy NGC 7331, Battaner et al. (2003); Mediavilla et al. (1997). With this aim, we are going to present and discuss new observations of the low-luminosity type 1.5 Seyfert galaxy, NGC 5033, taken with INTEGRAL a fibre based system to obtain 2D spectroscopy at the William Herschel Telescope.

NGC 5033 presents a very pronounced spiral structure and a nuclear bulge extending until a distance of r= 1700 pc from the nucleus with a mass estimated to be $2 \times 10^{10} M_{\odot}$ (Ford et al., 1971). The dynamics of stars and gas in NGC 5033 have been studied regarding its nuclear activity. Bosma (1981) remarked that NGC 5033 has a giant neighbor within a short distance: NGC 5005, a Seyfert SAB(rs) galaxy. Using the Very Large Array, Thean et al. (1997) found neutral gas within a few kiloparsecs (1" = 58 pc, D = 11.8 Mpc, H_o = 75 Km s^{-1} Mpc^{-1}) of the galactic centre which appears to be unaffected by the active nucleus. From measurements of the optical emission lines (mainly Hα) and Westerbork HI-observations, van der Kruit & Bosma (1978) did not detect sufficient strong non-circular motions attributable to a bar. However, more recently Curran et al. (2001) with the 20m Onsala and 15m SEST telescopes, detected a bar in HCN in NGC 5033. Ho & Ulvestad (2001), using VLA for radio continuum at 6 cm and 20 cm emission, found that the morphology of the radio emission is predominantly that of a compact core slightly resolved surrounded by a fluffy envelope with a major-axis diameter of $\approx$ 0.9 kpc, roughly along the east-west direction, accompanied by elongated, jet-like features. Koratkar et al. (1995) and Terashima et al. (1999) found that the X-ray emission is mostly or entirely nuclear ($\leq$ 500 pc) with a luminosity of 2.3×10^{41}ergs^{-1} in the 2-10 keV band. They also detected the Fe Kα emission line at 6.4 keV. Recently, Kohno et al. (2003) have detected a perturbed distribution of CO in the central region of this galaxy with two bright peaks near the nucleus.

In this paper we will present 2D spectroscopy of the circumnuclear region of NGC 5033 to (i) identify its structure of ionization from the [OIII]$\lambda\lambda 4959, 5007$ maps and (ii) study the kinematics of the ionized emitters from the comparison between the kinematics of stars and gas. We will use these results to discuss the application of the unified scheme and the origin of the activity in this object.

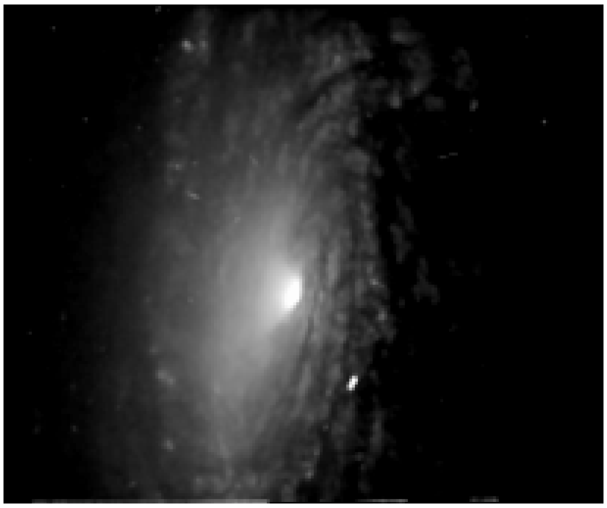

Figure 8.2— HST/PC (F5957) image of NGC 5033 (FOV: 36"x36"), obtained from the data archive at the Space Telescope Science Institute based on observations made with the NASA/ESA Hubble Space Telescope. East is to the left and North is up.

8.2 Observations and reduction

NGC 5033 was observed with the fibre system INTEGRAL (Arribas et al., 1998) in combination with the fibre spectrograph WYFFOS (Bingham et al., 1994) the 10 of April of 2001. The spectral resolution and coverage were 4.8Å and 1445Å and the central wavelength was 5003Å . This galaxy was observed with the SB3 bundle of INTEGRAL. This bundle is formed by 135 fibres, each 2".7 in diameter on the sky, and consists in a central rectangle of 30"×34" and an outer ring of 90" of diameter. 3 exposures of 1800s and 4 of 600s were taken from NGC 5033. These frames were combined, in each case, to increase the S/N ratio and to reject the cosmic rays. Afterwards, the spectrum corresponding to each fibre is extracted, calibrated in wavelength, and corrected from throughput. The reduction steps are made using the INTEGRAL data reduction package running in IRAF. More details about the reduction procedure can be found in Arribas et al. (1991).

For several spectral features of interest we have determined a grid of points at the locations of the fibres at the focal plane and have interpolated a map of the selected feature in the region of the central rectangle (see, e. g., Arribas et al. (1999). In Fig. 8.1 we present six maps obtained from the observations of NGC 5033. The stellar velocity field was obtained cross-correlating the spectra in the ∼5250Å-6000Å wavelength range. The continuum was integrated in the ∼4700Å-5840Å wavelength interval. To obtain the intensity and the velocity maps for the ionized gas we have performed Gaussian fittings to the [OIII]λ5007 and the Hβ emission lines.

8.3 Results

8.3.1 Continuum and line emission maps

The continuum intensity map looks very asymmetric with the optical nucleus apparently displaced about $2''.5$ toward the west from the photometric major axis (defined as the major axis of the outermost isophotes in Fig. 8.1). This map is morphologically identical to a map computed from the CaFe absorption feature (not shown here). This implies that it represents the distribution of stars and that the contribution from the Seyfert continuum is, as expected, negligible. Clear evidence of extinction in the west side of the galaxy (closer to us) is found in an optical image from the HST archive (Fig. 8.2). Thus, we are likely observing half of the spheroidal stellar bulge of the galaxy being the other half strongly obscured by extinction.

On the other hand, the peak of the [OIII] emission is close to the optical nucleus but the [OIII] emission has a banana-like shape that does not follow the stellar continuum map (see Fig. 8.1). The Hβ (narrow component) intensity map is very different from both the stellar and [OIII] intensity maps. In this map we can recognize several HII regions following a spiral or ring shaped pattern and a nuclear concentration displaced by about $2''$ westward respect to the [OIII] emission peak. There is also an elongated structure passing through the nucleus (PA $\sim 170^{\circ}$) roughly aligned with the HCN bar detected by Curran et al. (2001).

8.3.2 Stellar and ionized gas velocity fields

The stellar velocity field looks regular. The kinematic major axis defined by the approaching and receding poles is parallel to the photometric axis of the galaxy but displaced about $3''$ westwards (see Fig. 8.3). The optical nucleus is around $0''.7$ eastwards from the kinematic major axis which passes $0''.8$ eastwards from the [OIII] emission peak. The ionized gas velocity field inferred from the Gaussian fitting to the [OIII] lines is related to the shape of the [OIII] emission. The approaching (SE) pole morphology follows the bend of the [OIII] emission and the [OIII] emission peak appears strongly blueshifted. There are also noticeable departures from regular rotation in the region obscured by extinction ($\Delta\alpha < -8''$). The ionized gas velocity field corresponding to Hβ (see Fig. 8.1) is more regular than that of [OIII]. If we made exception of the strongly blueshifted region near to the center, it represents a kinematic pattern compatible with the one of the stellar velocity field.

8.4 Discussion

8.4.1 The Seyfert nucleus

We found broad Hβ emission in spectrum 71 located in coordinates $(-3''.2, 0''.0)$. This implies that the Seyfert nucleus is, under the limits imposed by our spatial sampling, displaced $\sim 3''.2$ westwards from the peak of the continuum emission. We can give as upper limit for the uncertainty in the Broad Line Region (BLR) location half the distance between the centers of two adjacent fibres, $\sim 1''.6$, but this limit is very conservative for it would imply that for an $1''$ seeing a noticeable

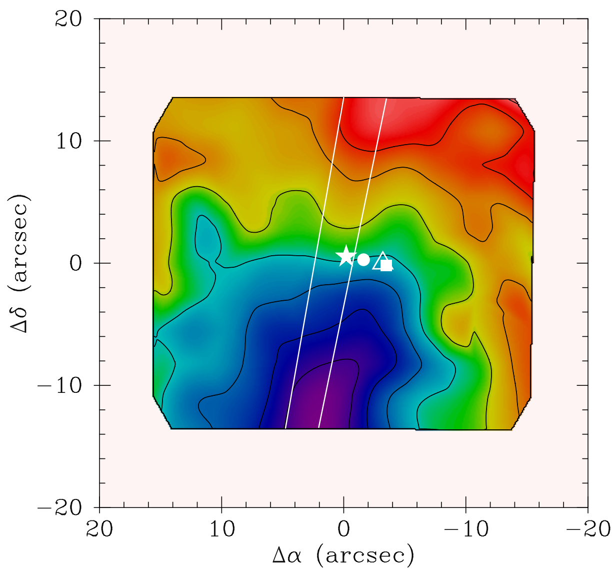

Figure 8.3— Photometric (Easter white line) and kinematic (western white line) major axis. The photometric major axis corresponds to the symmetric axis of the outermost isophotes. The kinematic axis is define as a straight line joining the blue and red poles of the stellar velocity field. The star, circle, triangle and square represent the stellar continuum emission peak, the [OIII] emission peak, BLR location and the Hβ emission peak respectively.

part of the light coming from the BLR would be thrown to the adjacent fibre(s) and we do not found evidences of broad emission in any other fibre.

Because of the offset between the BLR and the optical nucleus, previous spectra taken with long slits (Ho et al., 1997a,b) of different width and aligned at different PA which lead to the classification of NGC 5033 as a variable low luminosity Seyfert 1.5 nucleus could be not comparable. In addition, due to the strong absorption present in the Hβ spectral region, it is difficult to determine the intensity and broadening of the broad component.

8.4.2 Localization of the galaxy center

It is readily apparent that there are several non-coincident centers. They appear aligned almost perpendicular to the photometric major axis (see Fig. 8.3). The offsets relative to the optical nucleus (stellar emission peak) are: $\sim 2''.5$ eastward (photometric major axis), $\sim 1''.5$ westward ([OIII] emission peak); and $\sim 3''.5$ westward (Hβ emission peak). The Hβ emission peak is almost coincident with the location of the BLR. In principle, these displacements parallel to the photometric minor axis could be attributed to the strong absorption present in the west part of the disk of this galaxy. However, the location of the BLR (a 'point-like' feature) should be insensitive to the extinction marking the galaxy center (notice that the spatially coincident Hβ emission peak likely corresponds also to a 'point-like' nuclear region related to the active nucleus). In spite of this, the BLR location is clearly displaced ($\sim 2''.5$) westwards with respect to the kinematic major axis. That is, a displacement greater than the conservative upper limit for the uncertainty in the BLR localization (see previous section). It is true that the identification of the velocity map poles is relatively inaccurate but it seems clear from Fig. 8.3 that the kinematic major axis can hardly be displaced $2''.5$ toward the west.

A shift of the kinematic center may be explained combining increasing extinction toward the west and 3D kinematics in a stellar bulge. However it is simpler to consider the offcentering of the Seyfert nucleus. In fact, there are a number of galaxies in which the active nucleus is not located at the galaxy center like M 31 (see, e.g., del Burgo et al. (2000); Kormendy & Richstone (1995), NGC 1068 Arribas et al. (1996), NGC 3227 Mediavilla & Arribas (1993) and NGC 3516 (Arribas et al., 1997)). In some cases the offcentering of the Seyfert nucleus has been related to a galaxy merger. The BLR would correspond to the Seyfert nucleus of a merged galaxy, orbiting the dynamic center that could constitute the center of the primary galaxy before the merging. This complex kinematics could indicate the presence of a nonsymmetric contribution to the gravitational potential. According to theoretical considerations (e.g., MacKenty et al. (1994), and references therein), this type of potential could redistribute the angular momentum of nonnuclear material, thereby bringing it closer to the galaxy center, exciting and/or fueling the nuclear activity.

8.4.3 Biconical morphology of the high ionization region

The strong differences in morphology between the Hβ and [OIII] maps imply that the [OIII] map corresponds to highly ionized gas. A biconical structure can be recognized in this map if we take as cone apex the BLR location (see Fig. 8.4). Notice that not only the east cone can be easily seen but that also the west cone strongly obscured by dust extinction can be recognized in the two protrusions at coordinates $\sim(-4'', -8'')$ and $\sim(-7'', 6'')$. This is one of the few cases in which the biconical structure of ionization is so clearly depicted by the [OIII] emission. The apertures of the cones are very wide and their axes appear perpendicular to the disk galaxy plane. The cones seem to be hollow structures according to the banana shape morphology. This could be caused by a lack of gas outside the galaxy plane more than by a feature of the ionizing flux. All these morphological characteristics suggest that the large scale distribution of obscuring material in this galaxy is giving rise to the biconical morphology of ionization seen in the [OIII] map. This hypothesis is strongly supported by the discovery of a bipolar distribution of CO aligned with the galaxy disk plane (Kohno et al., 2003) which could be obscuring the emission along this direction. However, there are traces of more collimated emission not perpendicular to the galaxy plane that could be constrained by some mechanism acting at a smaller spatial scale. These are one jet-like structure of low intensity at the West (PA $\sim$ 310^o) and a broader and stronger feature at the East (PA $\sim$ 110^o).

The stellar continuum morphology is in excellent agreement with the presence of an obscuring structure of the same characteristics as that inferred from the ionized gas distribution (see Fig. 8.4). This reinforces the idea that obscuration induced by the galaxy disk is giving rise to the observed ionization structure.

8.4.4 Kinematics of the highly ionized gas

After comparison of the stellar velocity map with the ones representing the ionized gas inferred from the [OIII] and Hβ emission lines, it can be said that the active nucleus is affecting the ionized gas kinematics in several ways: (i) a region near the BLR location appears blueshifted in both the [OIII] and Hβ maps, (ii) the kinematic major axis corresponding to the [OIII] map is displaced with respect to that of the stars following the banana like shape of the [OIII] intensity map (notice the strong displacement of the blue pole of the [OIII] velocity field toward the east with respect to that of the stars), (iii) there are departures from regular rotation in the west region of the [OIII] velocity map (not present in the Hβ velocity field). Features (i) and (ii) can be related to the biconical

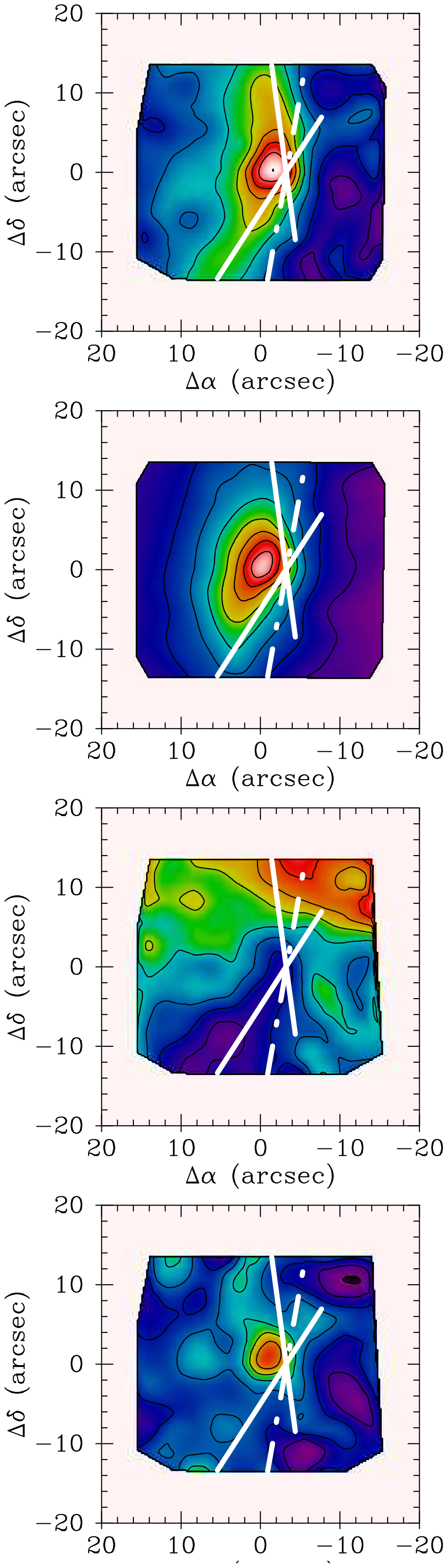

Figure 8.4— Ionization cones (white continuous lines) represented on top of the [OIII] line emission (top), stellar continuum (middle) and [OIII] velocity maps (down). The dotted dashed line is parallel to the photometric major axis.

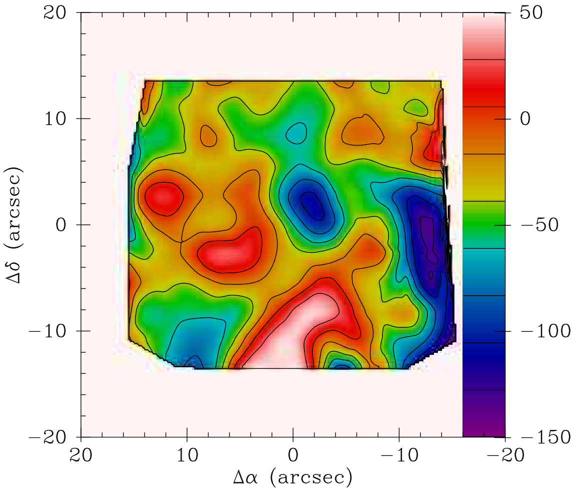

Figure 8.5— Residual velocity field obtained subtracting the stellar velocity map from the [OIII] velocity map.

geometry (see Fig. 8.4): the nuclear blueshifted region starts from the BLR location and extends along the NE cone border and the kinematic major axis in the SE region is also aligned with the SE cone border.

To study the non rotational kinematics we have computed a difference velocity map subtracting the stellar velocity map from the [OIII] velocity map. The resulting difference map (Fig. 8.5) is very irregular and difficult to interpret further than the previous comments. It is clear that the highly ionized gas is following a peculiar kinematics neither related to axisymmetric motions nor ruled by the dynamic influence of a bar, but it is difficult to recognize a velocity pattern in this map. In any case, we would like to remark that the role of activity is not limited to the illumination of the gas but it exerts a significant influence in the dynamics of the high ionization gas at kpc scale.

Regarding the jet-like feature likely representing more collimated emission toward the NW it is worth to comment that it appears strongly redshifted in the difference velocity map.

8.4.5 The ionization structure and the anisotropic unified models for AGNs in NGC5033

In spite of its biconical morphology, the ionization structure does not support the anisotropic unified models for AGNs in NGC 5033. The aperture of the cones is so wide and the shape of the high ionization region so in agreement with the extinction induced by the galaxy disc in the stellar bulge that there is no evidence against an isotropic ionization source. The bipolar CO structure (perhaps associated to a CO ring) detected by Kohno et al. (2003) close to the nucleus is likely related to the alignment of the ionizing flux. Thus, we find that the "microscopic" torus putative of some anisotropic models for AGNs is not needed to understand the geometry of the ionization in this galaxy which can be explained by illumination from a central isotropic source and partial obscuration by a large scale structure belonging to the galaxy disc.

The geometry of the ionization in this galaxy can be explained by illuminatioon from a central isotropic source and partial obscuration by a large structure belonging to the galaxy disc. This could be also the case of Mkn 509 (Mediavilla et al., 1998), other Seyfert 1 galaxy studied from 2D spectroscopy.

8.5 Conclusions

1 - The location of the Seyfert 1 nucleus of the galaxy that we infer from the location of the broad Hβ emission is $\sim 3''.2$ westwards from the continuum emission peak. The stellar rotation center seems to be located between the Seyfert 1 nucleus and the continuum emission peak but closer to the last. According to the uncertainties in the determination of the kinematic major axis and to the spatial resolution of the observations, both centers (galaxy mass centroid and active nucleus) can be only marginally reconciled. Observations with better spatial resolution are needed to confirm this offcentering of the Seyfert nucleus that in other active galaxies has been considered related to a past merger event possibly related to the origin or to the fueling of the activity.

2 - The [OIII] emission (associated to highly ionized gas) depicts a biconical structure with apex in the Seyfert 1 nucleus. The cones seem to be hollow structures of wide aperture and projected axis perpendicular to the galaxy major axis. These characteristics suggest that the biconical structure of ionization is generated by obscuring material in the galaxy disc probably related to the large scale CO structure detected by Kohno et al. (2003). The same geometrical model also explains the morphology of the stellar continuum emission (with half of the stellar bulge obscured). These results make unnecessary the presence in NGC 5033 of the inner torus of obscuring material whose orientation would give rise (according to the unified models) to the anisotropic ionization structure and to the distinction between Seyfert 1 and 2.

3 - Nuclear activity is affecting the kinematics of the highly ionized gas even at large (galactic) scales. There are some kinematic features that seem to be related to the biconical geometry.

9

Stellar and ionized gas kinematics in the circumnuclear region of the Virgo Cluster Galaxy NGC 4321

In this chapter we present the observations and the kinematical analysis for the circumnuclear region of the Virgo cluster galaxy NGC 4321. Integral field spectroscopy in the central region of this galaxy has been obtained using the fibre system INTEGRAL. The three fibre bundles have been used with a field of view of $34'' \times 29''$ for SB3, $16'' \times 12''$ for SB2 and $8'' \times 6''$ for SB1 fibre bundle. The data are mainly used to study the ionized gas and stellar kinematics. We have preferred to focus this chapter in the possibilities the integral field spectroscopy technique offers. Nevertheless we have studied in more detail some aspects in this analysis, as the position of the kinematical centre, the determination of the ionized gas rotation curve and the study of the non-circular motions in this galaxy. There are other interesting aspects that are actually work in progress as the study of different components in the NII and SII emission lines, the interpretation of the ratio maps H_α/[N II] and H_α/[S II] and the investigation of the possible correlations between the intensity, residual velocity and velocity dispersion profiles along the spiral arms. All these results will be published in the future.

9.1 Introduction

NGC 4321 (M 100), is a grand-design late-type, moderately barred spiral galaxy, which has hosted four supernovae since 1990, has a prominent star forming (SF) circumnuclear region and is located in the Virgo cluster (see Fig. 9.1). Although M100 has a dwarf companion NGC 4322, both the optical morphology and the H I distribution and kinematics (Knapen et al., 1993) does not show any indication of disturbance in the center.

The inner region of M100 has been extensively studied at different wavelengths. Optical (Pierce, 1986), Hα, near-infrared (Knapen et al., 1995a,b), CO images (Rand, 1995; Sakamoto et al., 1995), have showed many interesting features associated with its mild star formation activity in the central kpc.

The inner region of this galaxy shows different morphology in the optical and the NIR. In the optical is dominated by two spiral arms lying in an ovally shaped region of enhanced SF, while the

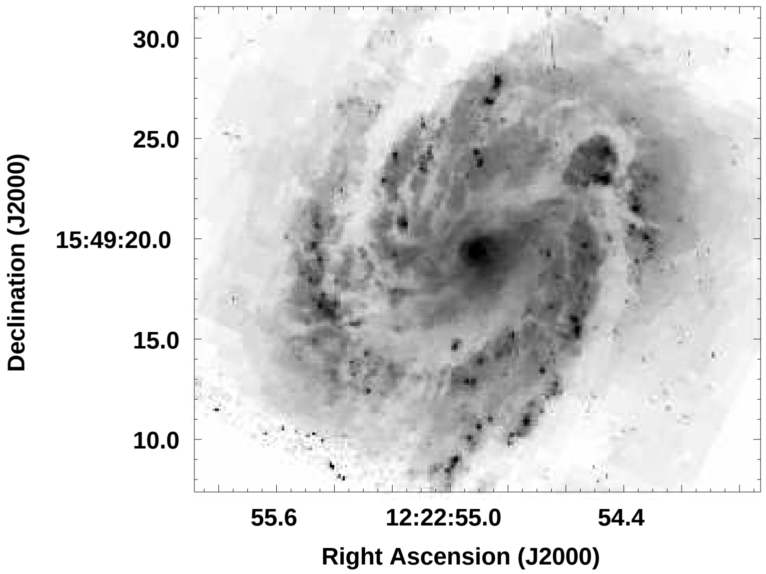

Figure 9.1— HST/WFPC2 (F555W) image of NGC 4321, obtained from the data archive at the Space Telescope Science Institute based on observations made with the NASA/ESA Hubble Space Telescope.

K-band image shows a $60''$semimajor axis inner bar, aligned with the 5 kpc stellar bar and a pair of leading arms emerging from its ends (Knapen et al., 1995a,b).

There is important Hα emission from the circumnuclear region and the disc of this galaxy. Knapen (1998) catalogued almost 2000 individual H II regions and presents an statistical analysis of their properties. Of the four main SF sites seen in Hα, two of them close to the nuclear bar ends (k1/2), have clear counterparts in the K-band, whereas the two strong and more extended Hα regions (Hα3/4), located near the extremities of the nuclear bar minor axis are hardly seen in K-band. The prominent nuclear ring of SF is claimed to lie in the vicinity of the inner Lindblad resonances (ILR(s)) (Arsenault et al., 1988; Pierce, 1986).

It is believed that there is a causal connection between the existence of a bar and circumnuclear SF activity. Through its non-axisymmetric potential, a bar can facilitate gas inflow by extracting angular momentum from the gas through gravitational torques. The inflowing gas may then accumulated in the vicinity of inner Lindblad resonances, triggering massive SF (see, e.g. review by Shlosman (1999)).

In the central 1 arcmin of M100, most of the molecular gas distributes within a $\sim$ 3 kpc diameter region. In this region, there are prominent two-armed molecular spiral arms which cross the inner bar at the location of the K1/2 regions, while the northern and southern parts are offset toward the outer edge of the Hα3/4 regions. The arms start at the ends of the nuclear stellar bar seen in the near-infrared images. Sakamoto et al. (1995) showed that the central CO peak is an excellent observational example of bar-driven gas accumulation often suggested as an important mechanism to feed AGNs. However, the fact that M100 does not have a significant AGN activity may indicate that the accumulation of gas to the central region is not a sufficient condition for AGN activities.

Knapen & Beckman (1996) found that the dust lanes running along most of the spiral arms (and coinciding with the CO spiral arms in part of them; Rand (1995)) are offset from the Hα arms and from the H I arms which coincide spatially with Hα. This is interpreted as an effect of the compression of gas by the density wave in the arm, with SF occurring downstream.

There are also MIR observations with the ISOCAM camera at ISO satellite. The main MIR features are two prominent peaks near the nuclear bar ends which approximately coincide with strong Hα and K-band emissions. A third local maximum, much less intense, is visible at the nucleus (Wozniak et al., 1997, 1998).

Kaaret (2001) reported on X-ray point sources found in high-angular resolution X-ray observations of M100 made with Chandra. M100 has more bright X-ray sources than typical spiral galaxies of its sizes. The Chandra sources lie either on spiral arms, in H II regions near spirals arms, or near the nucleus. This is likely related to active star formation taking place in the galaxy. None of these X-ray sources are coincident with the peak of the radio emission at the nucleus. The question of the association of an X-ray source with the nucleus remains open (Ho et al., 2001). The spectral class of the nucleus of this galaxy has been classified to be between a low-ionization nuclear emission-line region and a star-forming nucleus, i.e LINER/HII "transition" object, without evidence for broad emission lines in its nucleus.

Knapen et al. (2000) carried out two-dimensional kinematic observations in the spectral lines of Hα and CO (J=1$\rightarrow$0) of the circumnuclear starburst region in M100, using TAURUS II instrument in Fabry-Pérot mode at WHT. The Hα data show a rotation curve that is rapidly rising in the central $\sim$ 140pc, and stays roughly constant at the main disk value, further out. They studied noncircular motions from Hα and CO data, and interpreted them as the kinematic signatures of gas streaming along the inner part of the bar, and of density waves streaming motions across a two-armed minispiral.

In this thesis we develop two dimensional field spectroscopy observations with the instrument INTEGRAL-WYFFOS at WHT, to study the kinematics of the ionized gas using the Hα, NII and SII emission lines in the circumnuclear region of M100. We also detect the presence of Na II in absorption, although with significant signal in the nuclear region, which allow us for the study of the stellar component in this galaxy. With these new observations we are able to construct intensity, velocity and velocity dispersion maps for this galaxy. We compare both the ionized gas and stellar kinematics and derive the rotation curve using the Hα emission line. Residual velocity and velocity dispersion maps are also computed for the ionized gas. The assumed distance to NGC 4321 is 17.1 Mpc (Freedman, 1994) which on the sky corresponds to 83 pc arcsec^{-1}.

9.2 Data analysis

The data analysed in this chapter were obtained on 2002 March 16 at the Observatorio del Roque de los Muchachos (ORM) on the island of La Palma. The weather conditions during this night were fairly good, with a seeing of about 1$''$. As it is detailed in Table 7.3, the data discussed in this chapter were obtained with the standard bundles 3, 2 and 1 whose main characteristics are detailed in Table 7.1. The WYFFOS spectrograph was equipped with a 1200 grooves mm^{-1} grating centred on 6247 Å. The linear dispersion for the fibre bundles SB3, SB2 and SB1 are 1.09 Å pixel^{-1}, 1.19 Å pixel^{-1} and 1.22 Å pixel^{-1} respectively. With this configuration, and pointing to the central region of NGC 4321, we took three exposures of 1200 s each during the night.

The data reduction consists of two main steps: i) basic reduction of the spectra (i.e. bias, flatfielding, extraction, wavelength calibration, etc.) and ii) generation of maps of spectral features (e.g. line intensity, velocity fields, etc.) from the spectra.

The first step i) was performed in the IRAF environment and following the standard procedures detailed in Chapter 7. We obtained typical wavelength calibration errors of 0.15 Å, which give velocity uncertainties of $\pm$ 7 kms^{-1} for H$_{\alpha}$.

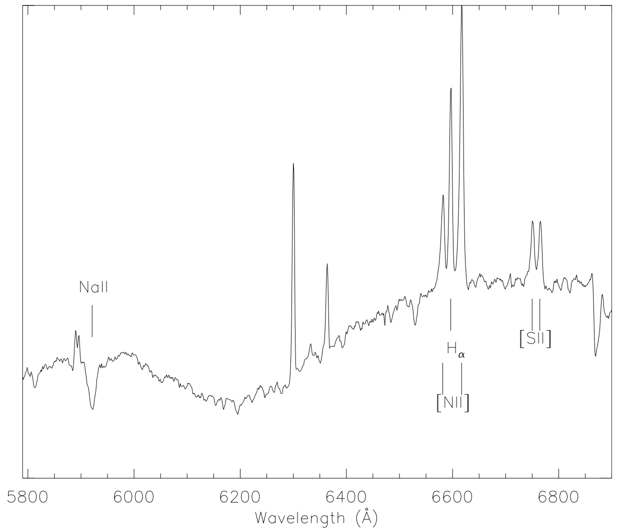

Figure 9.2— Nuclear spectrum (fibre #68 in bundle SB3) of NGC 4321 in the full spectral range observed (5790 - 6900 Å for SB3 fiber bundle).

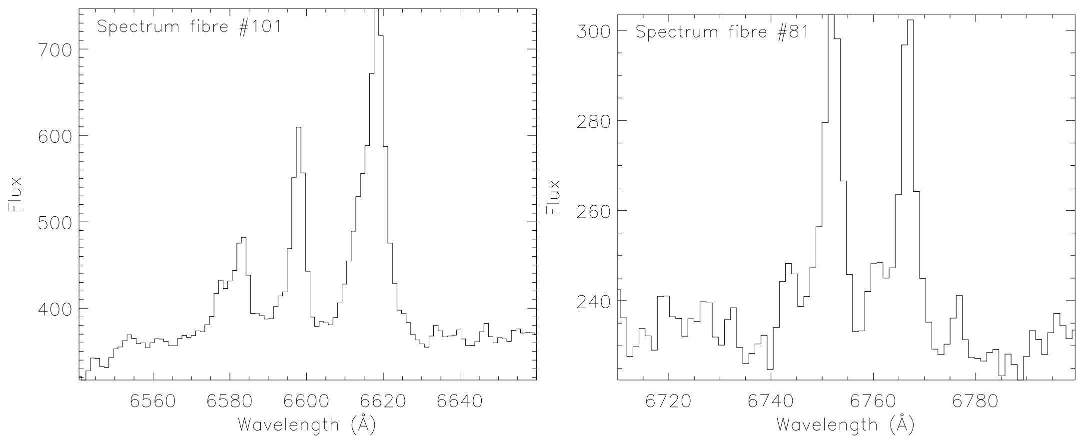

Figure 9.3— Several spectra reveal asymmetric profiles in [N II] (left) and [S II] (right) emission lines.

For step ii) we have developed own IDL programs. In particular we transform an ASCII file with the actual position of the fibres (accurately determined by a metrology machine), and the spectral feature corresponding to each fibre into a regularly spaced rectangular grid. In this way we build up images of 33 $\times$ 29 pixels for SB3 bundle, 45 $\times$ 34 pixels for SB2 bundle and 42 $\times$ 35 pixels for SB1 bundle, with a scale $\sim$ 0.95$''$pixel^{-1}, 0.35$''$pixel^{-1} and 0.18$''$pixel^{-1} for SB3, SB2 and SB1 fibre bundles respectively. These images can be treated with standard astronomical software. Maps generated in this way are presented in § 9.3 and beyond.

9.2.1 Spectra. Emission and absorption lines identification

Fig. 9.2 shows the nuclear spectrum of NGC 4321 in the full wavelength range observed (5790 - 6900 Å). We identified the emission lines of H_α + [N II] $\lambda\lambda$ 6548, 6583 and [S II] $\lambda\lambda$6716, 6731. This new data set observed with INTEGRAL also shows prominent stellar absorption line Na II

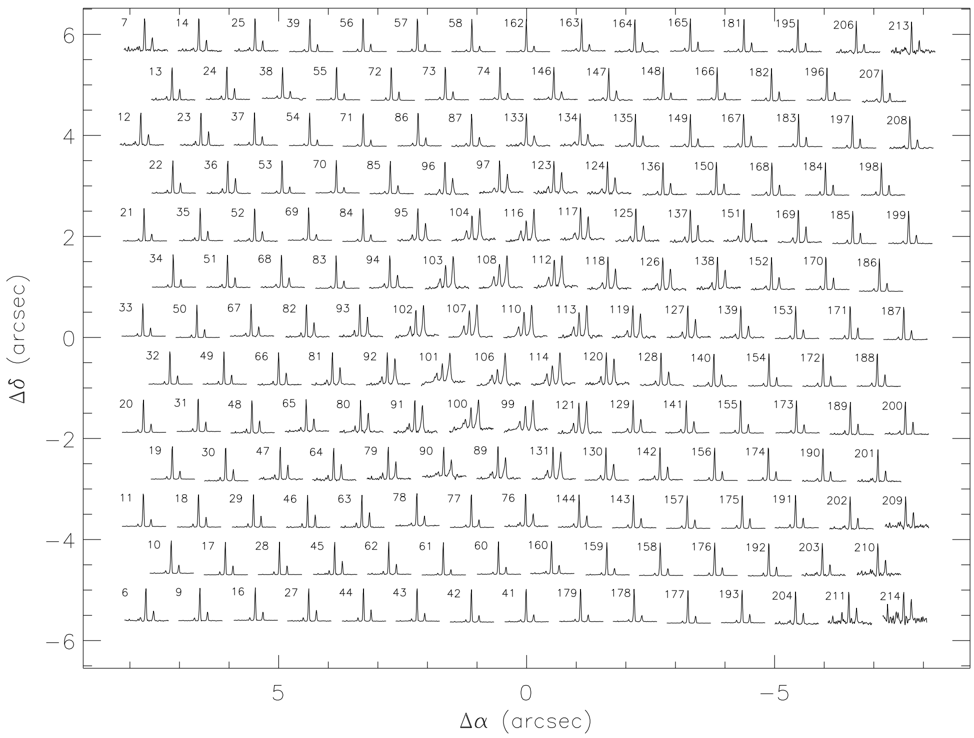

Figure 9.4— Spectra in the circumnuclear region of NGC 4321 for the fibre bundle SB2 in the ranges: 6541-6660 Å, including H_α + [N II] $\lambda\lambda$ 6548, 6583.

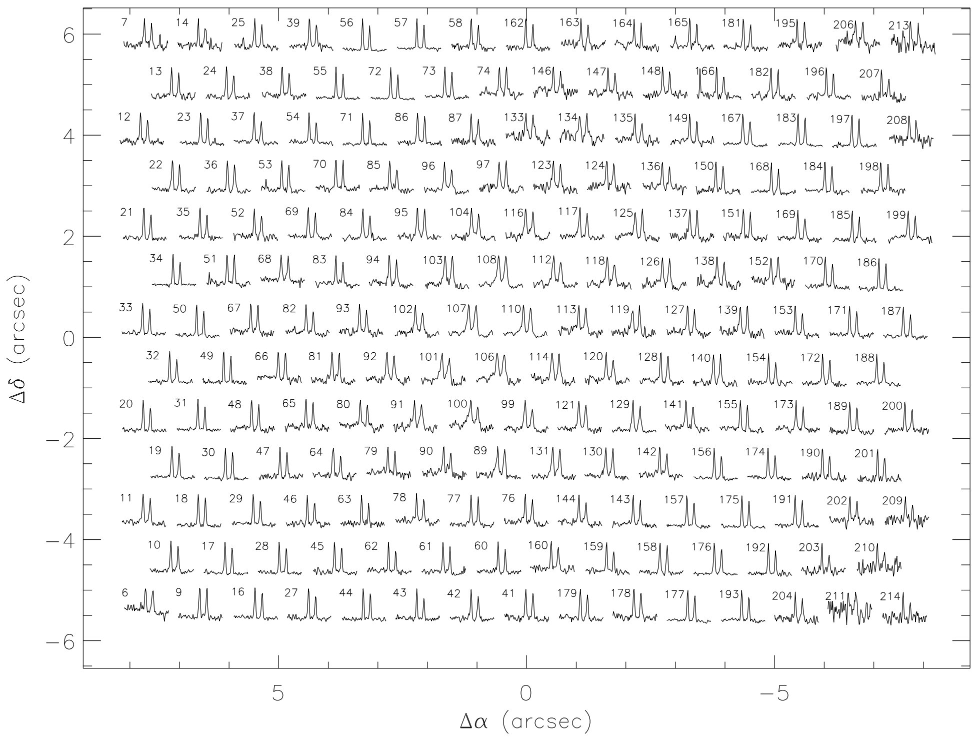

Figure 9.5— Spectra in the circumnuclear region of NGC 4321 for the fibre bundle SB2 in the ranges: 6700-6799 Å, including [S II] $\lambda\lambda$6716, 6731.

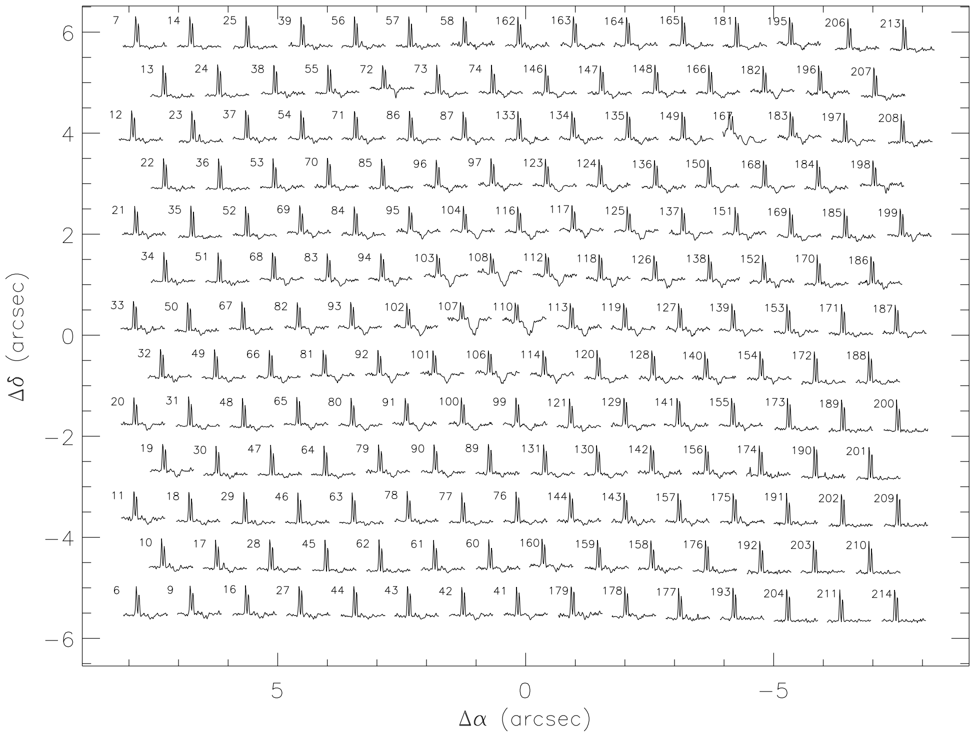

Figure 9.6— Spectra in the circumnuclear region of NGC 4321 for the fibre bundle SB2 in the ranges: 5861-5960 Å, including the absortion line NaII λ5890.

λ5890, not previosly observed in the circumnuclear region of the galaxy NGC 4321 which allows us to analyze and study the stellar component in the most inner region of this galaxy.

Figures 9.4, 9.5 and 9.6 show the individual spectra corresponding to the 189 observed positions (fibres) for SB2 bundle, in selected spectral ranges which include the H_α + [N II], [S II] and Na II lines. In a preliminary analaysis, the inspection of Fig. 9.4 and Fig. 9.5 reveals asymmetric profiles in [N II] and [S II] emission lines in different fibres (see, for instance, the fibre #80 and #81 in Fig. 9.3). Although this task needs to be studied in more detailed, the presence of this extra component in the [N II] and [S II] emission probably is related with the presence of gas bubbles in expansion in this galaxy in which case several kinematics components should be expected.

9.2.2 Gaussian Fits

To obtain the intensity, continuum and velocity maps mentioned in § 9.3 we have performed Gaussian fittings to the H_α, [N II] and [S II] emission lines for the ionized gas and to the Na II absorption line for the stellar component.

We use the programm **dipso** to develope the Gaussian fittings. This programm varies all Gaussian parameters (center, width, and intensity peak) to obtain the best fit. We restrict the wavelength range to 6540 - 6660 Å in the case of H_α + [N II] emission lines fitting procedure. Furthermore, we tied the ratio between the two intensity peaks in the [N II] emission lines to $I_3/I_1 = 3$ (Osterbrock, 1989) (where I_3 refers to the emission line located at greater wavelength). The widths for these two emission lines were related to be the same (i.e $w_1 = w_3$) while the Gaussian centers are tied in this way, $c_3 = c_1(1 + 35.4/6548.05)$. The continuum near these emission lines was fitted with a second degree polynomial.

The wavelength range 6710 - 6800 Å was used in the case of [S II] emission lines fitting procedure. The intensities peaks (I_1 and I_2) are now free. The Gaussian widths are assumed to be the same in both emission lines and the centers are related in this way, $c_2 = c_1(1+14.38/6716.44)$. The continuum near these emission lines was fitted as above with a second degree polynomial.

To fit the absorption line corresponding to Na II we proceed in the following way. We restrict the wavelength range to 5860 - 5960 Å. Near the absorption line there are two sky emission lines corresponding to Na doublet in our Galaxy, that are fitted at the same time with the absorption feature. We tied the relation between the Gaussian centers of these two emission lines ($c_2 = c_1 + 5.967$). At a first attempt we try to fit the absorption feature with only one Gaussian component. The results were not very satisfactory and we decided to include two Gaussian functions to fit the Na II absorption line. We tied the intensity peaks of the two gaussians by the relation $I_4 = I_3/1.33$ obtained after doing some statistics with the fibers with higher signal-to-noise ratio. In the same way we tied the intensity peaks of the two sky emission lines ($I_2 = I_1/1.33$). As in the other cases, we fit the continuum near the absorption line with a second degree polynomial.

We have developed the same procedure explained above for the emission and absorption lines observed with the three fibre bundles, SB3, SB2 and SB1.

As an example, we show in Tables 9.1, 9.2 and 9.3 the results obtained for the Gaussian fits in the case of the Hα-[N II], [S II] emission lines and Na II absorption line respectively, for the case of SB2 bundle. In Figs. 9.18, 9.19 and 9.20, the Gaussian fits to the highest signal-to-noise spectra are shown.

9.3 Integrated maps

Continuum, intensity, velocity and velocity dispersion maps are computed using the two-dimensional ensemble of spectra as those shown in Figs. 9.4, 9.5 and 9.6. We develope a home made programm in IDL to compute and manage these maps in an easy way. This programm reads and transforms the ASCII file with the positions of the fibres and the spectral feature corresponding to each fibre into a regularly spaced rectangular grid. The maps corresponding to the different spectral features and for the three bundles are shown in this section. In all the maps shown in the following sections North is up and East is left.

9.3.1 Astrometric calibration

The dimensions of the field of view ($34'' \times 30''$) of INTEGRAL (for SB3 fiber bundle) and the extense nature of our source, make the astrometric calibration a more complicated step. However we are interested in applying this calibration in order to compare the computed maps from the different lines and fiber bundles.

The astrometry calibration in the INTEGRAL Hα intensity maps is performed using the H_α continuum substracted image provided by J.Knapen. This image was obtained with the TAURUS instrument at the 4.2 WHT (Knapen, 1998) under subarcsecond seeing conditions.[1] The

[1]Due to the lack of a continuum frame for the Hα TAURUS image, it was calibrated by comparing the centroids of the HII regions in the Hα continuum substracted image with the centroids of the same regions in the already astrometric calibrated Hβ continuum substracted image, obtained with the ALFOSC instrument in the 2.5 NOT (Almudena Zurita, private communication). Furthermore, the central pixel positions of the residuals stars in the H_α continuum substracted image were compared with the physical coordenates given by the USNO catalog. The accuracy of this astrometry calibration is $\sim 0.6''$.

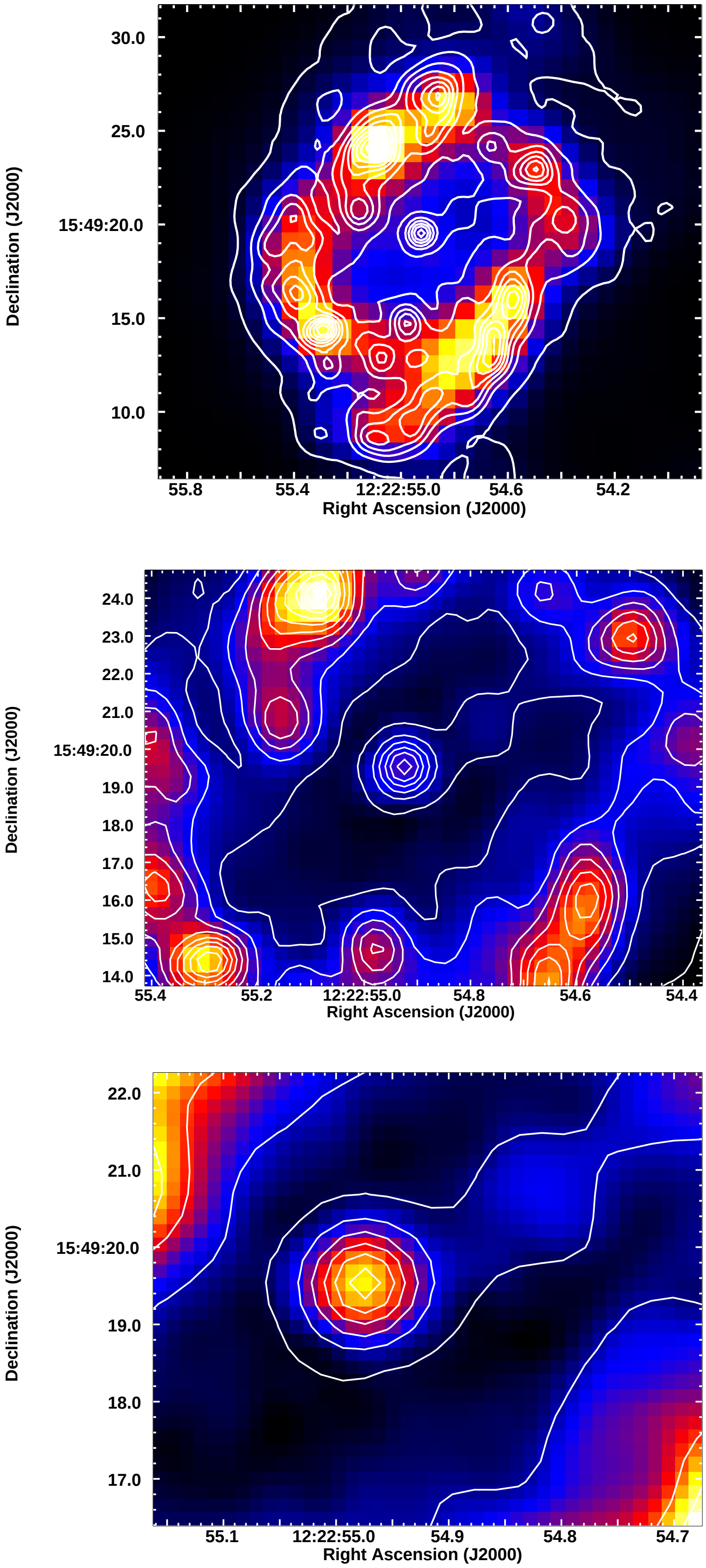

Figure 9.7— From top to bottom: SB3, SB2 and SB1 astrometric calibrated Hα emission maps. The white contours correspond to the Hα intensity image from Knapen (1998) which has been used for the astrometric calibration.

INTEGRAL Hα intensity maps corresponding to each fiber bundle are calibrated by comparing the centroids of the HII regions in both images, i.e. INTEGRAL and TAURUS Hα intensity images. As it is shown in Fig. 9.7 the agreement between the positions of the HII regions is quite good. Therefore, the error in our calibration is assumed to be same as the error in the astrometry calibration of the TAURUS Hα image from J.Knapen ($\sim 0.6''$, equivalent to less than 1 pixel in SB3, ~ 2 pixels in SB2 and ~ 3 pixels in SB1 fiber bundles INTEGRAL maps). We use the above astrometry to actualize the rest of the computed INTEGRAL maps.

9.3.2 Ionized gas

Ionized gas distribution

To compute the H_α, [N II] and [SII] emission lines maps, we subtract the underlaying continuum by fitting a second degree polynomial to the points at the blue and red sides of the line in each spectrum. Then, the continuum-free emission line was integrated, producing the line intensity maps shown in Figs. 9.21, 9.22 and 9.23. In the case of the [N II] $\lambda\lambda$ 6548, 6583, only the most intense emission line was integrated since the two intensity peaks are related. For [S II] $\lambda\lambda$6716, 6731, we added the emission coming from the two lines.

The Hα intensity map shows the emission distributed in a ring ovally shaped observed by other authors (Knapen et al., 2000) where several HII regions can be distinguished. Although M100 is not very Hα luminous in the most inner region, the central Hα emission is better observed with the higher angular resolution maps observed with SB2 and SB1 fibre bundles. The intensity maps computed from [N II] and [S II] emission lines are quite similar between them and the Hα intensitymap. They show a centrally peaked emission in addition to the emission connecting two bright Hα regions in th NE and SW directions.

Velocity field

Furthermore the velocity maps associated with each emission line are computed for the three different fibre bundles (see Fig. 9.24, 9.25 and 9.26). The derived velocity maps are quite similar between them, showing the basic spider pattern although highly distorted in the nuclear region and at the positions of the spiral arms in this galaxy indicating the presence of non-circular motions. The main characterisctics of these maps and the kinematical analysis developed with them are discussed in § 9.4.

The velocity dispersion

The fitted widths obtained in the Gaussian fitting procedure of the Hα emission line can be used to compute the velocity dispersion associated with the Hα ionized gas. We are interested in the dispersion due to the turbulent (non-thermal) motions of the gas ($\sigma_{\rm nt}$). We need to extract from the H_α emission line profile the contribution from other effects which help to broaden the observed line shape. These are the natural H_α emission line broadening ($\sigma_{\rm nat}$), thermal broadening ($\sigma_{\rm th}$) and instrumental broadening ($\sigma_{\rm inst}$). The natural Hα emission line broadening is ~ 3 kms^{-1} and the estimated thermal broadening is 9.1 kms^{-1}, assuming a temperature of 10^4K in the Hα emission regions. We derive estimations of the instrumental broadening of 85 kms^{-1}, 55 kms^{-1} and 47 kms^{-1} for SB3, SB2 and SB1 fiber bundles respectively. These components were substracted in quadrature from each point of the observed velocity dispersion map, $\sigma_{\rm nt} = (\sigma^2_{\rm obs} - \sigma^2_{\rm nat} - \sigma^2_{\rm th} - \sigma^2_{\rm inst})^{1/2}$. In this way we obtained the new velocity dispersion map due to the non-thermal motions of the ionized gas (H_α) shwon in Fig. 9.27. The higher velocities dispersions of the ionized gas are located at the galactic centre, with values around 85 kms^{-1}. The possible correlations between the velocity dispersion and other computed maps will be discussed in next section.

9.3.3 Stellar component

Stellar distribution: absorption and continuum maps

The Na II λ5890 absorption line allows us to trace the stellar component in this galaxy. To compute the Na II absorption line map, we subtract the underlaying continuum by fitting a second degree polynomial to the points at the blue and red sides of the line in each spectrum. In the case of the Na II intensity map, we added the absorptions coming from the two gaussians components fitted resulting the absorption line maps shown in Fig. 9.28. The intermediate angular resolution (0.45$''$) fiber bundel SB2 shows better how the the stellar component in this galaxy is elongated with a position angle of $\sim$ 130° (north over east). Knapen 1995 obtained a K-band image of the inner 40$''$of NGC 4321 observing an inner stellar bar with approximatly similar position angle.

We also derive the continuum map near the absorption line integrating the second degree polynomial already fitted in a certain wavelength range near the absorption (see Fig. 9.29). The resulted maps also show the presence of the inner leading arms emerging almost from the very centre of the galaxy.

Velocity field

Furthermore the velocity map associated with the Na II absorption line is computed for the first time in this galaxy using the three possible INTEGRAL angular resolutions, although the maps observed with the SB2 and SB1 fiber bundles have lower signal-to-noise ratio (see Fig. 9.30). The stellar velocity map shows a complicated pattern and is very complicated to interpret. The isovelocities are very distorted in the central region of the galaxy probably due to the presence of the inner stellar structure.

9.4 Kinematics

9.4.1 Ionized gas rotation curve

The velocity field in the inner region of this galaxy (see Fig. 9.24) shows the standard spider pattern which indicates circular motions in a rotating disk. But at the same time the velocity field shows the effect of the non-circular motions (see Fig. 9.16(a)). The kinematical minor axis is highly curved at the centre of the galaxy and the isovelocity contours are deformed following the structure of the spiral arms.

We describe the circular motions in NGC 4321 deriving the rotation curve from the ionized gas (Hα) velocity fields. The deviations from the circular motions are discussed in section 9.4.2. We have determined the rotation curve of the galaxy using the velocity maps of the ionized gas $H\alpha$ derived from SB3, SB2 and SB1 INTEGRAL fiber bundles with scales of: $\sim$ 0.95$''$pixel^{-1}, 0.35$''$pixel^{-1} and 0.18$''$pixel^{-1}, respectively. These maps give the projected velocity along the line of sight in each position of the galaxy.

The rotation curve is derived following the procedure described by Begeman (1989), by fitting tilted rings to the observed velocity field. In this method, the galaxy is divided in concentric elliptical annuli where each annulus is characterized by the inclination angle (i), the position angle of the major axis (P.A), the rotational velocity (v_c), the systemic velocity of the galaxy (v_{sys}) and the coordinates of the centre of each annulus (x_c, y_c). These parameters are fitted in each annulus following a least squares algorithm which uses the expression:

$$v(x, y) = v_{sys} + v_c(R)cos(\theta)sin(i), \tag{9.1}$$

where v(x, y) is the observed radial velocity at the sky coordinates (x,y) in the sky-projected image of the galaxy, R is the deprojected galactocentric radius and θ is the azimuthal angle in the plane of the galaxy measured from the major axis. This angle is related to the parameters, i, P.A and (x_c, y_c) by:

$$cos(\theta) = \frac{-(x - x_c)sin(P.A) + (y - y_c)cos(\phi)}{R} \tag{9.2}$$

$$sin(\theta) = \frac{-(x - x_c)cos(P.A) - (y - y_c)sin(\phi)}{Rcos(i)} \tag{9.3}$$

We have used the task ROTCUR from the data reduction software package GIPSY (Groningen Image Processing SYstem) to develope this fitting procedure.

The parameters v_{sys}, (x_c, y_c) depends on the symmetry of the velocity field and are the same for each ring. The main difficulty found in the determination of the kinematic centre, is related with the reduced field of view available ($34'' \times 29''$ for SB3 fiber bundle) and the presence of not only circular motions in the galactic disk which distorted the spider pattern of the velocity field. In these conditions, it is not an easy task to determine the centre of symmetry. And for this reason, we attempt to find the position of the kinematic centre using the velocity map with lower angular resolution ($2.7''$) and higher field of view where the symmetry in the velocity field is easier to distinguised. Once we have determined the coordinates of the kinematic centre there, we use this position in the other two higher resolutions maps to determine the rotation curve at the most inner region of the galaxy.

Kinematical centre candidates

We try to find the position of the kinematic centre using three definitions for this centre. Firstly, we use the ring model method mentioned above, taking annuli of $6''$ width in the velocity field from SB3 fiber bundle. We fixed values for the heliocentric systemic velocity, v_{sys} = 1567 kms^{-1} (as the mean value derived from the Hα velocity map), inclination angle at i = 30° (from RC3) and position angle at 153° (derived from H I aperture synthesis observations in Knapen et al. (1993)). In this way we obtain the position of the centre (x_c, y_c) using Eq. 9.1. The mean value of (x_c, y_c) for the rings inside $15''$corresponds to the coordinates $12^h22^m54.91^s(\pm0.02^s)$ $15°49'18.97''(\pm0.3'')$, J2000. We name this position as the *rotating ring model kinematical centre* (**RRMKC**).

As a second attempt, we find the position of the centre of gravity in the velocity map of the ionized gas Hα for the SB3 fiber bundle. The kinematical centre should be at this position if the galaxy had only circular rotation motions in the galactic disk. We computed this position weighting the velocity value in each pixel with the distance to a point of reference. We name

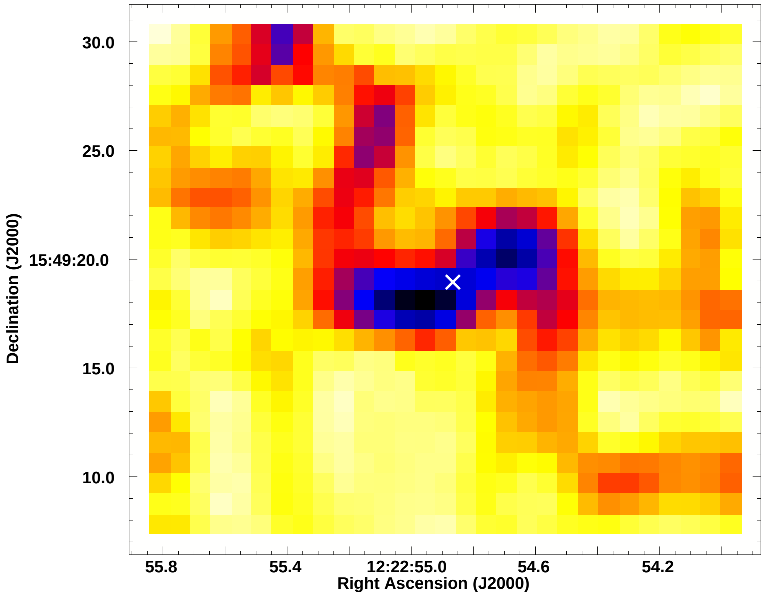

Figure 9.8— Hα "differential" velocity map for the SB3 fiber bundle with the position of the DVKC shown as a cross symbol.

this centre as the *centre of gravity kinematical centre* (**CGKC**). The resulting coordinates of this centre are $12^h22^m54.90^s(\pm0.04^s)$ $15°49'18.90''(\pm0.6'')$, J2000, not significantly different from the coordinates found for the RRMKC.

Lastly, to derive the kinematic centre we take the "differential" of the 2.7″ spatial resolution Hα velocity field using an own programm in IDL. In this program a new image is derived where each pixel is the average absolute difference between the corresponding pixel value in the velocity field and its inmediate neighbourhood (eight near pixels). In this way, we can located the regions where the velocities are changing more rapidly. In Fig. 9.8 the "differential" velocity map is shown, where a region with two maxima can be distinguished near the position of the optical nucleus. We take the mean position between these two maxima as the *differential velocity kinematical centre* (**DVKC**) whose coordinates are $12^h22^m54.87^s(\pm0.04^s)$ $15°49'18.95''(\pm0.6'')$, J2000.

The positions of the three defined centres coincide quite well, with differences of 0.6″ in the right ascention (less than 1 pixel in SB3 fiber bundle map and $\sim$ 2, $\sim$ 3 pixels for SB2 and SB1 fiber bundles maps respectively) and $\sim$ 0.07″ in declination. In Fig. 9.9 the three defined kinematic centres are located at the three different angular resolutions Hα velocity maps. The black contours overlaid corresponds to the contiuum image. The distance between the position of the maximum in the continuum and the positon of the defined kinematic centres is at most $\sim$ 0.7″ in the higher resolution map, being on the limit of our error in the astrometric calibration. We could say the kinematic centre coincide with the position of the optical nucleus within the errors. However, it is clear the optical nucleus has a position far from the isovelocity of the systemic velocity at the higher resolution map (see Fig. 9.9 for SB1 fiber bundle map).

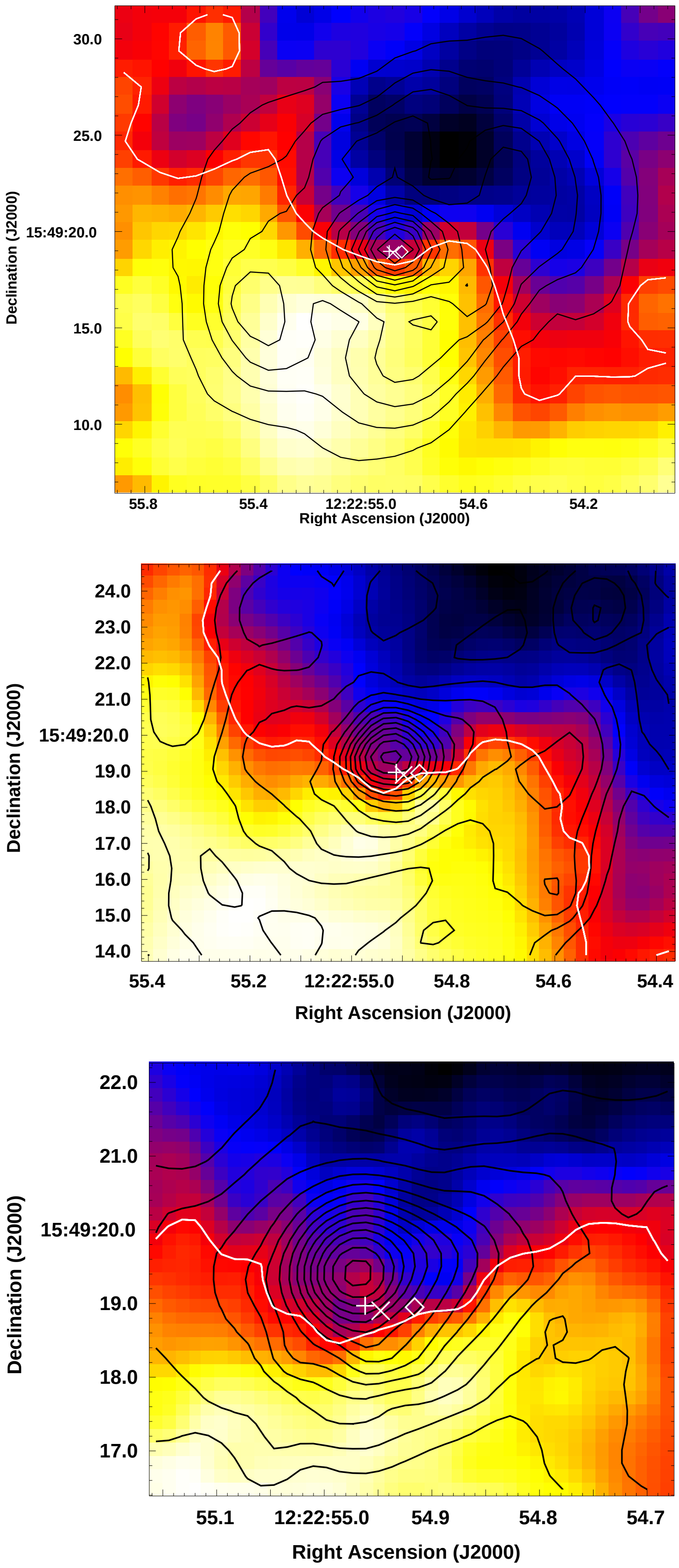

Figure 9.9— From top to bottom: SB3, SB2 and SB1 Hα velocity maps overlaid with the black contours from the continuum image. The white line indicates the isovelocity of the systemic velocity at 1567 kms^{-1}. The positions of the three kinematical centres defined are indicated in each angular resolution map. The plus symbol corresponds to RRMKC, the cross symbol to the CGKC and the diamond symbol to the DVKC.

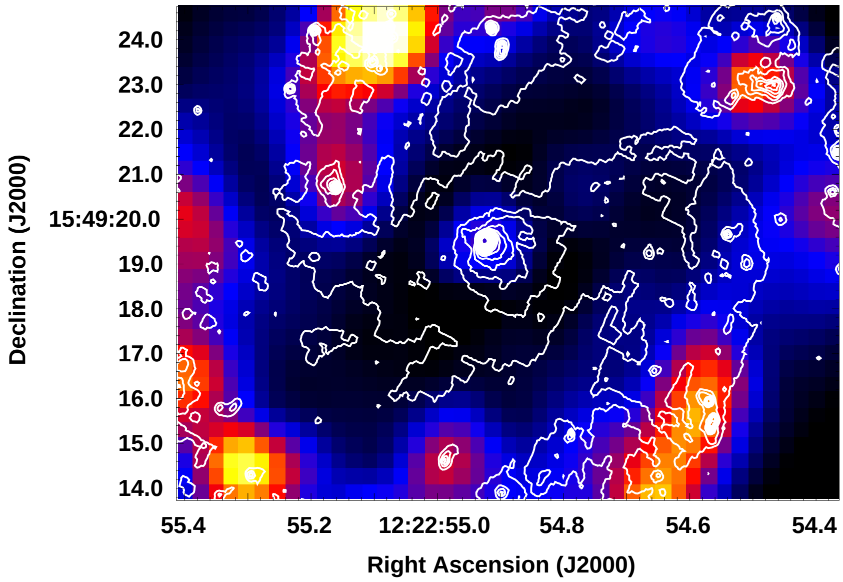

Figure 9.10— Hα intensity map (SB2 fiber bundle) with white contours overlaid from the HST/WFPC2 (F555W) image of NGC 4321.

Identification of the optical nucleus in the HST map

The optical nucleus appears located asymmetrically at the higher resolution continuum maps (see Fig. 9.9) and seem to be not coincident with the kinematical centres defined above. This asymmetry is lost when the lower resolution maps are used. The optical nucleus is situated in the "blue part" of the velocity field in a region of locally higher velocity as can be seen in Fig. 9.9 for the SB1 fiber bundle map.

The asymmetry of the optical nucleus and its asymmetric disposition with respect to the HII regions, can be seen better with the higher resolution continuum map provided by HST archive. In Fig. 9.10 the HST contours are overlaid with the image of the Hα intensity map obtained with SB2 fiber bundle.

Relation between different centres

The higher resolution maps (0.45″) are used to check if the centres defined in the intensity, continuum and velocity maps coincide between them. The Hα, NII and SII emission maximum are located at similar positions and at the same time coincide with the maximum in the continuum map. The position of the *ring rotating model kinematical centre* (RRMKC) is displaced about 0.7″to the south, with respect to the other mentioned centres. In Fig. 9.11 the asymetric optical nucleus from HST image is shown with the positions of different centres overlaid.

Rotating ring model around the RRMKC

We select the RRMKC as the kinematical centre to compute the rotation curve from the Hα velocitiy maps. The systemic velocity was obtained from the 2.7″ resolution velocity map (SB3) using rings of width 6″and separated 3″. The centre position was fixed to the value of the RRMKC

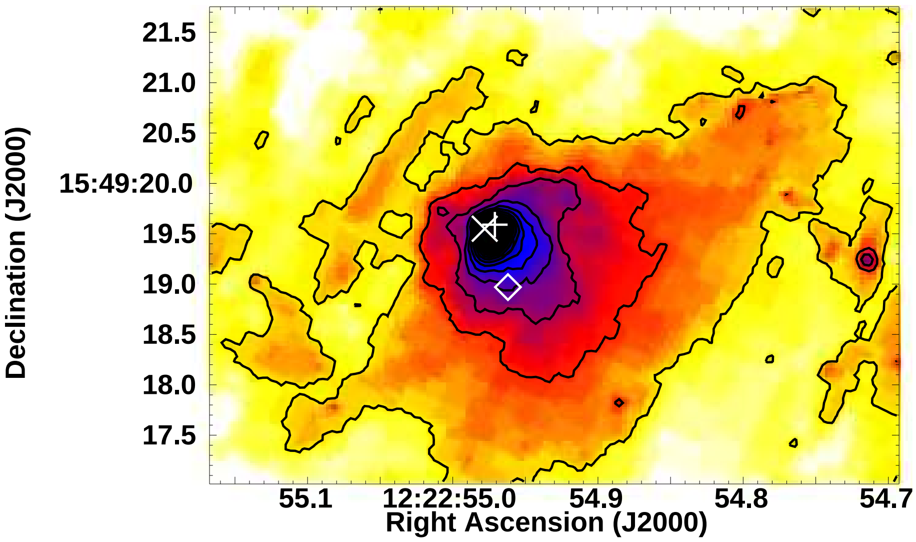

Figure 9.11— HST/WFPC2 (F555W) archive image of NGC 4321 with different position centres overlaid. The plus and the cross symbols represent the maximum in the Hα and continuum emission respectively. The diamond symbol is situated at the position of the kinematical centre defined as the RRMKC.

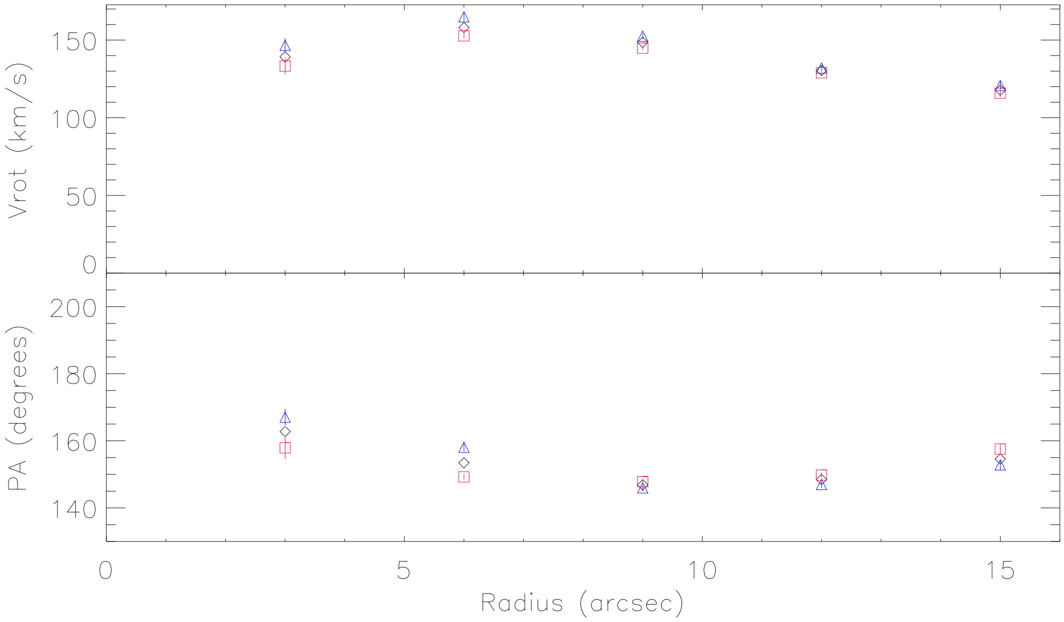

Figure 9.12— Hα rotation curve of the disc of NGC 4321, for the approaching (blue symbols) and receding (red symbols) sides of the galaxy separately. In black symbols the average rotation curve is shown. The agreement between both sides shows the symmetry of the velocity field and the reliability of the rotation center.

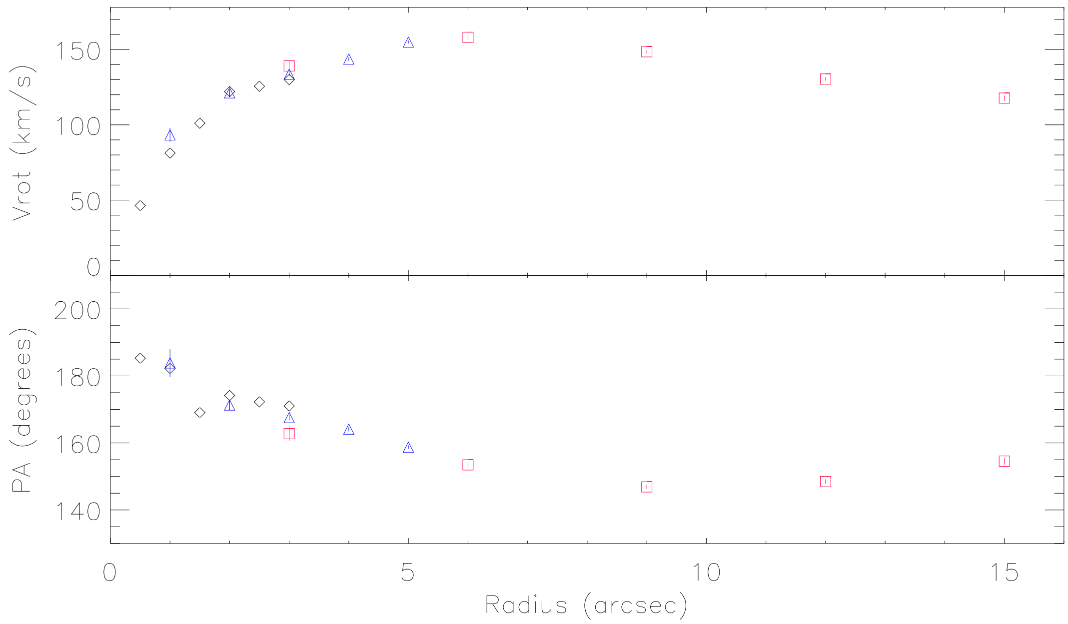

Figure 9.13— Hα rotation curve of the inner disc of NGC 4321 derived up to 15″ (1.2 kpc) from the galactic centre. The rotation curve was obtained by fitting tilted rings to the observed velocity fields of different angular resolutions, using the RRMKC as the kinematical centre and fixing the systemtic velocity at 1567 kms^{-1}

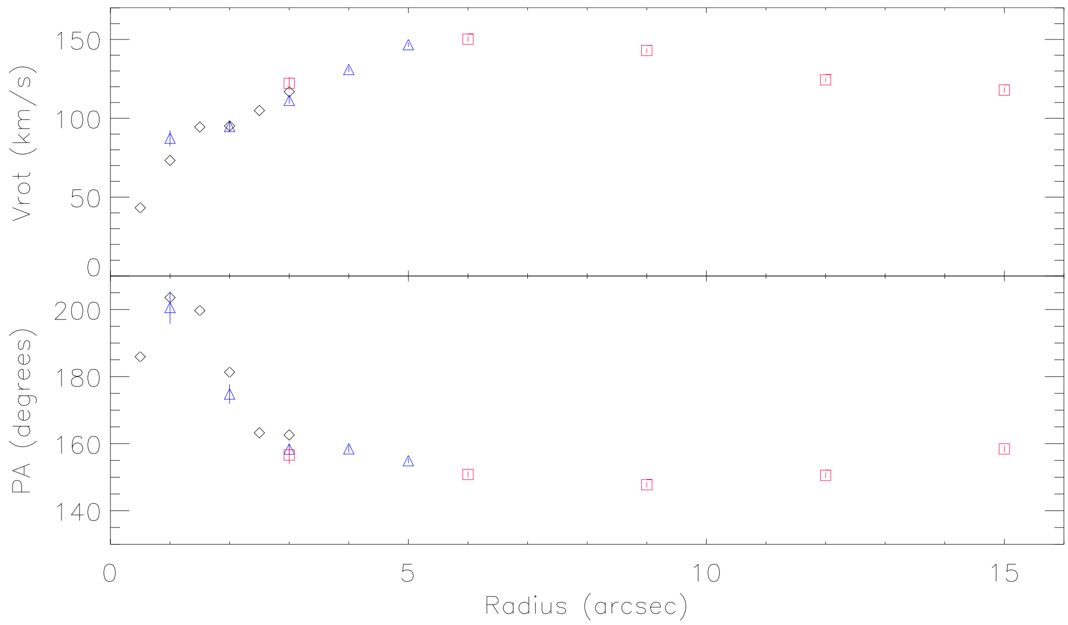

Figure 9.14— NII rotation curve of the inner disc of NGC 4321 derived up to 15″ (1.2 kpc) from the galactic centre. The rotation curve was obtained by fitting tilted rings to the observed velocity fields at different angular resolutions, using the RRMKC as the kinematical centre and fixing the systemic velocity at 1567 kms^{-1}.

and the inclination and position angle were fixed to the same values used to derive the kinematical centre ($i = 30°$, P.A $= 153°$). The mean systemic velocity (in the helilocentric system of reference) in all the rings out to 15″is 1566±0.8 kms^{-1}, where the error is the mean value of the corresponding errors in each ring. This value is slightly lower compared to the determination by Knapen et al. (1993) where a systemic velocity of $v_{sys} = 1570.8 \pm 0.8$ kms^{-1} is derived from H I aperture synthesis observations.

We test whether the rotation centre and the systemic velocity are well determined computing the rotation curves for the receding and approaching halves of the galaxy using the rotation centre and the systemic velocity found above. We can see in Fig. 9.12 the coincidence of the velocity values for both sides indicating the symmetry of the velocity field and the validity of the values for the kinematical centre position and the systemic velocity.

The rotation curve in the inner parts of the galaxy is determined with the higher resolution velocity maps obtain from SB2 and SB1 fiber bundles observations, and using rings of widths 2″ and 1″ respectively. In this case, we determine the rotation curve out to a radius of 5″ and 3″ with data points spaced 1″ and 0.5″ respectively. Fig. 9.13 displays the fitted values for the major axis position angle (P.A) and the circular velocity (v_c) obtained where we fixed the rotation centre at the position of the RRMKC, the inclination angle at 30° and the systemic heliocentric velocity at 1566 kms^{-1}.

The position angle (P.A) keeps a constant value around $151° \pm 3°$ for radii over 6″ (similar to the values found by Knapen et al. (2000) and Knapen et al. (1993)), while this value increases at radii near to the galactic centre due to the lack of symmetry and presence of non-circular motions there. The computed rotation curve is quite similar to the rotation curve obtained by Knapen et al. (2000) from the smooth Hα velocity map (4.6″ × 3.6″). The observed Hα rotation curve shows a steep rise in the rotation velocity, reaching $\sim$ 130 kms^{-1} in 3″ (249 pc), indicating a high concentration of mass at the galactic centre. The rotation curve reaches a local maximum of $\sim$ 160 kms^{-1} at a radius of $\sim$ 6″, coinciding approximately with the radius below which the major axis position angle starts increasing.

The fitted parameters (P.A and v_c) are not significantly different from the values found above, if the other two positions for the kinematical centre (CGKC, DVKC) are chosen. Moreover we check the shape of the rotation curve if the optical nucleus in each angular resolution map is chosen as the kinematic centre. In Fig. 9.15 we plot the fitted parameters showing similar values for the circular velocity and P.A for radii over 2″.

Furthermore, we derive the rotation curve from the NII and SII velocity maps using the same procedure described above. The rotation centre is fixed at the position of the RRMKC, the systemic velocity is fixed at 1567 kms^{-1} and the fitted values for the position angle and the circular velocity are shown in Fig. 9.14.

9.4.2 Residual velocities

Deviations from the circular motions in the ionized gas are seen directly in the observed velocity field. The isovelocities are distorted due to the streaming motions of the gas in the spiral arms. The non-circular motions within the galactic disk can be investigated computing a residual velocity map. After the mean rotation curve has been derived, we can make a two-dimensional projection of this curve and then subtract it from the observed velocity field. The model velocity field is derived from the rotation curve where each point is obtained avering the complete velocity information within a certain radial range. This two-dimensional projection could contain contributions from

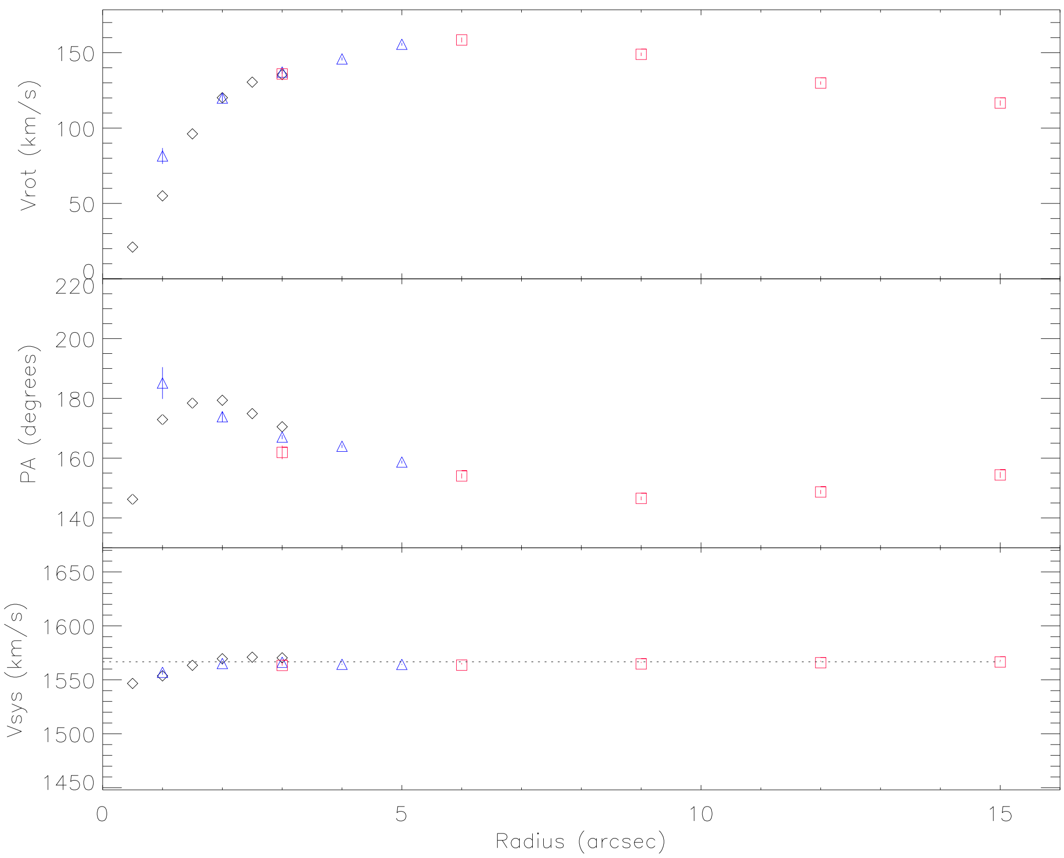

Figure 9.15— Hα rotation curve of the inner disc of NGC 4321 derived up to 15″ (1.2 kpc) from the galactic centre. The rotation curve was obtained by fitting tilted rings to the observed velocity fields of different angular resolutions, using the the position of the optical nucleus in each angular resolution map as the kinematical centre and leaving the systemic velocity as a free parameter.

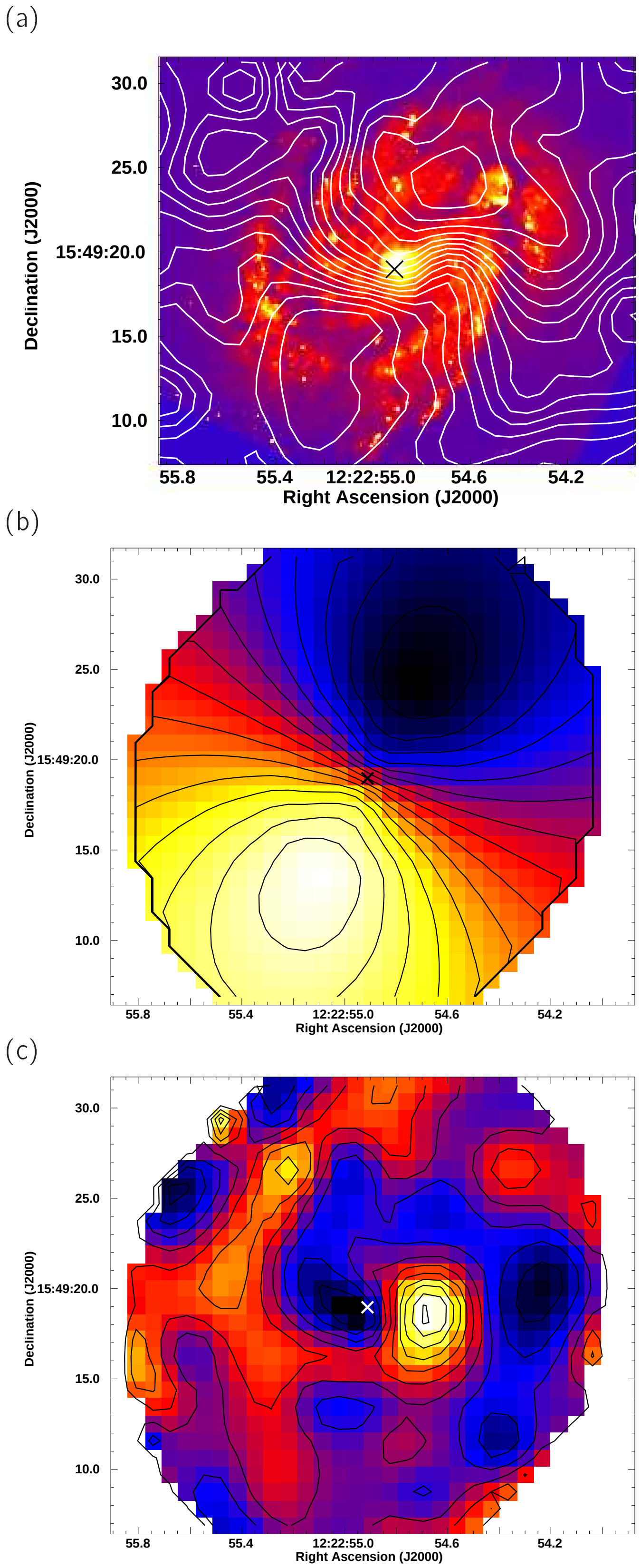

Figure 9.16— (a) HST/WFPC2 (F555W) image of NGC 4321 with white contours of Hα velocity field overlaid. The position of the kinematical centre RRMKC is shown as a cross symbol. (b) Model velocity map of NGC 4321, obtained from the Hα rotation curve of the galaxy shown in Fig. 9.13 but fixing the major axis position angle at 153° (see text for details). Contours levels are 1488-1648 kms^{-1} in steps of 10 kms^{-1}. (c) Map of residual velocities of NGC 4321 for the 2.7″resolution, derived by subtracting the model velocity field (b) from the observed velocity map (white contours in (a)). Contours levels are -29-41 kms^{-1} in steps of 7 kms^{-1}.

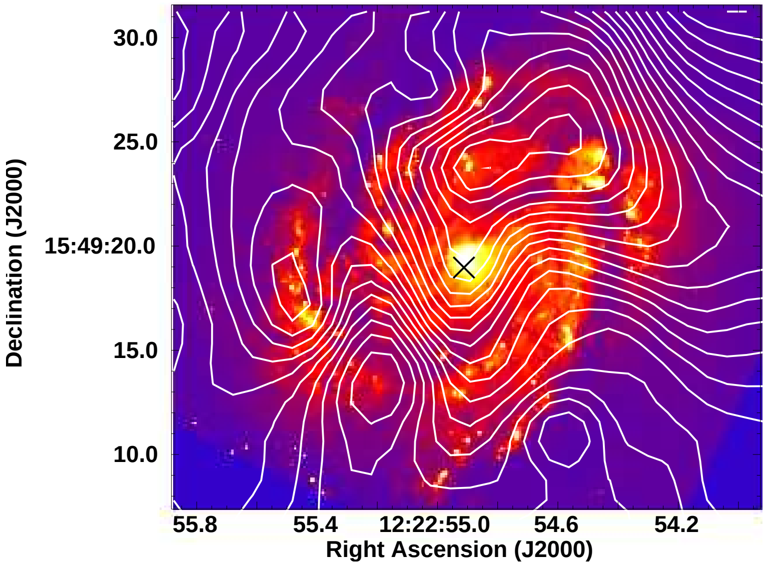

Figure 9.17— HST/WFPC2 (F555W) image of NGC 4321 with white contours of the stellar velocity field overlaid. The position of the kinematical centre RRMKC is shown as a cross symbol.

the non-circular motions which will therefore not appear to their full extent in the residual velocity map. In order to avoid the effect of this problem we use a modified version of the rotation curve in this analysis. We have fixed the major axis position angle at a value of 153° instead leaving this parameter as a free parameter in the rotation curve fitting. In this way, the model velocity field is less influenced by the non-circular motions.

The two-dimensional projection of the rotation curve is displayed in Fig. 9.16 (b). The residual velocity map for NGC 4321, shown in Fig. 9.16 (c), has been computed from the 2.7″resolution velocity map. The Hα residual velocity field confirms that regions of excess residual velocity are related to the inner spiral arms in the galaxy. Values of maximum (41 kms^{-1}) and minimum (-29 kms^{-1}) residual velocities are found at the position of the incoming spiral arms.

9.4.3 Velocity dispersion

The velocity dispersion maps for the three fiber bundles have been computed in the way explained in Section 9.3.2, using the width of the gaussian fit to the Hα emission line. The velocity dispersion is corrected for the instrumental, thermal and natural broadening. The non-thermal velocity dispersion for the circumnuclear region in NGC 4321 is shown in Fig. 9.27. The central Hα emission in this galaxy corresponds with the higher non-thermal velocity dispersion, with values of $\sim$ 80 kms^{-1}. Furthermore in the NE region, where various HII regions are located, values of $\sim$ 50 kms^{-1} are found for the velocity dispersion. We are studying the possible correlations between the Hα intensity, residual velocity and non-thermal velocity dispersion profiles along the most inner spiral arms.

9.4.4 Stellar velocity field

The stellar velocity field has been derived for the first time in this galaxy from the absorption Na II line. This velocity field shows some differences and similitudes when compared with the ionized gas one. The lower resolution stellar velocity map shows clearly two maxima not present in the ionized gas velocity field (see Fig. 9.30). The stellar isovelocities seen in Fig. 9.30 for the SB2 fiber bundle are extremely curved in the inner region of the galaxy near the galactic center probably related with the presence of another rotationg system. However, there are similitudes between both velocity fields (stellar and ionized gas) related with the distorsions produced in the velocity pattern by the spiral structure in this galaxy as can be seen in Fig. 9.17 where the stellar velocitiy field in white contours in overlaid with the HST image.

The kinematical centre candidate RRMKC derived from the ionized gas velocity field seems to be well located in the stellar velocity field to derive the circular motions (see Fig. 9.17), but we can not say this is the best position due to the complicated stellar kinematics.

Bidimensional spectroscopy studies have shown us how different could be the ionized gas and stellar velocity fields. And some questions arise from these observations: why the stellar velocity map is so distorted? Is the presence of the two maxima in the velocity field related with the presence of another kinematic system? or with a possible merger? How does the rotation curve look like in the inner region of a galaxy? Which is the true rotation curve?

9.5 Summary and conclusions

The 2D spectroscopy with optical fiber allow us to obtain simultaneously spatial and spectral information for extended objects. We have applied this technique to the study of the nuclear and circumnuclear region in NGC 4321 galaxy. The observations were made with INTEGRAL, a fiber based system operating at the WHT. We present 2D spectroscopy of this galaxy obtained at the three possible angular resolutions (2.7″, 0.9″and 0.45″). In the observed spectral range (5790 - 6900 Å) we are able to identify Hα, [N II] $\lambda\lambda$ 6548, 6583 and [S II] $\lambda\lambda$6716, 6731 emission lines. Furthermore the Na II λ5890 absorption line is observed. These observations allows us to computed intensity, continuum and veloctiy maps.

The kinematical study derived from the computed velocity maps can be summarized as follows:

- The Hα velocity field in the inner region of this galaxy shows the basic spider pattern which indicates circular motions in a rotating disk. But at the same time the velocity field shows the effect of the non-circular motions. We can see a curved kinematical minor axis indicating probably the presence of another kinematic system. Furthermore the isovelocity contours are deformed following the structure of the spiral arms.

- The position of the optical nucleus in the continuum map is coincident with the position of the kinematical centre for the lower resolution map. Nevertheless the optical nucleus appears located asymmetrically at the higher resolution continuum maps and seems to be not coincident with the kinematical centres defined. The optical nucleus appears located in the "blue part" of the velocity field and is located in a region of locally higher velocity.

- We have derived the Hα rotation curve out to 15″using the three available INTEGRAL angular resolutions. This curve shows a steep rise in the rotation velocity, reaching almost 150 kms^{-1} in 5″. Furthermore residual velocity maps have been derived to study the presence of non-circular motions showing higher absolute values at the positions ot the inner incoming spiral arms.

- The stellar velocity field derived from the Na absorption line is quite complicated and not easy to interpret. The lower resolution stellar velocity map shows clearly two maxima not present in the ionized gas velocity field. The higher resolutions velocity maps shows a dramatic difference between the stellar and ionized gas velocity field, with the stellar veloticity map extremely distorted in its inner region. However, there are similitudes between both velocity fields (ionized gas and stellar) related with the distorsions produced in the velocity field by the spiral structure in this galaxy.

Table 9.1— Gaussian fits to the Hα and [N II] λ6583 Å emission lines profiles. In each column the parameters for the two emission lines are shown respectively.

Fiber #	c[a]	Δc[b]	w[c]	Δw[d]	I[e]	ΔI[f]
53	6596.9 / 6617.6	0.01 / 0.05	3.1 / 3.4	0.03 / 0.13	1395.0 / 276.7	9.8 / 9.0
69	6597.0 / 6617.7	0.01 / 0.07	3.0 / 3.6	0.03 / 0.18	1956.0 / 346.4	15.7 / 13.9
70	6596.7 / 6617.5	0.01 / 0.08	3.1 / 3.5	0.03 / 0.20	1795.0 / 300.5	15.1 / 13.9
80	6598.2 / 6618.9	0.03 / 0.06	3.1 / 4.0	0.08 / 0.17	352.7 / 203.0	7.5 / 6.4
81	6597.6 / 6618.4	0.02 / 0.05	3.2 / 3.7	0.06 / 0.13	506.7 / 255.0	7.8 / 7.1
83	6596.9 / 6617.7	0.01 / 0.06	3.0 / 3.6	0.03 / 0.16	1787.0 / 386.8	14.5 / 13.0
84	6596.7 / 6617.5	0.01 / 0.07	3.1 / 3.7	0.04 / 0.19	1754.0 / 369.7	17.8 / 15.4
85	6596.3 / 6617.1	0.02 / 0.07	3.3 / 3.8	0.04 / 0.18	1130.0 / 265.4	11.3 / 10.1
91	6598.5 / 6618.7	0.05 / 0.09	3.3 / 5.5	0.13 / 0.28	306.6 / 224.4	9.9 / 7.8
92	6597.9 / 6618.7	0.04 / 0.06	3.3 / 5.0	0.10 / 0.20	346.7 / 260.8	8.9 / 7.3
93	6597.3 / 6618.2	0.02 / 0.05	3.3 / 4.0	0.06 / 0.13	562.0 / 300.6	8.6 / 7.7
94	6597.0 / 6617.8	0.02 / 0.06	3.3 / 4.1	0.06 / 0.16	774.8 / 293.4	10.8 / 9.2
95	6596.4 / 6617.3	0.03 / 0.06	3.6 / 4.5	0.07 / 0.16	582.9 / 299.9	9.5 / 8.2
96	6596.1 / 6617.1	0.02 / 0.06	3.7 / 5.1	0.06 / 0.16	631.6 / 271.4	8.0 / 6.7
97	6595.8 / 6616.9	0.03 / 0.06	3.6 / 4.8	0.07 / 0.19	451.5 / 230.6	7.7 / 6.6
99	6598.4 / 6618.7	0.07 / 0.07	4.3 / 5.8	0.19 / 0.19	315.8 / 364.8	10.8 / 8.9
100	6598.6 / 6618.2	0.13 / 0.13	3.8 / 6.8	0.32 / 0.36	228.2 / 290.3	15.2 / 11.1
101	6597.8 / 6617.7	0.12 / 0.12	3.9 / 7.2	0.32 / 0.35	224.0 / 316.9	14.8 / 10.6
102	6597.1 / 6617.7	0.06 / 0.06	3.9 / 5.3	0.14 / 0.17	308.5 / 333.6	9.1 / 7.8
103	6596.5 / 6617.1	0.07 / 0.05	4.3 / 5.6	0.17 / 0.15	298.1 / 406.6	9.8 / 8.3
104	6596.0 / 6617.0	0.05 / 0.05	4.0 / 5.4	0.13 / 0.14	290.8 / 346.6	7.8 / 6.5
106	6597.3 / 6617.8	0.14 / 0.08	4.6 / 6.3	0.37 / 0.23	215.0 / 427.4	13.5 / 11.2
107	6596.7 / 6616.9	0.08 / 0.07	4.9 / 6.4	0.21 / 0.22	797.1 / 964.9	27.7 / 23.6
108	6596.4 / 6616.7	0.08 / 0.07	5.0 / 6.2	0.21 / 0.20	661.7 / 877.3	22.9 / 20.1
110	6596.6 / 6617.0	0.07 / 0.06	4.8 / 5.8	0.18 / 0.16	788.2 / 1002.0	23.5 / 20.8
112	6596.1 / 6616.4	0.06 / 0.07	4.1 / 6.1	0.16 / 0.21	395.0 / 408.8	12.5 / 10.1
113	6596.7 / 6617.4	0.07 / 0.06	4.4 / 5.2	0.16 / 0.15	252.4 / 322.8	8.0 / 7.2
114	6598.3 / 6618.8	0.08 / 0.05	5.1 / 5.6	0.39 / 0.27	221.3 / 373.3	10.1 / 9.2
116	6595.8 / 6616.5	0.08 / 0.06	4.0 / 5.3	0.20 / 0.16	240.9 / 365.5	9.5 / 8.1
117	6595.9 / 6616.3	0.04 / 0.06	3.8 / 4.9	0.10 / 0.17	475.4 / 315.5	9.9 / 8.6
118	6596.6 / 6617.0	0.04 / 0.06	4.0 / 5.0	0.09 / 0.18	502.4 / 295.6	9.2 / 7.9
119	6597.5 / 6618.1	0.04 / 0.06	3.8 / 4.8	0.10 / 0.17	339.7 / 237.1	7.4 / 6.4
120	6597.9 / 6618.6	0.04 / 0.06	3.8 / 4.5	0.11 / 0.14	293.5 / 242.1	7.1 / 6.2
121	6598.1 / 6618.8	0.06 / 0.06	4.0 / 5.4	0.17 / 0.18	344.1 / 359.7	11.0 / 9.1
123	6595.5 / 6616.4	0.04 / 0.07	3.6 / 4.5	0.11 / 0.20	331.7 / 210.3	8.0 / 7.0
124	6595.6 / 6616.1	0.03 / 0.07	3.5 / 4.6	0.07 / 0.19	364.7 / 175.1	6.4 / 5.5
125	6596.0 / 6616.5	0.03 / 0.07	3.6 / 4.9	0.07 / 0.19	555.1 / 239.9	9.2 / 7.6
126	6596.8 / 6617.4	0.04 / 0.06	4.0 / 4.8	0.10 / 0.17	358.4 / 229.3	7.3 / 6.4
128	6597.7 / 6618.5	0.02 / 0.05	3.3 / 4.1	0.05 / 0.13	726.9 / 291.5	8.6 / 7.4
129	6597.8 / 6618.4	0.02 / 0.06	3.1 / 4.5	0.05 / 0.16	758.4 / 305.4	10.3 / 8.4
136	6595.6 / 6616.2	0.02 / 0.06	3.3 / 3.8	0.05 / 0.15	571.3 / 205.0	7.4 / 6.7

[a] Gaussian center (Å) [b] Error in the Gaussian center (Å)
[c] Gaussian width (Å) [d] Error in the Gaussian width (Å)
[e] Gaussian intensity peak [f] Error in the Gaussian intensity peak

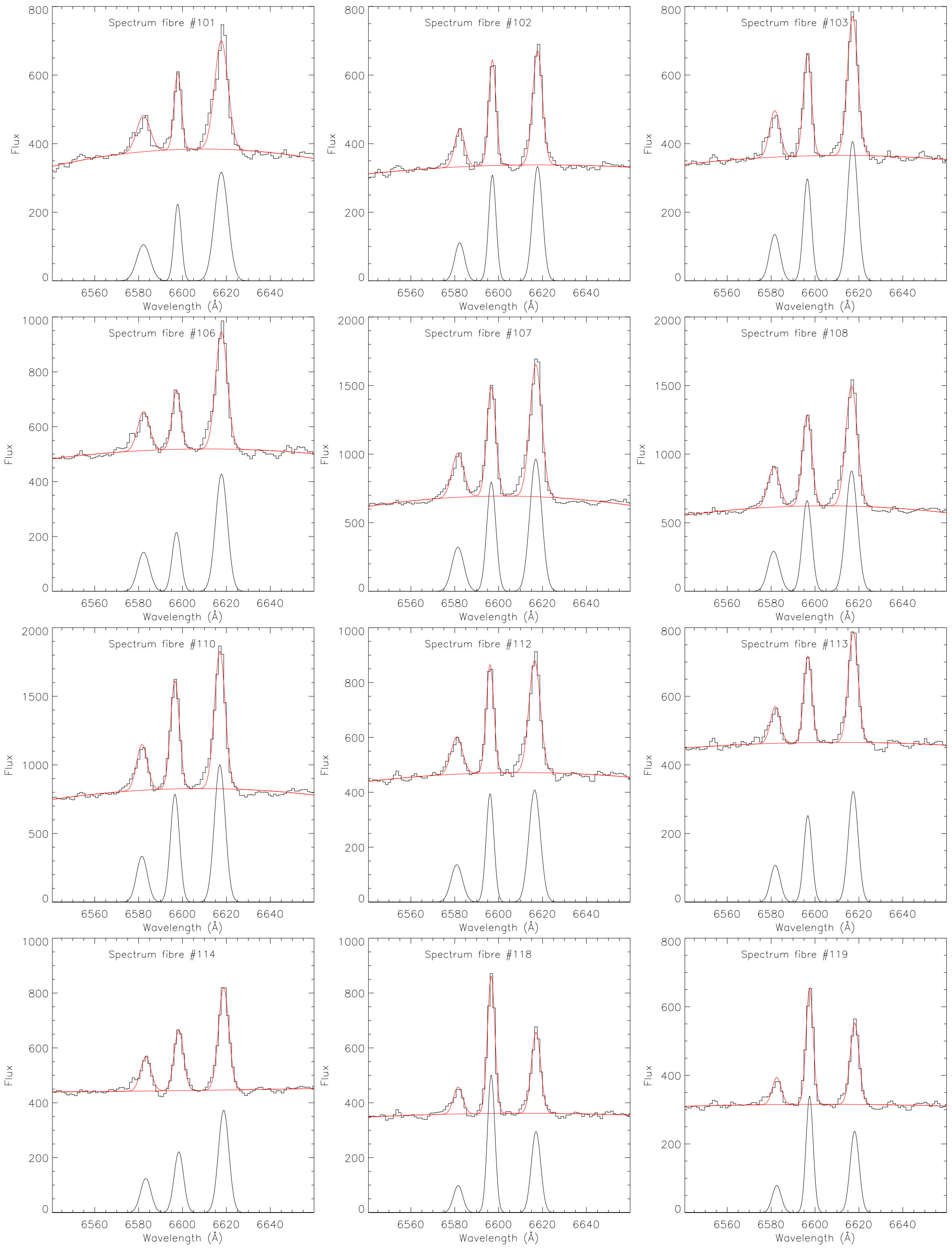

Figure 9.18— Gaussian fits to the Hα and [N II] λ6583 Å emission lines profiles. The fits to the fibres with higher signal-to-noise are shown.

Table 9.2— Gaussian fits to the [S II] λλ6716, 6731 Å emission line profiles. In each column the parameters for the two emission lines fitted are shown respectively.

Fiber #	c^a	Δc^b	w^c	Δw^d	I^e	ΔI^f
53	6751.4 / 6765.8	0.07 / 0.07	3.5 / 3.5	0.19 / 0.19	83.4 / 74.4	4.2 / 4.1
69	6751.3 / 6765.8	0.05 / 0.05	3.6 / 3.6	0.14 / 0.14	111.3 / 90.1	3.8 / 3.6
70	6751.1 / 6765.6	0.06 / 0.06	3.2 / 3.2	0.15 / 0.15	91.9 / 78.0	4.0 / 4.0
80	6752.6 / 6767.1	0.09 / 0.09	3.5 / 3.5	0.23 / 0.23	53.7 / 46.0	3.5 / 3.4
81	6752.2 / 6766.6	0.09 / 0.09	3.7 / 3.7	0.25 / 0.25	70.6 / 66.0	4.4 / 4.4
83	6751.5 / 6765.9	0.06 / 0.06	3.0 / 3.0	0.15 / 0.15	112.6 / 93.0	5.6 / 5.2
84	6751.3 / 6765.8	0.06 / 0.06	3.5 / 3.5	0.18 / 0.18	113.5 / 93.9	5.3 / 5.0
85	6750.6 / 6765.1	0.07 / 0.07	3.8 / 3.8	0.17 / 0.17	86.4 / 64.3	3.8 / 3.6
91	6752.4 / 6766.9	0.18 / 0.18	5.6 / 5.6	0.63 / 0.63	55.5 / 55.9	4.8 / 4.5
92	6752.2 / 6766.7	0.10 / 0.10	4.7 / 4.7	0.28 / 0.28	73.0 / 64.0	3.9 / 3.7
93	6751.9 / 6766.4	0.09 / 0.09	3.9 / 3.9	0.23 / 0.23	79.8 / 64.5	4.5 / 4.2
94	6751.3 / 6765.8	0.07 / 0.07	3.9 / 3.9	0.19 / 0.19	88.7 / 71.1	4.3 / 4.1
95	6751.1 / 6765.6	0.07 / 0.07	4.1 / 4.1	0.22 / 0.22	89.3 / 84.0	4.3 / 4.3
96	6750.6 / 6765.1	0.09 / 0.09	4.3 / 4.3	0.30 / 0.30	79.7 / 61.3	4.2 / 3.9
97	6750.5 / 6764.9	0.11 / 0.11	4.1 / 4.1	0.28 / 0.28	60.3 / 60.6	4.1 / 4.2
99	6752.6 / 6767.0	0.10 / 0.10	5.2 / 5.2	0.27 / 0.27	99.7 / 73.8	4.6 / 4.3
100	6752.4 / 6766.9	0.23 / 0.23	7.2 / 7.2	0.65 / 0.65	83.6 / 58.9	6.0 / 5.9
101	6751.6 / 6766.1	0.19 / 0.19	7.2 / 7.2	0.53 / 0.53	94.0 / 80.1	6.0 / 5.9
102	6751.4 / 6765.9	0.11 / 0.11	5.0 / 5.0	0.36 / 0.36	91.0 / 72.5	5.1 / 4.8
103	6751.0 / 6765.4	0.10 / 0.10	5.1 / 5.1	0.30 / 0.30	99.1 / 98.8	5.0 / 5.0
104	6750.6 / 6765.0	0.09 / 0.09	4.7 / 4.7	0.28 / 0.28	100.2 / 81.6	4.9 / 4.7
106	6751.7 / 6766.2	0.13 / 0.13	6.7 / 6.7	0.41 / 0.41	102.0 / 103.4	5.6 / 5.5
107	6750.5 / 6765.0	0.11 / 0.11	6.6 / 6.6	0.30 / 0.30	220.5 / 225.6	9.8 / 10.0
108	6750.3 / 6764.7	0.10 / 0.10	6.4 / 6.4	0.33 / 0.33	190.5 / 193.5	8.3 / 8.3
110	6750.6 / 6765.1	0.09 / 0.09	5.4 / 5.4	0.30 / 0.30	237.9 / 239.0	10.9 / 10.8
112	6750.0 / 6764.4	0.12 / 0.12	6.2 / 6.2	0.35 / 0.35	112.6 / 94.4	5.5 / 5.4
113	6751.3 / 6765.7	0.12 / 0.12	4.1 / 4.1	0.36 / 0.36	77.7 / 79.5	6.5 / 6.3
114	6752.6 / 6767.1	0.11 / 0.11	6.2 / 6.2	0.35 / 0.35	88.1 / 81.9	4.2 / 4.1
116	6750.2 / 6764.7	0.14 / 0.14	5.1 / 5.1	0.51 / 0.51	96.6 / 82.3	6.3 / 6.1
117	6749.9 / 6764.3	0.09 / 0.09	3.9 / 3.9	0.24 / 0.24	92.9 / 75.4	5.1 / 4.8
118	6750.6 / 6765.0	0.12 / 0.12	5.2 / 5.2	0.34 / 0.34	83.0 / 63.8	4.7 / 4.4
119	6751.9 / 6766.3	0.13 / 0.13	4.6 / 4.6	0.39 / 0.39	51.9 / 52.6	4.0 / 4.1
120	6752.5 / 6767.0	0.11 / 0.11	4.5 / 4.5	0.30 / 0.30	74.6 / 61.9	4.7 / 4.3
121	6752.8 / 6767.3	0.07 / 0.07	4.8 / 4.8	0.20 / 0.20	96.7 / 84.9	3.8 / 3.7
123	6750.1 / 6764.6	0.12 / 0.12	4.3 / 4.3	0.35 / 0.35	56.6 / 50.8	3.9 / 3.9
124	6749.5 / 6764.0	0.12 / 0.12	3.7 / 3.7	0.30 / 0.30	49.3 / 41.7	3.9 / 3.7
125	6750.3 / 6764.7	0.09 / 0.09	4.2 / 4.2	0.24 / 0.24	59.5 / 63.2	3.5 / 3.6
126	6751.4 / 6765.9	0.13 / 0.13	4.6 / 4.6	0.35 / 0.35	57.0 / 57.1	4.3 / 4.3
128	6752.3 / 6766.7	0.06 / 0.06	3.7 / 3.7	0.11 / 0.11	85.0 / 78.5	3.7 / 3.4
129	6752.3 / 6766.8	0.08 / 0.08	4.3 / 4.3	0.27 / 0.27	81.4 / 67.5	3.8 / 3.5
136	6750.0 / 6764.5	0.10 / 0.10	3.6 / 3.6	0.27 / 0.27	57.7 / 47.3	4.0 / 3.8

[a] Gaussian center (Å) [b] Error in the Gaussian center (Å)
[c] Gaussian width (Å) [d] Error in the Gaussian width (Å)
[e] Gaussian intensity peak [f] Error in the Gaussian intensity peak

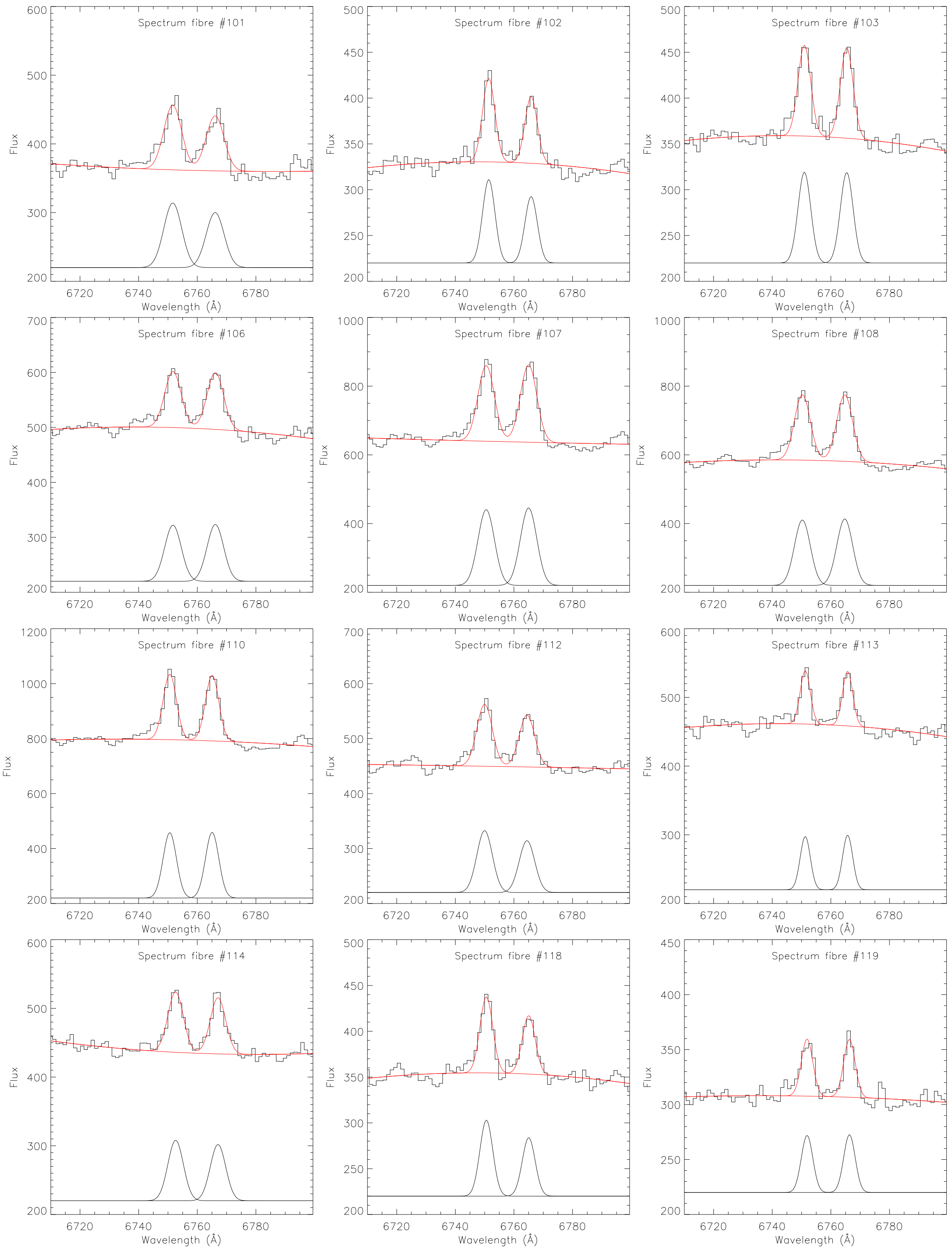

Figure 9.19— Gaussian fits to the [S II] $\lambda\lambda$6716, 6731 Å emission line profiles. The fits to the fibres with higher signal-to-noise are shown.

Table 9.3— Gaussian fits to the Na II λ5890 Å absorption line profiles. In each column the parameters for the two gaussians components are shown.

Fiber #	c^a	Δc^b	w^c	Δw^d	I^e	ΔI^f
53	5919.4 / 5925.4	0.40 / 0.40	5.6 / 5.6	0.73 / 0.73	-28.6 / -21.5	3.7 / 2.8
69	5919.4 / 5925.4	0.43 / 0.43	5.3 / 5.3	0.85 / 0.85	-34.5 / -26.0	5.3 / 4.0
70	5919.5 / 5925.5	0.45 / 0.45	5.5 / 5.5	0.84 / 0.84	-28.4 / -21.4	4.2 / 3.2
80	5920.2 / 5926.2	0.37 / 0.37	7.0 / 7.0	1.08 / 1.08	-32.8 / -24.7	4.0 / 3.0
81	5920.1 / 5926.1	0.34 / 0.34	7.8 / 7.8	1.14 / 1.14	-37.5 / -28.2	4.0 / 3.0
83	5919.4 / 5925.4	0.36 / 0.36	6.4 / 6.4	0.82 / 0.82	-39.1 / -29.4	4.4 / 3.3
84	5919.6 / 5925.6	0.51 / 0.51	6.3 / 6.3	1.11 / 1.11	-27.6 / -20.8	4.4 / 3.3
85	5919.7 / 5925.7	0.47 / 0.47	5.4 / 5.4	1.15 / 1.15	-26.0 / -19.5	4.5 / 3.4
91	5919.2 / 5925.2	0.37 / 0.37	7.3 / 7.3	1.05 / 1.05	-38.6 / -29.0	4.4 / 3.3
92	5919.3 / 5925.3	0.30 / 0.30	7.5 / 7.5	0.98 / 0.98	-48.9 / -36.8	4.8 / 3.6
93	5920.1 / 5926.1	0.27 / 0.27	6.2 / 6.2	0.76 / 0.76	-48.6 / -36.5	4.8 / 3.6
94	5920.0 / 5926.0	0.37 / 0.37	6.2 / 6.2	0.78 / 0.78	-42.3 / -31.8	4.6 / 3.5
95	5918.3 / 5924.3	0.47 / 0.47	7.5 / 7.5	1.18 / 1.18	-33.8 / -25.4	4.2 / 3.2
96	5918.3 / 5924.3	0.44 / 0.44	5.6 / 5.6	1.11 / 1.11	-34.7 / -26.1	5.4 / 4.1
97	5918.8 / 5924.8	0.41 / 0.41	5.7 / 5.7	1.15 / 1.15	-33.1 / -24.9	5.4 / 4.1
99	5919.7 / 5925.7	0.58 / 0.58	7.8 / 7.8	1.53 / 1.53	-24.9 / -18.7	4.0 / 3.0
100	5918.7 / 5924.7	0.45 / 0.45	11.2 / 11.2	1.52 / 1.52	-27.2 / -20.5	2.5 / 1.9
101	5918.5 / 5924.5	0.32 / 0.32	9.0 / 9.0	1.08 / 1.08	-49.8 / -37.4	4.2 / 3.1
102	5919.2 / 5925.2	0.31 / 0.31	8.6 / 8.6	1.12 / 1.12	-49.7 / -37.4	4.4 / 3.3
103	5918.7 / 5924.7	0.25 / 0.25	10.0 / 10.0	0.93 / 0.93	-60.6 / -45.6	3.7 / 2.8
104	5918.3 / 5924.3	0.30 / 0.30	8.9 / 8.9	1.03 / 1.03	-43.1 / -32.4	3.4 / 2.6
106	5918.9 / 5924.9	0.34 / 0.34	10.1 / 10.1	1.07 / 1.07	-48.3 / -36.4	3.6 / 2.7
107	5917.5 / 5923.5	0.25 / 0.25	13.2 / 13.2	0.73 / 0.73	-97.8 / -73.6	4.0 / 3.0
108	5917.6 / 5923.6	0.25 / 0.25	12.8 / 12.8	0.77 / 0.77	-82.4 / -62.0	3.5 / 2.7
110	5918.6 / 5924.6	0.32 / 0.32	13.5 / 13.5	1.06 / 1.06	-71.3 / -53.6	3.7 / 2.7
112	5918.7 / 5924.7	0.35 / 0.35	10.5 / 10.5	1.20 / 1.20	-47.5 / -35.7	3.5 / 2.6
113	5920.2 / 5926.2	0.30 / 0.30	6.8 / 6.8	0.93 / 0.93	-51.1 / -38.5	5.5 / 4.2
114	5919.7 / 5925.7	0.33 / 0.33	6.2 / 6.2	0.76 / 0.76	-46.7 / -35.1	5.0 / 3.8
116	5918.5 / 5924.5	0.38 / 0.38	10.2 / 10.2	1.21 / 1.21	-34.5 / -25.9	2.8 / 2.1
117	5918.6 / 5924.6	0.36 / 0.36	6.9 / 6.9	0.91 / 0.91	-41.8 / -31.4	4.5 / 3.4
118	5919.9 / 5925.9	0.26 / 0.26	5.4 / 5.4	0.46 / 0.46	-56.8 / -42.7	5.0 / 3.8
119	5919.5 / 5925.5	0.33 / 0.33	5.9 / 5.9	0.64 / 0.64	-38.6 / -29.1	4.0 / 3.0
120	5919.9 / 5925.9	0.38 / 0.38	5.9 / 5.9	0.79 / 0.79	-28.7 / -21.6	3.6 / 2.7
121	5919.9 / 5925.9	0.41 / 0.41	5.0 / 5.0	0.72 / 0.72	-27.2 / -20.4	3.8 / 2.9
123	5917.2 / 5923.2	0.36 / 0.36	11.6 / 11.6	1.02 / 1.02	-29.1 / -21.9	2.0 / 1.5
124	5918.3 / 5924.3	0.56 / 0.56	12.5 / 12.5	1.53 / 1.53	-22.8 / -17.1	2.2 / 1.6
125	5919.9 / 5925.9	0.35 / 0.35	9.4 / 9.4	2.21 / 2.21	-45.8 / -34.5	6.0 / 4.5
126	5919.9 / 5925.9	0.23 / 0.23	5.6 / 5.6	0.44 / 0.44	-54.5 / -41.0	4.0 / 3.0
128	5919.9 / 5925.9	0.51 / 0.51	6.6 / 6.6	1.22 / 1.22	-29.2 / -22.0	4.6 / 3.5
129	5919.9 / 5925.9	0.36 / 0.36	5.0 / 5.0	0.59 / 0.59	-29.1 / -21.9	3.7 / 2.8
136	5918.4 / 5924.4	0.36 / 0.36	4.9 / 4.9	0.81 / 0.81	-33.1 / -24.9	4.8 / 3.6

[a] Gaussian center (Å) [b] Error in the Gaussian center (Å)
[c] Gaussian width (Å) [d] Error in the Gaussian width (Å)
[e] Gaussian intensity peak [f] Error in the Gaussian intensity peak

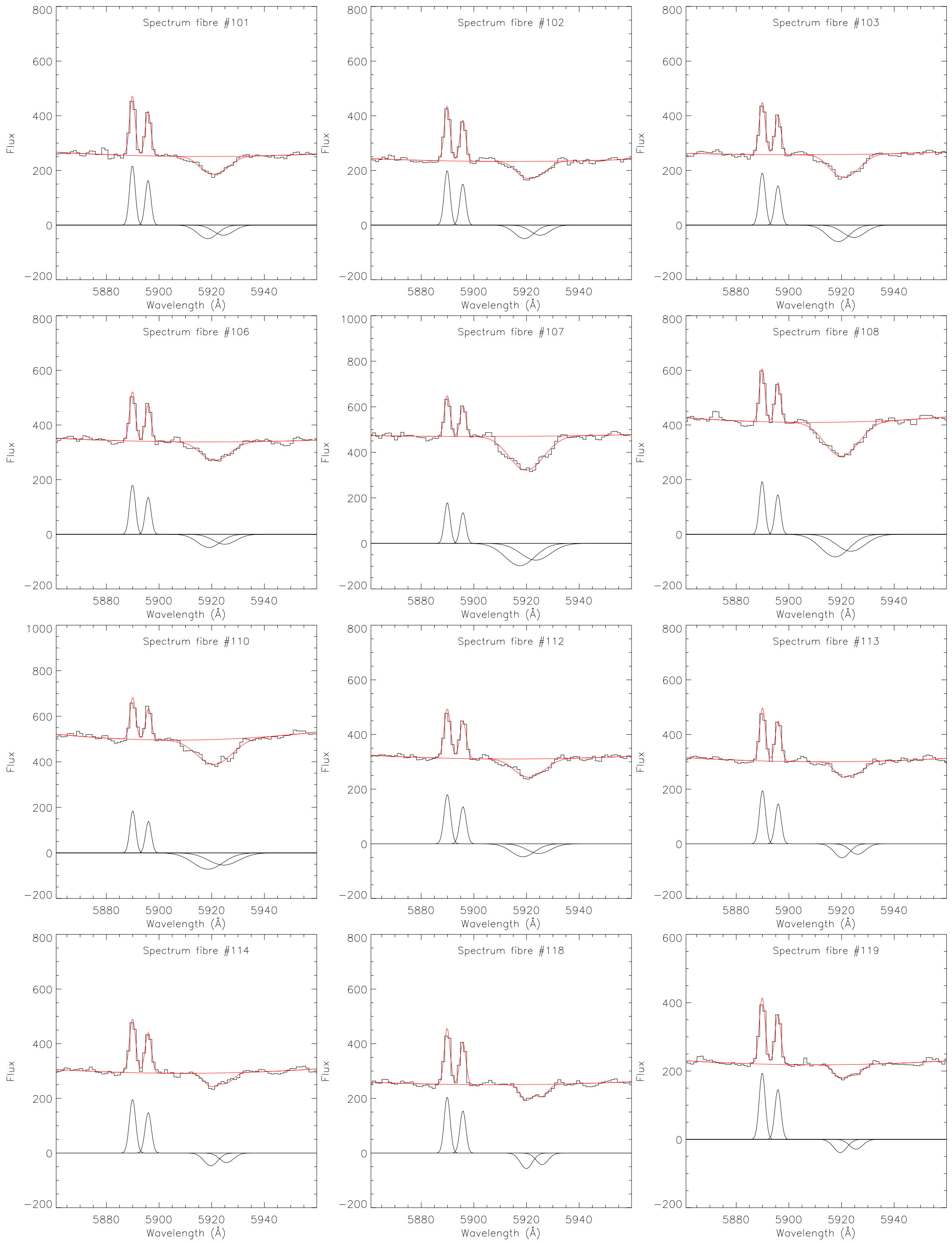

Figure 9.20— Gaussian fits to the Na II λ5890 AA absorption line profiles. The fits to the fibres with higher signal-to-noise are shown.

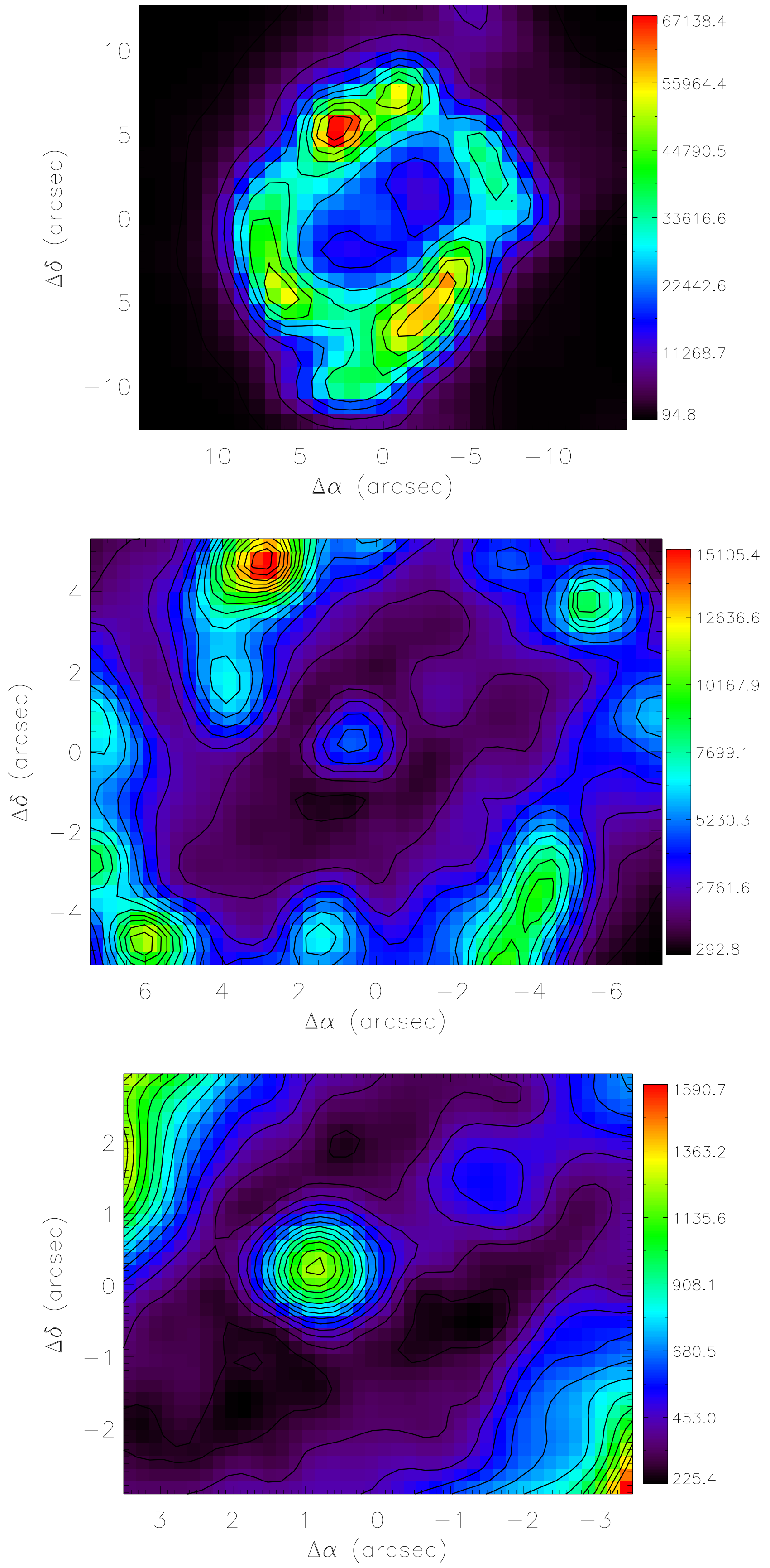

Figure 9.21— From top to bottom: SB3, SB2 and SB1 Hα intensity maps.

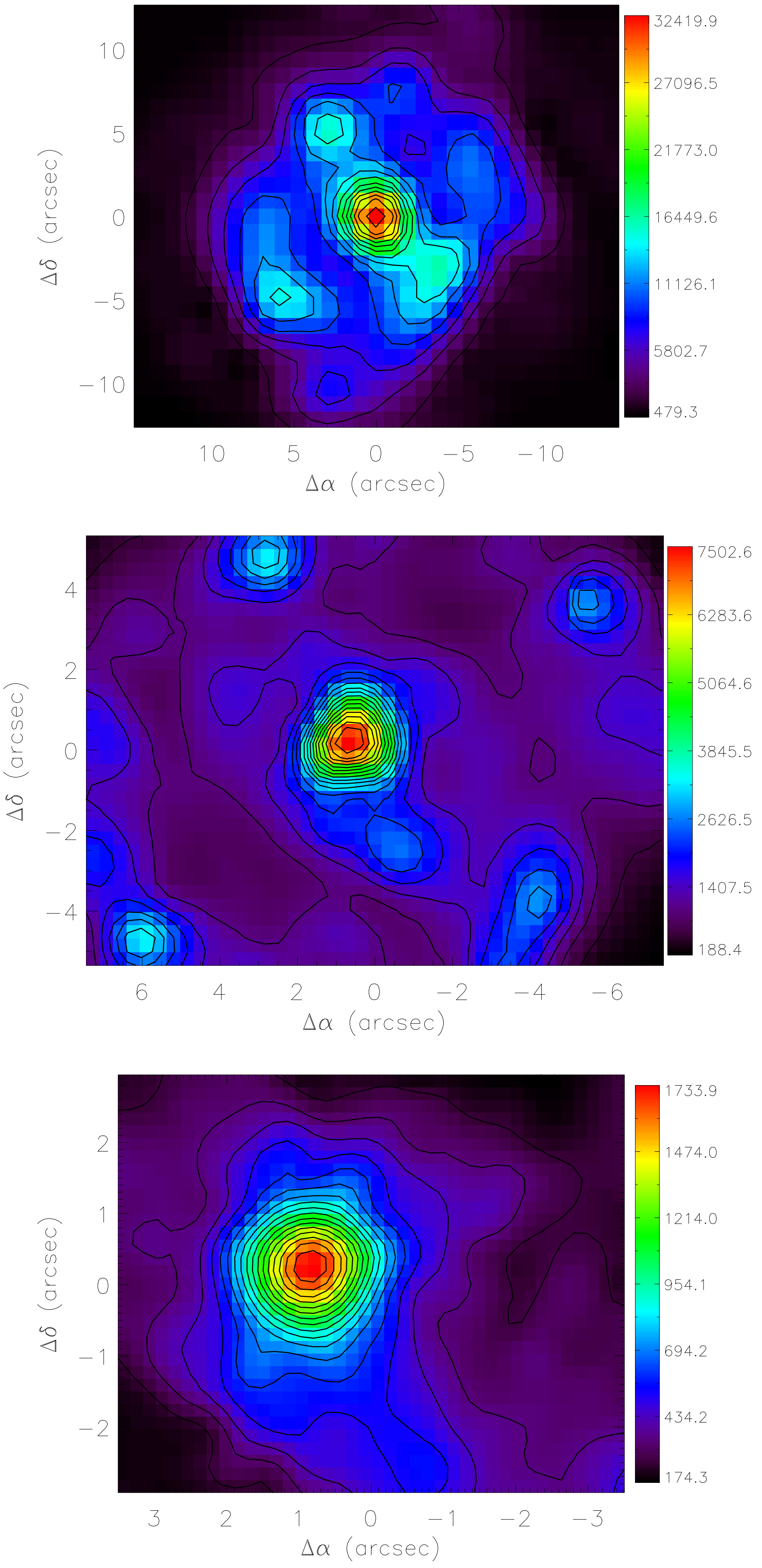

Figure 9.22— From top to bottom: SB3, SB2 and SB1 [NII] intensity maps.

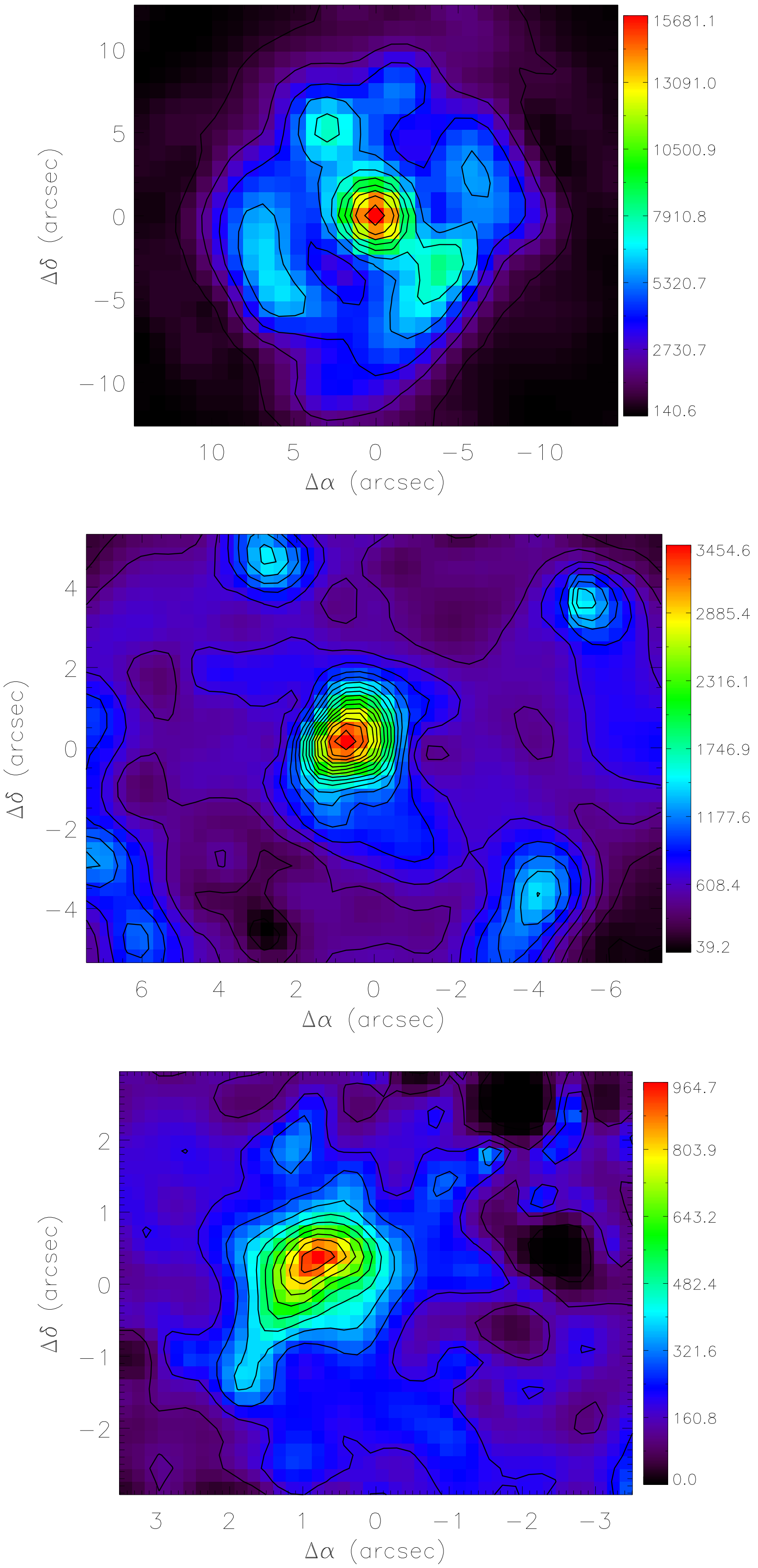

Figure 9.23— From top to bottom: SB3, SB2 and SB1 [SII] intensity maps.

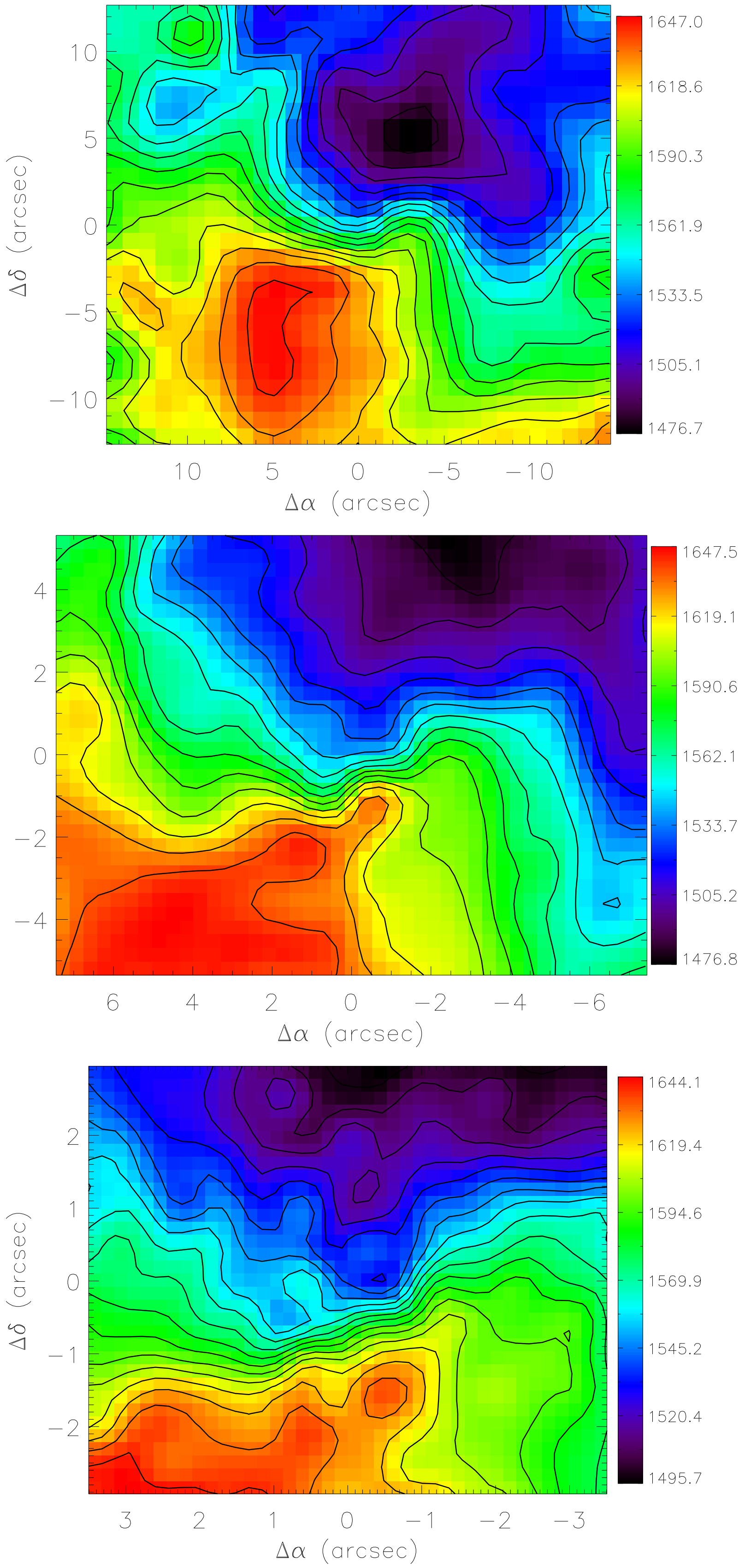

Figure 9.24— From top to bottom: SB3, SB2 and SB1 velocity maps derived from Hα emission line. The scale unit is kms^{-1}.

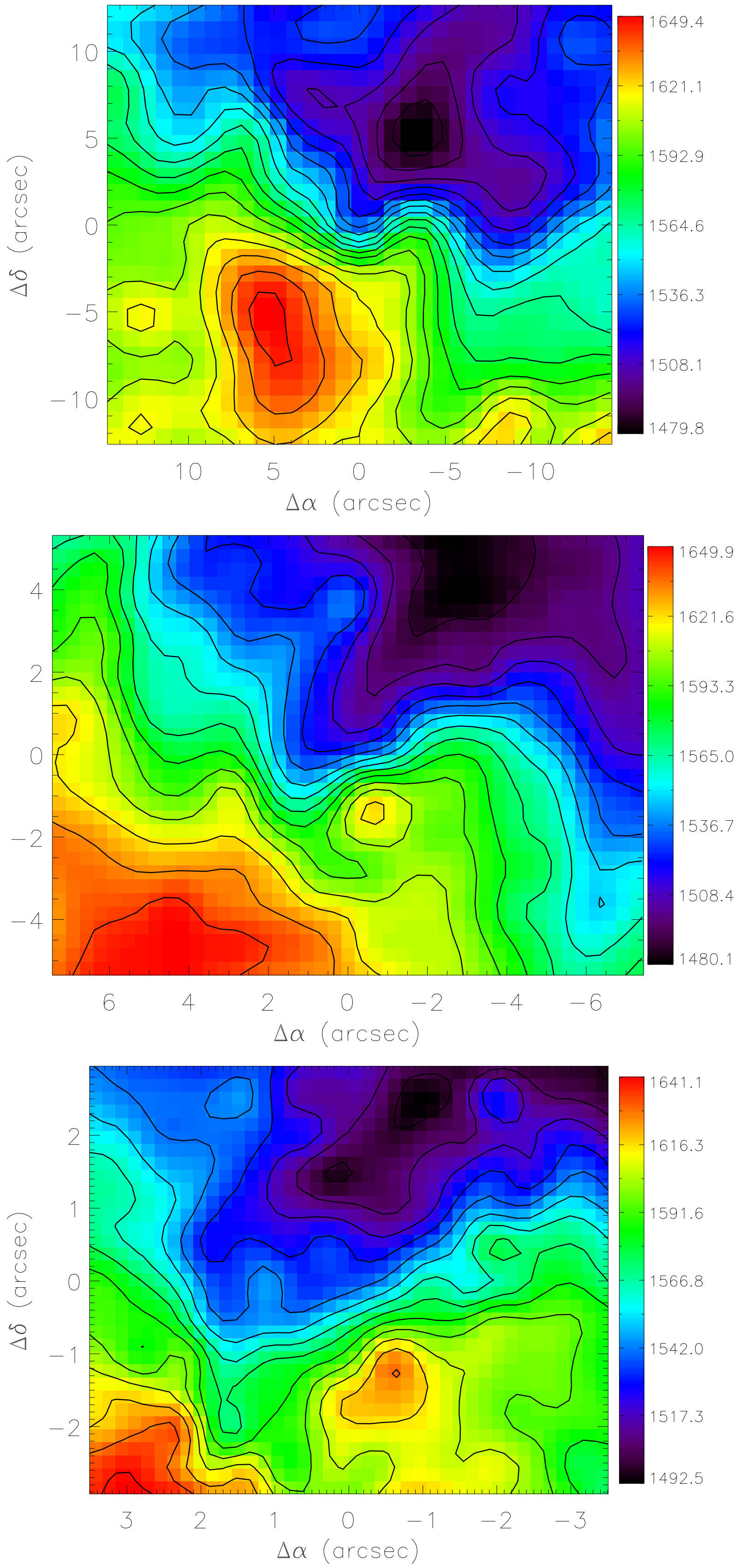

Figure 9.25— From top to bottom: SB3, SB2 and SB1 velocity maps derived from [NII] emission lines. The scale unit is $\mathrm{km s^{-1}}$.

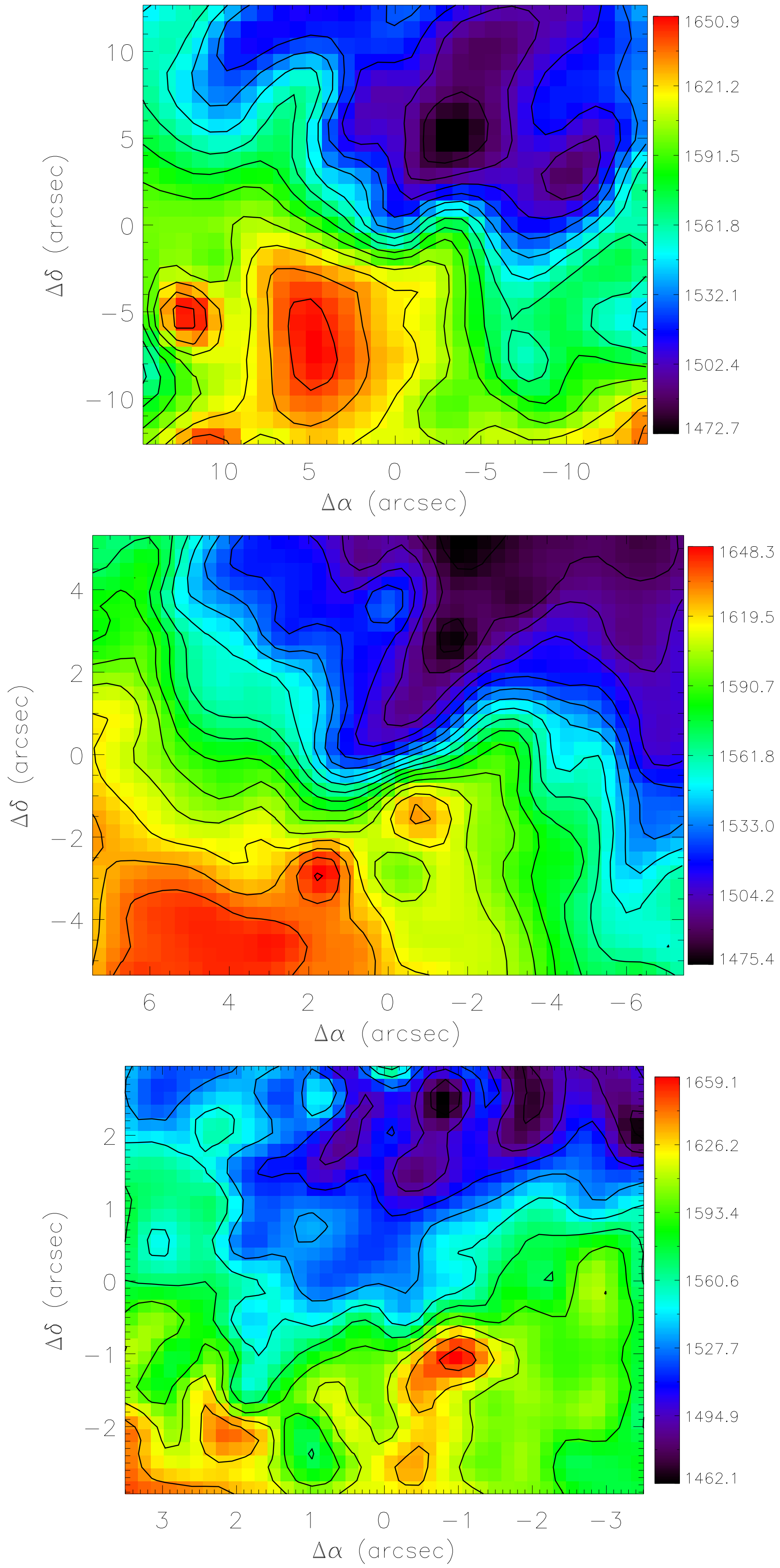

Figure 9.26— From top to bottom: SB3, SB2 and SB1 velocity maps derived from [SII] emission lines. The scale unit is kms^{-1}.

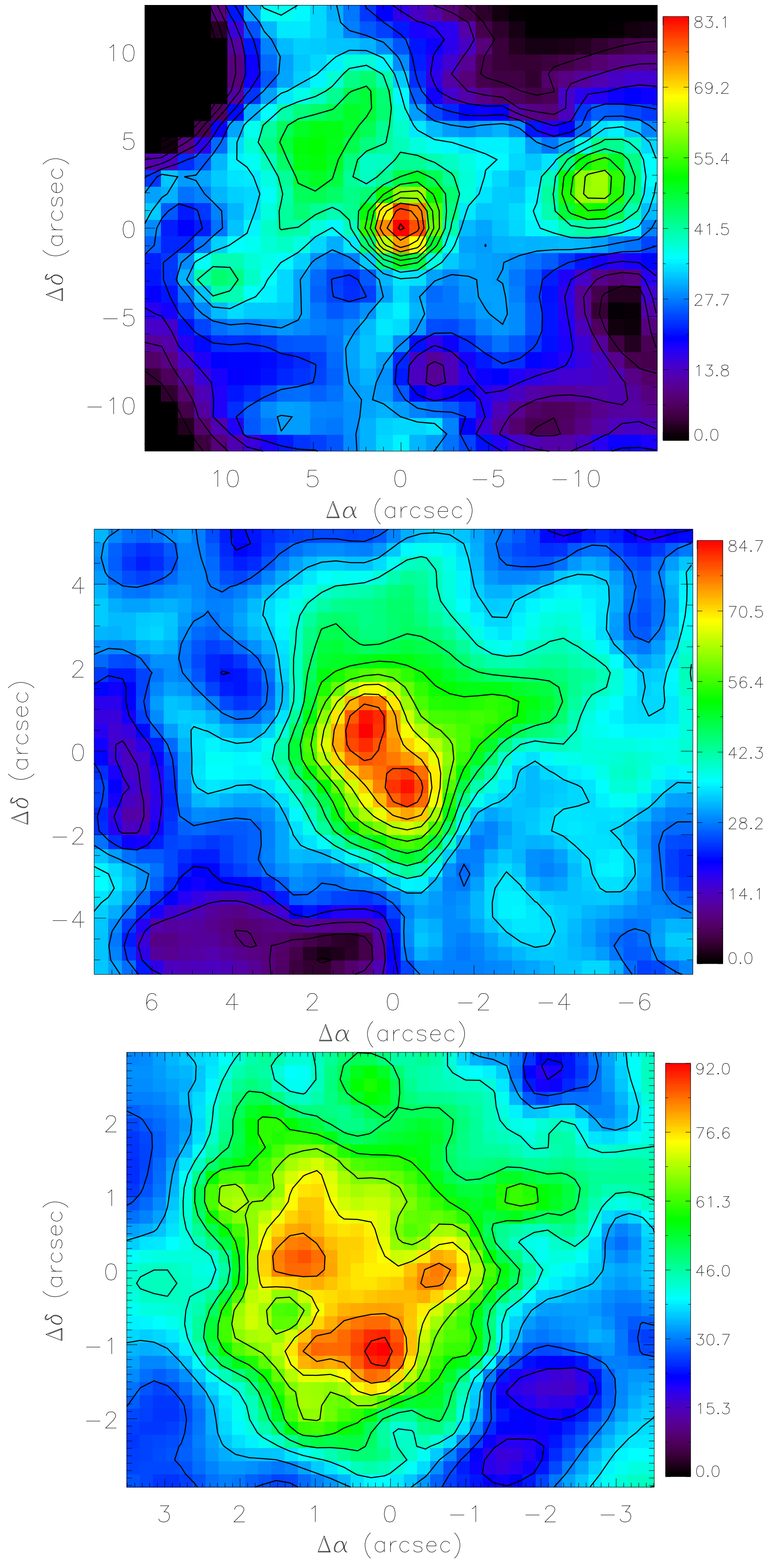

Figure 9.27— From top to bottom: SB3, SB2 and SB1 velocity dispersion maps due to the non-thermal motions of the ionized gas Hα. The scale unit is kms^{-1}.

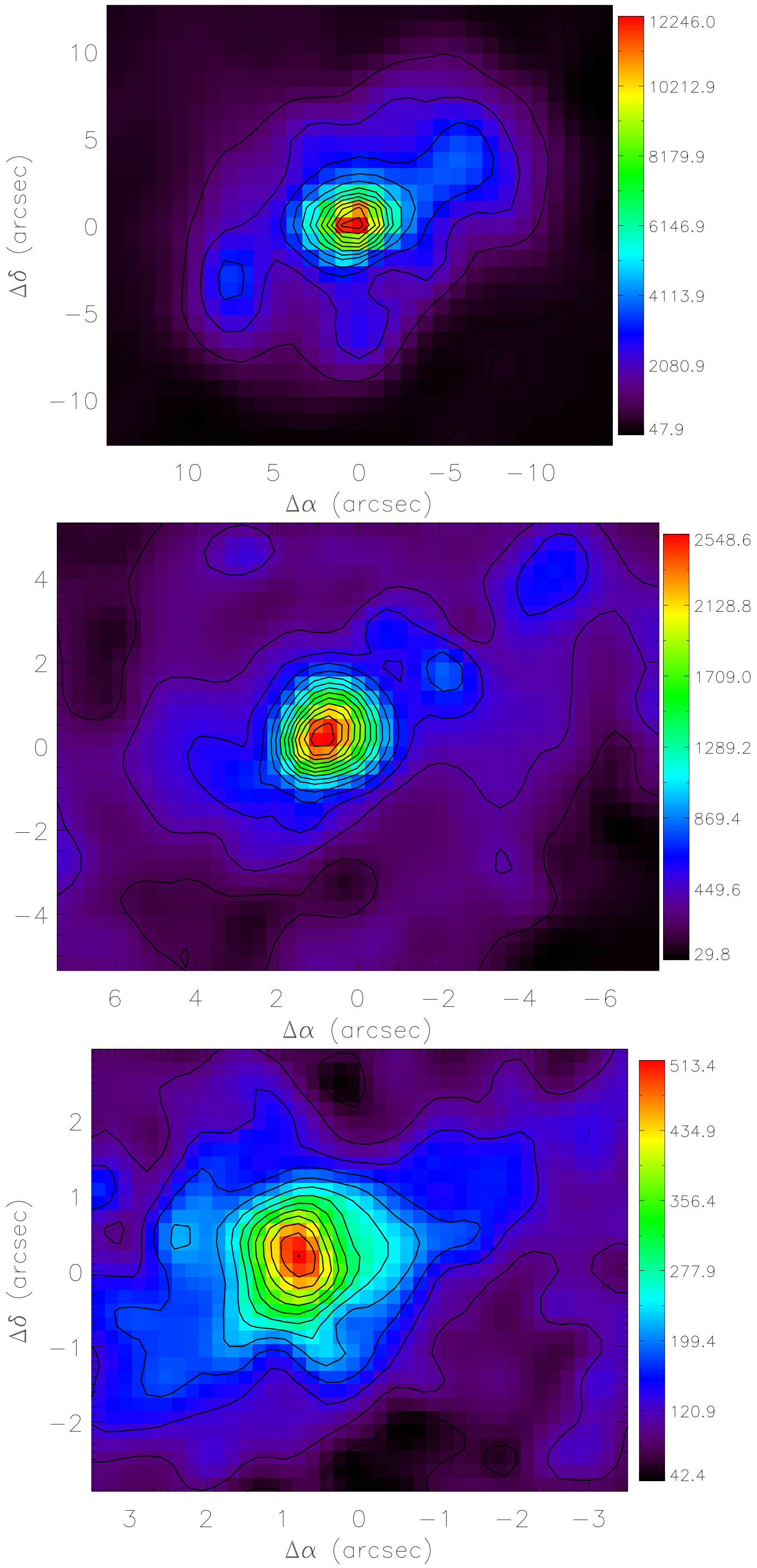

Figure 9.28— From top to bottom: SB3, SB2 and SB1 intensity maps computed over the absorption line Na II.

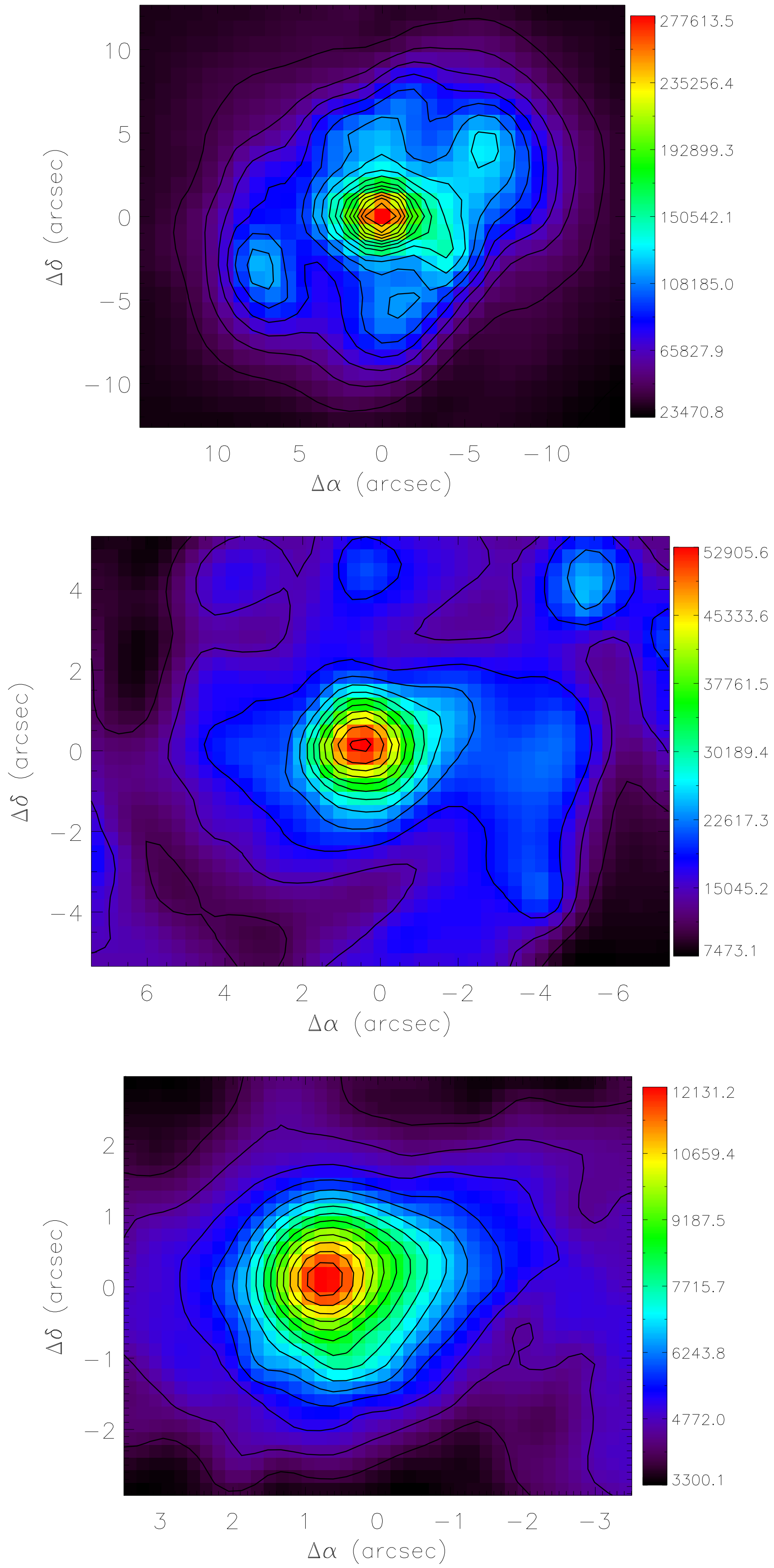

Figure 9.29— From top to bottom: SB3, SB2 and SB1 contiuum maps computed near the absorption line Na II.

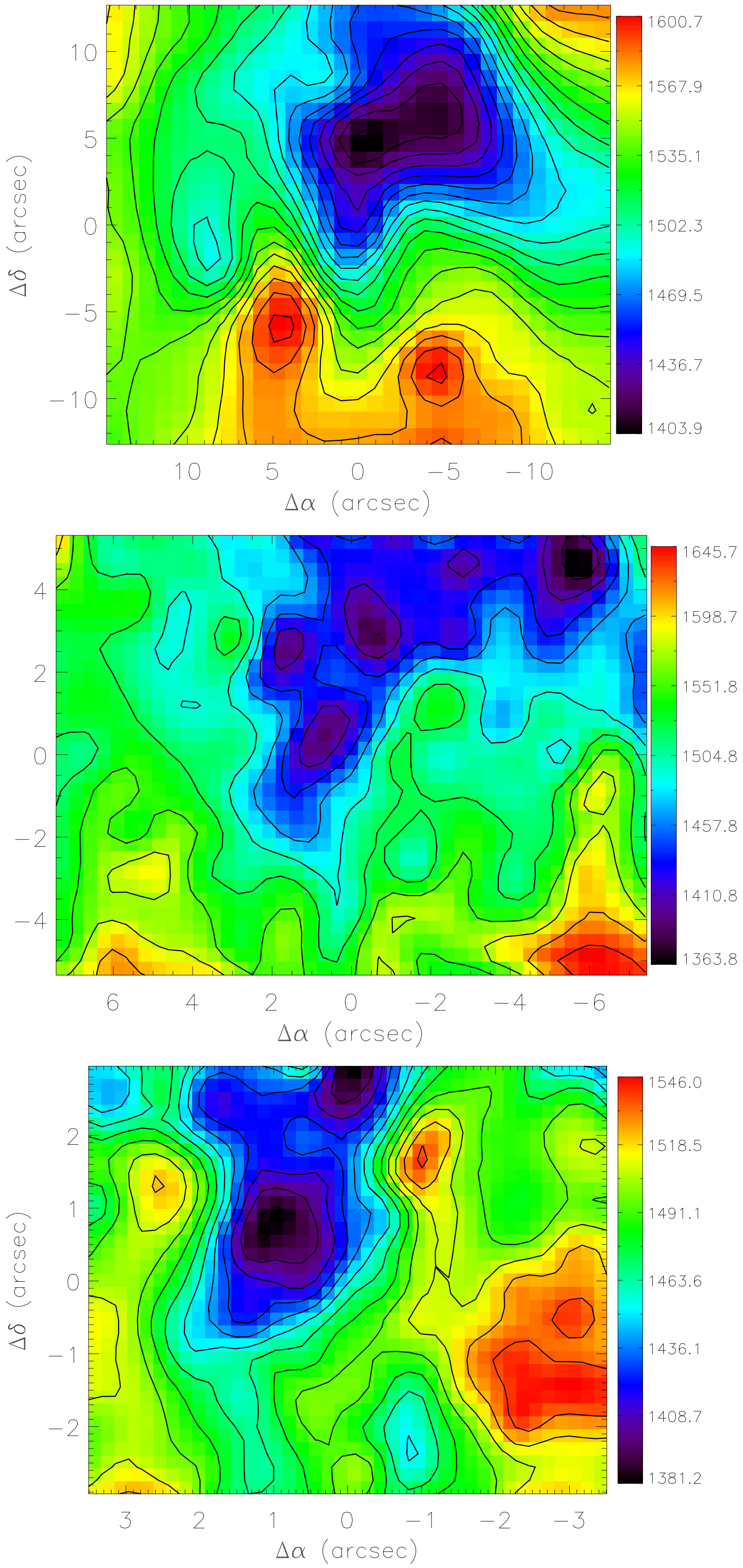

Figure 9.30— From top to bottom: SB3, SB2 and SB1 velocity maps computed for the absorption line Na II for the three fiber bundles. The scale unit is $\mathrm{km\,s^{-1}}$.

10

Summary and conclusions

The main results obtained in this thesis are summarized here:

- We have analysed a sample of ten nearby clusters of galaxies using the X-ray data provided by the ROSAT and ASCA satellites. For this sample physical quantities like gas mass, total mass, gas mass fraction and relative gas extent have been derived. Correlations between the above quantities have been studied and our findings are:

  - The gas mass fraction increases with radius for all our clusters implying that gas is more extended than dark matter, confirming previous results (David et al., 1995; Ettori & Fabian, 1999; Jones & Forman, 1999). This behaviour is more pronounced when temperature profiles are taking into account in the mass analysis.

  - Within r_{500}, the mean gas mass fraction obtained is $(0.16 \pm 0.04) h_{50}^{-3/2}$. We see no trend in the gas mass fraction with redshift.

  - The gas extent relative to the dark matter distribution shows a mild dependence on the total mass and gas temperature. Clusters with larger masses have smaller relative gas extents, as we would expect if non-gravitational processes are important in cluster formation. Hints for this kind of behaviour have been found previously in distant clusters. These new results confirm this trend.

  - Studying the mass-temperature relation we find a slope slightly steeper compared with the theoretical value of 3/2 although consistent within the errors. The self-similar slope 3/2 is found when using temperature gradient analysis. Other observational analyses, with only high-temperature clusters, have achieved results consistent with the theoretical prediction (Hjorth et al., 1998; Neumann & Arnaud, 1999; Nevalainen et al., 2000).

- The formation and evolution of clusters sensitively depends on cosmological parameters like the mean matter density in the Universe Ω_m (Beisbart et al., 2001; Jenkins et al., 1998; Thomas et al., 1998). Therefore it is important to determine the dynamical state of clusters at different redshifts, i.e. at different evolutionary states. The X-ray morphology alone is not the best indicator of the dynamical state, but it should be complemented with all other information available, e.g. the temperature map or the galaxy distribution. The combination of all data gives a detailed picture of the state of a cluster. We have done this analysis in this thesis for the moderately distant cluster CL 0939+4713 (z = 0.41), which can be used as a basis for comparisons at lower and higher redshifts. XMM-Newton satellite, with its major capabilities for spectroscopy, allows us to trace better temperature and metallicity maps.

- We confirm earlier results that CL 0939+4713 is a dynamically young system (Schindler et al., 1998; Schindler & Wambsganss, 1996). The X-ray morphology has pronounced substructure. New findings of a hot region between the two main clumps are particularly indicative of a merger process, in which the two major subclusters will collide in a few hundreds of Myr.

- Particularly interesting are the metallicity variations found in this cluster. Metallicity variations were found before as radial gradients in clusters with cD galaxies (De Grandi & Molendi, 2001; Gastaldello & Molendi, 2002; Kaastra et al., 2001; Lewis et al., 2002; Molendi & Gastaldello, 2001). Clusters without cD galaxies were found to show no radial gradients (Arnaud et al., 2001b; De Grandi & Molendi, 2001). The problem when binning the cluster into radial bins is, that one averages over metallicity values coming from very different regions of the clusters. Therefore it is not surprising that the profiles are usually flat for non-cD clusters. We took a different approach here and found a hint that the metal abundances vary over the cluster. Of course it is quite difficult to do this in a relatively distant cluster. We therefore suggest to use this method in nearby clusters, instead of determining radial metallicity profiles.

- Interaction of the different components in clusters of galaxies yields important information on physical quantities like e.g. the pressure, the energy or the strength of the magnetic field. The knowledge about these quantities enables us to understand cluster formation as well as physical processes in clusters, being both important steps to use clusters as diagnostic tools for cosmology. The unprecedented spatial resolution ($\sim 0.5''$) now available with the new generation of X-ray satellite CHANDRA allow us to study in more detail this interaction. We have presented CHANDRA observations of the X-ray luminous, distant galaxy cluster RBS797 at $z = 0.35$ and our findings are:

  - The X-ray luminous cluster RBS797 reveals remarkable depressions in the X-ray emission of the central region. The depressions are roughly circular and arranged symmetrically with respect to the cluster centre. They have diameters of 20 - 30 kpc and are very deep: a factor of 3-4 less emission than in the other directions. The discovery of these minima shows the ability of CHANDRA to investigate physical effects even in clusters as distant as RBS797 (z=0.35). These depressions suggest an interaction between the central radio galaxy and the intra-cluster medium, which would be the first detection in such a distant cluster.

  - The spectral and morphological analysis of RBS797 shows that the cluster has a high temperature of $T = 7.7$ keV, a metallicity $Z = 0.2 - 0.3$, and a high luminosity $L_X(\mathrm{bol}) = 6.7 \times 10^{45}$erg/s. The total mass within r_{500} is $M_{\mathrm{tot}}(r_{500}) = 6.5 \times 10^{14} M_\odot$ with a gas mass fraction $f_{\mathrm{gas}}(r_{500}) = 0.17$.

  - In follow-up radio observations the interaction between the radio lobes and the intra-cluster gas will be studied in detail.

- The 2D spectroscopy with optical fibre allow us to obtain simultaneously spatial and spectral information for extended objects. This technique can be applied here to the study of nuclear and circumnuclear regions in galaxies. We have presented 2D spectroscopy of NGC 5033, a low luminosity Seyfert galaxy. The observations were made with INTEGRAL, a fibre based system operating at the WHT, and our main findings are:

- The location of the Seyfert 1 nucleus of the galaxy that we infer from the location of the broad Hβ emission is $\sim 3''.2$ westwards from the continuum emission peak. The stellar rotation center seems to be located between the Seyfert 1 nucleus and the continuum emission peak but closer to the last. According to the uncertainties in the determination of the kinematic major axis and to the spatial resolution of the observations, both centers (galaxy mass centroid and active nucleus) can be only marginally reconciled. Observations with better spatial resolution are needed to confirm this offcentering of the Seyfert nucleus that in other active galaxies has been considered related to a past merger event possibly related to the origin or to the fueling of the activity.

- The [OIII] emission (associated to highly ionized gas) depicts a biconical structure with apex in the Seyfert 1 nucleus. The cones seem to be hollow structures of wide aperture and projected axis perpendicular to the galaxy major axis. These characteristics suggest that the biconical structure of ionization is generated by obscuring material in the galaxy disc probably related to the large scale CO structure detected by Kohno et al. (2003). The same geometrical model also explains the morphology of the stellar continuum emission (with half of the stellar bulge obscured).

- Nuclear activity is affecting the kinematics of the highly ionized gas even at large (galactic) scales. There are some kinematic features that seem to be related to the biconical geometry.

- We also have presented the INTEGRAL observations and the kinematical analysis for the circumnuclear region of the Virgo cluster galaxy NGC 4321. In the observed spectral range (5790 - 6900 Å) we are able to identify Hα, [N II] $\lambda\lambda$ 6548, 6583 and [S II] $\lambda\lambda$6716, 6731 emission lines. Furthermore the Na II λ5890 absorption line is observed. These observations allows us to computed intensity, continuum and veloctiy maps.

  This galaxy shows a prominent Hα emission in the circumnuclear region where are located several HII regions. The NII and SII emissions maps are very similar and are characterized by a enhanced central emission. The Na II absorption line map shows the stellar distribution in this galaxy.

  The kinematical study derived from the computed velocity maps can be summarized as follows:

  - The Hα velocity field in the inner region of this galaxy shows the basic spider pattern which indicates circular motions in a rotating disk. But at the same time the velocity field shows the effect of the non-circular motions. We can see a curved kinematical minor axis indicating probably the presence of another kinematic system. Furthermore the isovelocity contours are deformed following the structure of the spiral arms.

  - The position of the optical nucleus in the continuum map is coincident with the position of the kinematical centre for the lower resolution map. Nevertheless the optical nucleus appears located asymmetrically at the higher resolution continuum maps and seems to be not coincident with the kinematical centres defined. The optical nucleus appears located in the “blue part” of the velocity field and is located in a region of locally higher velocity.

  - We have derived the Hα rotation curve out to $15''$using the three available INTEGRAL angular resolutions. This curve shows a steep rise in the rotation velocity, reaching almost

130 km/s in $3''$. Furthermore residual velocity maps have been derived to study the presence of non-circular motions showing higher absolute values at the positions ot the inner incoming spiral arms.

- The stellar velocity field derived from the Na absorption line is quite complicated and not easy to interpret. The lower resolution stellar velocity map shows clearly two maxima not present in the ionized gas velocity field. The higher resolutions velocity maps shows a dramatic difference between the stellar and ionized gas velocity field, with the stellar veloticity map extremely distorted in its inner region. However, there are similitudes between both velocity fields (ionized gas and stellar) related with the distorsions produced in the velocity field by the spiral structure in this galaxy.

A

Nearby sample of clusters of galaxies

In this Appendix we present the sample of ten nearby clusters of galaxies analyzed in Chapter 4. For every cluster of galaxies, four different plots are shown:

- The X-ray emission from ROSAT/PSPC observations shown in logarithmic scale.
- The X-ray surface brightness profile derived from the X-ray image displayed with the best β-model fit.
- Profiles for the computed gas mass profiles and the total mass profiles assuming isothermal gas and introducing an ASCA gradient of temperature into the hydrostatic equation.
- Gas mass fraction (M_{gas}/M_{total}) profiles derived assuming isothermal gas and taking the ASCA gradient of temperature. The error estimations are shown at two different radii, $r_{500}/2$ and r_{500}.

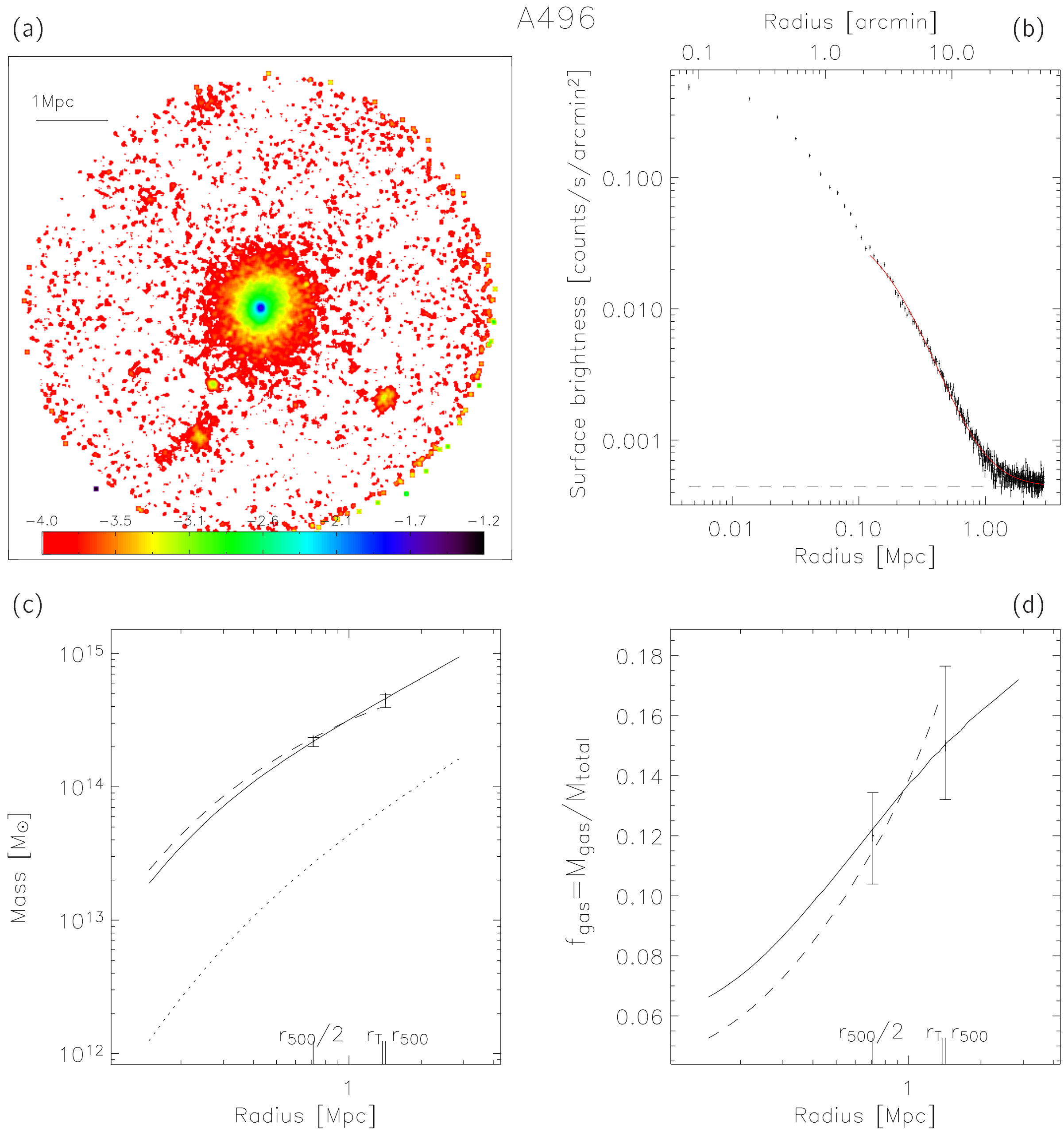

Figure A.1— (a) X-ray emission from ROSAT/PSPC observation. (b) X-ray surface brightness profile with the beta-model fit drawn on top (red line). (c) Total mass profile assuming isothermal gas (solid line) and taking a gradient of temperature (dashed line); gas mass profile (pointed line). (d) Gas mass fraction profiles derived using the hypothesis of isothermal gas (solid line) and introducing a temperature gradient (dashed line).

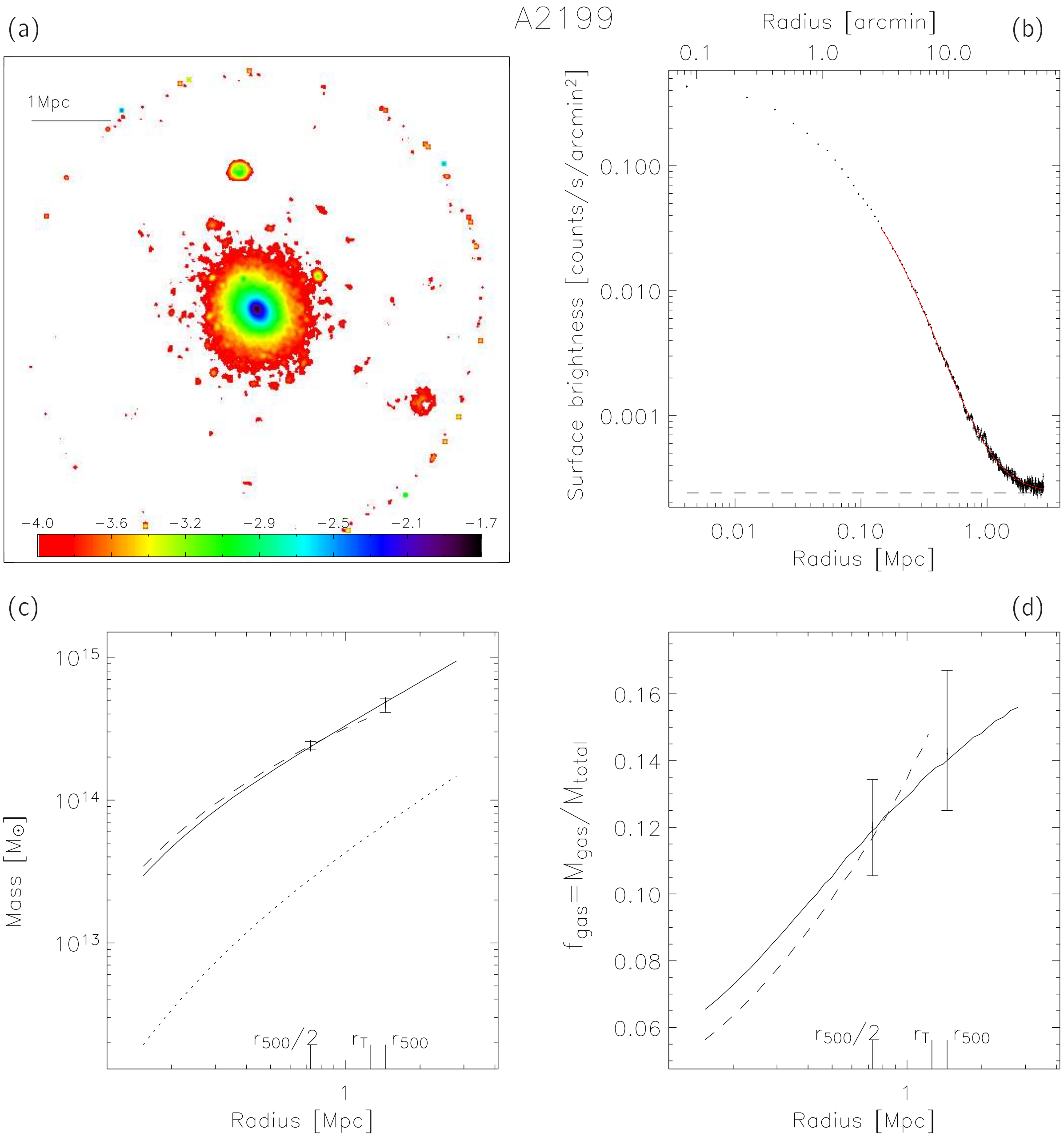

Figure A.2— (a) X-ray emission from ROSAT/PSPC observation. (b) X-ray surface brightness profile with the beta-model fit drawn on top (red line). (c) Total mass profile assuming isothermal gas (solid line) and taking a gradient of temperature (dashed line); gas mass profile (pointed line). (d) Gas mass fraction profiles derived using the hypothesis of isothermal gas (solid line) and introducing a temperature gradient (dashed line).

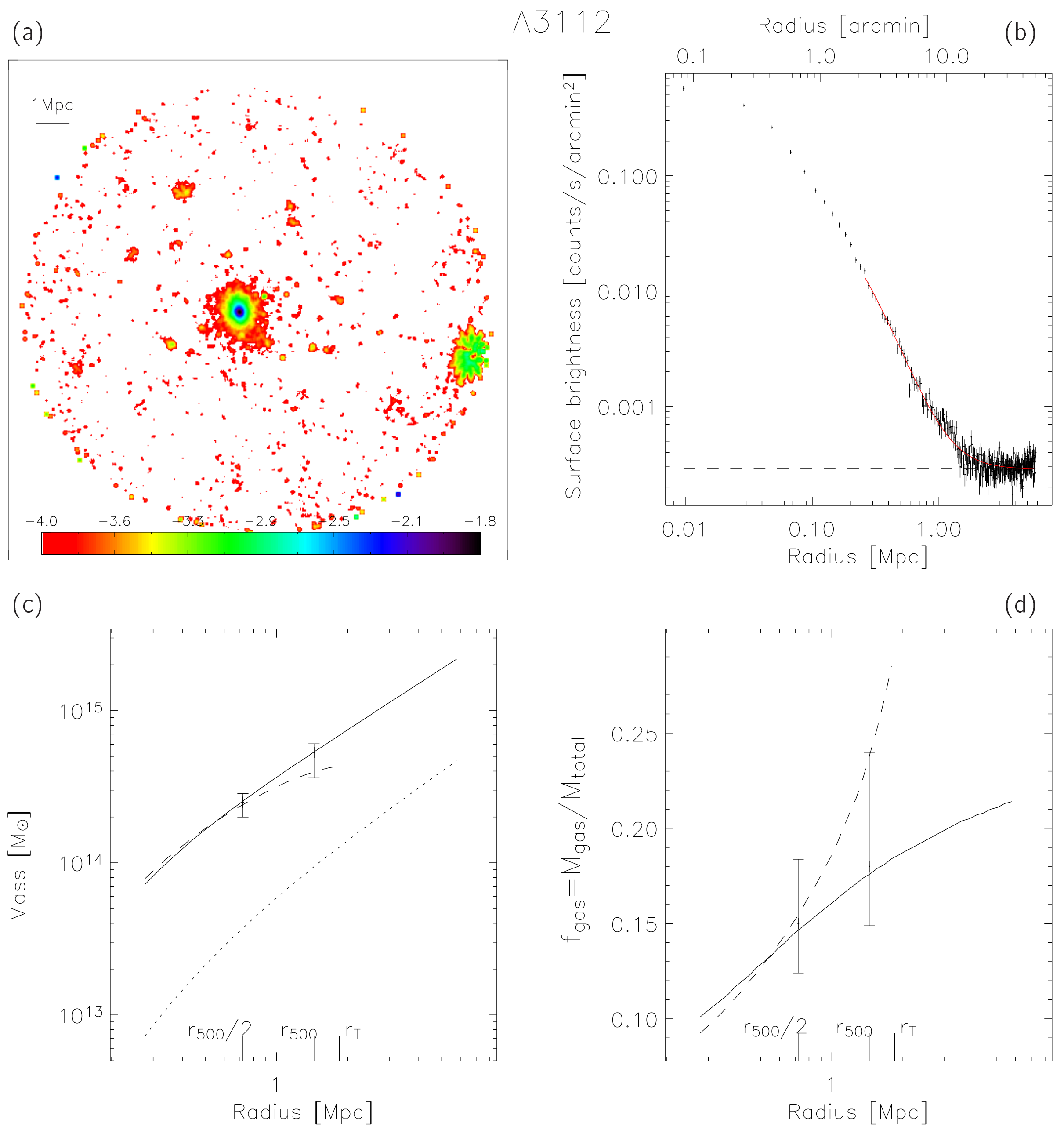

Figure A.3— (a) X-ray emission from ROSAT/PSPC observation. (b) X-ray surface brightness profile with the beta-model fit drawn on top (red line). (c) Total mass profile assuming isothermal gas (solid line) and taking a gradient of temperature (dashed line); gas mass profile (pointed line). (d) Gas mass fraction profiles derived using the hypothesis of isothermal gas (solid line) and introducing a temperature gradient (dashed line).

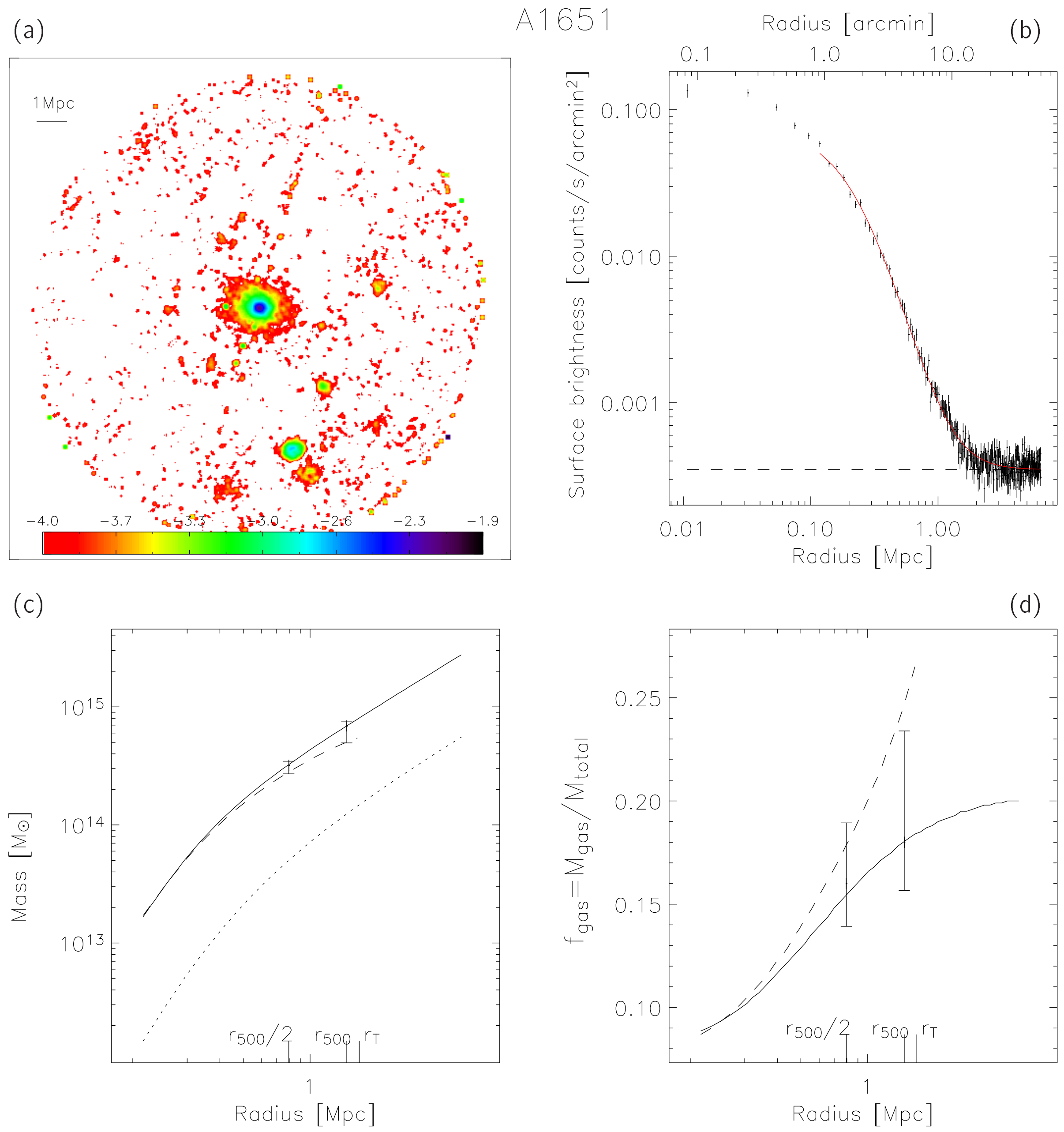

Figure A.4— (a) X-ray emission from ROSAT/PSPC observation. (b) X-ray surface brightness profile with the beta-model fit drawn on top (red line). (c) Total mass profile assuming isothermal gas (solid line) and taking a gradient of temperature (dashed line); gas mass profile (pointed line). (d) Gas mass fraction profiles derived using the hypothesis of isothermal gas (solid line) and introducing a temperature gradient (dashed line).

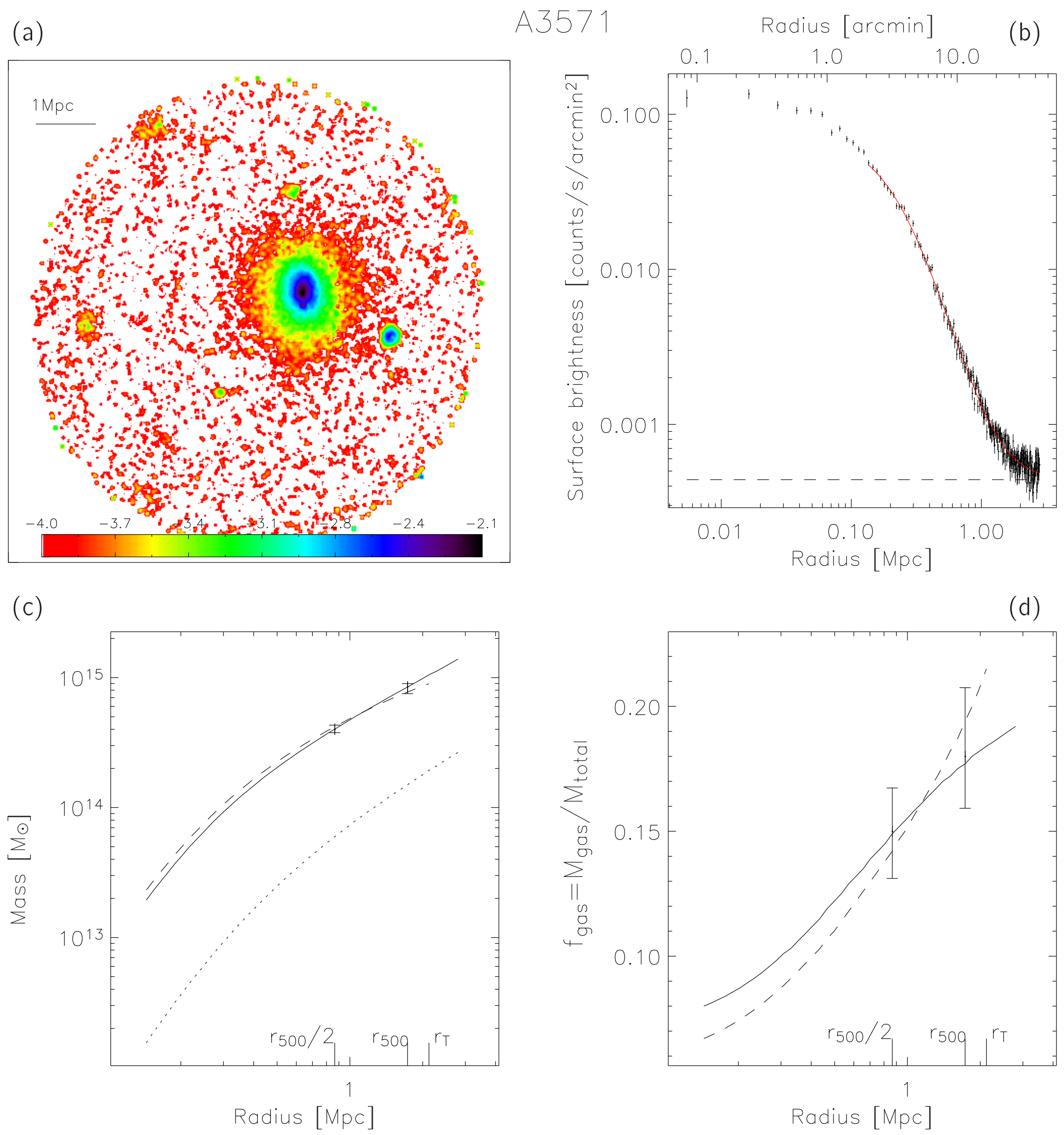

Figure A.5— (a) X-ray emission from ROSAT/PSPC observation. (b) X-ray surface brightness profile with the beta-model fit drawn on top (red line). (c) Total mass profile assuming isothermal gas (solid line) and taking a gradient of temperature (dashed line); gas mass profile (pointed line). (d) Gas mass fraction profiles derived using the hypothesis of isothermal gas (solid line) and introducing a temperature gradient (dashed line).

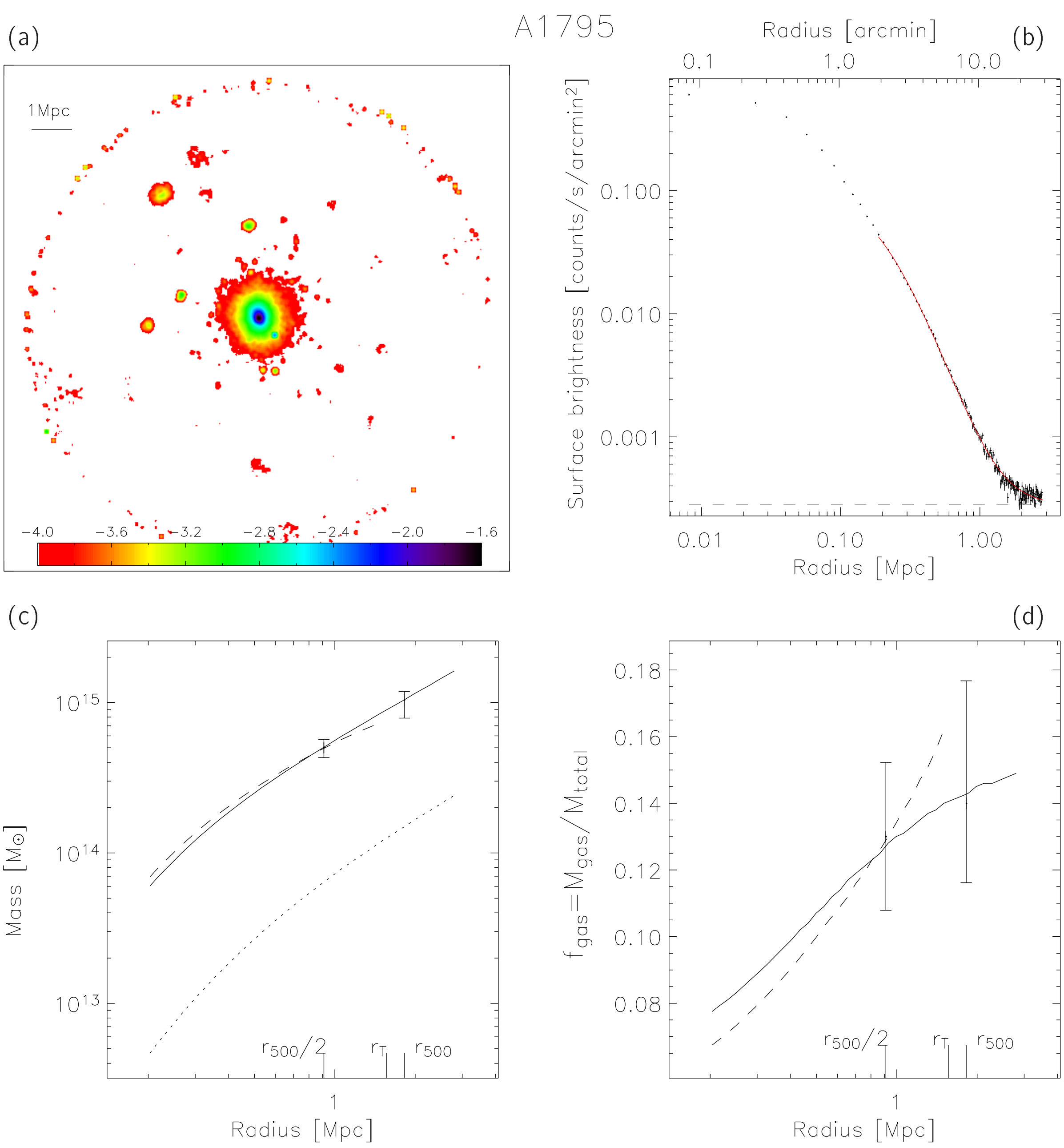

Figure A.6— (a) X-ray emission from ROSAT/PSPC observation. (b) X-ray surface brightness profile with the beta-model fit drawn on top (red line). (c) Total mass profile assuming isothermal gas (solid line) and taking a gradient of temperature (dashed line); gas mass profile (pointed line). (d) Gas mass fraction profiles derived using the hypothesis of isothermal gas (solid line) and introducing a temperature gradient (dashed line).

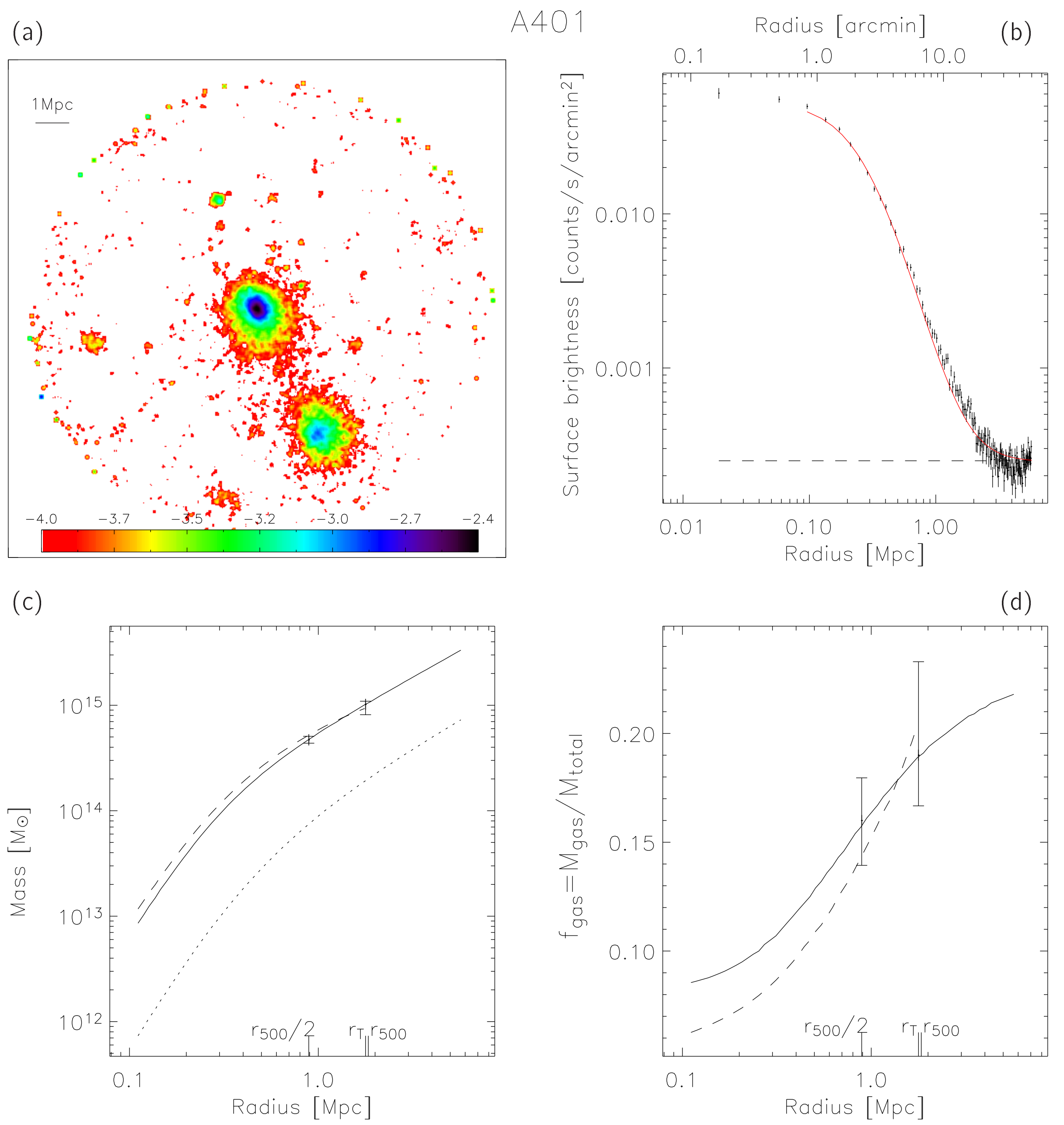

Figure A.7— (a) X-ray emission from ROSAT/PSPC observation. (b) X-ray surface brightness profile with the beta-model fit drawn on top (red line). (c) Total mass profile assuming isothermal gas (solid line) and taking a gradient of temperature (dashed line); gas mass profile (pointed line). (d) Gas mass fraction profiles derived using the hypothesis of isothermal gas (solid line) and introducing a temperature gradient (dashed line).

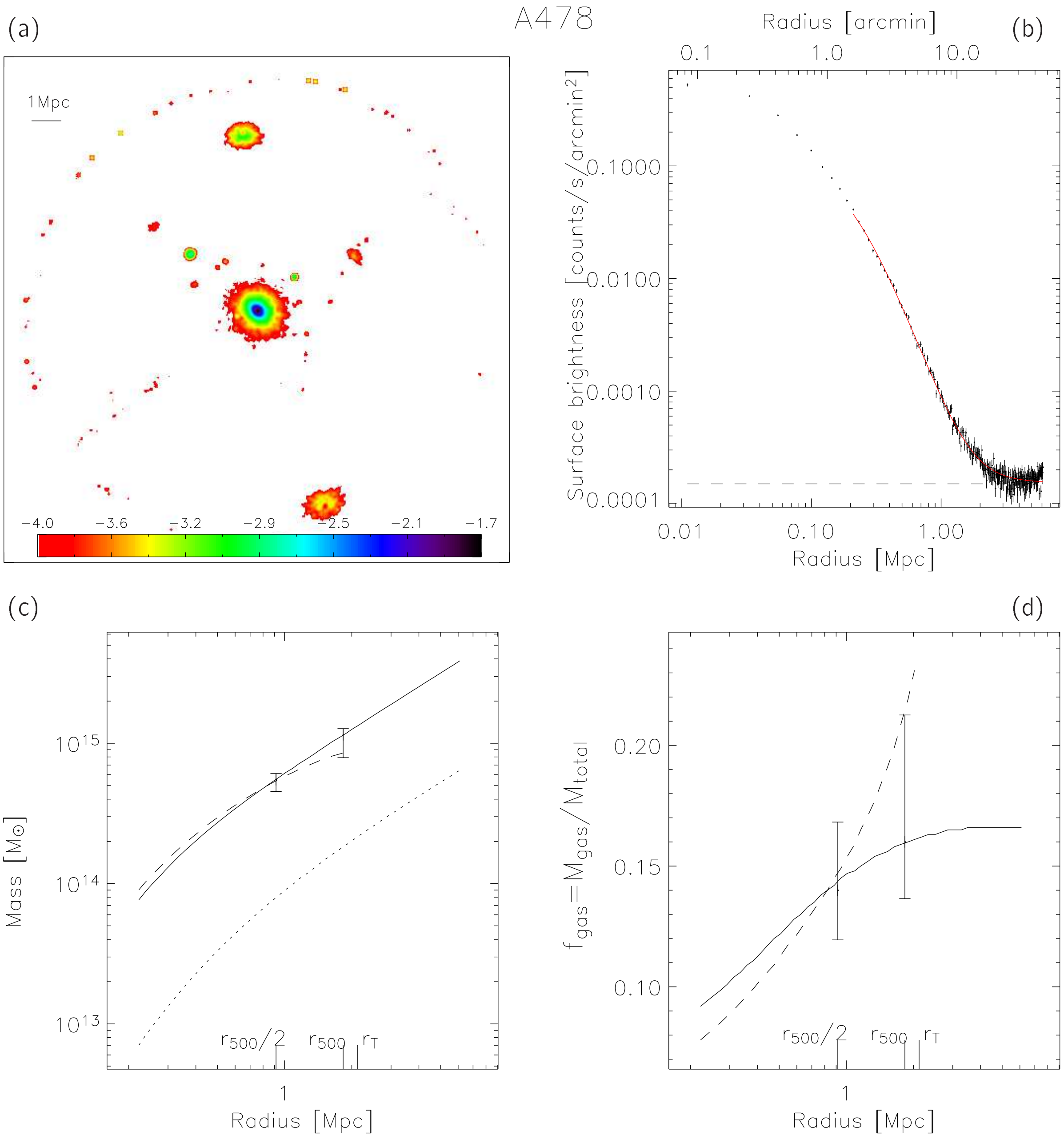

Figure A.8— (a) X-ray emission from ROSAT/PSPC observation. (b) X-ray surface brightness profile with the beta-model fit drawn on top (red line). (c) Total mass profile assuming isothermal gas (solid line) and taking a gradient of temperature (dashed line); gas mass profile (pointed line). (d) Gas mass fraction profiles derived using the hypothesis of isothermal gas (solid line) and introducing a temperature gradient (dashed line).

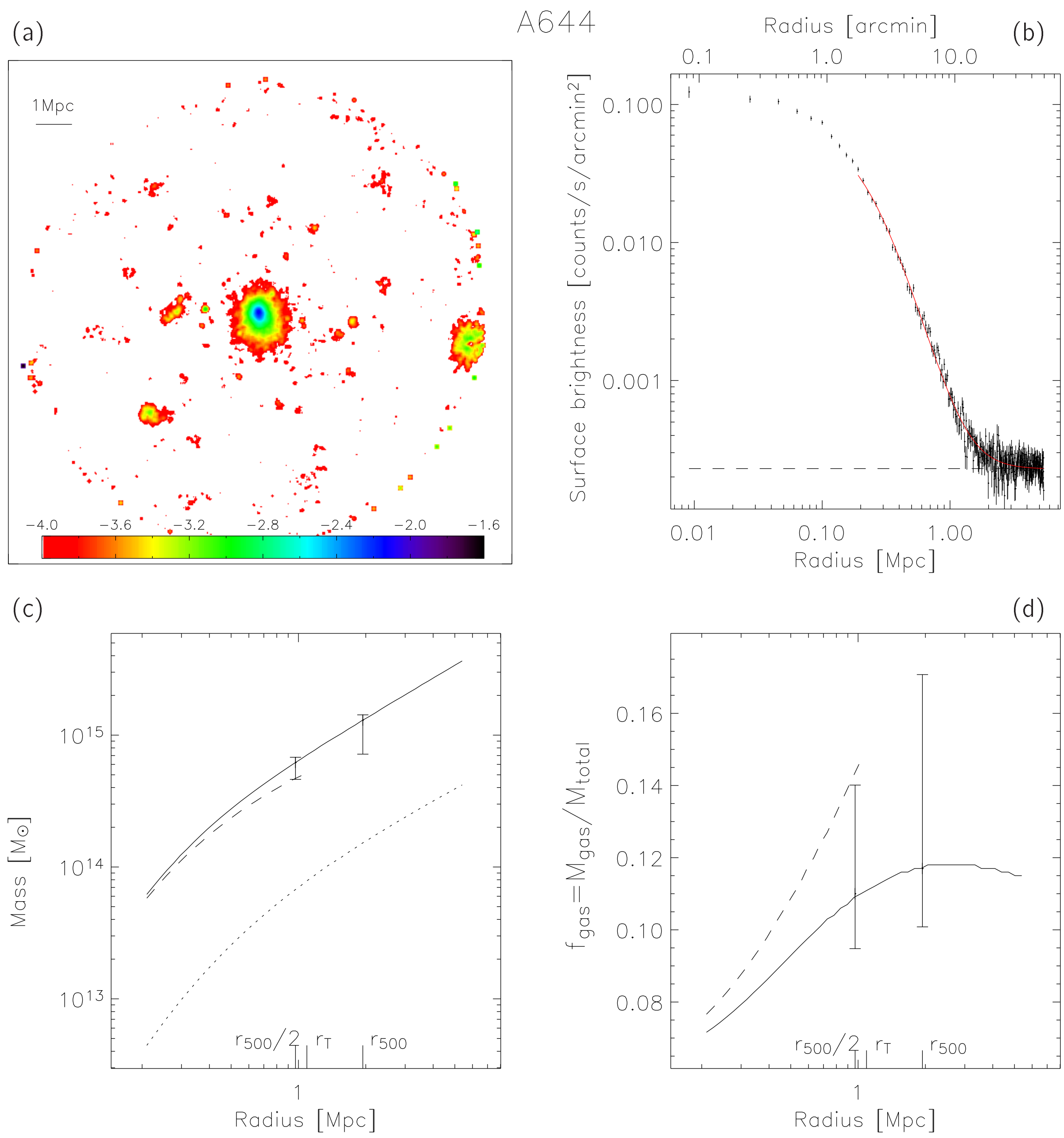

Figure A.9— (a) X-ray emission from ROSAT/PSPC observation. (b) X-ray surface brightness profile with the beta-model fit drawn on top (red line). (c) Total mass profile assuming isothermal gas (solid line) and taking a gradient of temperature (dashed line); gas mass profile (pointed line). (d) Gas mass fraction profiles derived using the hypothesis of isothermal gas (solid line) and introducing a temperature gradient (dashed line).

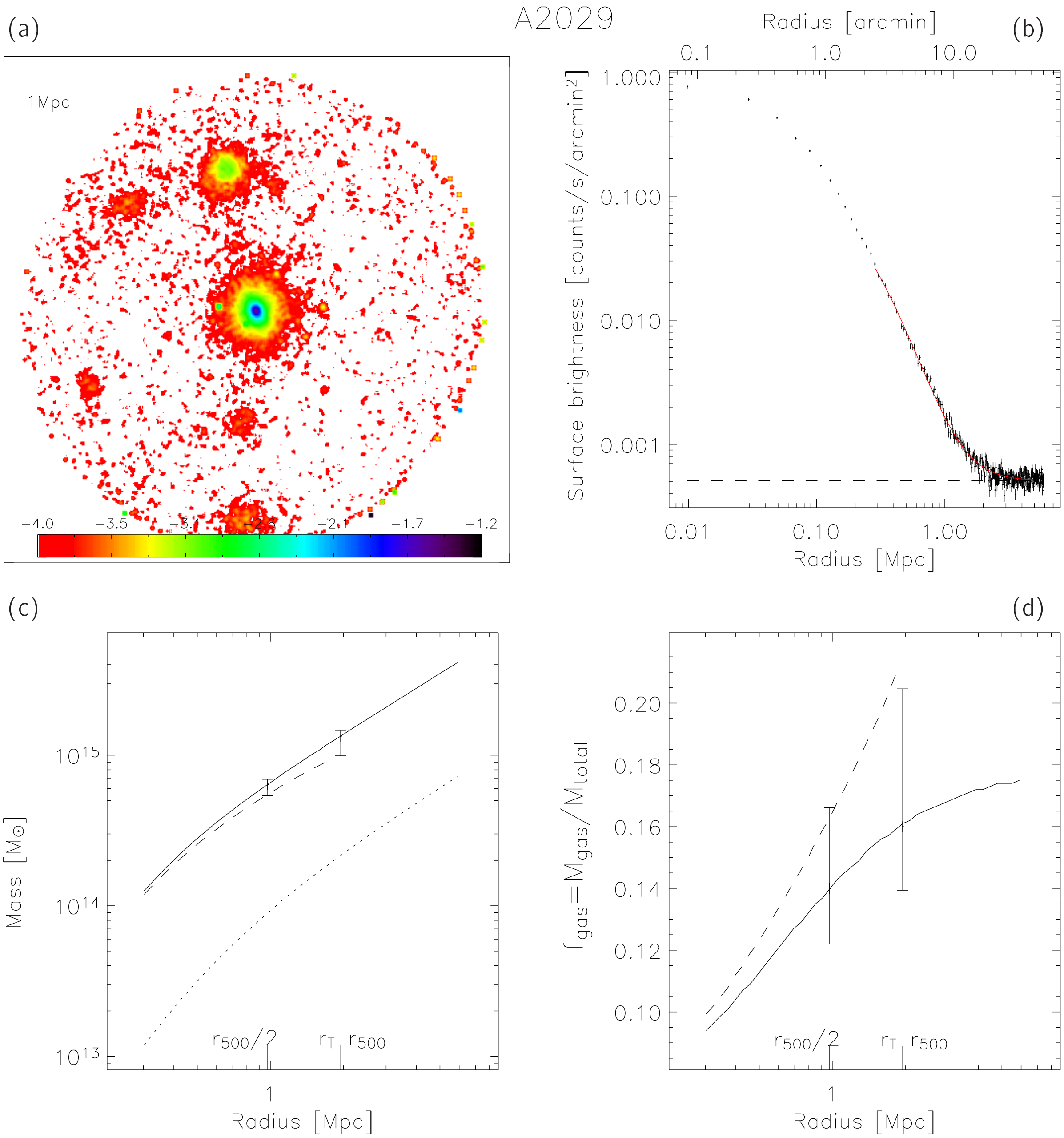

Figure A.10— (a) X-ray emission from ROSAT/PSPC observation. (b) X-ray surface brightness profile with the beta-model fit drawn on top (red line). (c) Total mass profile assuming isothermal gas (solid line) and taking a gradient of temperature (dashed line); gas mass profile (pointed line). (d) Gas mass fraction profiles derived using the hypothesis of isothermal gas (solid line) and introducing a temperature gradient (dashed line).

B

Temperature gradients obtained with ASCA for the nearby sample of clusters of galaxies

In this Appendix the temperature gradients derived by Markevitch et al. (1998) for the ten nearby clusters of galaxies analyzed in Chapter 4 are shown. In our total cluster mass analysis (see Section 4.3.2), the projected temperature profiles are parametrized using a linear function of the form $T_{gas}(r) = T(0) - \alpha r$. The parameters T(0) and α are determined by fitting a straight line to the projected temperature profiles mentioned before, excluding the central cluster region in the case of clusters with central X-ray excess. It is not useful to fit a more complex function because the temperatures for consecutive annuli are determined with low accuracy and for some clusters only two measured temperatures are available.

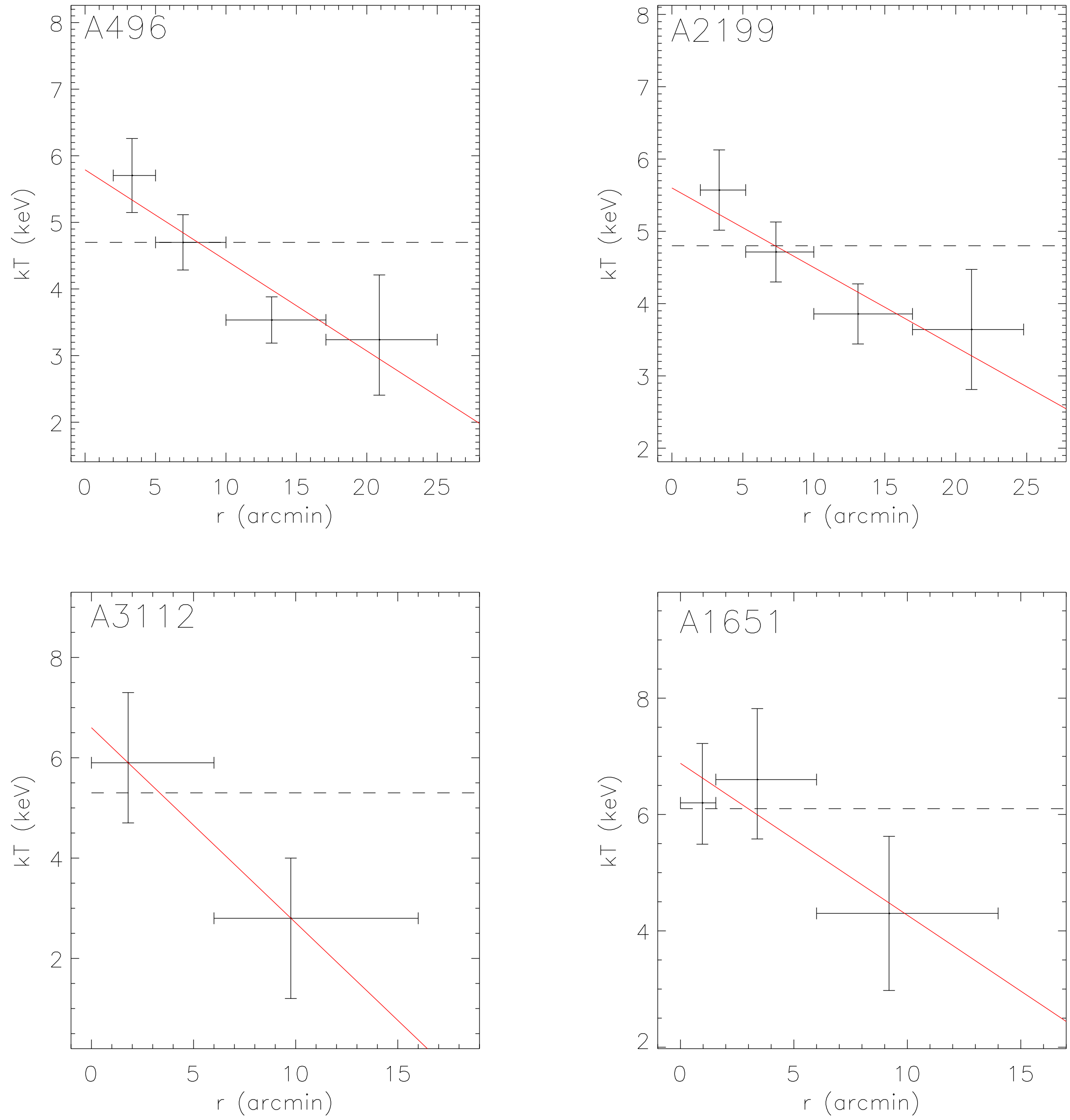

Figure B.1— Temperature gradients derived by Markevitch et al. (1998) from ASCA satellite observations. The red line shows the linear fit to the measured temperatures.

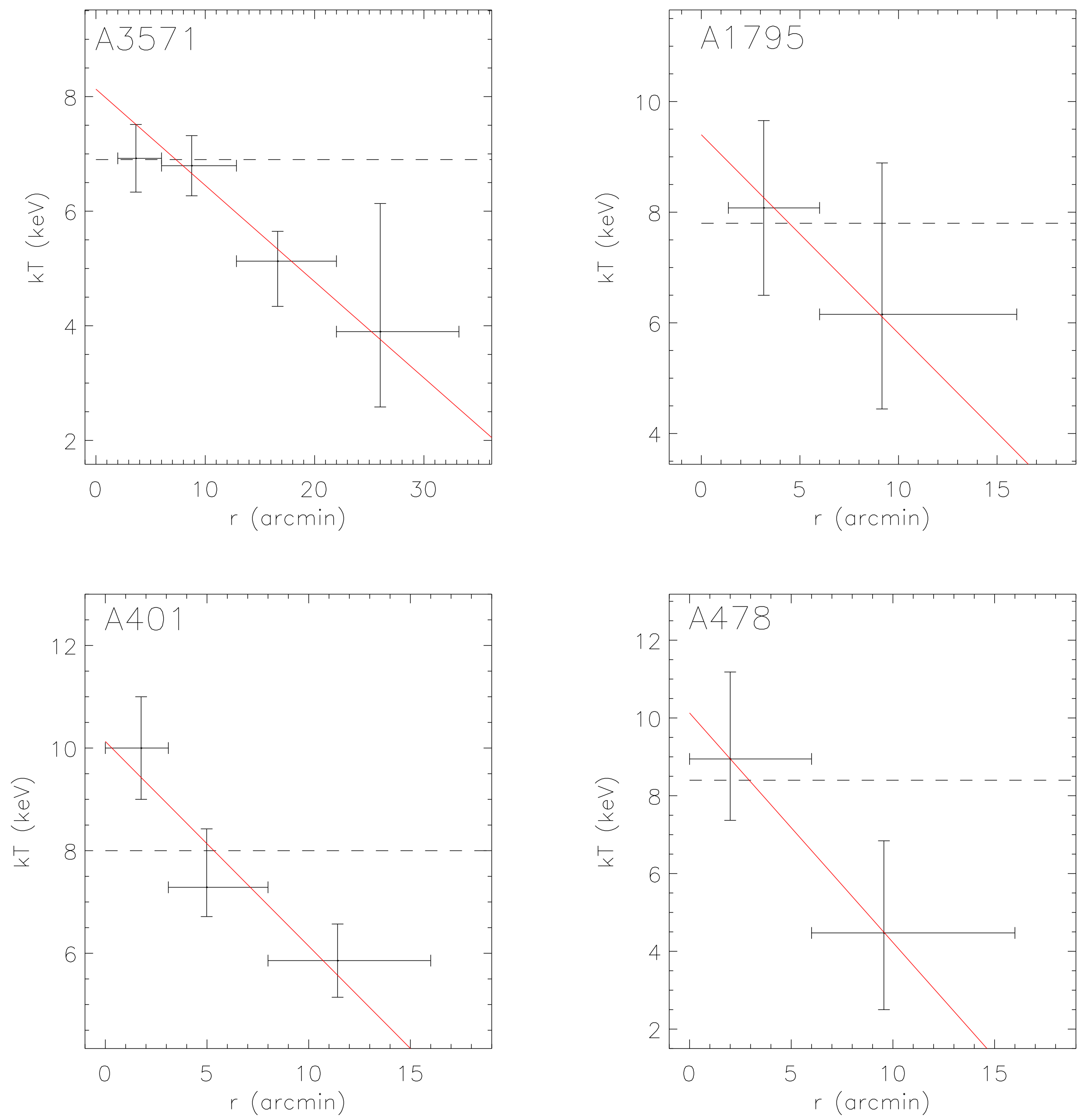

Figure B.2— Temperature gradients derived by Markevitch et al. (1998) from ASCA satellite observations. The red line shows the linear fit to the measured temperatures.

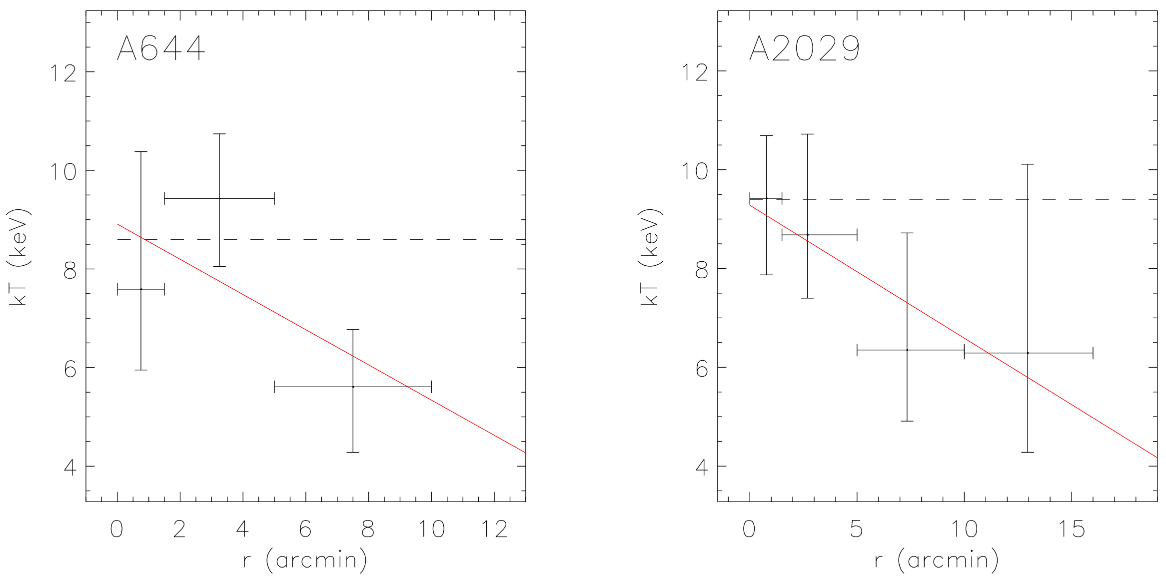

Figure B.3— Temperature gradients derived by Markevitch et al. (1998) from ASCA satellite observations. The red line shows the linear fit to the measured temperatures.

Bibliography

Aguirre, A., Hernquist, L., Schaye, J., et al. 2001, ApJ, 561, 521

Alfven, H. 1949, Phys. Rev, 75, 1732

Allen, S. W. & Fabian, A. C. 1997, MNRAS, 286, 583

Andreon, S., Davoust, E., & Heim, T. 1997, A&A, 323, 337

Arnaud, M., Aghanim, N., Gastaud, R., et al. 2001b, A&A, 365, L67

Arnaud, M. & Evrard, A. E. 1999, MNRAS, 305, 631

Arnaud, M., Majerowicz, S., Lumb, D., et al. 2002, A&A, 390, 27

Arnaud, M., Neumann, D. M., Aghanim, N., et al. 2001a, A&A, 365, L80

Arribas, S., Carter, D., Cavaller, L., et al. 1998, in Proc. SPIE Vol. 3355, p. 821-827, Optical Astronomical Instrumentation, Sandro D'Odorico; Ed., 821–827

Arribas, S. & Mediavilla, E. 1993, ApJ, 410, 552

Arribas, S., Mediavilla, E., del Burgo, C., & García-Lorenzo, B. 1999, ApJ, 511, 680

Arribas, S., Mediavilla, E., & Garcia-Lorenzo, B. 1996, ApJ, 463, 509

Arribas, S., Mediavilla, E., Garcia-Lorenzo, B., & del Burgo, C. 1997, ApJ, 490, 227

Arribas, S., Mediavilla, E., & Rasilla, J. L. 1991, ApJ, 369, 260

Arsenault, R., Boulesteix, J., Georgelin, Y., & Roy, J.-R. 1988, A&A, 200, 29

Aschenbach, B. 1985, Reports of Progress in Physics, 48, 579

Athreya, R. M., Kapahi, V. K., McCarthy, P. J., & van Breugel, W. 1998, A&A, 329, 809

Barrow, J. D., Ferreira, P. G., & Silk, J. 1997, Physical Review Letters, 78, 3610

Battaner, E. & Florido, E. 2000, in ASP Conf. Ser. 200: Clustering at High Redshift, 144

Battaner, E. & Lesch, H. 2000, Anales de Física, 95, 213

Battaner, E., Mediavilla, E., Guijarro, A., Arribas, S., & Florido, E. 2003, A&A, 401, 67

Bauer, F. & Sarazin, C. L. 2000, ApJ, 530, 222

Beck, R. 1991, A&A, 251, 15

—. 2002, Highlights in Astronomy, 12, 712

—. 2004, Ap&SS, 289, 293

Beck, R., Brandenburg, A., Moss, D., Shukurov, A., & Sokoloff, D. 1996, ARA&A, 34, 155

Beck, R. & Hoernes, P. 1996, Nature, 379, 47

Begeman, K. G. 1989, A&A, 223, 47

Beisbart, C., Valdarnini, R., & Buchert, T. 2001, A&A, 379, 412

Belloni, P., Bruzual, A. G., Thimm, G. J., & Röser, H.-J. 1995, A&A, 297, 61

Belloni, P. & Röser, H.-J. 1996, A&AS, 118, 65

Berghöfer, T. W., Bowyer, S., & Korpela, E. 2000, ApJ, 535, 615

Berkhuijsen, E. M., Beck, R., & Hoernes, P. 2003, A&A, 398, 937

Bingham, R. G., Gellatly, D. W., Jenkins, C. R., & Worswick, S. P. 1994, in Proc. SPIE Vol. 2198, p. 56-64, Instrumentation in Astronomy VIII, David L. Crawford; Eric R. Craine; Eds., 56–64

Blanton, E. L., Sarazin, C. L., & McNamara, B. R. 2003, ApJ, 585, 227

Bosma, A. 1981, AJ, 86, 1791

Brüggen, M. & Kaiser, C. R. 2002, Nature, 418, 301

Brandenburg, A. 2000, Royal Society of London Philosophical Transactions Series A, 358, 759

Brandenburg, A. & Kandaswamy, S. 2004, astro-ph/0405052

Bregman, J. N. & David, L. P. 1988, ApJ, 326, 639

Breitschwerdt, D., Voelk, H. J., & McKenzie, J. F. 1991, A&A, 245, 79

Buczilowski, U. R. & Beck, R. 1991, A&A, 241, 47

Burles, S. & Tytler, D. 1998a, ApJ, 499, 699

—. 1998b, ApJ, 507, 732

Buson, L. M., Bertola, F., Cappellari, M., et al. 2000, ApJ, 531, 684

Carilli, C. L. & Taylor, G. B. 2002, ARA&A, 40, 319

Castillo-Morales, A. & Schindler, S. 2003, A&A, 403, 433

Cavaliere, A. & Fusco-Femiano, R. 1976, A&A, 49, 137

Cavaliere, A., Menci, N., & Tozzi, P. 1999, MNRAS, 308, 599

Cayatte, V., van Gorkom, J. H., Balkowski, C., & Kotanyi, C. 1990, AJ, 100, 604

Cho, J., Lazarian, A., Honein, A., et al. 2003, ApJL, 589, L77

Churazov, E., Brüggen, M., Kaiser, C. R., Böhringer, H., & Forman, W. 2001, ApJ, 554, 261

Churazov, E., Sunyaev, R., Forman, W., & Böhringer, H. 2002, MNRAS, 332, 729

Ciotti, L. & Ostriker, J. P. 2001, ApJ, 551, 131

Clarke, T. E., Kronberg, P. P., & Böhringer, H. 2001, ApJL, 547, L111

Colgate, S. A., Li, H., & Pariev, V. I. 2001, in AIP Conf. Proc. 586: 20th Texas Symposium on relativistic astrophysics, 259

Condon, J. J., Cotton, W. D., Greisen, E. W., et al. 1998, AJ, 115, 1693

Cowie, L. L., Barger, A. J., & Kneib, J.-P. 2002, AJ, 123, 2197

Curran, S. J., Polatidis, A. G., Aalto, S., & Booth, R. S. 2001, A&A, 373, 459

Dahlem, M., Petr, M. G., Lehnert, M. D., Heckman, T. M., & Ehle, M. 1997, A&A, 320, 731

David, L. P., Jones, C., & Forman, W. 1995, ApJ, 445, 578

David, L. P., Nulsen, P. E. J., McNamara, B. R., et al. 2001, ApJ, 557, 546

Davis, L. J. & Greenstein, J. L. 1951, ApJ, 114, 206

De Filippis, E., Schindler, S., & Castillo-Morales, A. 2003, A&A, 404, 63

De Grandi, S. & Molendi, S. 2001, ApJ, 551, 153

De Young, D. S. 1978a, ApJ, 223, 47

—. 1978b, ApJ, 223, 47

del Burgo, C. 2000, PhD Thesis

del Burgo, C., Mediavilla, E., & Arribas, S. 2000, ApJ, 540, 741

Dickey, J. M. & Lockman, F. J. 1990, ARA&A, 28, 215

Dolag, K., Bartelmann, M., & Lesch, H. 1999, A&A, 348, 351

—. 2002, A&A, 387, 383

Dolag, K. & Schindler, S. 2000, A&A, 364, 491

Dolag, K., Schindler, S., Govoni, F., & Feretti, L. 2001, A&A, 378, 777

Donnelly, R. H., Forman, W., Jones, C., et al. 2001, ApJ, 562, 254

Dressler, A. 1980, ApJ, 236, 351

Dressler, A. & Gunn, J. E. 1992, ApJS, 78, 1

Dressler, A., Oemler, A. J., Butcher, H. R., & Gunn, J. E. 1994, ApJ, 430, 107

Dressler, A., Oemler, A. J., Gunn, J. E., & Butcher, H. 1993, ApJL, 404, L45

Dressler, A., Smail, I., Poggianti, B. M., et al. 1999, ApJS, 122, 51

Dumke, M., Krause, M., Wielebinski, R., & Klein, U. 1995, A&A, 302, 691

Dupke, R. & White, R. E. 2003, ApJL, 583, L13

Dupke, R. A. & White, R. E. 2000a, ApJ, 528, 139

—. 2000b, ApJ, 537, 123

Ehle, M., Beck, R., Haynes, R. F., et al. 1996, A&A, 306, 73

Eilek, J. 1999, in Diffuse Thermal and Relativistic Plasma in Galaxy Clusters, 71

Eke, V. R., Navarro, J. F., & Frenk, C. S. 1998, ApJ, 503, 569

Ensslin, T. A., Biermann, P. L., Klein, U., & Kohle, S. 1998, A&A, 332, 395

Enßlin, T. A. & Gopal-Krishna. 2001, A&A, 366, 26

Ettori, S. & Fabian, A. C. 1999, MNRAS, 305, 834

Evrard, A. E. 1991, MNRAS, 248, 8P

Evrard, A. E., Metzler, C. A., & Navarro, J. F. 1996, ApJ, 469, 494

Ezawa, H., Fukazawa, Y., Makishima, K., et al. 1997, ApJL, 490, L33

Fabian, A. C. 1994, ARA&A, 32, 277

—. 2001, Proc. of XXI Moriond Conference: Galaxy Clusters and the High Redshift Universe Observed in X-rays, ed. by D. Neumann, F. Durret, & J. Tran Thanh Van, in press

Fabian, A. C. & Allen, S. W. 2003, in Texas in Tuscany. XXI Symposium on Relativistic Astrophysics, 197

Fabian, A. C., Sanders, J. S., Ettori, S., et al. 2000, MNRAS, 318, L65

Feretti, L. 1999, in Diffuse Thermal and Relativistic Plasma in Galaxy Clusters, 3–8

Feretti, L., Dallacasa, D., Govoni, F., et al. 1999, A&A, 344, 472

Feretti, L., Fusco-Femiano, R., Giovannini, G., & Govoni, F. 2001, A&A, 373, 106

Fermi, E. 1949, Phys. Rev, 75, 1169

Ferreras, I. & Silk, J. 2000, ApJL, 541, L37

Finoguenov, A., Reiprich, T. H., & Böhringer, H. 2001, A&A, 368, 749

Fischer, G.and Schwope, A. D., H., B., Boller, T., et al. 1998, Astronomische Nachrichten, 319, 347

Fitt, A. J. & Alexander, P. 1993, MNRAS, 261, 445

Florido, E. & Battaner, E. 1997, A&A, 327, 1

Ford, K. W., Rubin, V. C., & Roberts, M. S. 1971, AJ, 76, 22

Freedman, W. L. 1994, Bulletin of the American Astronomical Society, 26, 1473

Fujita, Y., Takizawa, M., Nagashima, M., & Enoki, M. 1999, PASJ, 51, L1

Fujita, Y., Takizawa, M., & Sarazin, C. L. 2003, ApJ, 584, 190

Fukazawa, Y., Makishima, K., Tamura, T., et al. 1998, PASJ, 50, 187

Fukugita, M., Doi, M., Dressler, A., & Gunn, J. E. 1995, ApJ, 439, 584

Furlanetto, S. R. & Loeb, A. 2001, ApJ, 556, 619

Fusco-Femiano, R., Dal Fiume, D., De Grandi, S., et al. 2000, ApJL, 534, L7

Fusco-Femiano, R., dal Fiume, D., Feretti, L., et al. 1999, ApJL, 513, L21

Gabici, S. & Blasi, P. 2003, ApJ, 583, 695

Gastaldello, F. & Molendi, S. 2002, ApJ, 572, 160

Geiger, B. & Schneider, P. 1999, MNRAS, 302, 118

Giovannini, G. & Feretti, L. 2000, New Astronomy, 5, 335

Giovannini, G., Tordi, M., & Feretti, L. 1999, New Astronomy, 4, 141

Girardi, M., Giuricin, G., Mardirossian, F., Mezzetti, M., & Boschin, W. 1998, ApJ, 505, 74

Gitti, M., Brunetti, G., & Setti, G. 2002, A&A, 386, 456

Gnedin, N. Y. 1998, MNRAS, 294, 407

Goldshmidt, O. & Rephaeli, Y. 1993, ApJ, 411, 518

Golla, G., Allen, M. L., & Kronberg, P. P. 1996, ApJ, 473, 244

Golla, G. & Hummel, E. 1994, A&A, 284, 777

Govoni, F., Feretti, L., Giovannini, G., et al. 2001a, A&A, 376, 803

Govoni, F., Taylor, G. B., Dallacasa, D., Feretti, L., & Giovannini, G. 2001b, A&A, 379, 807

Gunn, J. E. & Gott, J. R. I. 1972, ApJ, 176, 1

Hall, J. S. 1949, Science, 109, 166

Han, J. L. & Qiao, G. J. 1994, A&A, 288, 759

Hanasz, M. & Lesch, H. 1993, in IAU Symp. 157: The Cosmic Dynamo, 403

Heiles, C. 1990, in IAU Symp. 140: Galactic and Intergalactic Magnetic Fields, 35–40

Heinz, S., Reynolds, C. S., & Begelman, M. C. 1998, ApJ, 501, 126

Hiltner, W. A. 1949, Science, 109, 165

Hjorth, J., Oukbir, J., & van Kampen, E. 1998, MNRAS, 298, L1

Ho, L. C., Feigelson, E. D., Townsley, L. K., et al. 2001, ApJL, 549, L51

Ho, L. C., Filippenko, A. V., & Sargent, W. L. W. 1997a, ApJ, 487, 568

—. 1997b, ApJ, 487, 579

Ho, L. C. & Ulvestad, J. S. 2001, ApJS, 133, 77

Horner, D. J., Mushotzky, R. F., & Scharf, C. A. 1999, ApJ, 520, 78

Huang, Z. & Sarazin, C. L. 1998, ApJ, 496, 728

Ikebe, Y., Makishima, K., Ezawa, H., et al. 1997, ApJ, 481, 660

Ikebe, Y., Makishima, K., Fukazawa, Y., et al. 1999, ApJ, 525, 58

Irwin, J. A., Bregman, J. N., & Evrard, A. E. 1999, ApJ, 519, 518

Iwasawa, K., Fabian, A. C., Allen, S. W., & Ettori, S. 2001, MNRAS, 328, L5

Iye, M., Iwamuro, F., Maihara, T., et al. 2000, PASJ, 52, 9

Jenkins, A., Frenk, C. S., Pearce, F. R., et al. 1998, ApJ, 499, 20

Johnstone, R. M., Allen, S. W., Fabian, A. C., & Sanders, J. S. 2002, MNRAS, 336, 299

Jones, C. & Forman, W. 1999, ApJ, 511, 65

Kaaret, P. 2001, ApJ, 560, 715

Kaastra, J. S., Ferrigno, C., Tamura, T., et al. 2001, A&A, 365, L99

Kaastra, J. S. & Mewe, R. 1993, A&AS, 97, 443

Kahn, F. D. 1994, Ap&SS, 216, 325

Kaiser, C. R. & Binney, J. 2003, MNRAS, 338, 837

Kempner, J. C. & Sarazin, C. L. 2001, ApJ, 548, 639

Kikuchi, K., Furusho, T., Ezawa, H., et al. 1999, PASJ, 51, 301

Kim, W. & Narayan, R. 2003, ApJL, 596, L139

King, I. 1962, AJ, 67, 471

Klein, U., Wielebinski, R., & Morsi, H. W. 1988, A&A, 190, 41

Knapen, J. H. 1998, MNRAS, 297, 255

Knapen, J. H. & Beckman, J. E. 1996, MNRAS, 283, 251

Knapen, J. H., Beckman, J. E., Heller, C. H., Shlosman, I., & de Jong, R. S. 1995a, ApJ, 454, 623

Knapen, J. H., Beckman, J. E., Shlosman, I., et al. 1995b, ApJL, 443, L73

Knapen, J. H., Cepa, J., Beckman, J. E., Soledad del Rio, M., & Pedlar, A. 1993, ApJ, 416, 563

Knapen, J. H., Shlosman, I., Heller, C. H., et al. 2000, ApJ, 528, 219

Knapik, J., Soida, M., Dettmar, R.-J., Beck, R., & Urbanik, M. 2000, A&A, 362, 910

Kodama, T., Smail, I., Nakata, F., Okamura, S., & Bower, R. G. 2001, ApJL, 562, L9

Kohno, K., Vila-Vilaró, B., Sakamoto, S., et al. 2003, PASJ, 55, 103

Koratkar, A., Deustua, S. E., Heckman, T., et al. 1995, ApJ, 440, 132

Kormendy, J. & Richstone, D. 1995, ARA&A, 33, 581

Kronberg, P. P. 1994, Rep. Prog. Phys., 57, 325

—. 1996, Space Science Reviews, 75, 387

Kronberg, P. P., Lesch, H., & Hopp, U. 1999, ApJ, 511, 56

Kronberg, P. P. & Perry, J. J. 1982, ApJ, 263, 518

Kulsrud, R. M. 1999, ARA&A, 37, 37

Lesch, H. & Chiba, M. 1997, Fundamentals of Cosmic Physics, 18, 273

Lewis, A. D., Stocke, J. T., & Buote, D. A. 2002, ApJL, 573, L13

Liang, H., Hunstead, R. W., Birkinshaw, M., & Andreani, P. 2000, ApJ, 544, 686

Liedahl, D. A., Osterheld, A. L., & Goldstein, W. H. 1995, ApJL, 438, L115

Lieu, R., Mittaz, J. P. D., Bowyer, S., et al. 1996, Science, 274, 1335

Lumb, D. H., Warwick, R. S., Page, M., & De Luca, A. 2002, astro-ph/0204147, A&A accepted

MacKenty, J. W., Simkin, S. M., Griffiths, R. E., Ulvestad, J. S., & Wilson, A. S. 1994, ApJ, 435, 71

Majerowicz, S., Neumann, D. M., & Reiprich, T. H. 2002, A&A, 394, 77

Markevitch, M., Forman, W. R., Sarazin, C. L., & Vikhlinin, A. 1998, ApJ, 503, 77

Markevitch, M., Vikhlinin, A., Forman, W. R., & Sarazin, C. L. 1999, ApJ, 527, 545

Martin, C. L., Lotz, J., & Ferguson, H. C. 2000, ApJ, 543, 97

Matsumoto, H., Koyama, K., Awaki, H., et al. 1996, PASJ, 48, 201

Matsumoto, H., Tsuru, T. G., Fukazawa, Y., Hattori, M., & Davis, D. S. 2000, PASJ, 52, 153

McNamara, B. R. 2001, Proc. of the IAP 2000 Conf. Constructing the Universe with Clusters of Galaxies, ed. F. Durret, & D. Gerbal [astro-ph/0012331]

McNamara, B. R., Wise, M., Nulsen, P. E. J., et al. 2000, ApJL, 534, L135

Mediavilla, E. & Arribas, S. 1993, Nature, 365, 420

Mediavilla, E., Arribas, S., Garcia-Lorenzo, B., & del Burgo, C. 1997, ApJ, 488, 682

—. 1998, ApJL, 494, L9

Mellier, Y. 1999, ARA&A, 37, 127

Metzler, C. A. & Evrard, A. E. 1994, ApJ, 437, 564

—. 1997, astro-ph/0204147

Mohr, J. J. & Evrard, A. E. 1997, ApJ, 491, 38

Mohr, J. J., Mathiesen, B., & Evrard, A. E. 1999, ApJ, 517, 627

Molendi, S. & Gastaldello, F. 2001, A&A, 375, L14

Molendi, S. & Pizzolato, F. 2001, ApJ, 560, 194

Molikawa, K., Hattori, M., Kneib, J., & Yamashita, K. 1999, A&A, 351, 413

Moss, D. & Shukurov, A. 1996, MNRAS, 279, 229

Murakami, I. & Babul, A. 1999, MNRAS, 309, 161

Mushotzky, R. F. & Loewenstein, M. 1997, ApJL, 481, L63

Narayan, R. & Medvedev, M. V. 2001, ApJL, 562, L129

Navarro, J. F., Frenk, C. S., & White, S. D. M. 1995, MNRAS, 275, 56

Neininger, N. 1992, A&A, 263, 30

Neumann, D. M. & Arnaud, M. 1999, A&A, 348, 711

Nevalainen, J., Markevitch, M., & Forman, W. 2000, ApJ, 532, 694

Osterbrock, D. E. 1989, Astrophysics of gaseous nebulae and active galactic nuclei (Research supported by the University of California, John Simon Guggenheim Memorial Foundation, University of Minnesota, et al. Mill Valley, CA, University Science Books, 1989, 422 p.)

Peres, C. B., Fabian, A. C., Edge, A. C., et al. 1998, MNRAS, 298, 416

Peterson, J. R., Paerels, F. B. S., Kaastra, J. S., et al. 2001, A&A, 365, L104

—. 2003, High Resolution Spectroscopy of 14 Cooling-Flow Clusters of Galaxies Using the Reflection Grating Spectrometers on XMM-Newton, in New visions of the Universe in the XMM-Newton and Chandra era, in the press.

Petrosian, V. 2001, ApJ, 557, 560

Phillipps, S., Kearsey, S., Osborne, J. L., Haslam, C. G. T., & Stoffel, H. 1981, A&A, 98, 286

Pierce, M. J. 1986, AJ, 92, 285

Piffaretti, R., Jetzer, P., & Schindler, S. 2003, A&A, 398, 41

Poggianti, B. M., Smail, I., Dressler, A., et al. 1999, ApJ, 518, 576

Ponman, T. J., Cannon, D. B., & Navarro, J. F. 1999, Nature, 397, 135

Pratt, G. W., Arnaud, M., & Aghanim, N. 2002, Conf. proc. 'Galaxy Clusters and the High Redshift Universe Observed in X-rays', XXIth Moriond Astrophysics Meeting, astro-ph/0105431

Rand, R. J. 1995, AJ, 109, 2444

Rees, M. J. 1994, in NATO ASIC Proc. 422: Cosmical Magnetism, 155

Reiprich, T. H. & Böhringer, H. 1999, in Proceedings of the Workshop: Diffuse Thermal and Relativistic Plasma in Galaxy Clusters, 157

Rephaeli, Y., Gruber, D., & Blanco, P. 1999, ApJL, 511, L21

Reuter, H.-P., Klein, U., Lesch, H., Wielebinski, R., & Kronberg, P. P. 1992, A&A, 256, 10

—. 1994, A&A, 282, 724

Reynolds, C. S., Heinz, S., & Begelman, M. C. 2001, ApJL, 549, L179

Richstone, D., Loeb, A., & Turner, E. L. 1992, ApJ, 393, 477

Ricker, P. M. & Sarazin, C. L. 2001a, ApJ, 561, 621

—. 2001b, ApJ, 561, 621

Ritchie, B. W. & Thomas, P. A. 2002, MNRAS, 329, 675

Roettiger, K., Stone, J. M., & Burns, J. O. 1999, ApJ, 518, 594

Ruzmaikin, A., Sokolov, D., & Shukurov, A. 1989, MNRAS, 241, 1

Ruzmaikin, D. D., Shukurov, A. M., A. A., & Sokolov. 1988, Magnetic fields of galaxies (Kluwer Academic Publisher, Dordrecht)

Sakamoto, K., Okumura, S., Minezaki, T., Kobayashi, Y., & Wada, K. 1995, AJ, 110, 2075

Sakelliou, I., Peterson, J. R., Tamura, T., et al. 2002, A&A, 391, 903

Sanders, J. S. & Fabian, A. C. 2002, MNRAS, 331, 273

Sarazin, C. L. 1999, ApJ, 520, 529

—. 2001, Proc. of XXI Moriond Conference: Galaxy Clusters and the High Redshift Universe Observed in X-rays, ed. by D. Neumann, F. Durret, & J. Tran Thanh Van, in press

Sarazin, C. L., Wise, M. W., & Markevitch, M. L. 1998, ApJ, 498, 606

Schindler, S. 1996a, MNRAS, 280, 309

—. 1996b, A&A, 305, 756

—. 1999, A&A, 349, 435

—. 2002, Review for Astrophysics and Space Science Library: Mergering Processs in Galaxy Clusters' L. Feretti, I.M. Gioia and G. Giovannini (eds.) Kluwer Academic Publishers, Dordrecht, 229

Schindler, S., Belloni, P., Ikebe, Y., et al. 1998, A&A, 338, 843

Schindler, S., Castillo-Morales, A., De Filippis, E., Schwope, A., & Wambsganss, J. 2001, A&A, 376, L27

Schindler, S. & Müller, E. 1993, A&A, 272, 137

Schindler, S. & Wambsganss, J. 1996, A&A, 313, 113

Schmidt, R. W., Allen, S. W., & Fabian, A. C. 2001, MNRAS, 327, 1057

Schmidt, R. W., Fabian, A. C., & Sanders, J. S. 2002, MNRAS, 337, 71

Schwope, A., Hasinger, G., Lehmann, I., et al. 2000, Astronomische Nachrichten, 321, 1

Seitz, C., Kneib, J.-P., Schneider, P., & Seitz, S. 1996, A&A, 314, 707

Shlosman, I. 1999, in ASP Conf. Ser. 187: The Evolution of Galaxies on Cosmological Timescales, 100–114

Smail, I., Morrison, G., Gray, M. E., et al. 1999, ApJ, 525, 609

Smith, D. A., Wilson, A. S., Arnaud, K. A., Terashima, Y., & Young, A. J. 2002, ApJ, 565, 195

Snowden, S. L., Egger, R., Freyberg, M. J., et al. 1997, ApJ, 485, 125

Soida, M., Beck, R., Urbanik, M., & Braine, J. 2002, A&A, 394, 47

Spergel, D. N., Verde, L., Peiris, H. V., et al. 2003, astro-ph/0302209

Stanford, S. A., Eisenhardt, P. R. M., & Dickinson, M. 1995, ApJ, 450, 512

Stanford, S. A., Holden, B., Rosati, P., et al. 2001, ApJ, 552, 504

Tüllmann, R., Dettmar, R.-J., Soida, M., Urbanik, M., & Rossa, J. 2000, A&A, 364, L36

Takizawa, M. 1999, ApJ, 520, 514

—. 2000, ApJ, 532, 183

Tamura, T., Day, C. S., Fukazawa, Y., et al. 1996, PASJ, 48, 671

Tamura, T., Kaastra, J. S., Peterson, J. R., et al. 2001, A&A, 365, L87

Taylor, G. B., Govoni, F., Allen, S. W., & Fabian, A. C. 2001, MNRAS, 326, 2

Terashima, Y., Kunieda, H., & Misaki, K. 1999, PASJ, 51, 277

Thean, A. H. C., Mundell, C. G., Pedlar, A., & Nicholson, R. A. 1997, MNRAS, 290, 15

Thomas, P. A., Colberg, J. M., Couchman, H. M. P., et al. 1998, MNRAS, 296, 1061

Tsuru, T. G., Matsumoto, H., Koyama, K., et al. 1997, [astro-ph/9711353]

Tucker, W. H. & Rosner, R. 1983, ApJ, 267, 547

Vallee, J. P. 1997, Fundamentals of Cosmic Physics, 19, 1

van der Kruit, P. C. & Bosma, A. 1978, A&AS, 34, 259

Vikhlinin, A., Forman, W., & Jones, C. 1999, ApJ, 525, 47

Voigt, L. M. & Fabian, A. C. 2004, MNRAS, 347, 1130

Voigt, L. M., Schmidt, R. W., Fabian, A. C., Allen, S. W., & Johnstone, R. M. 2002, MNRAS, 335, L7

Wambsganss, J. 1998, Living Reviews in Relativity, 1, 12

White, D. A. 2000, MNRAS, 312, 663

White, D. A., Jones, C., & Forman, W. 1997, MNRAS, 292, 419

White, S. D. M., Navarro, J. F., Evrard, A. E., & Frenk, C. S. 1993, Nature, 366, 429

Widrow, L. M. 2002, Reviews of Modern Physics, 74, 775

Wilson, A. S., Braatz, J. A., Heckman, T. M., Krolik, J. H., & Miley, G. K. 1993, ApJL, 419, L61

Wozniak, H., Friedli, D., Martinet, L., & Pfenniger, D. 1997, in Extragalactic Astronomy in the Infrared, 77

Wozniak, H., Friedli, D., Martinet, L., & Pfenniger, D. 1998, A&A, 330, L5

Xu, H., Ezawa, H., Fukazawa, Y., et al. 1997, PASJ, 49, 9

Ziegler, B. L., Saglia, R. P., Bender, R., et al. 1999, A&A, 346, 13

Zweibel, E. G. & Heiles, C. 1997, Nature, 385, 131

Zwicky, F. 1933, Helv. Phys. Act 6, 110